Solid organics in small icy bodies : experimental approaches and interpretation of VIRTIS/Rosetta spectral data

Istiqomah Istiqomah

THÈSE

Pour obtenir le grade de

DOCTEUR DE l' UNIVERSITE GRENOBLE ALPES

Spécialité : Sciences de la Terre et de l'Univers et de l'Environnement (CESTUE)

Arrêté ministériel : 25 mai 2016

Présentée par

ISTIQOMAH

Thèse dirigée par **Eric QUIRICO,** Enseignant-chercheur, Université Grenoble Alpes, et
codirigée par **Patrice THEULÉ,** Enseignant-chercheur, Université d'Aix-Marseille

préparée au sein d**e l'nstitut de Planétologie et d'Astrophysique de Grenoble**
dans **l'École Doctorale Terre, Univers, Environnement**

Solides organiques dans les petits corps glacés : approches expérimentales et interprétation des données spectrales issues de mission VIRTIS/Rosetta

Solid organics in small icy bodies: experimental approaches and interpretation of VIRTIS/Rosetta spectral data

Thèse soutenue publiquement le **12 mars 2020**,
devant le jury composé de :

M. Eric QUIRICO
Professeur, Université Grenoble Alpes, Directeur de thèse
M. Patrice THEULÉ
Maître de conférences, Université d'Aix-Marseille, Co-directeur de thèse
M. Rosario BRUNETTO
Chargé de recherche, Université Paris-Sud, Rapporteur
M. Nicolas FRAY
Maître de conférences, Université Paris-Est Créteil, Rapporteur
Mme. Aurore BACMANN
Astronome, Université Grenoble Alpes, Présidente
Mme. Cécile ENGRAND
Directrice de recherche, Université Paris-Sud, Examinatrice

Acknowledgement

Foremost, I would like to express my sincere gratitude to my supervisors Eric Quirico and Patrice Theulé for the continuous support of my study and research, for their patience, motivation, enthusiasm, and immense knowledge. Their guidance helped me in all the time of research and writing of this thesis. I could not have imagined having better supervisors and mentors for my study.

My sincere thanks also goes to colleagues of Classolarys team: Bernard Schmitt and Pierre Beck for their scientific discussion about reflectance measurements, Olivier Poch for teaching me to prepare ice-dust mixture, Olivier Brissaud and Sandra Potin for their assistance during my experiment with spectrometer, Lydie Bonal and Jolantha Eschrig for helping me in micromanipulation room and operating microscope IR, Robin Sultana for his discussion of grinding protocols and SEM results, Thi Hai Van Phan for helping me with IGOR, Laurenne Flandinet for her kindness to help me in chemical room, and also Valerie Chopin and Fabienne Boucard for helping me in administration stuff. I also thank the colleagues whom I have chance for their collaboration and discussion: Alexandre Faure, Donia Baklouti, Mauro Ciarniello, Gianrico Fillachione, Andrea Raponi, Ljuba Moroz and Batiste Rousseau.

I would like also to express my gratitude to the LPDP (Indonesia Endowment Fund for Education) scholarship and my working place, National Standardization Agency (BSN) for giving me opportunity to continue my study.

Last but not the least, I would like to thank my family: my parents, my sister and my husband for supporting me spiritually throughout my life.

. . . .everything is gliding along smoothly in its orbit.

Abstract

The Rosetta space mission explored comet 67P/Churyumov-Gerasimenko between July 2014 and September 2016. During two years, extensive mappings in the visible and infrared ranges have been achieved by the VIRTIS imaging spectrometer (Visible InfraRed Thermal Imaging Spectrometer). This instrument has revealed a very dark and reddish surface, which has been interpreted by the presence of a dark carbonaceous material mixed up with opaque minerals (presumable Fe-Ni alloys and pyrrhotite). VIRTIS has also revealed, for the first for a comet, a broad band at 3.2 µm. The nature of this band was unclear at the beginning of this thesis, and two main semi-volatile compounds were suspected: ammonium salts and carboxylic acids.

In this thesis, we have investigated these two hypotheses through laboratory experiments. We first conducted FTIR transmission experiments on pure solid carboxylic acids and ammonium salts. In a second step, we collected reflectance spectra of analogs of the refractory crust. A particular attention was devoted to the production of such analogs, and we developed dedicated grinding and mixing protocols. We found that the most suitable analogs are those produced from the sublimation of ice + refractory + semi-volatile mixtures in a vacuum chamber. They account well for the fine-grained and highly porous cometary material. Our experiments show that the 3.2 µm band in VIRTIS spectra is consistent with the presence of ammonium salt, which is ubiquitous across the surface of the comet. These ammonium salts constitute a new reservoir of nitrogen in comet, which might at least partially account for the missing nitrogen in comets.

The abundance of the ammonium salt could however not be determined. Our experiments reveal the lack of between the band depth and the ammonium abundance in the samples, pointing that the parameters that control the band depth are not elucidated yet. This result points to the difficult question of the characterization of the porous texture of the sublimation residues and of their complex geometries. The grain size distribution is definitely only one parameter among other ones, and future studies should focus on this point. At last, the modeling approaches based on Hapke models are definitely not suitable for these dark semi-volatile bearing materials, and great care should be devoted with values published so far in literature.

Keywords: comet 67P/ Churyumov-Gerasimenko, Rosetta/VIRTIS, reflectance spectroscopy, carboxylic acids, ammonium salt

Résumé

La mission spatiale Rosetta a exploré la comète 67P/Churyumov-Gerasimenko entre Juillet 2014 et Septembre 2016. Pendant deux ans, des cartographies du noyau dans le visible et l'infrarouge ont été conduites par l'instrument VIRTIS (Visible InfraRed Thermal Imaging Spectrometer). Cet instrument a révélé une surface rougissante très sombre, interprétée par la présence d'un composé carboné réfractaire mélangé à des minéraux opaques (alliages Fe-Ni et/ou pyrrhotite). VIRTIS a aussi révél, pour la première fois dans le cas d'une comète, une bande large centrée à 3.2 µm. La nature de cette bande n'était pas clairement identifiée au début de cette thèse, et deux composés semi-volatile étaient suspectés: l'ion ammonium et un/des acides carboxyliques.

Dans cette thèse, nous avons exploré ces deux hypothèses au travers d'expériences de laboratoire. Nous avons en premier lieu conduit des mesures FTIR en transmission sur des acides carboxyliques l'état solide et des sels d'ammonium. Dans un second temps, nous avons collectés des spectres de réflectance de matériaux modèles de la croûte cométaire. Une attention particulière a été déployée à la synthèse de ces matériaux modèle, et nous avons développé des protocoles dédiés de broyage et de mélange. Nous montrons que les matériaux modèle les plus représentatif de la croûte cométaire sont des résidus de sublimation formé en chambre sous vide à partir de mélange glace + réfractaires + semi-volatiles. Ils rendent bien compte de son état finement divisé et de forte porosité. Nos expériences montrent que la bande à 3.2 µm dans les spectres VIRTIS est liée à la présence de l'ion ammonium, qui semble ubiquite à la surface de la comète. Ces sels d'ammonium constitue un nouveau réservoir d'azote cométaire, et pourrait, au moins partiellement, rendre compte de l'azote manquant dans les comètes.

La concentration des sels d'ammonium n'a toutefois pas pu être déterminée. Nos expériences ne montrent pas de corrélation entre la profondeur de la bande et la tenur en ions ammonium dans les échantillons, montrant que les paramètres contrôlant l'intensité de cette bande ne sont pas élucidés. Ce résult renvoie à la question difficile de la caractérisation de la porosité des échantillons et de leur géométrie complexe d'un point de vue topologique. La distribution en taille de grain n'est qu'un paramètre parmi d'autres, and les études futures devront se concentrer sur ce point. Enfin, l'approche de modélisation basée sur de modèles de Hapke n'est pas adaptée à ce type de matériaux très sombre, and les résultats publiés antérieurement doivent être considérés avec prudence.

Table of contents

Introduction

Comets are assumed to be the most primitive bodies in our solar system. They were formed on the eve of our solar system 4.567 gigayears ago, in low temperature conditions that led to the accretion of local gases as ices. In addition, they have largely escaped post-accretional processes, and in this respect they potentially provide insightful information on the gas and dust composition, and the physical conditions that were at play in the solar nebula. In particular, their organics should provide insights into the carbon chemistry in the proto-solar disk and/or the local interstellar medium, and overall the origin of volatiles in telluric planets.

The Rosetta mission explored the comet 67P/Churyumov-Gerasimenko during July 2014 and September 2016. It was the first space mission that escorted a comet during two years, boarding 20 instruments that have provided unprecedented data on surface composition and morphology, the internal structure of the nucleus, the composition of the coma (dust and gas), and overall it monitored the comet activity before and after perihelion, providing insightful data on the mechanisms of cometary activity.

The VIRTIS imaging spectrometer has extensively mapped the surface of the nucleus in the visible and near-infrared (VNIR) (Capaccioni et al., 2015). The spectra revealed a rather homogeneous, dehydrated, reddish and dark crust, and for the first time in the case of comets, a broad band centered at 3.2 µm band, whose interpretation was unclear at the beginning of this thesis. At that time, two plausible candidates emerged (Quirico et al., 2016): carboxylic acids in the solid state and ammonium salts.

The objective of this thesis was to investigate these hypotheses by means of laboratory experiments. We will show that the 3.2 µm band is mostly due to the presence of ammonium ions that are distributed homogeneously at the surface of the nucleus. For this purpose, we have developed experimental protocols for producing relevant cometary analogs and measured their optical properties, in particular by means of the spectro-gonio-radiometer instruments developed at IPAG. This thesis was part of an international collaboration with the VIRTIS team, in particular with Gianrico Fillachione, Mauro Ciarniello and Andrea Raponi (INAF - Roma).

The manuscript is organized as following, Chapter 1 presents generalities on the Rosetta mission and the VIRTIS instrument. Chapter 2 presents the instrumental set-ups that were used, and details on the procedure that were developed for producing analogs. Chapter 3 reports transmission FTIR measurements made on carboxylic acids and ammonium salts. Chapter 4

reports the reflectance measurements collected in the range 0.4-5.0 μm by means of the SHINE spectro-gonio-radiometer. Finally, a conclusion summarizes the main results and outlines several pending issues that should be investigated in the future.

Chapter 1

The comet 67P/Churyumov-Gerasimenko investigated by the Rosetta mission

Our solar system is estimated to have formed 4.567 billions of years ago. Star explosion made an interstellar cloud squeezed and then underwent gravitational contraction which formed a protosun. The dust and gas around the protosun formed a protosolar disk, also named solar nebula. This disk grew denser and hotter at the center, and cool at the edges. Due to rotation, the disk became thinner and the particles stuck to each other to form bigger objects as planets, moons and small bodies. Close to the protosun, only gas and rocky materials were stable, whereas above the so-called snow line icy-rocky material could settle, forming the core of the giant planets, and icy small bodies.

Icy small bodies, i.e. comets, Trans-Neptunian Objects and Centaurs, are very primitive objects in the sense they escaped post-accretional processes like heating or fluid circulation. They can provide information on composition and early processes that were at play in the early solar system. In this framework, comets are of particular interest. Due to their small size and their perihelion close to the sun, a very primitive material made of ice and dust is accessible to ground-based observations and space mission exploration.

1.1 Reservoirs and internal structure and composition

Comets are classified as short and long period comets. Short period comets have periodicities below 200 years, whose around 60 % of them have periods between 5 and 6.5 years. The Kuiper belt is believed to be the main reservoir of short period comets. Short period comets are further divided into two groups: the Jupiter-family comets and Halley-type comets. The Jupiter family comets perform orbital periods smaller than 20 years, and are the most targeted by space missions, e.g. comets 2P/Encke, 9P/Tempel 1, 10P/Tempel 2, 19P/Borrelly, 21P/Giacobini-Zinner, 46P/Wirtanen, 67P/Churyumov-Gerasimenko, 81P/Wild 2, and 103P/Hartley. Halley-type comets have orbital periods ranging between 20 and 200 years, and the Halley comet was the target of the space missions GIOTTO and VEGA (Weissman et al., 2002). Long period comets have orbital periods larger than 200 years and they mainly originate from the Oort cloud. This reservoir is located beyond the outer solar system and extends halfway to alpha Centaury (around 50000 UA from the Sun). It was formed in the early time of the Solar System, by the

ejection of icy small bodies from the protosolar disk by gravitational perturbations triggered by giant planets migration (Rickman and Huebner, 1990; Oort, 1990).

The whole population of comet is estimated to be 10^{13} in the inner Oort cloud and 10^{11} numbers in the outer Oort cloud. The trajectory of long period comets can be perturbed by giant planets, when entering the solar system. Besides, some comets are ejected to become long period comets due to gravitational effects of Jupiter. Therefore, Jupiter family comets can be originated from both the Kuiper Belt and Oort cloud (A'Hearn, 2006).

Comets are small icy bodies that contain ice and dust. In 1950, Whipple proposed the cometary nucleus as conglomerates of water and volatile ices mixed with meteoritic material (refractory mineral) as dirty snowballs. This view has been more or less confirmed thanks to several cometary surveys by space missions, in particular the Rosetta mission. While the dust to mass ratio is still a controversial issue, we now know that a cometary nucleus is highly porous (>50 %) and brittle, and contains much refractories. It is basically made of three components: (1) simple ices, as H_2O, CO, CO_2, CH_3OH, etc. (Mumma and Charnley, 2011); (2) refractory dust, composed of ultramafic silicates (olivine and pyroxene), sulfides, glass and accessory minerals, along with a refractory carbonaceous material that resembles insoluble organic matter recovered in primitive meteorites (Fray et al., 2016; Bardyn et al., 2017); (3) semi-volatiles species, comprising organics and salts (Quirico et al., 2016). When the comet approaches the Sun, the heating of its surface and subsurface triggers ices sublimation, the formation of the coma and of jets. The ejection of dust and gas makes the bulk material accessible to remote sensing.

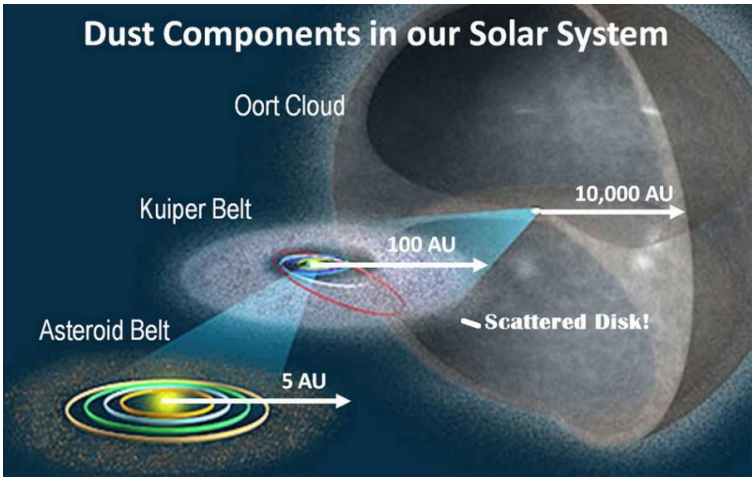

Figure 1.1. The Kuiper belt and Oort Cloud reservoirs, respective sources of short and long-period comets, credit: Jedimaster (https://www.schoolsobservatory.org).

1.2 Missions to comets: from 1986 to the Rosetta mission

Several missions have targeted comets in the past. The International Cometary Explorer (ICE) spacecraft has investigated the plasma tail of comet Giacobini-Zinner (G/Z) on September 11, 1985. The mission showed that the magnetic tail lobes are oppositely-polarized and separated by a current sheet (Brandt and Chapman, 1985).

In 1986, comet 1P/Halley was investigated by the missions Vega 1 and Vega 2, Sakigake, Suisei and Giotto. In the same time, the comet was observed from the ground (Reinhard, 1986). The Vega mission was composed of two independent and identical spacecrafts, Vega 1 and Vega 2. It contained 14 instruments dedicated to the study of the gas and dust composition, as well as structure and dynamics of the coma. The mass spectrometers of Vega revealed that cometary dust was dominated by sub-micrometric particles, which possibly consisted in a chondritic core coated by an organic mantle composed by unsaturated compounds (Kremnev, 1986). The infrared spectrometer detected H_2O and CO_2, and possibly C-H bearing materials. This spectrometer also recorded the temperature of the surface nucleus, as 300-400 K. The Giotto spacecraft operated by ESA investigated the nucleus of comet Halley. The camera (HMC) collected the first images of a cometary nucleus, revealing a dark (geometric albedo ~4 %) and irregular body with features of activity. Its surface was found to contain craters, valleys and hills. The density was estimated to be very low 0.2-0.55 g cm^{-3}, pointing to a very high porosity (Reinhard, 1986; Keller et al., 1987). Giotto also observed that the gas and dust emissions from the nucleus were not uniform, but mostly appeared as discrete jets coming from specific local area. The active area was only 10 % of the whole ssurface on the afternoon hemisphere, no active jets were detected during night time (Keller et al., 1986). The chemical composition of jets emission was also investigated. Simple molecules as water, carbon dioxide, formaldehyde, methane, methanol, ethane, ethylene, ammonia, acetylene, hydrogen sulfide and hydrogen cyanide were detected (Eberhardt, 1999). In addition, the PUMA mass spectrometer revealed for the first time the presence of a highly complex carbonaceous dust (Fomenkova and Chang, 1994).

In 1998, the Deep space spacecraft was designed to investigate comet 19P/Borelly. The cometary nucleus was found to consist of smooth and mottled terrains. Active jets were observed for the smooth terrains. The mottled terrains showed irregular pits, bumps, ridges and troughs. The geometric albedo of comet was found to range 0.01-0.03, where the smooth terrains were the darkest. The temperature of the comet surface was 300-345 K, which means the surface was basically devoid of ice materials (Soderblom et al., 2002).

In 2004, the Stardust mission investigated comet 81P/Wild and collected dust samples that were returned to Earth for analysis in the laboratory. The mineralogical composition of the dust was strikingly improved. Pyroxene, olivine and Ca-Al refractories were clearly identified, revealing that a large fraction of minerals were crystalline, reinforcing the view that comets were formed in the Solar System and weakening the idea of a significant interstellar heritage (Brownlee et al, 2004). Analysis of the carbonaceous material suggested a material sharing similarities with IOM extracted from chondrites, however contamination issues in the aerogel detectors seriously blurred the conclusions (Sandford et al., 2006, and see the comment addressed to this publication in a following issue of Science). Besides, comet Wild 2 was found to have an oblate shape, more spherical and round than comet Halley and its geometric albedo was 0.03.

In 2005, the investigation of comet 9P/Temple 1 by the Deep Impact mission revealed a very dark nucleus, and surface features interpreted as geological activities (A'Hearn et al., 2005). Infrared measurements potentially detected C-H bonds, and volatiles such as H_2O, C_2H_6, CH_3OH and HCN (A'Hearn et al., 2005). Combined ground-based observations detected strong volatiles emission after impact and revealed the existence of sub micrometric dust grains (Mumma et al., 2005).

The Stardust-NExT mission investigated Comet 9P/Tempel 1 and mostly revealed jet activity, morphological evolution of the surface with time, and the presence of complex molecules in dust particles (Veverka et al, 2013).

The ROSETTA mission is the more recent mission targeting a comet. It was operated by ESA and was the first mission escorting a comet that collected measurements during two years (July 2014-Septembre 2016). ROSETTA was a very ambitious mission, composed of an orbiter and a lander boarding 20 scientific instruments, and it provided a wealth of information that revolutionizes our view on comets. The target was comet 67P/Churyumov-Gerasimenko. This is a periodic Jupiter Family comet originating from the Kuiper Belt. It was discovered in 1969, and its orbit was modified several times in the past (at least in 1840 and 1959) due to the presence of Jupiter. The present orbital period is 6.57 years, and the perihelion is located at 1.24 AU.

The ROSETTA spacecraft was launched on March 2nd 2004 by an Ariane-5 rocket from the Guyana Space Center in Kourou. During its journey, Rosetta employed four planetary gravity assists (Earth-Mars-Earth-Earth) to collect sufficient energy for reaching the comet. Rosetta also surveyed two asteroids: 2867 Steins and 21 Lutetia. For energy saving, Rosetta started hibernation on July 2011 and was awakening on January 2014. On August 2014, Rosetta started

escorting the comet and collected the first global mapping. On November 2014, the Philae lander was delivered on the surface for performing in situ scientific measurements.

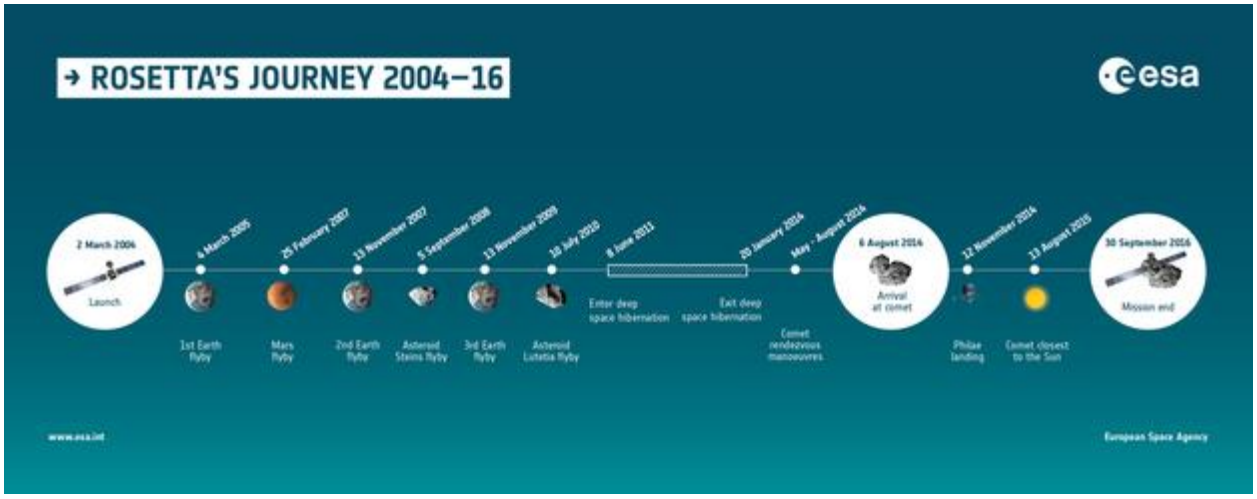

Figure 1.2. The dates of the Rosetta mission, credit: ESA.

The goals of the Rosetta mission were the general characterization of the nucleus, its surface morphology and composition, determination of chemical, mineralogical and isotopic compositions of volatiles and refractories in the cometary nucleus, the determination of the physical properties of the interior, the monitoring of the cometary activity and the processes in the surface layer of the nucleus and inner coma. To accomplish these goals, Rosetta was equipped with 10 scientific instrument on the orbiter and 10 instruments on the Lander, Philae.

The instruments of interest regarding the nucleus composition and surface are listed in the following table:

Table 1.1. Instruments of Rosetta orbiter and lander (Schulz and Schwehm, 1996; ESA)

Rosetta Orbiter Instruments		
Instrument		**Function**
Alice	Ultraviolet Imaging Spectrometer	Characterize the composition of the nucleus and coma by measuring noble gas abundances in the coma, the atomic budget in the coma, and major ion abundances in the tail and in the region where solar wind particles interact with the ionosphere of the come

Rosetta Orbiter Instruments		
Instrument		**Function**
CONSERT	Comet Nucleus Sounding Experiment by Radio wave Transmission	Performed tomography of the comet nucleus, by varying propagation delay as the radio waves pass through different parts of the nucleus to determine the dielectric properties of the nuclear material
COSIMA	Cometary Secondary Ion Mass Analyser	Secondary ion mass spectrometer equipped with a dust collector, a primary ion gun, and an optical microscope to characterize cometary dust particle
GIADA	Grain Impact Analyser and Dust Accumulator	Measure the scalar velocity, size and momentum of dust particles in the coma of the comet
MIDAS	Micro-Imaging Dust Analysis System	Micro-textural and statistical analysis of cometary dust particles based on the technique of atomic force microscopy
OSIRIS	Optical, Spectroscopic, and Infrared Remote Imaging System	It consisted dual camera to produce high spatial resolution images of the come nucleus by narrow angle camera and to image dust and gas above the surface of nucleus by wide angle camera
ROSINA	Rosetta Orbiter Spectrometer for Ion and Neutral Analysis	Determine the composition of the comet's atmosphere and ionosphere, measuring the temperature and bulk velocity of the gas and ions, and investigate their reactions
VIRTIS	Visible and Infrared Thermal Imaging Spectrometer	Performing spectral mapping and spectroscopy of nucleus surface
Rosetta Lander instruments		
APXS	Alpha Proton X-ray Spectrometer	Determining chemical composition of the landing site and its potential alteration during approaching the Sun

Rosetta Orbiter Instruments		
Instrument		**Function**
CIVA	Six identical micro-cameras take panoramic pictures	Study the composition, texture and albedo (reflectivity) of samples collected from the surface
CONSERT	COmet Nucleus Sounding Experiment by Radio-wave Transmission	Also founded in Orbiter
COSAC	COmetary SAmpling and Composition experiment	Detection and identification of complex organic molecules
Ptolemy	Termed of MODULUS Methods Of Determining and Understanding Light elements from Unequivocal Stable	▪ Evaluating the link between water ice on a comet and major bodies of water on Earth ▪ Determining the nature of low temperature mineral components present on a comet and decipher the formation history of such materials ▪ Assessing the relationship of organic compounds in comet with equivalent materials known from other solar system reservoirs
SD2	Sampling, drilling and distribution	Providing microscopes and advanced gas analysers with samples collected at different depths below the surface of the comet

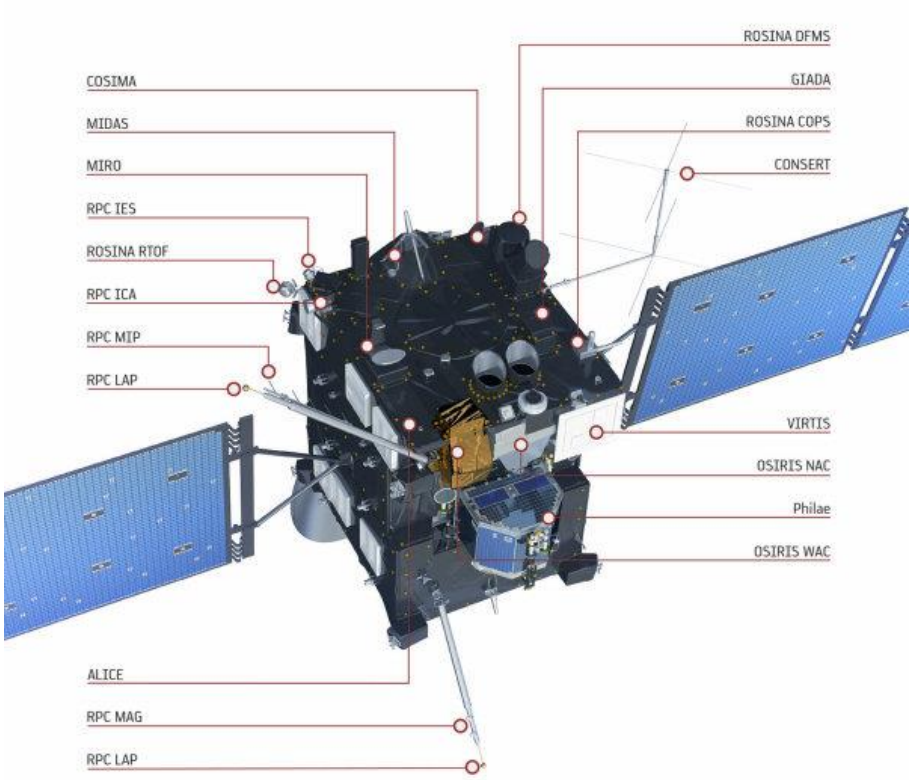

Figure 1.3. Rosetta Orbiter and its instruments, credit: ESA.

At the beginning of this thesis, several results had been obtained. The nucleus of the comet has a bi-lobed irregular shape. It looks like a duck, consisting in two lobes connected through a short neck. The size of the small lobe is around 2.50 km x 2.14 km x 1.64 km large, and the lobe size is around 4.10 km x 3.52 km x 1.63 km large. The bulk density is estimated to 0.532 g/cm^3, smaller than ice density, corresponding to a porosity of around 80 %. Along with COSIMA, GIADA and MIDAS observation, the refractory dust appears as a very fine-grained material, forming a very brittle bulk material (Rotundi et al., 2015; Bentley et al., 2016). The CONSERT measurements suggest a low porosity in the uppermost subsurface, which remains however elevated (~50 %) (Ciarletti et al., 2017). The gas composition in the coma has been thoroughly characterized by the ROSINA instrument (LeRoy et al., 2015; Altwegg et al., 2019). The analysis of refractory dust in the coma by the COSIMA instrument has shown they are composed of 55 % of a carbonaceous macromolecular material and 45 % of anhydrous minerals (Bardyn et al., 2017; Fray et al., 2016). Unfortunately, semi-volatile species could not be thoroughly analyzed by the COSAC and PTOLEMY instruments, due to the lack of ground sampling by the lander due to its attitude after landing. Nevertheless, as we shall see below, the VIRTIS instrument finally provided new clues on the nature of semi-volatiles. The ROSINA instrument led to similar detections and interpretations in the same time.

1.3 The VIRTIS instrument

Hyperspectral imaging in the visible and infrared ranges (VNIR) is a valuable technique for investigating the composition of planetary surfaces. It provides chemical and mineralogical insights into the composition of the surface and the temperature if the thermal flux is collected. The near infrared region displays vibrational bands of many molecules. Here, we describe the Visible InfraRed and Thermal Imaging Spectrometer VIRTIS that was aboard the Rosetta spacecraft.

VIRTIS consists in three channels. The two channels of VIRTIS-M, in the visible (0.25-1 µm) and infrared ranges (1-5 µm), operate in imaging mode with a high spatial resolution and are suitable for nucleus spectral imaging at moderate spectral resolution. The high spectral resolution channel VIRTIS-H is dedicated to the spectroscopy of the coma. The scientific goals of VIRTIS are to study of the cometary nucleus and its environment, to determine the nature of the solids at the nucleus surface, to evaluate the nucleus surface temperature and to characterize the physical conditions and composition of the coma, including dust and gas (Coradini et al., 2007).

The optical system of VIRTIS-M and VIRTIS-H is housed in a cold box at 130 K (Fig. 1.4). VIRTIS-M uses a silicon charge coupled device (CCD) for imaging in the range 0.25-1 µm, and a mercury cadmium telluride infrared focal plane array (IRFPA) for imaging in the range 1-5 µm. VIRTIS-H uses a similar HgCdTe IRFPA to operate in the range 2-5 µm. The electronic device is under cooling to minimize the detector dark current. The CCD is cooled at 155 K and the IRFPA is connected to a Stirling cycle cooler to reach 70 K. VIRTIS-M and VIRTIS-H instruments are protected from direct Sun illumination and keep the cold environment inside the Cold Box by covers (Coradini et al., 2007).

VIRTIS-M collects hyperspectral images as data cubes. The split opening of the spectrometer gives the first spatial dimension. The scanning due to the displacement of the spacecraft on its trajectory makes it possible to acquire the second spatial dimension and thus obtaining cartographies at high spatial resolution. To describe the three dimensions of a data cube, specific terms are used. Spectroscopic information is recorded on the spectral axis that is divided into different bands. After calibration, each band can be associated with a wavelength λ. The spatial information is recorded along the axis of the slit and the scan axis due to the spacecraft motion, and is respectively associated with a position (x, y) of the image (Fig. 1.5). The optical instrument combines a Shafer telescope and an Offner grating spectrometer (Fig. 1.6) to disperse a line image across two focal plane arrays. The advantage of the Offner

spectrometer is to simplify the fabrication process and to minimize the volume and mass (Coradini et al, 2007).

The spectral resolution of VIRTIS-M lies in the range 100-300 and allows detecting strong and intense absorption bands such as the band of water ice at 3 μm and organic compounds at 3.4 μm. The high spatial resolution VIRTIS-M (which may be less than one meter per pixel for some distances from the cometary nucleus probe) must make it possible to precisely describe the spatial distribution of surface composition and to follow the localized evolution due to the cometary activity in some regions. Finally, the VIRTIS instrument measures the temperature of the surface cometary during its orbital evolution.

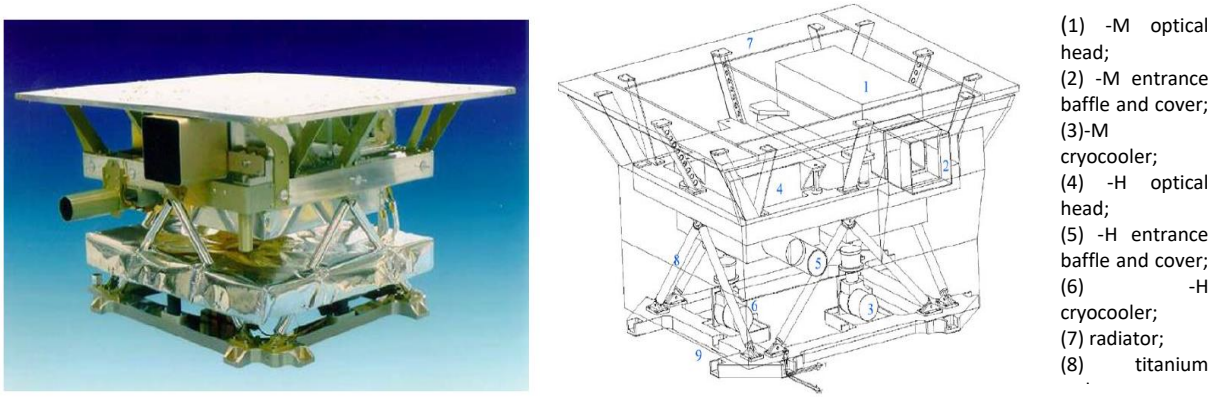

Figure 1.4. Left*:* VIRTIS prior to its integration on the Rosetta spacecraft. The VIRTIS-M imaging spectrometer is recognizable by its square shaped baffle, while VIRTIS-H with its cylindrical one. A layer separates the cold part of the experiment, where the two optical heads are housed. Right: VIRTIS Optics Module design (Coradini et al., 2007).

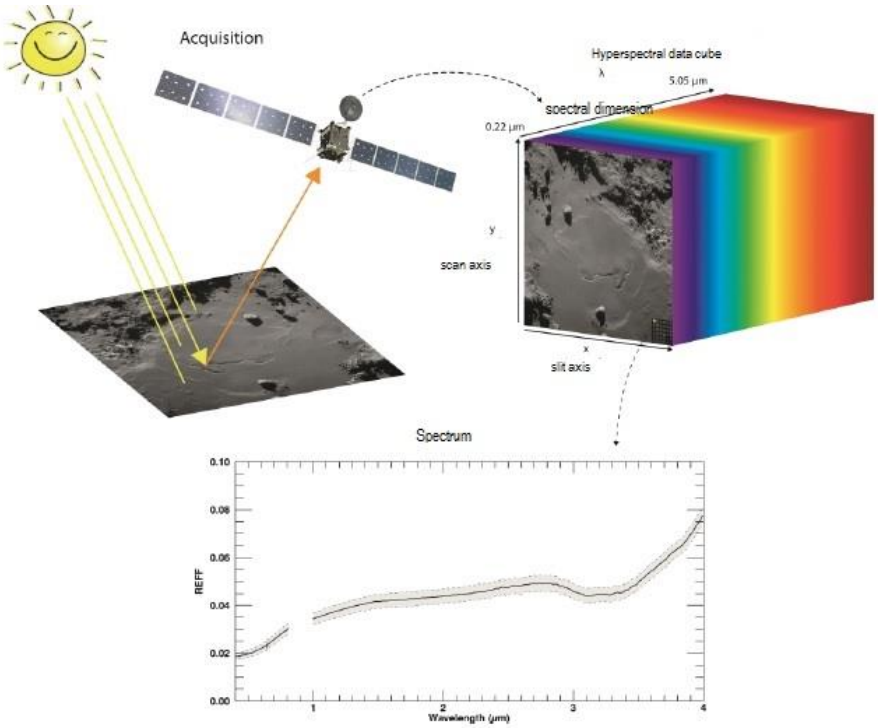

Figure 1.5. Schematic diagram of hyperspectral imaging. The spectro-imager produces a data cube containing two spatial dimensions and one spectral dimension. At each pixel of the image corresponds a spectrum. The image is from Rosetta's navigation camera (Rousseau, 2017a).

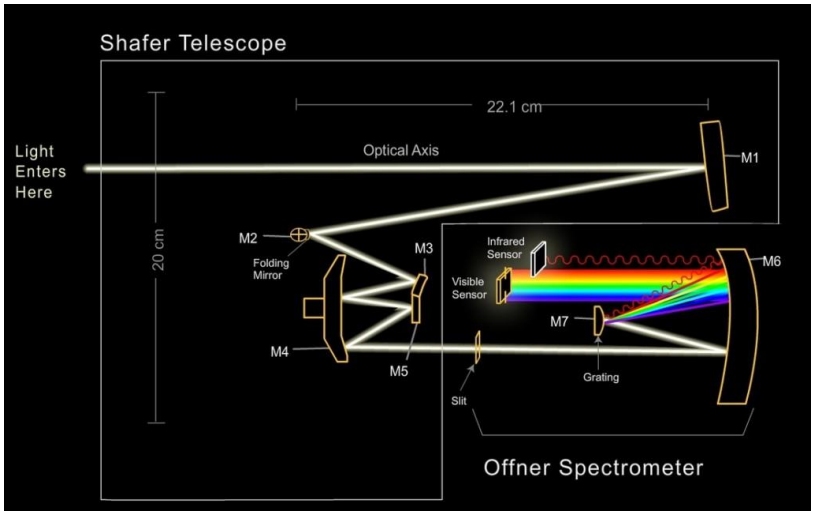

Figure 1.6. Diagram of a Shafer telescope combined with an Offner spectrometer. After a series of reflection on different mirrors (from M1 to M5), the light enters through the slit equipped with an electromechanical shutter, then the light is reflected by the mirror M7 to be diffracted by grating M7 as visible and infrared beams. The two infrared and visible beams are uncorrelated spatially. The infrared signal is then directed to the focal plane of the infrared detector, and the visible signal to that of the visible detector. On each detector is arranged filters to filter the different orders of the network. (Credit NASA/JPL).

1.4 Reflectance spectra collected by VIRTIS-M

In this thesis we mostly focused on a data set collected between July 2014 and February 2015. After data reduction, each pixel of the hyperspectral image provides a radiance factor *RADF* or *I/F* as function of the wavelength λ, under geometrical conditions characterized by the incidence angle *i*, the emergence angle *e* and the phase angle *g*. *I* is the radiance of the nucleus at the pixel of the image and *F* is the radiance of a Lambertian surface at normal incidence with respect to sun illumination.

The reflectance factor (REFF) is defined as the ratio of the bidirectional reflectance of a surface and the bidirectional reflectance of a lambertian (scatters isotropically) surface (Hapke, 2012). It also corresponds to the ratio of the respective radiances. REFF is then derived from *I/F* by:

$$REFF(i,e,g) = \frac{I/F\ (i,e,g)}{cos(i)}$$

REFF of analog is directly measured in the laboratory using spectro-gonio-radiometer. They can be directly compared to the reflectance factors extracted from VIRTIS-M data cubes, provided that the observation geometry is similar, and neglecting topography effect (i.e. assuming that each pixel corresponds to a flat terrain).

1.5 The preliminary results on comet 67P/CG composition: 2014-2016

At the beginning of this thesis, several results had been obtained on surface optical properties thanks to the VIRTIS-M instrument. The normal albedo *An* of a surface element, which is defined by REFF(*i,e,0*) at 0.55 μm, was estimated to be *An* = 0.06 ± 0.003 (Capaccioni et al. 2015). The photometric properties of the comet have been investigated in details by Ciarniello et al. (2015). The geometric albedo of the whole body *Ap* was estimated to be 0.062 ± 0.03. These values are consistent with estimates obtained from the OSIRIS camera (e.g. Fornasier et al., 2015). These results show that the surface of comet 67P/CG is very dark. This dark property, in both the visible and the infrared ranges, likely results from the presence of dark opaque minerals, presumably pyrrhotite (Capaccioni et al., 2015; Quirico et al., 2016).

Spectral slopes, single scattering albedo, scattering parameter, roughness and phase reddening have been determined by applying a Hapke model. They were found consistent with earlier values obtained for other comets (Ciarniello et al., 2015). Figure 1.7 displays the reflectance spectra of the nucleus for four different macro-regions. They display red slopes in

the visible and the infrared, low radiance factor. Note however that the neck region has a slightly higher reflectance. At last, a striking feature is a broad 3.2 µm band that appears in both VIRTIS-H and VIRTIS-M spectra.

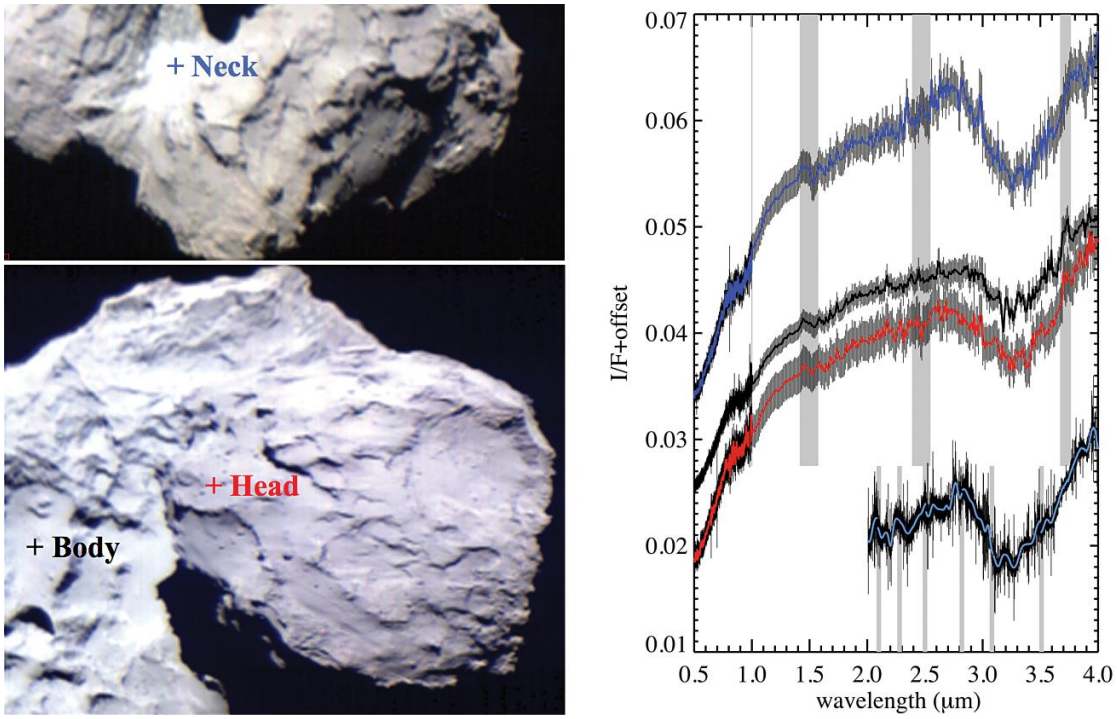

Figure 1.7. Nucleus spectral image collected by VIRTIS-M and representative spectra of four macro-regions (Capaccioni et al., 2015).

In tiny local area, close to cliffs or shadowed area, VIRTIS-M observed absorption features at 1.05 µm, 1.25 µm, 1.5 µm and 2.0 µm due to water ice that correspond to bright albedo patches (Barucci et al., 2016). Carbon dioxide ice has also been detected (Filacchione et al., 2016).

The interpretation of the 3.2 µm band is a challenging issue. Capaccioni et al. (2015) suggested that carboxylic acids are plausible candidates, regarding the broad band in the 3 µm range observed in the liquid phase. Quirico et al. (2016) showed that NH_4Cl could partially fit the 3.2 µm band, and finally that both ammonium sulfates and carboxylic acids are plausible candidates.

The broad 3.2 µm band is very noisy at the scale of a single pixel (Faure, 2016), and here we have focused on an average spectrum calculated from several millions of pixels of the dataset collected in August-September 2014. In 2019, the photometric calibration was refined by Andrea Raponi using the average spectrum of the Lutetia asteroid, collected during the Rosetta spacecraft journey towards comet 67P/CG and inter-calibrated with VIMS-Casini. The

thermal emission was re-estimated and removed (see Raponi et al., 2020 and Poch et al., 2020 for extensive details). Finally, the re-calibrated averaged spectrum has a much better signal-to-noise ratio, displays a shape that is slightly different in the wing towards long wavelengths, and the substructure of the band appears very clearly with main peaks at 3.11 and 3.26 µm, and peaks of weak intensity at 3.38, 3.42 and 3.47 µm Fig. 1.8).

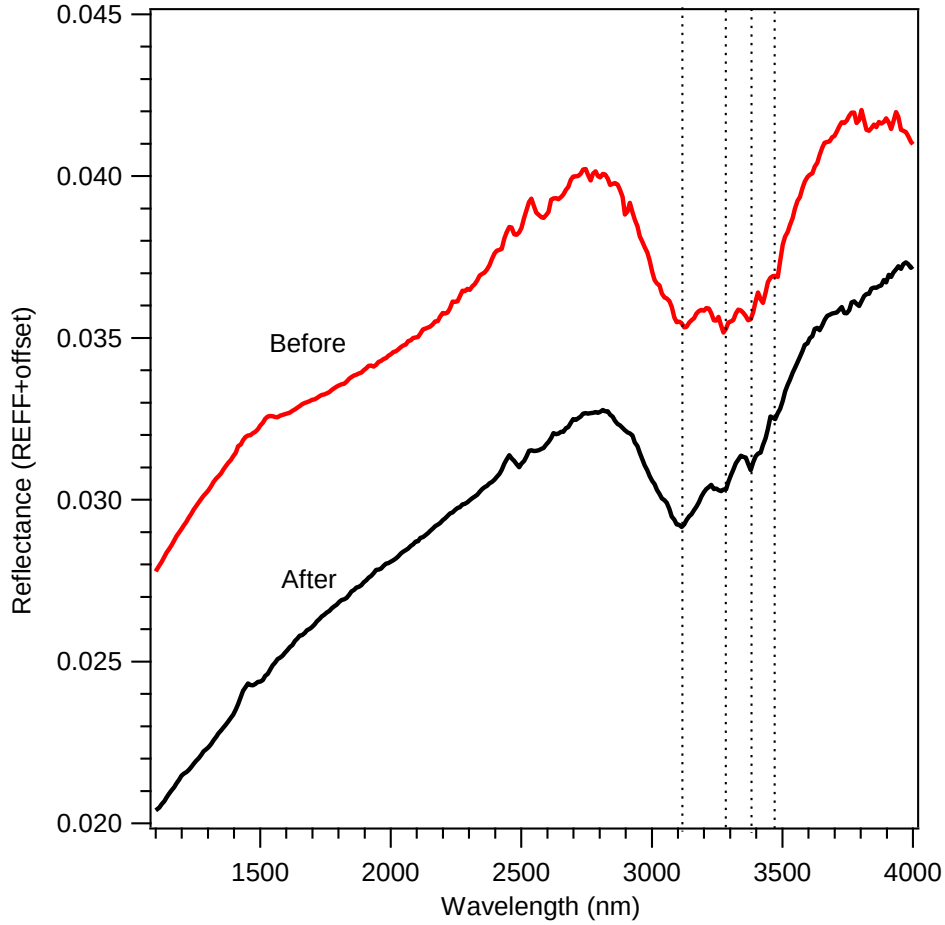

Figure 1.8. The 3.2 µm absorption feature of the average reflectance spectrum of comet 67P before and after the re-calibration made by Andrea Raponi.

The objective of this thesis is to interpret the origin of the 3.2 µm band. For this purpose, we have conducted systematic measurements on carboxylic acids in the solid state and ammonium salts. Transmission and reflectance measurements were collected at IPAG and a specific effort has been devoted to produce samples relevant to the porous and brittle cometary crust. These experimental data have been used for interpreting the VIRTIS spectra, and we have shown that mode of the band at 3.2 µm is controlled by ubiquitous ammonium salts at the surface.

Chapter 2

Materials and methods

In this chapter we describe the instruments that were used for spectroscopic measurements and sample preparation. We also provide details on the protocols that were developed for producing the cometary analogs, as well as the materials that were used.

2.1 Sample and sample preparation

2.1.1 Sample description

Different analogs of opaque minerals present in the surface of comet 67P/CG were used: graphite, anthracite (PSOC 1468), pyrrhotite and pyrite. Graphite was purchased from Sigma Aldrich. It is an industrially synthesized compound by carbonization/graphitization of desulfurized petroleum coke. The anthracite sample is a natural coal provided by the Penn Sate data bank (http://www.energy.psu.edu/csb/index.html). Its elemental composition is H/C=0.17 and O/C=0.01, and its mean vitrinite reflectance *Rm* is 5.45 %. Both these carbonaceous materials are devoid of any 3 μm feature, due to the lack of –OH bonds in the macromolecular structure. Their presence in a cometary nucleus is however unlikely (no thermal metamorphism in the nucleus), and they were selected due to their optical properties that fairly mimic those of a dark surface in the visible and infrared spectral ranges. As detailed below, these materials have different mechanical properties than sulfides and silicates, and their grinding leads to grains with different shapes, allowing the production of crust analogs with very specific textures.

Micrometer-sized iron(ii) sulfide (FeS) was purchased from Sigma-Aldrich Company. Millimeter-sized pyrrhotite grains ($Fe_{1-x}S$, with $0 < x < 0.2$) were purchased from Alfa Aesar, and Bijoux Minerals. Pyrrhotite is more relevant than pyrite, as it is the main sulfide in carbonaceous chondrites, stratospheric IDPs and Antarctic micro-meteorites. Pyrite (FeS_2) was tested as it can be easily purchased from many suppliers. In practice, it was found less opaque than pyrrhotite and contaminated by water and organic compound (Fig. 2.5). At the time of writing, pyrrhotite was no longer available from Alfa Aesar France, and renewing our stock has been a puzzling issue. Finally we got 1 gram of pyrrhotite from Bijoux Mineral.

Bright silicates were also used as pure matrix or mixed up with the opaque compounds above mentioned. Natural basalt samples were chunks of rocks sampled in Massif Central, France.

Milimeter-sized olivine grains of natural origin were purchased from Donghai Pellocci Crystal Products Co (China). Their composition was estimated to be $Mg_{2x}Fe_{2(1-x)}SiO_4$ with x=0.95±0.01 (density 3.28 $g.cm^{-3}$). Sand from the Fontainebleau area was purchased from VWR chemicals. As mentioned below, a main issue with these materials was their significant water/hydroxyl content, even in "anhydrous" minerals like olivine.

The acids and salts powders were purchased from several suppliers, from Sigma-Aldrich: 1-hydroxy-2-naphtoic-acid (> 97 %), 3-hydroxy-2-naphtoic-acid (98 %), 6-hydroxy-2-naphtoic-acid (98 %), ammonium formate (99.995 %), ammonium sulfate (≥ 99 %), ammonium carbamate (99 %) ; from Acros Organics: Glycolic acid (99 %), Fumaric acid (>99 %), Propionic acid (99 %), Butyric acid (99 %), Acetic acid (99.8 %), Formic acid (99 %). Ammonium chloride (≥ 99.5 %) was purchased from Carlo Erba, L-lactic acid anhydrous (98 %) from Alfa-Aesar, as well as ammonium citrate $(NH_4^+)_3CH_2COO^-$-$C(OH)COO^-$-CH_2COO^-, ammonium acetate $NH_4^+CH_3COO^-$, ammonium phosphate $(NH_4^+)_3PO_4^-$, ammonium bicarbonate $NH_4^+COOOH^-$, glycine, alanine and sarcosine.

Table 2.1. Semi-volatile compounds

No	Name	Molecule structure	Appearance at room temperature
1	Formic acid		Colorless and odor liquid
2	Acetic acid	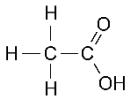	Colorless and odor liquid
3	Propionic acid	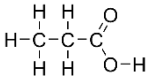	Colorless and odor liquid
4	Butyric acid	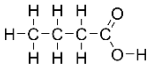	Colorless, fatty and odor liquid
5	Valeric acid	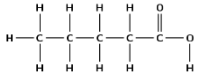	Colorless, fatty and odor liquid
6	Glycolic acid	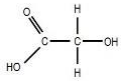	Transparent, milimeter-sized grains and hygroscopys
7	Lactic acid	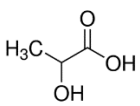	Transparent, milimeter-sized grains and hygroscopys

No	Name	Molecule structure	Appearance at room temperature
8	Fumaric acid	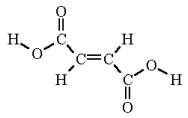	White powder, micrometer-sized grains
9	1-hydroxy-2-naphtoic acid	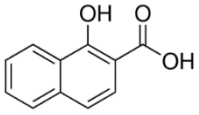	White powder, micrometer-sized grains
10	3-hydroxy-2-naphtoic acid	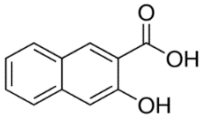	Grey powder, micrometer-sized grains
11	6-hydroxy-2-naphtoic acid	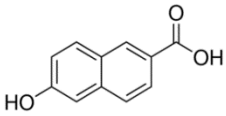	Yellow powder, micrometer-sized grains
12	Glycine	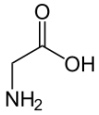	Transparent, milimeter-sized grains
13	Alanine	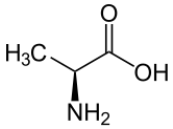	Transparent, milimeter-sized grains
14	Sarcosine	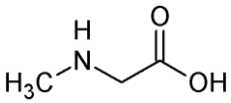	Transparent, milimeter-sized grains
15	Ammonium chloride		Transparent, milimeter-sized grains
16	Ammonium phosphate	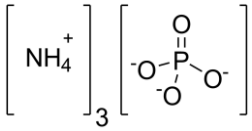	Transparent, milimeter-sized grains
17	Ammonium sulfate	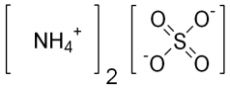	Transparent, milimeter-sized grains
18	Ammonium carbamate	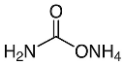	Transparent, milimeter-sized grains and hygroscopys

No	Name	Molecule structure	Appearance at room temperature
19	Ammonium formate	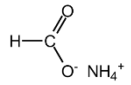	Transparent, milimeter-sized grains and hygroscopys
20	Ammonium acetate	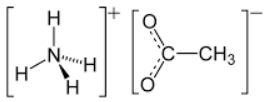	Transparent, milimeter-sized grains and hygroscopys
21	Ammonium bicarbonate	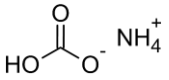	Transparent, milimeter-sized grains
22	Ammonium citrate	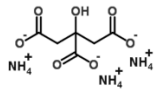	Transparent, milimeter-sized grains

Molecule structures are from NIST.

2.1.2 Milling process

Cometary refractory materials are sub-micrometric assemblages composed of ultramafic silicates, opaque minerals (e.g. pyrrhotite) and refractory organics. Therefore we need to synthetize sub-micrometric powders in the laboratory. For this purpose, we have used a Retsch PM100 planetary grinder, equipped with a ZrO_2 50 ml bowl and ZrO_2 balls with various sizes (2 cm, 1.5 cm, 1 cm, 2 mm, 500 µm). The basic principle of planetary grinding is that a bowl set on a supporting rotating disk rotates around itself in the opposite direction to that of the disk (Fig. 2.1). The bowl is filled with the granular sample and balls, which, due to Coriolis drag, are deviated and hit the wall and sample grains at high velocity. This configuration promotes a high ball kinetic energy and an efficient crushing, leading in some cases sizes as small as tens of nanometers.

The power delivered to the sample can be written (Abdellaoui and Gaffet, 1995):

$$P = \frac{M_b}{m_p} \cdot {}^1\!/_2 \, (V(\Omega,\omega))^2 \cdot f(\Omega,\omega)$$

with M_b and m_p are the masses of the balls and sample, respectively, V the ball maximum speed, f the impact frequency, ω and Ω the rotation speeds of the disk and bowl, respectively. In practice, $\Omega=\omega/2$, and the main parameters to fix are the mass balls (in fact, their size), the

rotation speed, the sample volume and the balls volume. Two configurations can be used with this set-up: dry and colloidal grinding. Colloidal grinding is run in the presence of a liquid (typically ethanol in our case). The liquid promotes the dispersion of the grains, avoiding the formation of aggregates and reaching lower sizes. The Retsch company provides tables recommending balls and sample volume and ball size for different feeding sizes of the sample. In practice, specific protocols had to be developed for each material. In particular, great care was devoted to avoid amorphization or phase transition for the most fragile materials. The sample size was determined from Scanning Electron Microscopy, operated at CMTC at Université Grenoble Alpes.

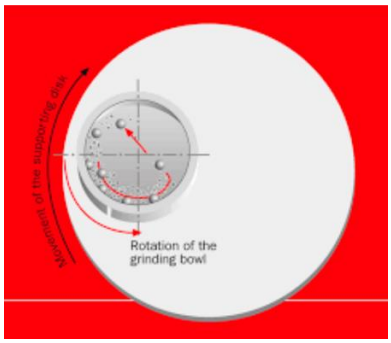

Figure 2.1. Schematic of the planetary grinder (credit: Fritsch GMBH).

The general procedure for sample grinding is presented in Figure 2.2. The first step of the milling process is a dry grinding, for which the Retsch Company recommends a minimum size of ball equal to 3 times to that of the mineral grain. The second step is a colloidal grinding, where 2/3 of the jar volume is filled with balls, 1/3 is filled with mineral grains, and ethanol is added until the mixture of balls and minerals looks like a viscous oil. The duration of the dry grinding depends on mineral hardness. For soft mineral, it takes 20-30 minutes, and for hard minerals it takes 45-60 minutes. In the case of colloidal grinding, the duration for soft minerals was around 3 hours, and for hard mineral it was 5 hours. Table 2.2 reports the experimental conditions for each mineral and displays SEM. The grain size of SEM image is analyzed by the free software ImageJ.

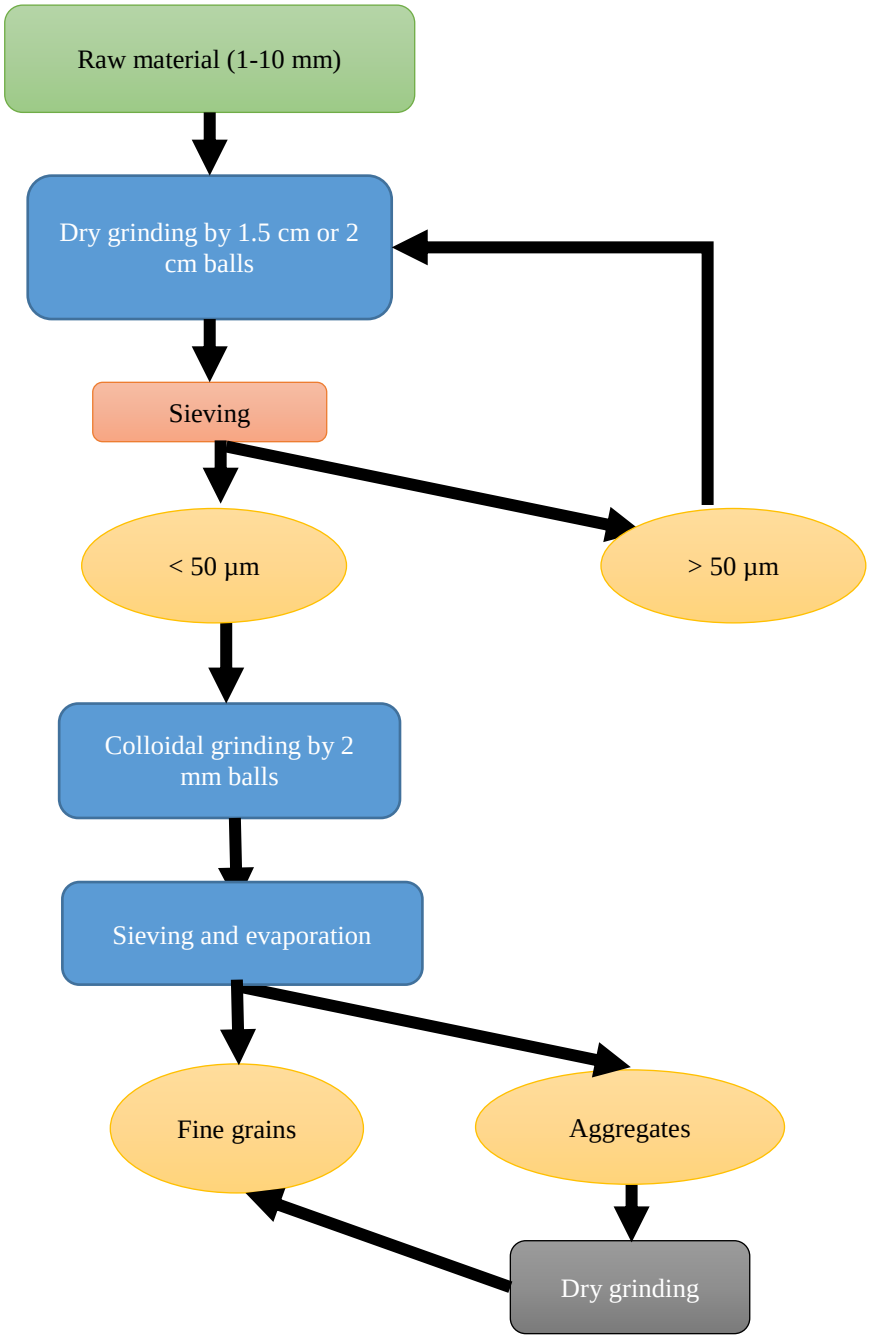

Figure 2.2. General flowchart of milling process.

Table 2.2. Milling procedure for different opaque mineral

No	Mineral	Procedure	SEM image
1	Graphite	- Initial size < 20 µm - Colloidal grinding 3 hours with 0.5 mm balls - Inverse rotation, speed 450 rpm, interval 5 minutes, pause 20 second	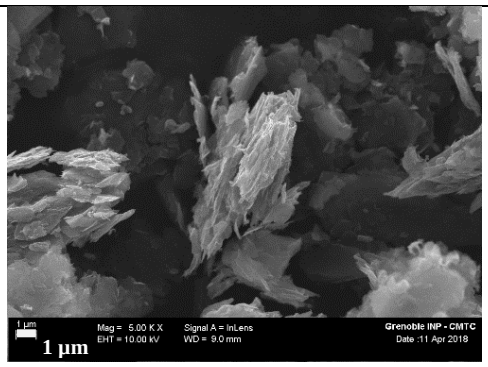 Irregularly shaped micrometer-sized flakes. Flake size 1-3 µm (50 %), 4-6 µm (30 %), 7-9 µm (13 %), 10-13 µm (8 %), <1 µm (1 %).
2	Basalt	- Initial size 5 mm - Dry grinding by 1.5 cm balls during 30-45 minutes - Colloidal grinding by 0.5 mm balls during 3 hours - Inverse rotation, speed 450 rpm, interval 5 minutes, pause 20 second	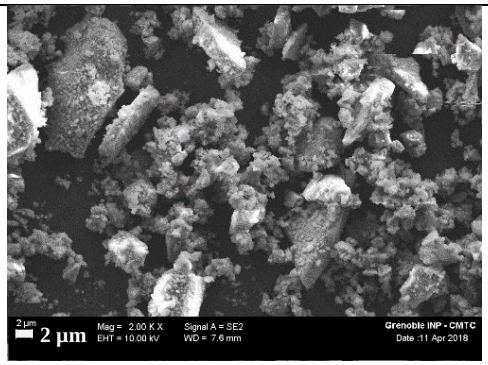 Irregularly shaped micrometer-sized grains with angular outline and chunks coated by smaller grains. Size distribution: <1 µm (50 %), 1-3 µm (34 %), 4-5 µm (6 %), 5-7 µm (3 %), 8-9 µm (6 %), 14-17 µm (1 %).

3	PSOC 1468 (anthracite)	- Initial size < 50 µm - Colloidal grinding 3 hours with 2 mm balls - Dry grinding 2 mm balls during 20 minutes to disrupt platelets - Inverse rotation, speed 450 rpm, interval 5 minutes, pause 20 second	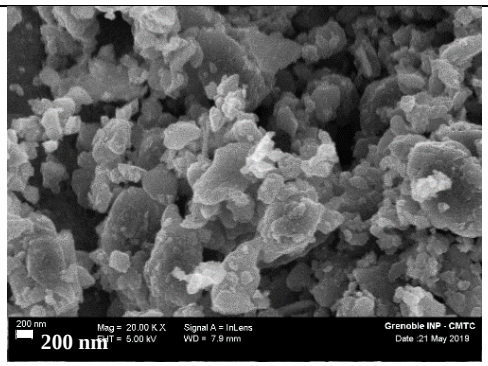 Irregularly shaped sub-micrometer-sized grains with some platelets. Size distribution: 100-300 nm (75 %), 300-600 nm (15 %) , (800-1000) nm (10 %).
4	Sand	- Initial size 1 mm - Dry grinding by 1.5 cm balls during 30-45 minutes - Dry grinding by 2 mm balls during 3 hours - Inverse rotation, speed 450 rpm, interval 5 minutes, pause 20 second	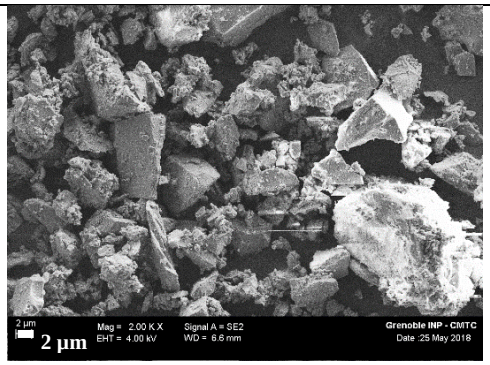 Irregularly shaped micrometer-sized grains with angular outline and chunks coated by smaller grains. Size distribution size <1 µm (30 %), 1-3 µm (40 %), 4-6 µm (18 %), 7-10 µm (11 %), 8-9 µm (6 %), 13-17 µm (1%).
5	Olivine	Procedure A - Initial size 5 mm - Dry grinding by 1.5 cm balls during 30-45 minutes - Colloidal grinding by 0.5 mm balls during 3 hours	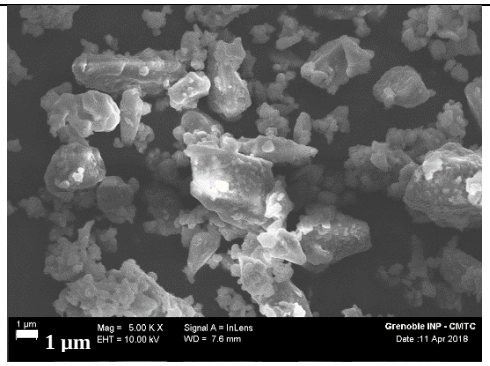

		- Inverse rotation, speed 450 rpm, interval 5 minutes, pause 20 second Procedure B - Initial size < 5 mm - Dry grinding by 1.5 cm balls during 30-45 minutes - Colloidal grinding by 2 mm balls during 5 hours - Inverse rotation, speed 450 rpm, interval 5 minutes, pause 20 second	Irregularly shaped micrometer-sized grains with angular outline and some bigger grains. Size distribution <1 µm (54 %), 1-3 µm (35 %), 3-4 µm (7 %), 5-7 µm (4 %). 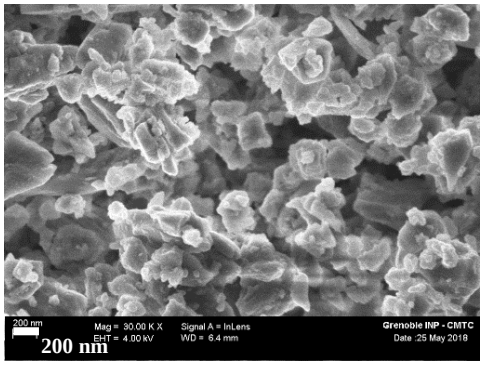 Irregularly shaped sub-micrometer-sized grains with some angular platelets. Size distribution 100-200 nm (70 %), 200-300 nm (15 %), 300-400 nm (4 %), 400-500 nm (3 %), 500-600 nm (3 %), 600-700 nm (3 %).
6	Pyrrhotite	Procedure A (Pyrrhotite-$_{fg\text{-}pl}$) (Rousseau et al., 2017b) - initial size < 200 µm - dry grinding by 2 mm balls during 90 minutes - colloidal grinding by 0.5 mm balls during 3 hours - Inverse rotation, speed 550 rpm, interval 10 minutes, pause 30 second - Ethanol evaporation by heating 60 °C on the hotplate	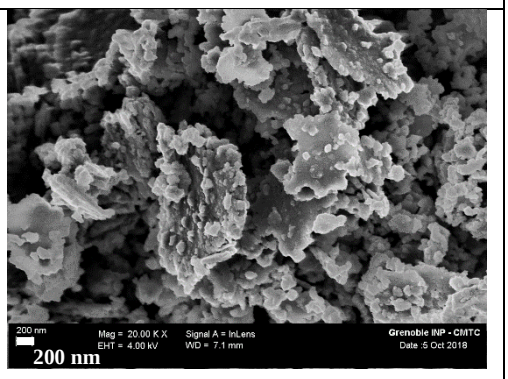 Irregularly shaped sub-micrometer-sized grains with aggregates Size distribution 70-200 nm (20 %), 300-600 nm (25 %), 600-900 nm (30 %), 900-1100 nm (10 %), 1100-1400 nm (10 %), 2400-3000 nm (5 %).

		Procedure B (Pyrrhotite$_{-fg}$) - Initial size < 5 mm - Dry grinding by 2 cm balls during 30 minutes - Colloidal grinding by 2 mm balls during 3 hours - Ethanol evaporation by heating 60°C on the hotplate - Dry grinding by 2 mm balls during 10 minutes Inverse rotation, speed 500 rpm, interval 10 minutes, pause 30 second	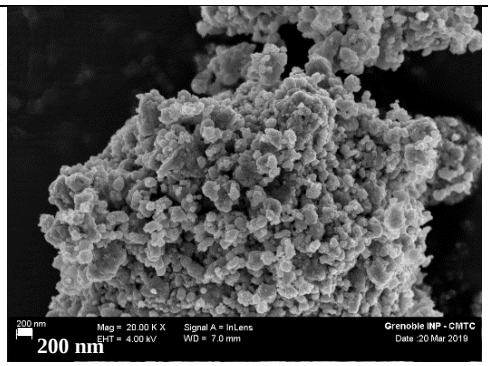 Rounded shaped of sub-micrometer-sized grains with aggregates. Size distribution 50-100 nm (50 %), 100-160 nm (30 %), 160-220 nm (16 %), 220-275 nm (3 %), 500-565 nm (1 %).
7	Iron(ii) sulfide	- Initial size < 100 µm - Dry grinding by 1 cm balls during 20 minutes - Colloidal grinding by 2 mm balls during 3 hours - Ethanol evaporation by heating 60° c on the hotplate - Dry grinding by 2 mm balls during 10 minutes Inverse rotation, speed 500 rpm, interval 10 minutes, pause 30 second	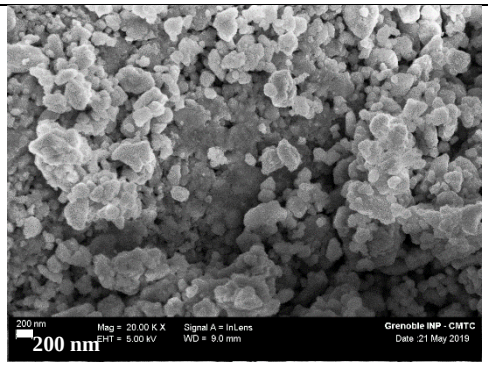 Irregularly shaped sub-micrometer-sized grains with some platelets. Size distribution 70-160 nm (35 %), 160-250 nm (40 %), 250-350 nm (15 %), 350-420 nm (6 %), 540-630 nm (1 %), 630-725nm (1 %), 900-1000 nm (1 %).

8	Pyrite	- Initial size < 5 mm - Dry grinding by 2 cm balls during 30 minutes - Colloidal grinding by 0.5 mm balls during 3 hours - Ethanol evaporation by heating 60 °C on the hotplate - Dry grinding by 2 mm balls during 10 minutes Inverse rotation, speed 500 rpm, interval 10 minutes, pause 30 second	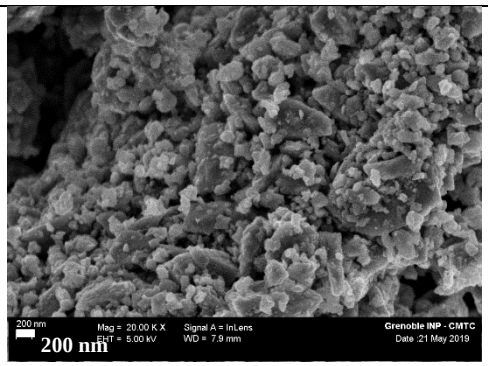 Irregularly shaped sub-micrometer-sized grains with some angular platelets. Size distribution 100-300 nm, (72 %), 300-550 nm (8 %), 550-750 nm (10 %), 750-1000 nm (6 %), 1-1.5 µm (4 %).
9	Ammonium salt	Ammonium salts are hygroscopic compounds, colloidal grinding cannot be done, therefore dry grinding and mortar grinding the best way although longer duration can generate crust rather than fine powder.	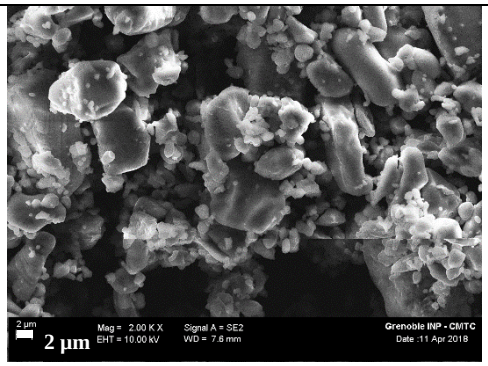 Angular shaped micrometric-sized grains. Size distribution < 1 µm (30 %), 1-3 µm (58 %), 4-6 µm (3 %), 6-8 µm (3 %), 8-10 µm (3 %), 10-12 µm (2 %), 13-16 µm(1 %).

2.1.3 Sample dehydration

Silicates often contain water in their lattice, therefore a heating procedure had to be applied after grinding process for removing structural water. The heating procedures were used: (1) heating under air with a Nabertherm furnace and (2) a heating under secondary vacuum (~10^{-6} mbars) using a Carbolite tube furnace. The temperature varied from 600 to 1000 °C, depending on the melting temperature of the samples. Olivine was heated during one night in the range 800-1000 °C, basalt in the range 600-900 °C and sand in the range 900-1200 °C. Anthracite, graphite, pyrite, iron(ii) sulfide and pyrrhotite were not treated. Note, however that pyrrhotite and iron(ii) sulfide were slightly heated (< 80 °C) to accelerate ethanol evaporation after the colloidal grinding.

Despite these harsh conditions, it was not possible to eliminate all the water trapped in some samples. Figure 2.3 shows the effect of heating in the reflectance spectra of olivines. Before heating, olivine has a green color and after heating and cooling under air it becomes red as display by red slope in visible due to iron oxidation. The other effect of heating is shifting the absorption band at 1.1 µm ,which is the contribution of thermal expansion and distortion around the Fe^{2+} sites in the olivine structure (Sung et al., 1977).

For micrometer-sized grain (Olivine A) a heating at 1000 °C was effective to eliminate water. However, for sub-micrometric-sized grains (Olivine B), heating at 1000 °C still contained a strong water band (Fig. 2.3).

Basalt has stepper slope at range 0.4-0.9 µm and flatter slope until 2.5 µm and strong water band centered at 2.9 µm (Fig.2.4). After heating the sample became red as display by the red slope in visible, unfortunately the water band does not vanish. Similar behavior was observed with sand, though a heating at 1200 °C under vacuum it still showed a strong water band at 2.9 µm.

Figure 2.5 displays dark refractories as pyrite, pyrrhotite, anthracite, graphite and iron(ii) sulfide. Anthracite has a stepper slope in visible and IR regions. Graphite, iron(ii) sulfide, pyrite and pyrrhotite have stepper slope in visible range, however pyrite has strong water band and organic band. Therefore, in this experiment, we discarded pyrite for mixture preparation.

As we have two different suppliers of pyrrhotite, we have two different spectra. Pyrrhotite (BM) from Bijoux Mineral has a slightly higher reflectance than Pyrrhotite (AA) from Alfa Aesar. This might be due to the fact that this pyrrhotite has a different percentage of Fe.

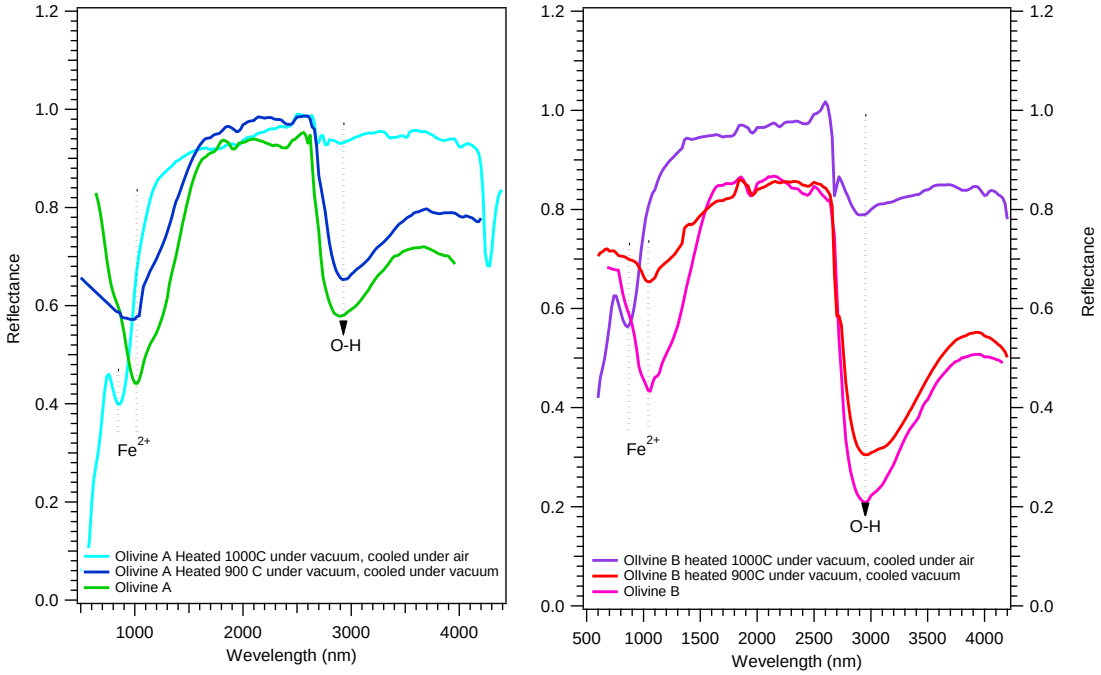

Figure 2.3. Olivine spectra at different heating temperature, where olivine A is micrometric-sized grain and Olivine B is sub-micrometric-sized grains.

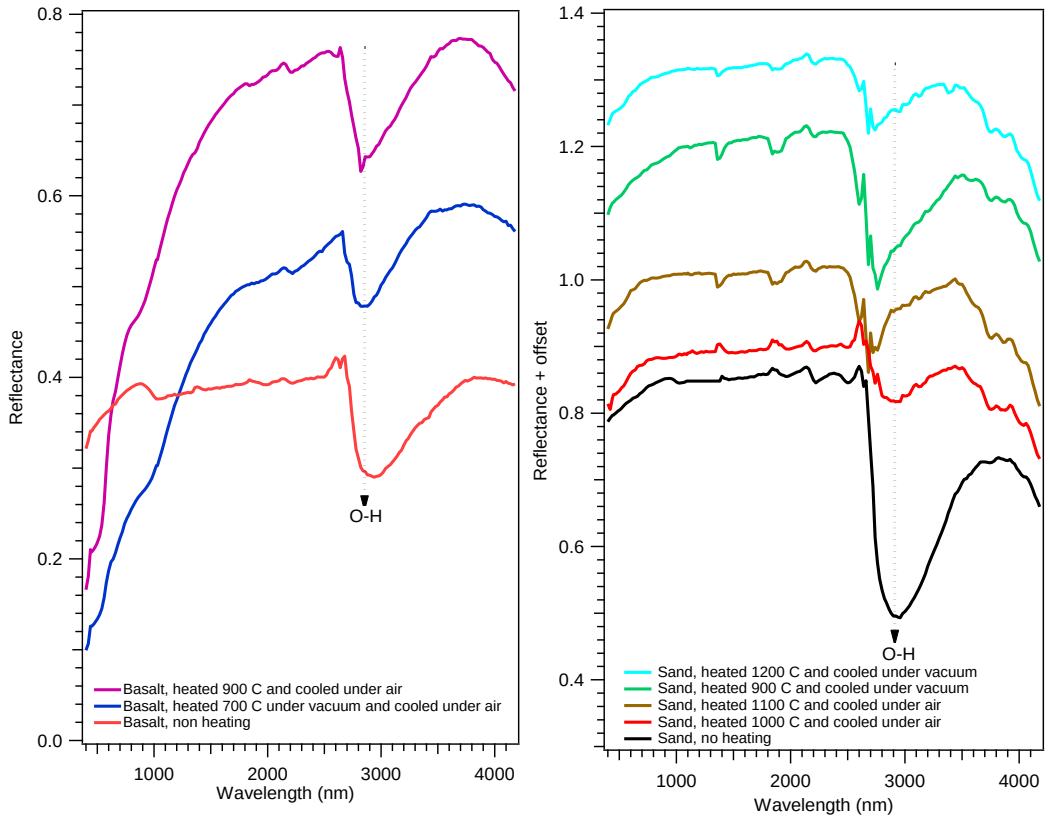

Figure 2.4. Spectra of basalt (left) heated at different temperature and sand (right) with offset for clarity.

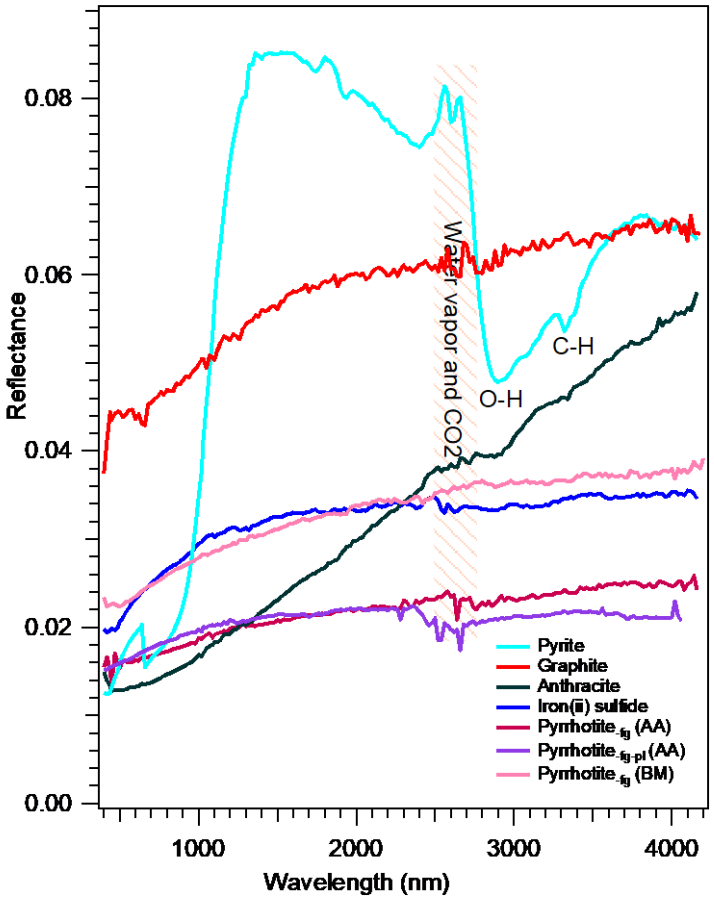

Figure 2.5. Spectra of dark refractories (here, there is contribution of water vapor in the room where the measurements were done).

2.1.4 Opaques and semi-volatiles mixing

Mixing opaque minerals and semi-volatile compounds is a difficult issue. Here, we have used two main methods. The first consists in a mechanical mixture of different powders, and the second consists in forming a porous crust by sublimating ice-dust mixtures (Poch et al., 2016ab).

A. Mechanical mixing

Almost 90 % of the mechanical mixtures were prepared by mortar mixing. Minerals and volatiles were mixed by pestle in a mortar during 3-5 minutes. The mixture was poured into a sample holder (diameter 1 cm and depth 1-2 mm) and flattened with a spatula. The sample holder was placed inside the SERAC chamber (Spectroscopy in Reflection under Controlled atmosphere) during reflectance measurements (see below).

Some of the semi-volatiles are sticky and easily adsorb water, therefore the mixture can produce small aggregates, which were broken with a spatula. Rousseau et al. 2017b proved that mortar mixing produced homogenous mixtures. For the rest of the samples, around 10 %, we used different methods, which have more disadvantages, such as the mixture with a pellet grinder MM200 during 10 minutes. In practice, this system mostly separate grains with different densities. Rousseau et al. (2017b) revealed that these mixtures were usually coated, and we basically observed refractory grains covered by semi-volatiles. We also tried chemical mixture for which acids were previously diluted in ethanol, added to the refractory powder, hand mixed with a spatula, and then ethanol was sublimated under a fume hood. This method was expected to deliver more homogenous mixtures, where semi-volatiles coating the refractory minerals. We observed however that ethanol had a strong contribution in the spectra. We also produced mixture with the planetary grinding using 3 balls with a diameter of 1 cm, and a 450 rpm rotation speed during 10 minutes. This method produced big aggregates (Fig. 2.6). Finally, we tried to hand-mix with a pencil brush, and produce semi-volatile grains coated with small grains of pyrrhotite.

Figure 2.6 displays SEM images of mechanical mixtures made of pyrrhotite-ammonium sulfates. The black traces are suspected to be ammonium sulfates because they were unstable under the electron beam. The mixture contained compact aggregates grains of various sizes, where the ammonium salt played the role of glue. Some small patches of ammonium appear as black traces on the surface of big aggregates. For the mixtures obtained from the planetary grinder, it produces large compact aggregates, where the ammonium salt as cement that binds the refractory grains altogether.

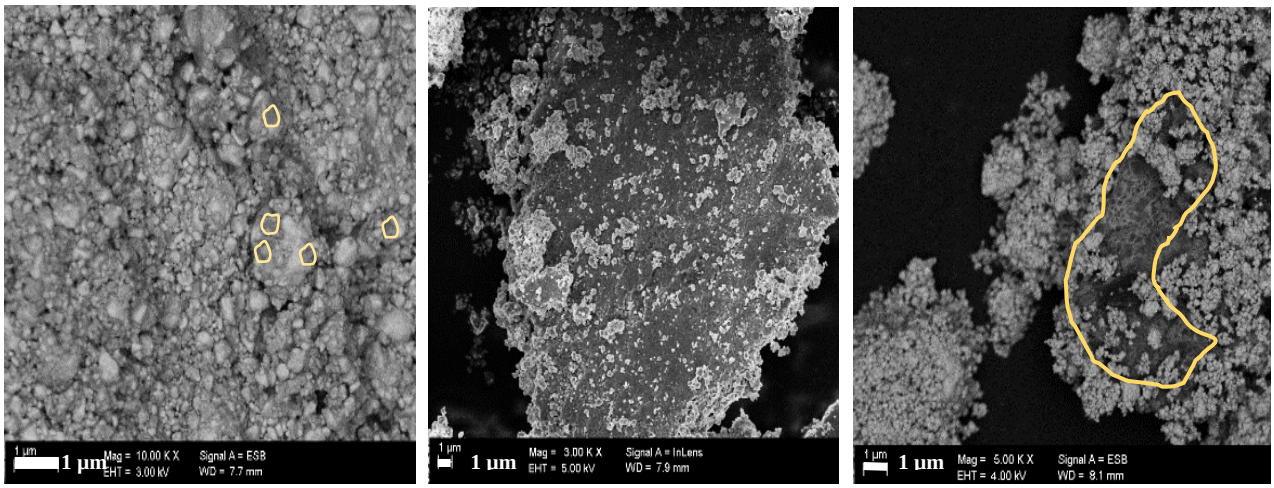

a. Mortar b. Planetary grinder c. Pencil brush

Figure 2.6. SEM images of different mechanical mixtures. The black traces on the left image are ammonium sulfate grains, which are unstable under the electron beam. The yellow line on the right depicts the segregation of grains.

B. Sublimating ice-dust mixtures

Sublimation experiments were run from ice-dust mixtures synthesized with the SPIPA-B setup (Setup for the Production of Icy Planetary Analogs), described in Poch et al. (2016ab). This set up can produce intra-particle mixtures composed of spherical icy particles that contains semi-volatiles species and refractories. The size of the spherical icy particles is 67 ± 31 µm (Poch et al., 2016ab). The SPIPA-B setup has two main components: an ultrasonic nebulizer (Hippomed AIR ONE) and a peristaltic pump (Fig. 2.7). The ultrasonic nebulizer generates suspension of fine droplets, which freeze when they get in contact with the cold air and eventually fall in an aluminium bowl filled with liquid nitrogen. The peristaltic pump delivers a liquid mixture (water+refractory+semi-volatiles) to the sonotrode of ultrasonic nebulizer.

The liquid mixture has the composition 0.1-0.3 % semi-volatiles, 1 % of refractories and 99 % of water in mass percentage. This liquid mixture was placed in a beaker glass then mixed by ultrasounds generated by the sonotrode during 2x30 s, with a break in-between to avoid the temperature increase of the suspension (Poch et al., 2016a). The suspension was put on a stirrer at the highest velocity 2000 rpm to maintain its homogenous state during the nebulizing process.

The nebulizing process starts when the peristaltic pump delivers the suspension into the sonotrode by a 2 mm pipe. The sonotrode has a cone-shaped-nozzle to produce thin film. This thin film was broken apart by ultrasonic vibration from Hielscher 200Ht ultrasonic unit to

generate micro-droplets. Then the micro-droplets were spread out from the sonotrode nozzle into liquid nitrogen then freeze as intra-mixture ice particle progressively.

After the liquid nitrogen sublimate, the ice particles were sieved with a 400 µm grid spacing sieve to obtain homogenous particles, and then filled into a sample holder with a diameter 5 cm and depth 0.5 cm. The sample was kept inside an insulation box containing liquid nitrogen to maintain its temperature below 170 K before reflectance measurements.

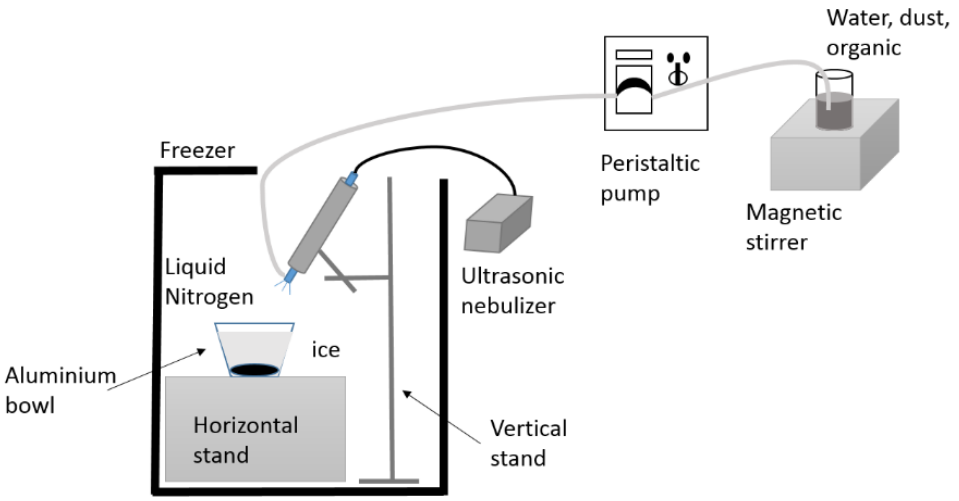

Figure 2.7. Sketch of the SPIPA B device (Setup for the Production of Icy Planetary Analogs – B). Adapted from Zurine Yoldi (2015).

The sample was finally placed in the CarboN-IR chamber (Fig 2.10) at 170 K and under vacuum (10^{-5} mbar). There, the surface of the sample absorbs heat emitted by the walls of the chamber and controls ice sublimation. As the water ice sublimates, the surface of the sample gets darker and lower than the sample holder level and darker (Fig. 2.8). After at minimum 24 hours the sample transformed into a porous crust analog. Reflectance measurements were run during the whole sublimation process. After the completion of the optical measurements, the sample was recovered for SEM measurements. In some cases, the sample was heated until 230 K to study its evolution.

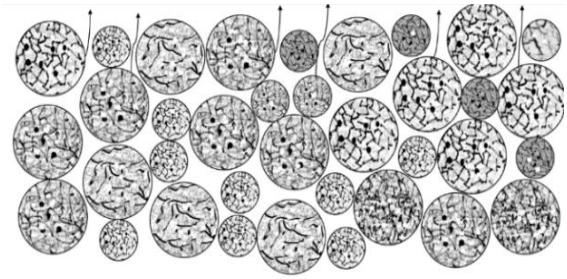

Spherical water ice contains dust and salt/acids placed at environmental cell 170 K

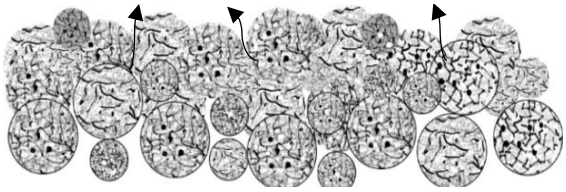

After 10 hours, the water ice on the surface of sample sublimated

At least after 24 hours, a porous sublimation residue was generated.

Sample before sublimation (diameter 5 cm, depth 5 mm)

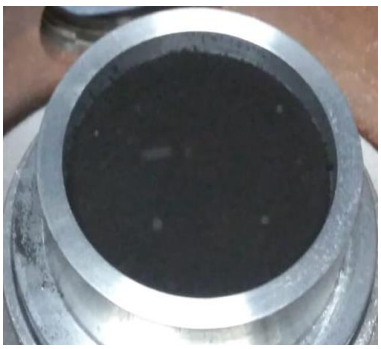

Sample after sublimation (diameter 5 cm, depth 2 mm)

Figure 2.8. Description of the sample evolution during the sublimation process (adapted from Poch et al., 2020).

2.2 Reflectance measurements

2.2.1 Spectro-gonio radiometer

The reflectance measurements were run on the SHINE spectro-gonio-radiometer at the Institut d'Astrophysique et de Planétologie de Grenoble (IPAG). This set up allows collecting reflectance spectra of planetary surface analogues in the Visible-NIR range. The geometry of measurements is adjustable, allowing a direct comparison hyperspectral data collected by spacecraft.

As described by Brissaud et al. (2004), the spectro-gonio radiometer has two arms. An illumination arm rotates from 0-85° incidence angle (θ_i), and an observation arm as emergence angle (θ_e) from 0-83°. The azimuth angle can be adjusted from 0 to 180°. The source of illumination is a parallel monochromatic and linearly polarized beam issued from a 250 W quartz tungsten halogen lamp. There are two detectors: a silicon photodiode that covers the spectral range 185-1200 nm, and an InSb photovoltaic detector for the range 800-5200 nm.

In our work, the reflectance spectra were collected in the 500-4200 nm range with an incidence angle of 0° and an emission angle of 30° and an azimuth angle 0°. The spectral sampling was 20 nm and spectral resolution was 19 nm in the wavelength 500-3000 nm and 39 nm in the wavelength range 3000-4200 nm. As SHINE is designed to measure the reflectance of brighter ice with larger illumination and our sample has lower albedo, therefore during our measurements we used small spot of illumination light (diameter = 5.2 mm) to increase signal to noise ratio.

Nearly Lambertzian references were used, as the Spectralon® and Infragold® from Labsphere Inc.. Each spectrum was divided by the references, providing REFF (Reflectance Factor) spectra. The water vapor in the room during measurements was very fluctuating, resulting in absorption bands residues in the range 2500-2800 nm. In order to minimize this problem, the Infragold® reference was measured daily.

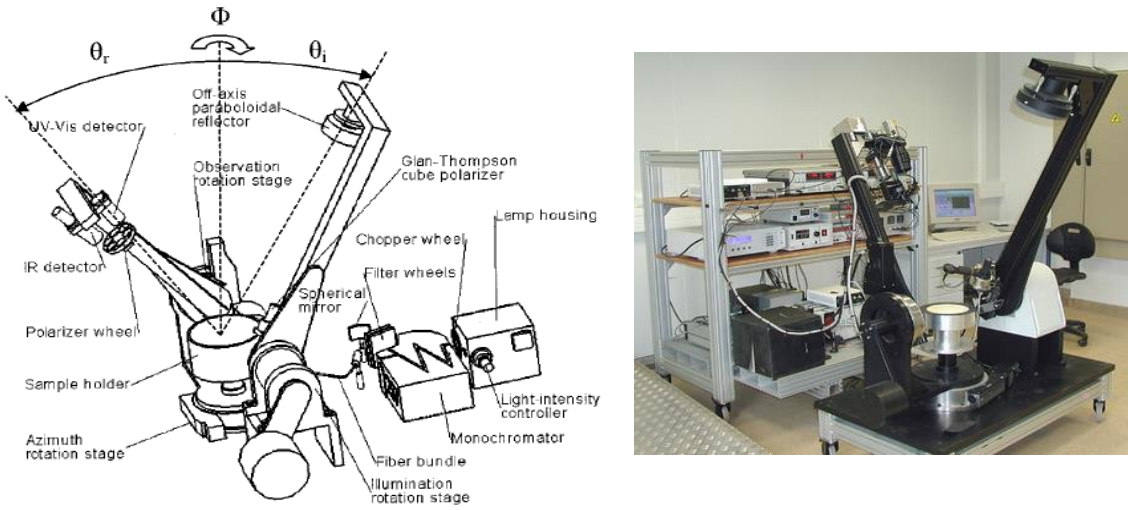

Figure 2.9. Spectro-gonio radiometer set up in IPAG laboratory (credit: Olivier Brissaud).

2.2.2 Environmental cells

The spectro-gonio radiometers at IPAG can be equipped with two types of environmental cells: CarboNIR and SERAC. CarboNIR is designed for experiments at low temperature until 40 K, and SERAC is designed for high temperature until 60 °C. Both these cells are connected to primary and secondary pumps.

The CarboNIR cell refers to *glace* ***carbo****nique* (dry ice) in **N**ear **I**nfra-**R**ed cell which allows running experiments under controlled temperature and pressure. This cell is designed to be compatible with the SHINE spectrogonio-radiometer. This cell was made with cooper that has good heat conduction specificities at low temperature. Three windows allow monitoring the

sample through vertical observation using a sapphire window with diameter 6.5 cm, and through lateral observation using 2 lateral glass windows with diameters equal to 3.4 cm. Indium gaskets are used to insure a good thermal conductivity and a good vacuum. Reflectance measurements are run through the sapphire window. The chamber contains a sample holder that is connected to a cryo-cooler. Theoretically the temperature can reach 40 K, however in our experiment, we only cooled down the sample down to 170 K, where the water ice starts sublimating under vacuum.

The SERAC cell (Spectroscopy in Reflection under Controlled atmosphere) is designed to measure the reflectance of samples under controlled water vapor conditions. The cell is equipped with a sapphire window on its top to allow reflectance measurements in the visible and NIR ranges. It is connected to a pumping device and a heating system to dehydrate samples. Besides the heating system which can reach 60 °C, SERAC is also connected to peltier setup which can reach the temperature of -15 °C.

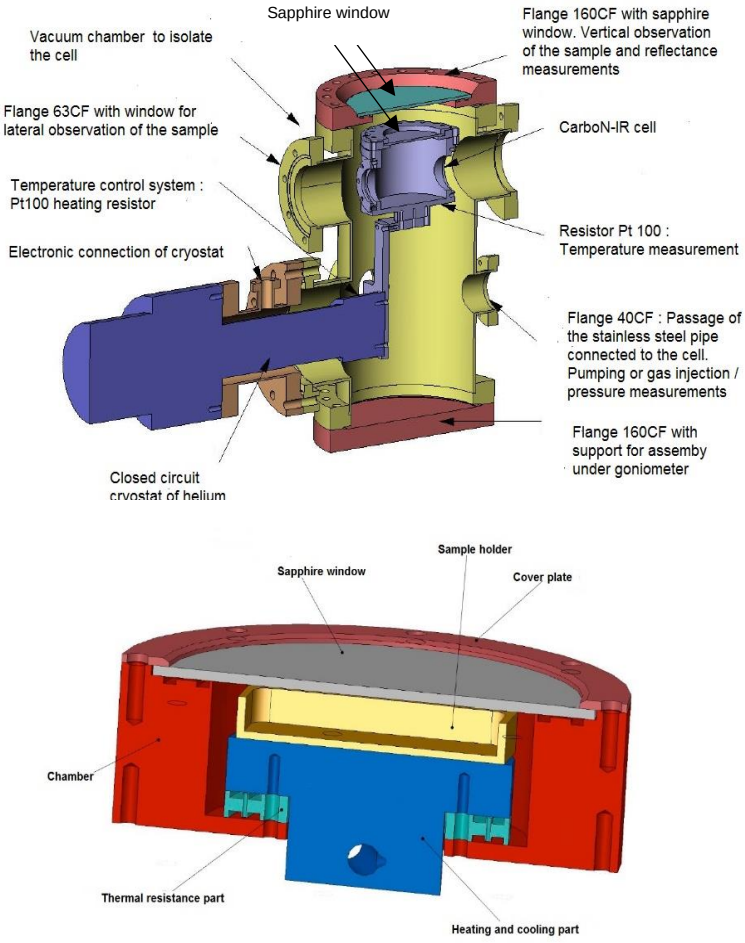

Figure 2.10. Environmental cell set up, CarboNIR (top), SERAC (bottom) (Credit: Olivier Brissaud).

2.3 Transmission measurements

The semi-volatile species depicted in table 2.1 were measured by FTIR in transmission. This provided their absorption spectral properties, and thus a first appraisal whether or not they are plausible candidates for the 3.2 µm band. We prepared the samples as thin films or sub-micrometric grains trapped in a KBr pellet.

2.3.1 Pellet preparation

Most of the samples were available as solid powders at room temperature and they were prepared as KBr pellets. 1 mg of a semi-volatile compound with 300 mg of pure KBr was mixed with a MM200 grinder during 10 minutes. The mixture was poured into a stainless steel cylindrical mould (diameter 13 mm), sealed at top and bottom with small plain cylindrical pieces, and then compressed to 400 mbars during 2 hours. During compression, the pellet underwent a mild heating at 60 °C and was maintained under vacuum at 10^{-2} mbar, in order to remove water. The thickness of the pellet was around 2 mm and the diameter was 13 mm.

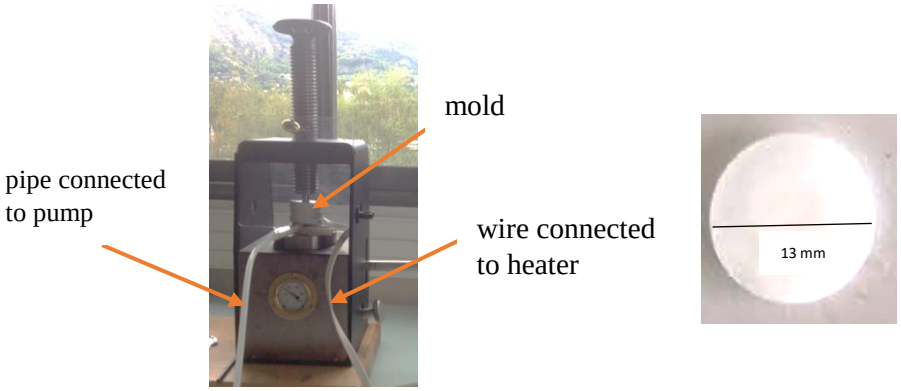

Figure 2.11. Set up of pellet pressing (left) and the acid/salt pellet.

2.3.2 Thin film preparation by spin coating

Hydroxylated carboxylic acids were prepared as thin films with a spin coater. First, the acid was dissolved in a solvent and few droplets were deposited on the surface of a window. The window was placed in the spin coater POLOS SPIN 150i and was rotated. The rotation allowed the solution to spread on the window and to speed up the solvent evaporation. The success of this technique depends on the choice of the solvent and of the rotation speed. We used this

technic for glycolic acid diluted in ethanol. Five droplets of solution (0.5 g/ml) were deposited on a ZnSe window, which was rotated at 200 rpm during 30 minutes.

Figure 2.12. The steps of formation of a thin film by spin coater (Faure, 2016).

2.3.3 Thin film preparation in cryogenic cell

FTIR transmission measurements on liquid carboxylic acids were run with a FTIR spectrometer and a cryogenic chamber (Fig.2.13). Thin films were formed on KBr a window placed at the top of the finger of a cryocooler Cryogenic system (ADP cryogénics, model SHI CH-202B-HC-4E). The chamber was maintained under ultra-vacuum (10^{-8} mbar). The heating system consisted in a thermal resistance wrapped around the cold finger. The diodes, stuck on the cold finger and the sample holder were connected to a PID controller Lake Shore 331.

The liquid was injected into the chamber through the deposition line. The injection rate was controlled through a micro-valve. The thickness of the thin films was measured through an interferometric approach, consisting of a He-Ne laser oriented at 45° with respect to KBr window. During the experiment, the interference, temperature and pressure were monitored by a LabView acquisition program. Thin films were formed at 25 K, and then were heated until sublimation with a ramp rate of 10 K min^{-1}. Heating-cooling cycles were applied.

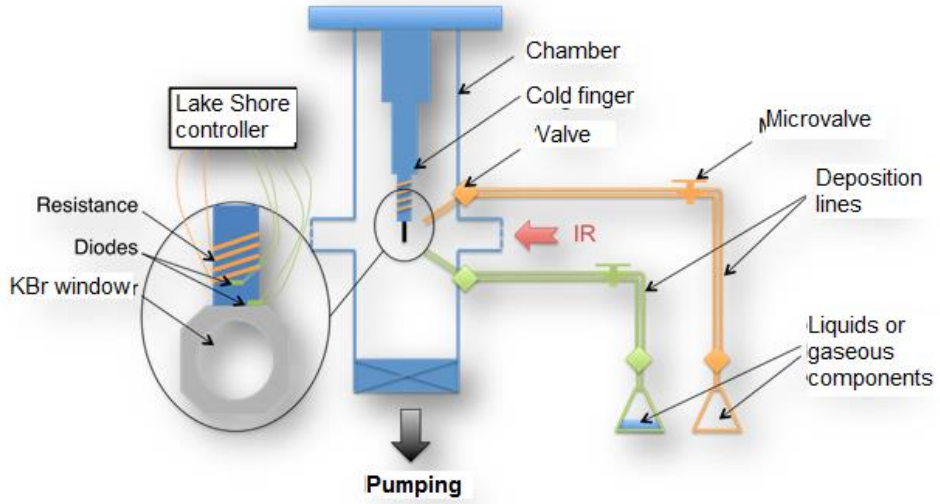

Figure 2.13. Schematic diagram of the cryogenic experimental setup (Credit: Mathilde Faure 2016).

Mid-infrared spectra (400-4000 cm^{-1}) with a 4 cm^{-1} spectral resolution were collected with a Bruker Vertex 70v FTIR spectrometer equipped with a GLOBAR source and a DTGS detector. The principle of an IR spectrometer is that a light beam passes through Michelson interferometer (as dispersive system) placed before the sample and the detector (Fig. 2.14).

In the Michelson interferometer the light beam is splitted in two beams by a beam splitter. The movable mirror generates a phase difference and a modulation at the exit of the spectrometer. In practice, as a polychromatic source is used, the detector collects the Fourier transform of the spectrum.

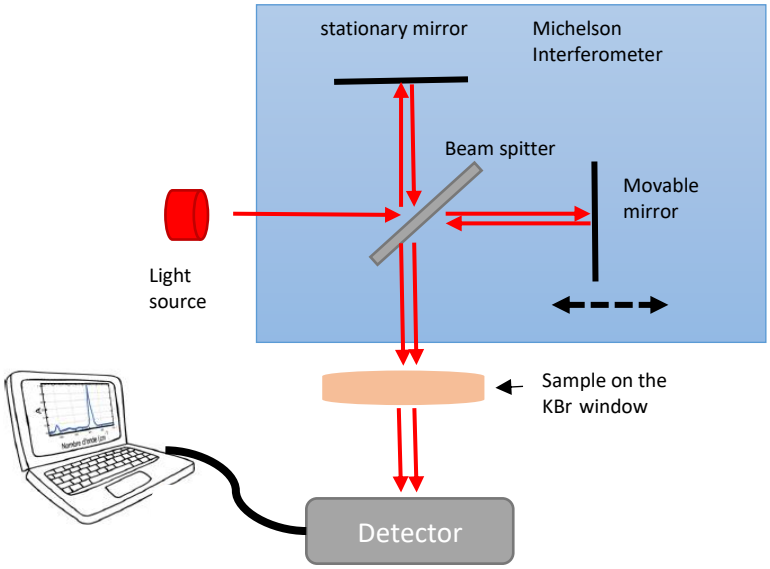

Figure 2.14. FTIR schema.

2.3.4 Thickness estimation of thin films

The thickness of thin films was obtained with an interferometric technique consisting of a He-Ne laser oriented at 45° with respect to the film surface. The number of fringes in the interference pattern as a function of deposition time provided the thickness according to the following equation:

$$d = k \frac{\lambda}{2n_f \sqrt{1-\frac{\sin^2 i}{n^2 f}}}$$

where *d* is the thickness, *k* is the number of fringes, λ the wavelength of the He-Ne laser (λ =632.8 nm), n_f the refractive index of the sample and *i* the incidence angle (i = 45°) (Bouilloud et al, 2015). In this work, for the calculation of thickness, we used the refractive index of liquid carboxylic acids from the NIST handbook because there were no measurements for pure solid at low temperature. The refractive index of formic acid, acetic acid, propionic acid, butyric acid and valeric acid are 1.37, 1.37, 1.38, 1.39 and 1.41.

During the vapor deposition of acid films on the KBr window, the interference fringes were monitored so their thickness can be measured (Figure 2.15 a). In some cases, the optical quality was not optimal, generating scattering and we observed the decrease of the amplitude of the fringes. For fatty acids (butyric and valeric acid), their optical quality were good and their signal displayed a double modulation, showing that thin films grew on both sides of the window (Fig. 2.15 c).

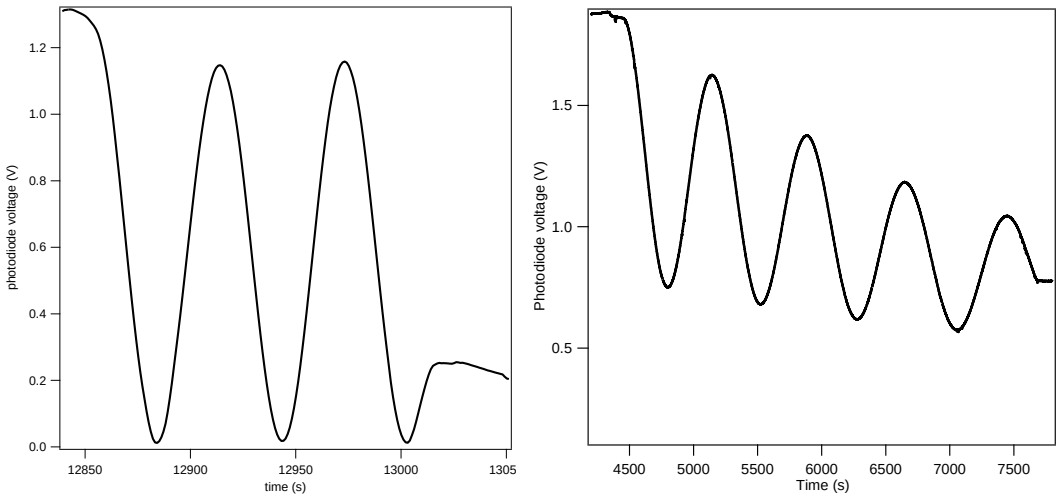

a. Constant amplitude b. Decreased amplitude

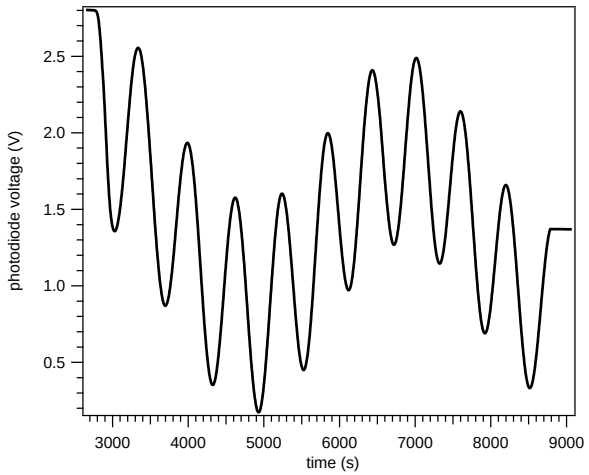

c. Two pattern of amplitude which means growth on two sides of the window

Figure 2.15. Interference pattern during acid deposition.

2.3.5 Microscopic measurements

This method was used for ammonium salt compounds because some of them are higly hygroscopic, and the pellet technique was not suitable. Here, individual grains were placed in an environmental cell, where they were maintained under vacuum at a mild temperature. This method was adapted from the method used for analyzing meteorite grains (Battandier, 2018).

Big ammonium salt grains were crushed between two glass slides, and ~50 µm grains were picked up with a tungsten needle and transferred on the diamond window. The first window was inserted in the lower part of a press, and a second window was placed on the top of the first one, and both were manually pressed. When separating the two windows, the crushed grains were usually mostly on the surface of one the two windows. However, sometimes the sample got fragmented on both windows, and in this case, the window with the largest part of the sample was selected (Fig. 2.16).

Spectral measurements were done with a FTIR microscope BRUKER HYPERION 3000 which equipped with an enviromental cell (Fig. 2.18) allowing the acquisition of the spectra under vacuum (P = 10^{-6} mbar) and with a moderate heating (T = 30-80 °C) (Beck et al., 2010). During our experiments the spectral range was 600-4000 cm^{-1} and the number of scans was typically 200. The spectra were acquired with a spectral resolution of 4 cm^{-1} and a MCT detector

cooled by liquid nitrogen. Before each measurement, a reference background was done on the window next to sample zone.

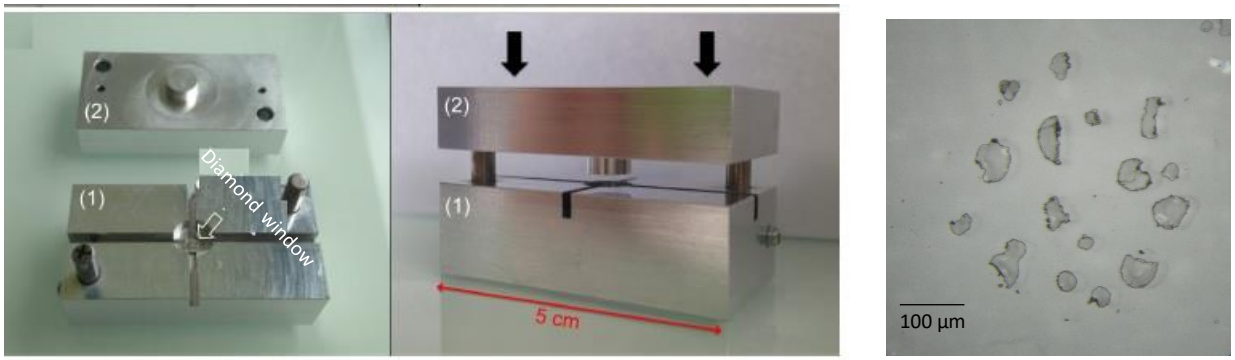

Figure 2.16. On the left, press for crushing grains between two diamond windows, the size of diamond window is diameter 3.5 mm and thickness 0.5 mm. On the right, microscope image of the grains after crushing by two diamond windows.

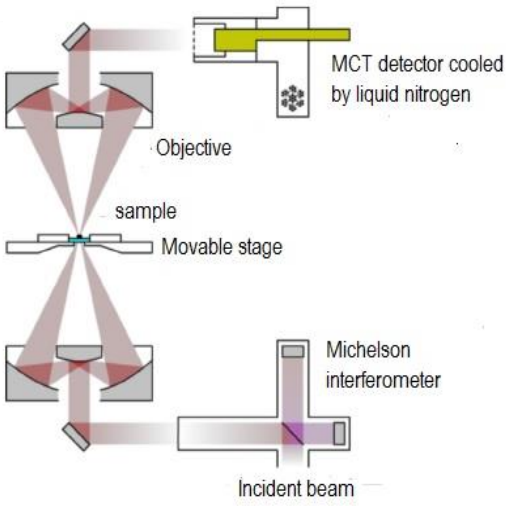

Figure 2.17. Sketch of the FTIR microscope Bruker Hyperion 3000 (Credit: Battandier, 2018).

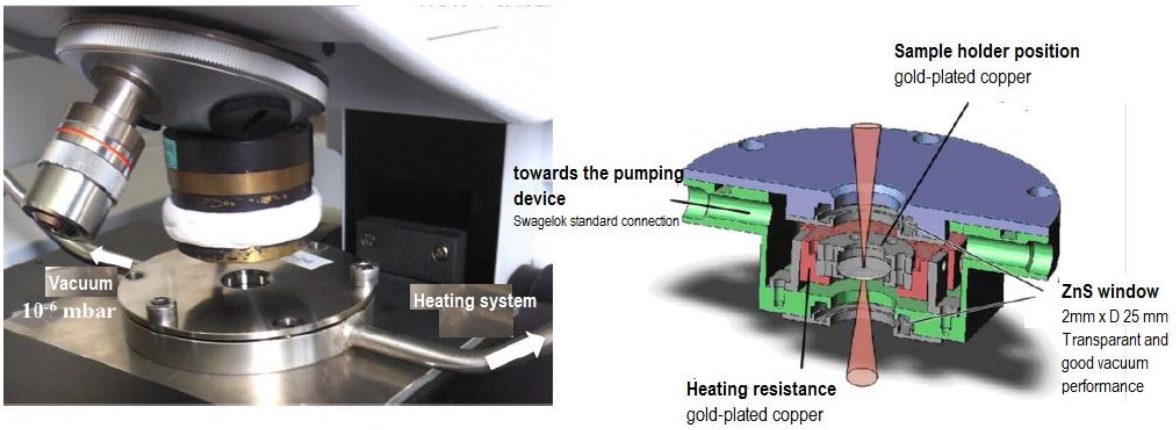

Figure 2.18. Environmental cell, where the samples are placed during IR measurement, connected to a turbomolecular pump and a heating system. To allow acquisition of the measurements, the cell is equipped with two ZnS windows (Credit: Battandier, 2018).

Chapter 3
Transmission spectra of pure carboxylic acids and ammonium salts

Carboxylic acids and the NH_4^+ ion have been proposed as candidates of the 3.2 µm band of comet 67P/CG, because these molecules display a broad absorption band in the 3 µm region (Quirico et al, 2016). Simple carboxylic acids have also been detected by COSIMA and ROSINA instruments (Bardyn et al., 2017; Altweg et al., 2017; Rubin et al., 2015). In primitive meteorites, several types of carboxylic acids have been identified so far, such as monocarboxylic, dicarboxylic and hydroxylated acids (Sephton, 2002). However, the spectral properties of these compounds are poorly known. Spectra of carboxylic acids in the solid state are scarce in literature, and we are lacking comprehensive studies covering a broad range of temperature. In the case of ammonium salts, Quirico et al. (2016) made comparison of VIRTIS data only with NH_4Cl and for spectra collected at room temperature.

This chapter reports transmission spectra of series of carboxylic acids and NH_4^+ salts. Liquid monocarboxylic acids (C1-C5 aliphatic chains), dicarboxylic acid and hydroxylated carboxylic acids with aliphatic chains (C2,C3,C4) and aromatic chains were prepared as thin film thanks to the cryogenic setup presented in Chapter 2 (Fig. 2.13). Heavier carboxylic acids and ammonium salts were prepared as pellets or thin films produced by a spin coater.

3.1 Transmission measurements

3.1.1 Formic acid

In our measurements, thin films of formic acid were produced by depositing liquid phase of formic acid on a KBr window maintained at 25 K. After deposition, the spectrum presented several bands (Fig. 3.1, Tab. 3.1). We basically observe six bands below 1800 cm^{-1}, and a broad feature with several peaks between 2500 cm^{-1} and 3500 cm^{-1}. Interestingly, the spectrum looks pretty similar to that of the liquid phase. Upon heating up to 175 K, several changes are observed: the bands at 1713 cm^{-1}, 1371 cm^{-1} and 1211 cm^{-1} split into two components, while the features at 1072 cm^{-1} cm^{-1}, 927 cm^{-1} and 720 cm^{-1} get narrower (Fig. 3.2). Significant changes also appear in the broad band between 2500 cm^{-1} and 3500 cm^{-1}: the band gets slightly narrower (drop of the wing towards high wavenumbers) and display three major peaks at 2451 cm^{-1}, 2784 cm^{-1} and 2898 cm^{-1}. When cooling down the sample from 175 K to 25 K, no dramatic

evolution is observed, which means that the sample deposited at 25 K experienced an amorphous to crystalline transition upon heating between 125 K and 150 K.

In the crystalline state, formic acid exists as long polymer chains of molecules bridged by an hydrogen bond between two adjacent O atoms (Fig. 3.3; Millikan and Pitzer, 1958). In the liquid phase, cyclic dimers are a key element that interacts more largely with other –OH bonds (Fig. 3.3; Chelli et al., 2005). The spectral similarity between the amorphous and liquid phases suggests that these dimers are also present in the amorphous state. In the crystalline state, solid-state effects controlled by the translational order lead to the narrowing and splitting of the features below 1800 cm^{-1}. The relative intensities in the broad feature between 2500 cm^{-1} and 3500 cm^{-1} are significantly modified, but except slight spectral shift of the peaks, the main components seem to be present in both the spectra of the amorphous and crystalline forms.

Our spectra are very similar to the spectra collected by Cyriac and Pradeep (2005) and Millikan and Pitzer (1958) (Tab. 3.1). The spectrum of solid HCOOD at 175 K shows that all the features in the range 2500-3500 cm^{-1} (except the C-H bands) shifts towards low wavenumbers (Fig. 3.1; note that in this spectrum the bands are only partly shifted, due to a likely partial hydrogen-deuterium exchange between HCOOD and water contamination in the flask or in the experiment). This shows that they imply –O…H…O– hydrogen bonds except C-H stretching modes. However, the bands peaking between 2400 and 2800 cm^{-1} have a much lower frequency than that reported in Millikan and Pitzer (1958). They are likely combination modes, which involve the –OH bond.

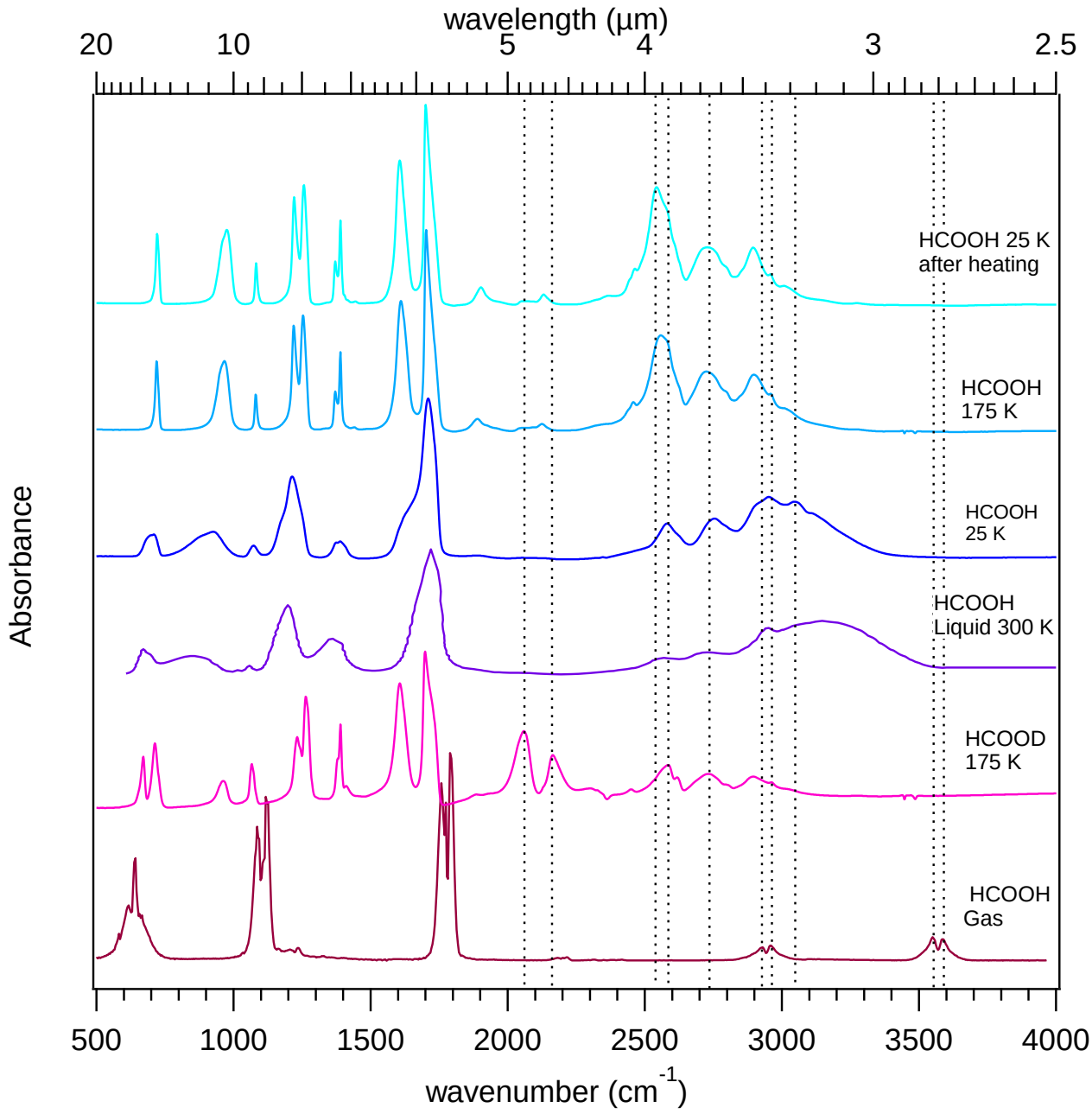

Figure 3.1. Comparison spectra of solid formic acid at 25 K, 175 K and 25 K after heating and cooling; Spectrum of deuterated formic acid at 25 K and 175 K; spectrum of liquid formic acid (Cyriac and Pradeep, 2005) and spectrum of gas formic acid (NIST). Dotted line is used to clarify the spectra evolution.

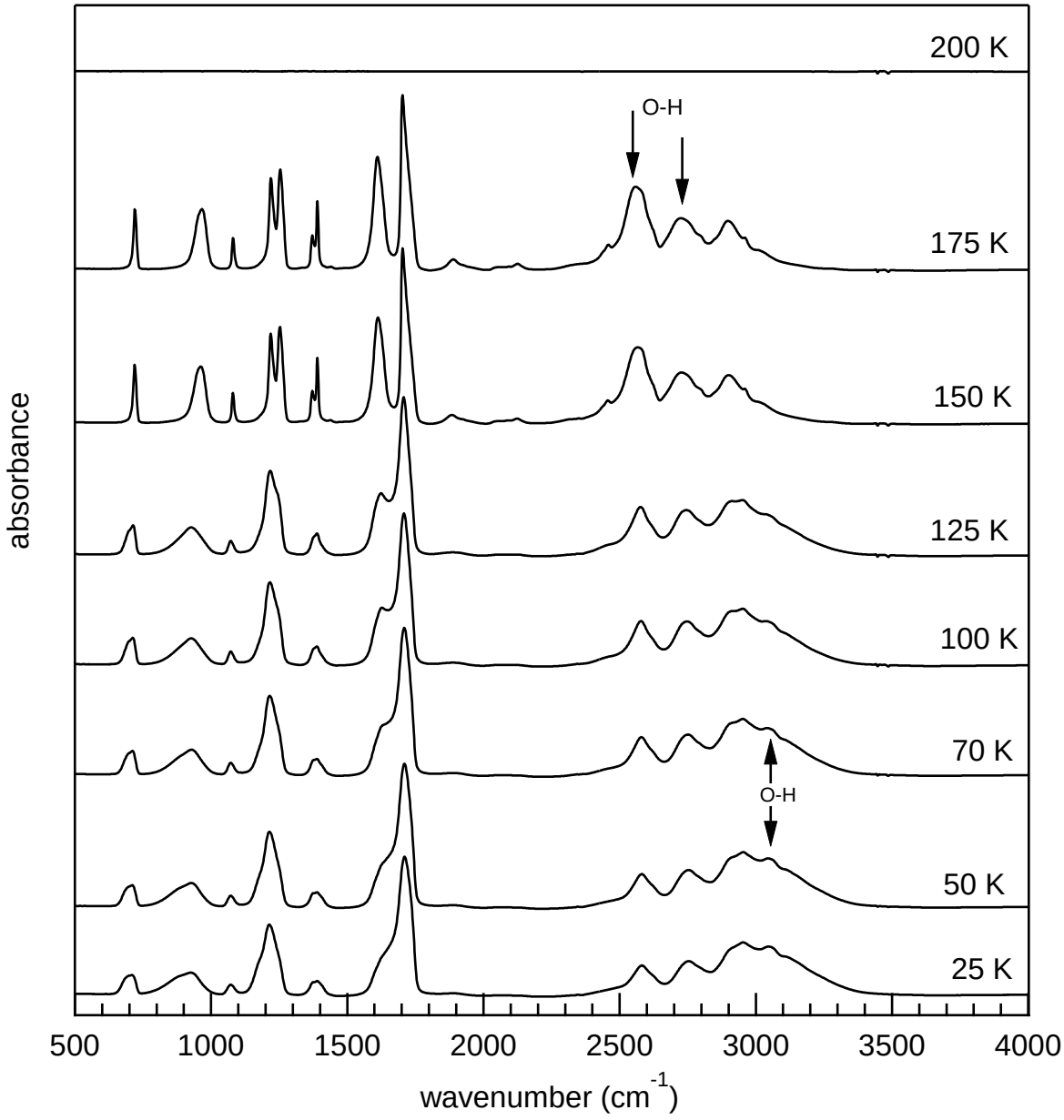

Figure 3.2. Spectral evolution of formic acid thin film with temperature thickness of 811 ± 7 nm). The arrow signs point to an –OH feature that appear to crystalline form. The spectra are offseted for clarity.

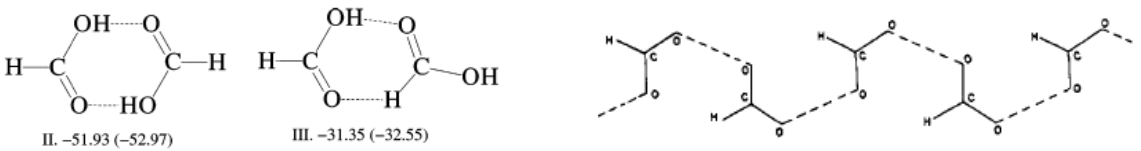

Figure 3.3. Possible configurations of dimeric formic acid in the liquid state (left) (Chelli et al., 2005), and the planar chain structure of crystalline formic acid (Millikan and Pitzer, 1958) (right).

Table 3.1. Absorption band of Solid Formic acid at 25K and 175 K and Deuterated formic acid at 175 K (Bisschop et al., 2007; Cyriac and Predeep, 2005; Millikan and Pitzer, 1958)

HCOOH 25 K (amorphous)			**HCOOH 175 K (crystalline)**		**Vibration mode**	**HCOOD 175K**		**Vibration mode**
Wavenumber (cm^{-1})	**Cyriac (2005)**	**Bisschop (2007)**	**Wavenumber (cm^{-1})**	**Millikan (1958)**		**Wavenumber (cm^{-1})**	**Millikan (1958)**	
3111	3153	3115	2997	3020	O-H stretching			
3048					O-H stretching			
2953	2953	2953	2962	2958	C-H stretching	2969	2969	C-H stretching
			2898	2892	C-H stretching	2891	2904	C-H stretching
2753	2726	2754	2784	2712	Overtones and combination bands	2734, 2621	2725	OH stretching
2583	2569	2582	2561	2532	Overtones and combination bands			
			2451	2459	Overtones and combination bands	2587	2585	OH stretching
			2120	2141		2541		
1890	1890		1890	1900				
						2170	2175	OD stretching
						2170	2175	OD stretching
						1068	1081	OH bending
1713	1725	1714	1709	1718	C=O stretching	1699	1694	C=O stretching
1640	1713	1650	1610	1609	C=O stretching	1607	1602	C=O stretching
1391	1389	1387	1390	1391	C-O-H bending	1391	1396	C-O-H bending
1371	1373		1372	1370	H-C-O bending			H-C-O bending
1211	1202	1211	1254	1255	C-O stretching	1268	1277, 1268	C-O stretching
			1218	1224	C-O stretching	1229		C-O stretching
1072	1072	1073	1081	1083	C-H bending (out-of-plane)	1368	1385	C-H bending (out-of-plane)
927	927	930	966	974	O-H bending (out-of-plane)	713	713	O-H bending (out-of-plane)
713	711	705	720	721	O-C-O bending	671	674	C-H stretching

* The absorption coefficients are presented in Table A.1.

3.1.2. Acetic acid

For acetic acid deposited at 25 K, we first observe a broad band from 2570 cm^{-1} to 3050 cm^{-1} that comprises vibration modes of –OH and CH bonds. Hence, by comparing with the spectra of deuterated acid CH_3COOD, we observe a global shift of this feature towards low wavenumbers, except the faint features due to CH (Fig. 3.4). The lack of broad features in the 3000 cm^{-1} region in the spectrum of acetate also supports this view. The spectrum of liquid acetic acid from NIST is fairly similar with that of the solid, but the positions of the bands are slightly shifted (Fig.3.4). The bands below 2000 cm^{-1} seem also in agreement between the solid and liquid phases. Interestingly, we observe that the peaks of the CH vibration bands are slightly shifted between the solid and liquid phases, but also between CH_3COOH and CH_3COOD. For this latter, it may point to non-negligible interactions between these vibration modes and the –OH groups.

The Figure 3.5 presents the spectral evolution of carboxylic acids from 25 K until 200 K. By increasing the temperature, we observe the narrowing and splitting of the bands, indicating an amorphous-crystalline transition. At 175 K, the sample is totally crystalline. The thin film of acetic acid is totally sublimated from the KBr window at 200 K.

The band assignment of the liquid phase has been proposed by Bratoz et al. (1956). The –OH stretching mode is observed at 3080 cm^{-1} and the CH at 2941 cm^{-1}. The bands at 2561 cm^{-1}, 2632 cm^{-1}, 2688 cm^{-1} and 2793 cm^{-1} are assigned to combination modes. The frequencies of the 42 normal vibration modes of cyclic dimers have been calculated by Lewandowski et al. (2005). Only half of those modes are infrared active. This study confirms that the –OH stretching mode consists in a single feature at ~3050 cm^{-1}, and that the other features in this region are combination bands. Interestingly, these calculations provide insights into the real quantitative contributions of the main bond deformations modes to the normal coordinates. As such, the assignment indications provided in earlier publications (and these applies as well to the assignment of the vibration modes of formic acid) point to the main contributors. In some cases, the band results from the significant contribution of several bond deformations, e.g. the 27^{th} normal vibration at 1478 cm^{-1} due to δCOH, $\nu_a CC\text{-}O$ and $\delta'_s CH_3$. Finally, the detailed assignments are presented in Table 3.2.

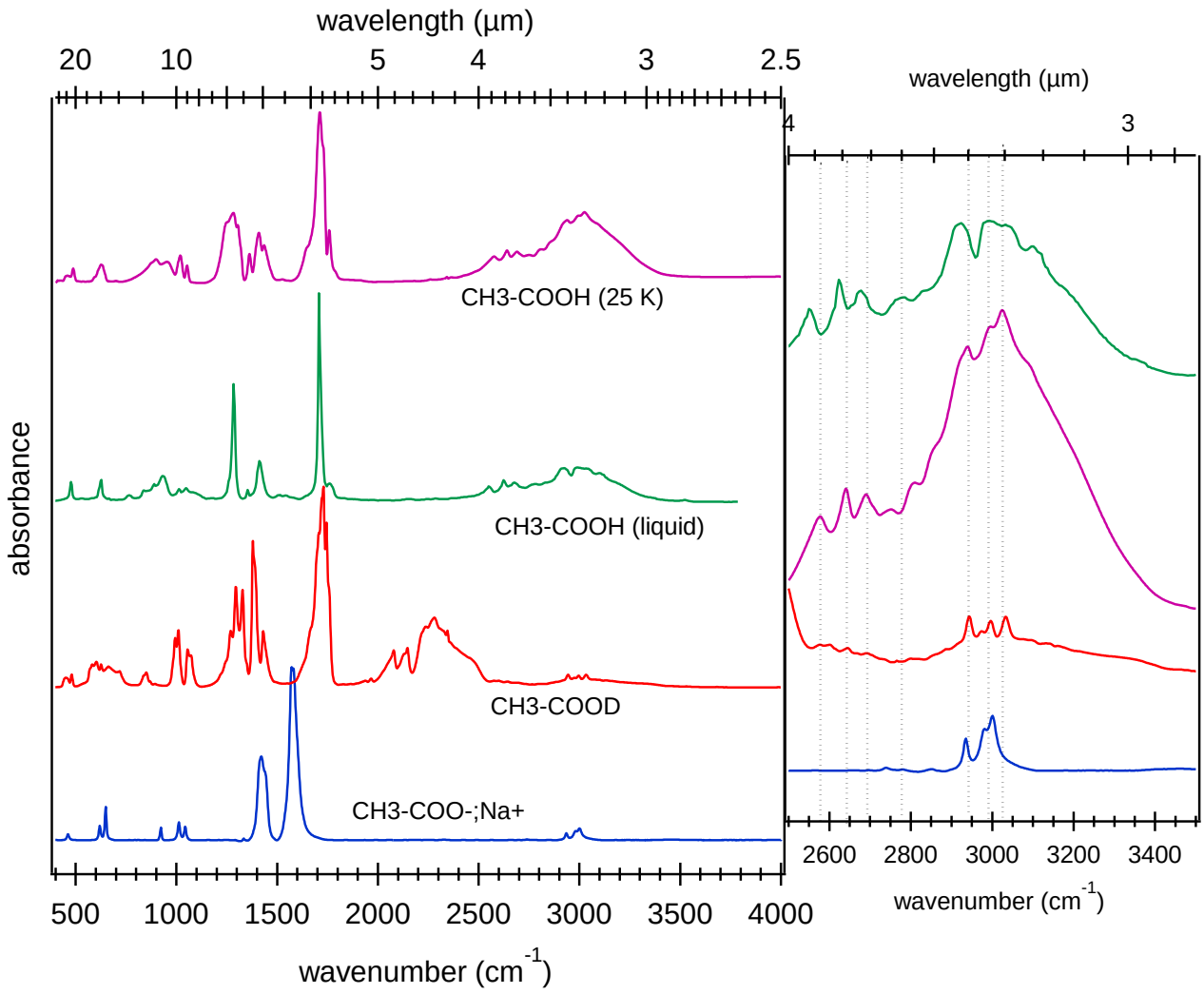

Figure 3.4. Comparison spectra of solid acetic acid at 25 K, deuterated acetic acid at 25 K and sodium acetate at room temperature.

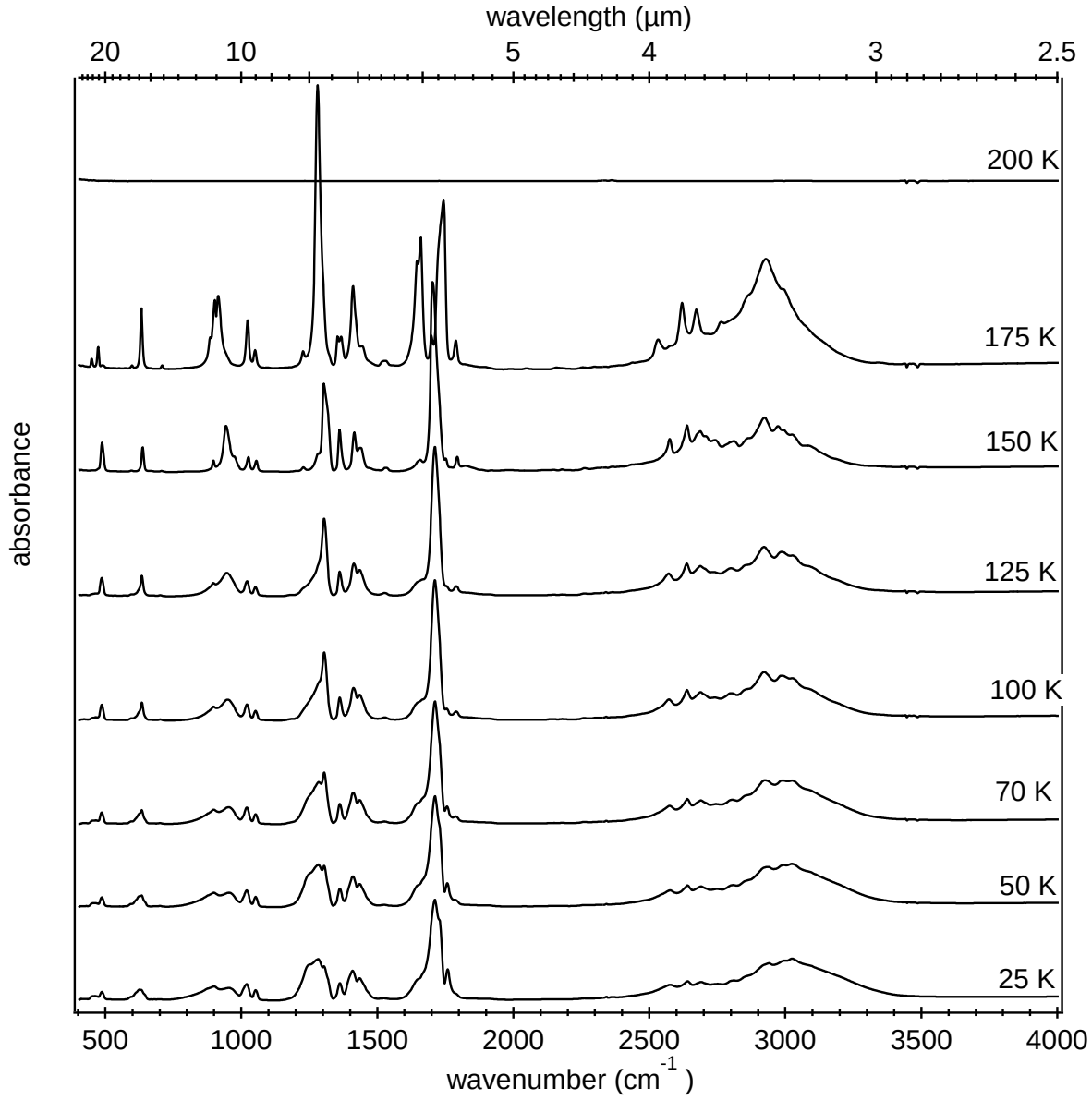

Figure 3.5. Spectra evolution of solid acetic acid with thickness 1096 ± 9 nm.

Table 3.2. Absorption band of solid acetic acid at 25 K and 175 K ([a]Bennet and Kaiser, 2007; [b]Lewandowsky et al, 2004; [c]Bratoz et al., 1956; [d]Lin-Vien et al., 1991)

25 K (amorphous)	**175 K (Crystalline)**	**References**				**Vibration mode**
Wavenumber (cm^{-1})	**Wavenumber (cm^{-1})**	**Solid 12 K** [a]	**Gas (dimeric)** [b]	**Liquid** [c]	**Solid 150 K** [c]	
3026			3034-3053	3080		OH stretching [b,c]
2994	2992					Superimposition of CH stretching, OH stretching [c]
2942	2930			2941	2924	
2812	2762				2820	Overtones and combinations band enhanced by Fermi resonance with the broad OH stretch band [c]
2804				2793		

25 K (amorphous)	175 K (Crystalline)	References				Vibration mode
Wavenumber (cm^{-1})	Wavenumber (cm^{-1})	Solid 12 K [a]	Gas (dimeric) [b]	Liquid [c]	Solid 150 K [c]	
2740	2762					
2690	2676			2688	2674	
2641	2621			2632	2618	
2578	2532			2561	2538	
	1788				1802	
1759	1741	1757		1759		C=O stretching (as)[d], CC-O stretching (as) [b], COH bending [b]
1713	1700	1723	1674-1712	1718		
	1659				1658	C=O stretching (s) [d]
	1646				1645	C=O stretching (s) [d]
1517	1528					
1438	1445		1437-1463	1432		CH_3 bending (s) [b], COH bending [b]
1412	1409		1410-1436	1412		COH bending [b], CC-O stretching (s) [b], CH_3 bending (s) [b]
1365	1368					CH_3 bending (s) [b], COH bending [b], CC-O stretching (a) [b]
	1353	1350	1357-1375			
1308						
1284	1283		1273-1302	1290, 1279		CC-O stretching (a) [b], COH bending [b], CH_3 bending (s) [b]
1247	1230					
1053	1051	1051	1071			CH_3 rocking [a]
1021	1024		1008-1021			CH_3 rocking(//) [b], CC-O stretching (a) [b]
957	915	957				CH_3 rocking [a]
900	902					CC-O stretching (s)[b], OH….O out-of-plane wag [d]
	886		866-878			
628	709					
	633		607-620			CO_2 bending, CC stretching
	598		572-576			CO_2 rocking (|) [b], CH_3 rocking(|) [b]
488	492		468-473			CO_2 rocking(//) [b], CH_3 rocking(//) [b]
456	474		444			

* The absorption coefficients are presented in Table A.2.

3.1.3 Propionic acid

The spectrum of solid propionic acid deposited at 25 K is presented in Figure 3.6, and the spectra upon temperature in Figure 3.7. We basically observe similar trends with respect to formic and acetic acids: a broad and quite complex band between 2500 cm^{-1} and 3100 cm^{-1}, which is controlled by the –OH bond (this band is absent in the spectrum of sodium propionate),

and an amorphous-crystalline phase transition that led to narrowing and/or splitting of the bands below 2000 cm^{-1}. The broad band gets more structured. The thin film totally sublimate at 210 K.

We did not found earlier studies that assign the bands of solid propionic acid, including the NIST database. However, the spectrum can be fairly assigned thanks to the assignment of formic and acetic acid. In the range 2500 cm^{-1} cm^{-1} 2900 cm^{-1}, we observe combination bands involving the –OH bond. The –OH and CH stretching modes appear above 2900 cm^{-1} (Fig. 3.6). Note that here the CH features are more prominent, and clearly appears in the spectrum while they were faint for formic and acetic acid. The bands at 1744 cm^{-1} and 1713 cm^{-1} have strong peaks due to C=O stretching. The fingerprint region also contains many absorption bands which are mainly due to bending and other deformation vibration modes. Comparing with the spectrum of sodium propionate, the CH stretching band and fingerprint region of acid shift to higher wavenumber. This is due to a change in the configuration of the ions, in particular its symmetry. The assignment is presented in Tab. 3.3, based on the bands assignment done for acetic acid and on the handbook of organic molecules by Lin-Vien et al. (1991).

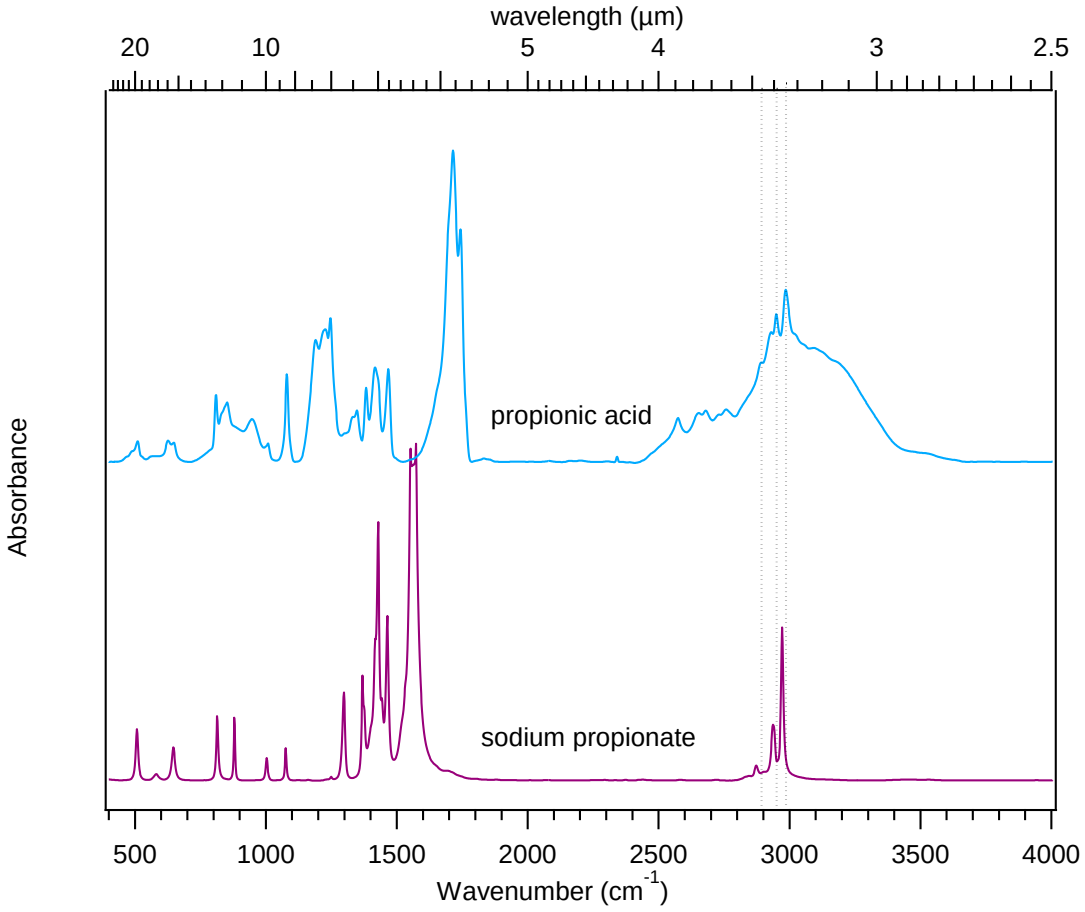

Figure 3.6. Comparison spectra of propionic acid at 25 K and sodium propionate at room temperature.

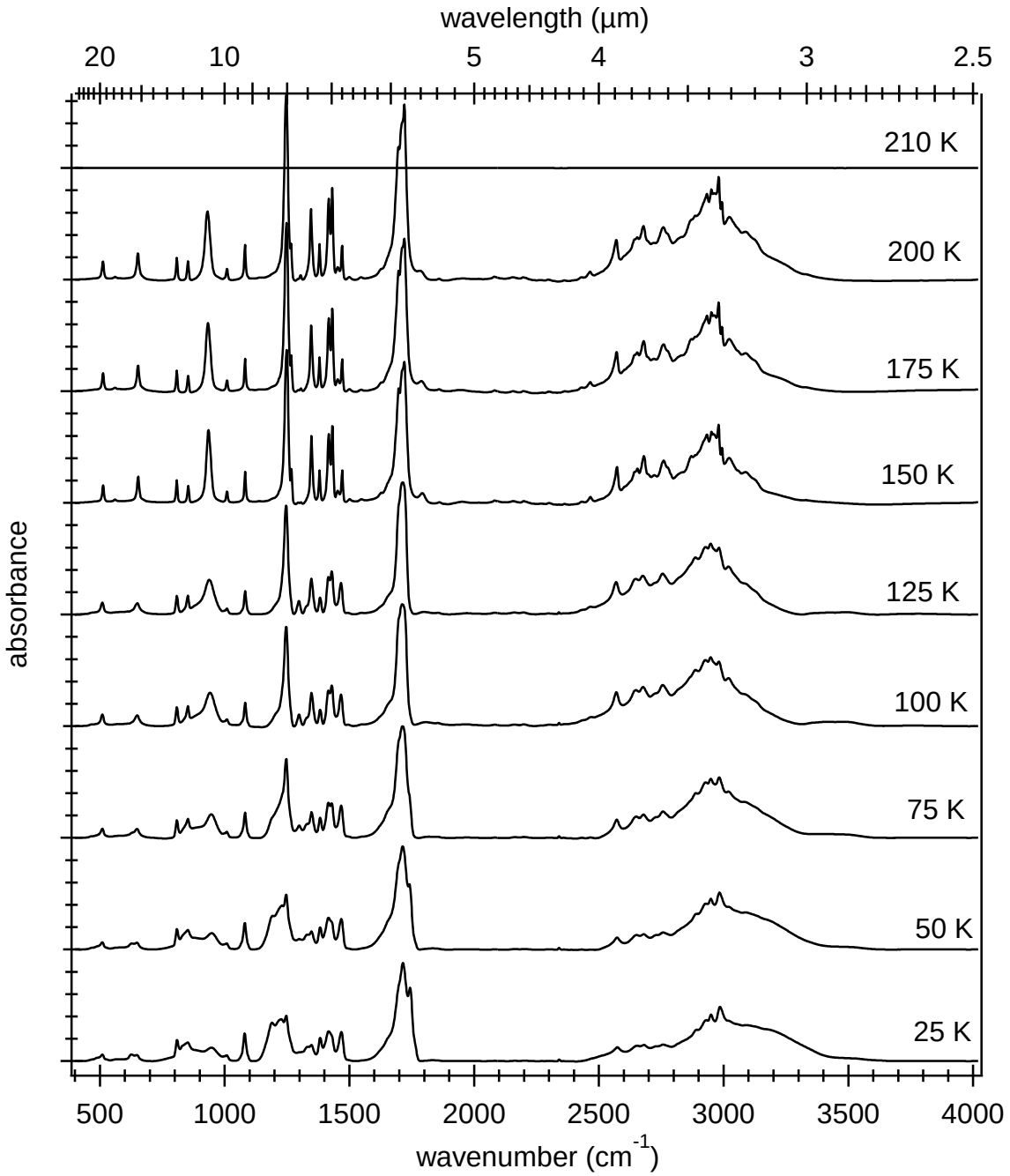

Figure 3.7. Spectral evolution of solid propionic acid with thickness 8329 ± 66 nm.

Table 3.3. Absorption band of solid propionic acid at 25K and 175 K

25 K (amorphous)		**175 K (crystalline)**		**Reference** (Lin-Vien et al., 1991)	**Vibration mode**
Wavenumber (cm^{-1})	**Absorption Coefficient (cm^{-1})**	**Wavenumber (cm^{-1})**	**Absorption Coefficient (cm^{-1})**		
3173	*1465+ 11*	3091	*1935 + 19*		OH stretching
3097	*1659 + 13*	3023	*2488 + 25*		OH stretching
2987	*2488 + 19*	2995	*3179 + 32*		CH stretching
		2980	*4396 + 44*	2890-3000	CH stretching

25 K (amorphous)		175 K (crystalline)		Reference (Lin-Vien et al., 1991)	Vibration mode
Wavenumber (cm^{-1})	**Absorption Coefficient (cm^{-1})**	**Wavenumber (cm^{-1})**	**Absorption Coefficient (cm^{-1})**		
		2965	*3760 + 38*		CH3 stretching (as)
2950	*1935 + 15*	2951	*3870 + 39*	2952-2972	CH3 stretching (as)
2928	*1852 + 15*	2933	*3732 + 37*	2890-3000	CH stretching
2891	*1548 + 12*	2885	*2626 + 26*		CH_3 stretching (s)
		2871	*2599 + 26*	2862-2883	CH_3 stretching (s)
		2831	*1797 + 18*		OH stretching & overtone CH bending
		2775	*2018 + 20*		Overtones and combinations band
2759	*691 + 6*	2759	*2350 + 24*		
2727	*1061 + 8*	2720	*1603 + 16*		
2681	*802 + 6*	2679	*2516 + 25*		
2653	*774 + 6*	2655	*1935 + 19*		
		2643	*1825 + 18*		
		2603	*1106 + 11*		
2574	*691 + 6*	2572	*1990 + 19*	2500-2700	
		2465	*525 + 5*		Overtones and combinations band
		2429	*249 + 2*		
		2362	*83 + 1*		
		2299	*111 + 1*		
		2198	*166 + 2*		
		2155	*166 + 2*		
		2081	*194 + 2*		
		1946	*166 + 2*		
		1860	*166 + 2*		
1743	*3622 + 29*	1788	*581 + 6*		C=O stretching
1715	*4838 + 38*	1721	*7602 + 76*		
		1698	*6027 + 60*		
		1629	*498 + 5*	1660-1740	
		1548	*138 + 1*		
		1500	*138 + 1*		
1469	*1797 + 14*	1471	*1576 + 16*	1430-1470	CH3 bending
1418	*1797 + 14*	1454	*608 + 6*		C—OH in plane bending
1417	*1493 + 15*	1431	*6032 + 60*		
1383	*1133 + 11*	1381	*5622 + 56*	1395-1440	
1348	*802 + 8*	1346	*1659 + 17*	1345	CH2 wagging
1331	*719 + 7*	1306	*3317 + 33*		C-O stretching
		1293	*249 + 2*		
1247	*2212 + 22*	1268	*194 + 2*	1280-1315	
1226	*2046 + 21*	1248	*1880 + 18*		CH2 wagging
1191	*1935 + 19*			1180-1345	
1081	*1382 + 14*	1081	*1659 + 17*		CH bending out-of-plane
1010	*276 + 3*	1009	*553 + 5*		CH3 rocking
947	*663 + 7*	934	*3373 + 34*		OH---O wagging
852	*912 + 9*	854	*829 + 8*	875-960	
810	*1051 + 11*				
		653	*1244 + 12*		

25 K (amorphous)		175 K (crystalline)		Reference (Lin-Vien et al., 1991)	Vibration mode
Wavenumber (cm^{-1})	**Absorption Coefficient (cm^{-1})**	**Wavenumber (cm^{-1})**	**Absorption Coefficient (cm^{-1})**		
648	*304 + 3*	560	*166 + 2*		
511	*332 + 3*	512	*829 + 8*		

3.1.4 Butyric acid

The spectra are displayed in Figure 3.8 and 3.9. As reported previously, the broad band between 2500-3500 cm^{-1} involves the –OH bond, as the –OH stretching and combination modes with fundamental vibrations below 2000 cm^{-1}. Sharp peaks at 2968 cm^{-1}, 2941 cm^{-1} and 2881 cm^{-1} are superimposed on this broad massif. They are due to the CH_3 and the CH_2 symmetric and asymmetric stretching modes (Lin-Vien et al., 1991).

Below 2000 cm^{-1}, the strongest feature peaks at 1700 cm^{-1} and is due to the C=O stretching. However, in sodium butyrate, C=O stretching band appears at lower wavenumber because in salt, the CO_2^- substitutes the COOH bond of acid as bond-and-a-half bond. This bond vibrates out of phase and in phase and generates features in the 520-1630 cm^{-1} region for asymmetric stretching, and in the 1340-1480 cm^{-1} region for symmetric modes (Lin-Vien et al., 1991).

Figure 3.9 presents the spectral evolution of butyric acid upon temperature. Increasing the temperature affects the shape of bands (narrowing), and an irreversible amorphous-crystalline transition is observed. Butyric acid starts to sublimate at 230 K. The detailed band assignment is presented on Table 3.4.

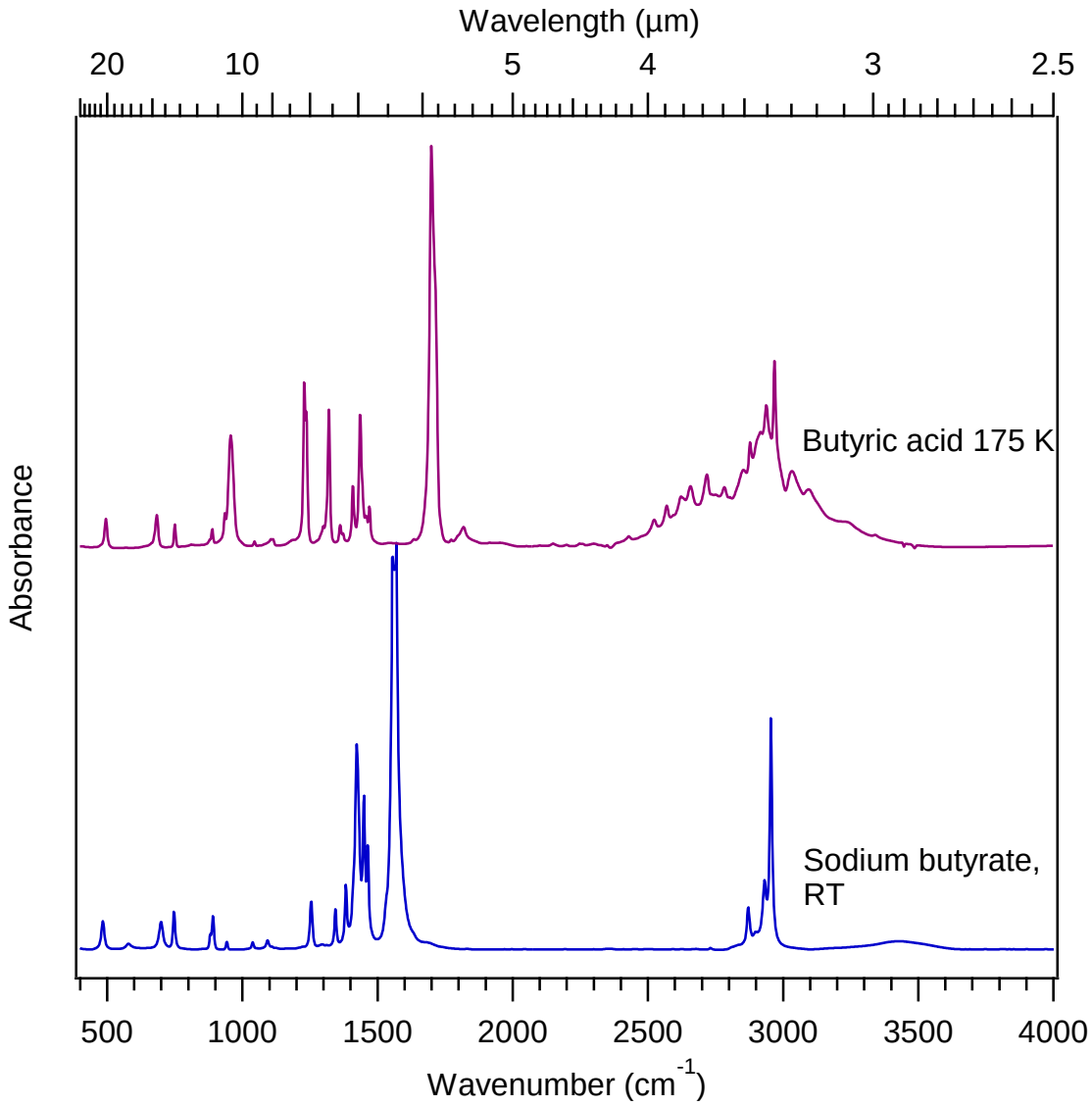

Figure 3.8. Spectra of solid butyric acid deposited and measured at 25 K, and sodium butyrate measured at room temperature.

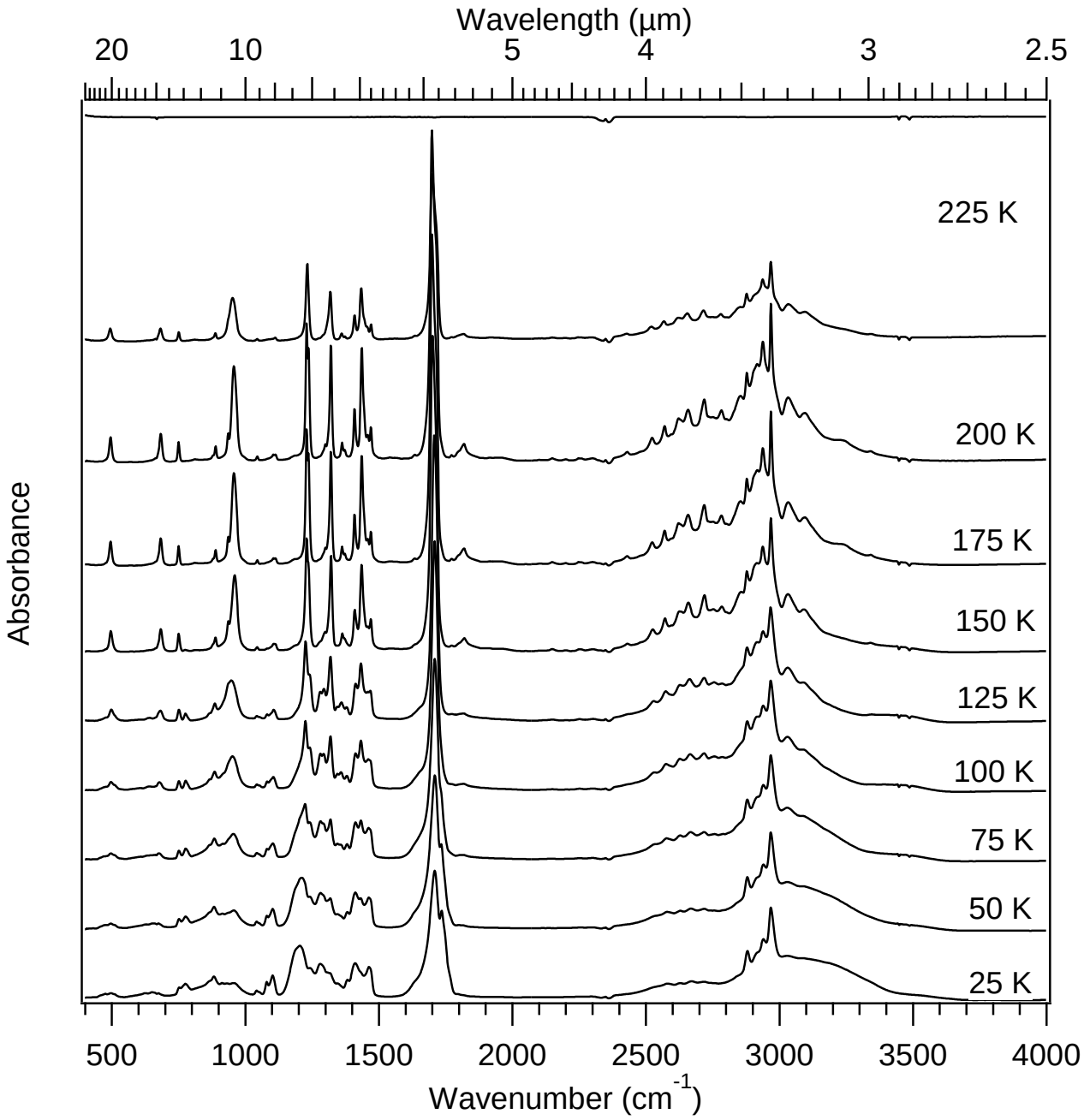

Figure 3.9. Spectral evolution of solid butyric acid (thickness 5243 ± 42 nm).

Table 3.4. Band assignment of butyric acid (Lin-Vien et al., 1991)

25 K (amorphous)		**175 K (crystalline)**		**Reference**	**Vibration mode**
Wavenumber (cm^{-1})	**Absorption Coefficient (cm^{-1})**	**Wavenumber (cm^{-1})**	**Absorption Coefficient (cm^{-1})**		
3534	*217+ 2*				OH stretching
		3337	*651 + 5*		OH stretching
		3244	*1302 + 10*		OH stretching
3094	*2388 + 19*	3094	*2930 + 23*		OH stretching
3032	*2496 + 20*	3032	*3907 + 31*		OH stretching

25 K (amorphous)		175 K (crystalline)		Reference	Vibration mode
Wavenumber (cm^{-1})	**Absorption Coefficient (cm^{-1})**	**Wavenumber (cm^{-1})**	**Absorption Coefficient (cm^{-1})**		
2969	*5535 + 56*	2969	*9659 + 77*	2952-2972	CH3 stretching (as)
2943	*3582 + 36*	2938	*7380 + 59*	2890-3000	CH stretching
	2822 + 28	2919	*5969 + 48*	2916-2936	CH2 stretching (as)
2880	*2388 + 19*	2880	*5427+ 43*	2862-2882	CH3 stretching (s)
		2854	*5861+ 46*	2843-2863	CH2 stretching (s)
		2783	*3039+ 24*	2500-2700	Overtones and combinations band
2720	*858 + 7*	2718	*3799+ 30*		
2671	*858 + 7*				
2628	*760 + 6*	2658	*3147+ 25*		
		2622	*2605+ 21*		
2580	*760 + 6*	2573	*2171+ 17*		
		2525	*1411+ 11*		
		2430	*543+ 4*		
		1820	*1085+ 9*		Overtones OH---O wagging
1737	*5427 + 43*			1660-1740	C=O stretching (as)
1710	*7597 + 61*	1699	*20621+ 165*		
1465	*1845 + 15*	1471	*2062+ 17*	1430-1470	CH3 bending (as)
		1459	*1628+ 13*		
		1436	*6837+ 55*	1395-1440	C-OH in-plane bending
1411	*2062 + 17*	1409	*3147+ 25*		
1383	*977 + 8*	1373	*760+ 6*	1365-1395	CH3 bending (s)
1347	*760 + 6*	1362	*1194+ 10*		
1318	*1411 + 11*	1321	*7163+ 57*	1280-1315	C-O stretching
1283	*1954 + 16*	1299	*1085+ 9*		
1243	*1737 + 14*	1237	*7055+ 57*		
1103	*3147 + 25*	1113	*543+ 4*		
1081	*1194 + 10*	1105	*434+ 4*		
1044	*868 + 7*	1046	*326+ 3*	1028	CH2 wagging
956	*315 + 3*	958	*5752+ 46*	875-960	OH---O wagging
931	*825 + 7*	936	*1845+ 15*		
911	*760 + 7*				
884	*825 + 7*	889	*868+ 7*		
776	*1302 + 10*			730-720	CH2 rocking
753	*868 + 7*	750	*1302+ 10*		CH2 rocking
675	*651 + 5*	684	*1737+ 14*		
652	*326 + 3*				
623	*326 + 3*				
495	*326 + 3*	496	*1519+ 12*		
476	*326 + 3*				

3.1.5. Valeric acid (pentanoïc acid)

The spectrum of solid valeric acid deposited at 25 K displays a broad band between 2400 and 3400 cm^{-1} onto which are superimposed three strong peaks at 2875 cm^{-1} as CH_3 symmetric stretching, 2938 cm^{-1} as CH_2 asymmetric stretching and 2961 cm^{-1} as CH_3 symmetric stretching (Fig. 3.10; Lin-Vien et al., 1991). Structure-less shoulders are observed on both sides of these aliphatic features. By increasing the temperature, sharp peaks appear on this broad band. As reported before, we have here overtones and combination bands that involve the OH bond, as well as the –OH stretching mode above 3000 cm^{-1}. The detailed assignment is presented in Table 3.5.

Table 3.5. Absorption band of solid valeric acid at 25 K and 175 K

25 K (amorphous)		**175 K (crystalline)**		**Reference** (Lin Vien at al, 1991)	**Vibration mode**
Wavenumber (cm^{-1})	**Absorption Coefficient (cm^{-1})**	**Wavenumber (cm^{-1})**	**Absorption Coefficient (cm^{-1})**		
		3238	*656 + 5*		OH stretching
3094	*1235 + 10*	3092	*1389 + 11*		OH stretching
3028	*3203 + 25*	3032	*1853 + 14*		OH stretching
		3016	*1853 + 14*		OH stretching
2961	*3203 + 25*	2961	*4516 + 36*	2952-2972	CH3 stretching (as)
2938	*2277 + 18*	2943	*3898 + 31*	2916-2936	CH2 stretching (as)
		2913	*2972 + 23*	2890-3000	CH stretching
		2897	*2702 + 23*		
		2873	*2972 + 24*	2862-2882	CH3 stretching (s)
		2856	*2238 + 18*	2843-2863	CH2 stretching (s)
		2764	*1505 + 12*	2500-2700	Overtones and combination band
		2729	*1312 + 10*		
		2705	*1505 + 12*		
2682	*463 + 4*	2686	*1544 + 12*		
		2641	*1274 + 10*		
2620	*386 + 3*	2620	*1544 + 12*		
2585	*386 + 3*	2545	*965 + 8*		
		2486	*386 + 3*		
		1805	*232 + 2*		Overtones OH---O wagging
1740	*2393 + 19*	1784	*193 + 2*	1660-1740	C=O stretching
1708	*3551 + 28*	1708	*8838 + 70*		C=O stretching
1468	*926 + 7*	1468	*1351+ 10*		
		1455	*772 + 6*		
		1430	*2702 + 22*	1395-1440	COH in-plane bending
1411	*888 + 7*	1405	*1235+ 10*		
1382	*463 + 4*				
1330	*579 + 5*				
1306	*579 + 5*			1280-1315	CO stretching
1291	*733 + 6*				

25 K (amorphous)		175 K (crystalline)		Reference (Lin Vien at al, 1991)	Vibration mode
Wavenumber (cm^{-1})	**Absorption Coefficient (cm^{-1})**	**Wavenumber (cm^{-1})**	**Absorption Coefficient (cm^{-1})**		
1265	*1196 + 10*	1288	*3589+ 29*		
1230	*849 + 7*	1228	*1544 + 12*		
		1216	*3474 + 28*		
1188	*1312 + 10*				
1108	*849 + 7*	1114	*810 + 6*		
964	*386 + 3*			875-960	OH---O wagging
939	*502 + 4*	947	*2084 + 17*		
912	*463 + 4*	917	*463 + 4*		
880	*386 + 3*	894	*193 + 2*		
839	*386 + 2*			837-869	CCC stretching
806	*270 + 2*	803	*386 + 3*		
748	*213 + 2*	732	*386 + 3*	720-730	CH2 rocking
		684	*579 + 5*		
670	*193 + 2*	672	*733 + 6*		
648	*232 + 2*				
519	*77 + 1*	534	*502 + 4*		
472	*69 + 3*				

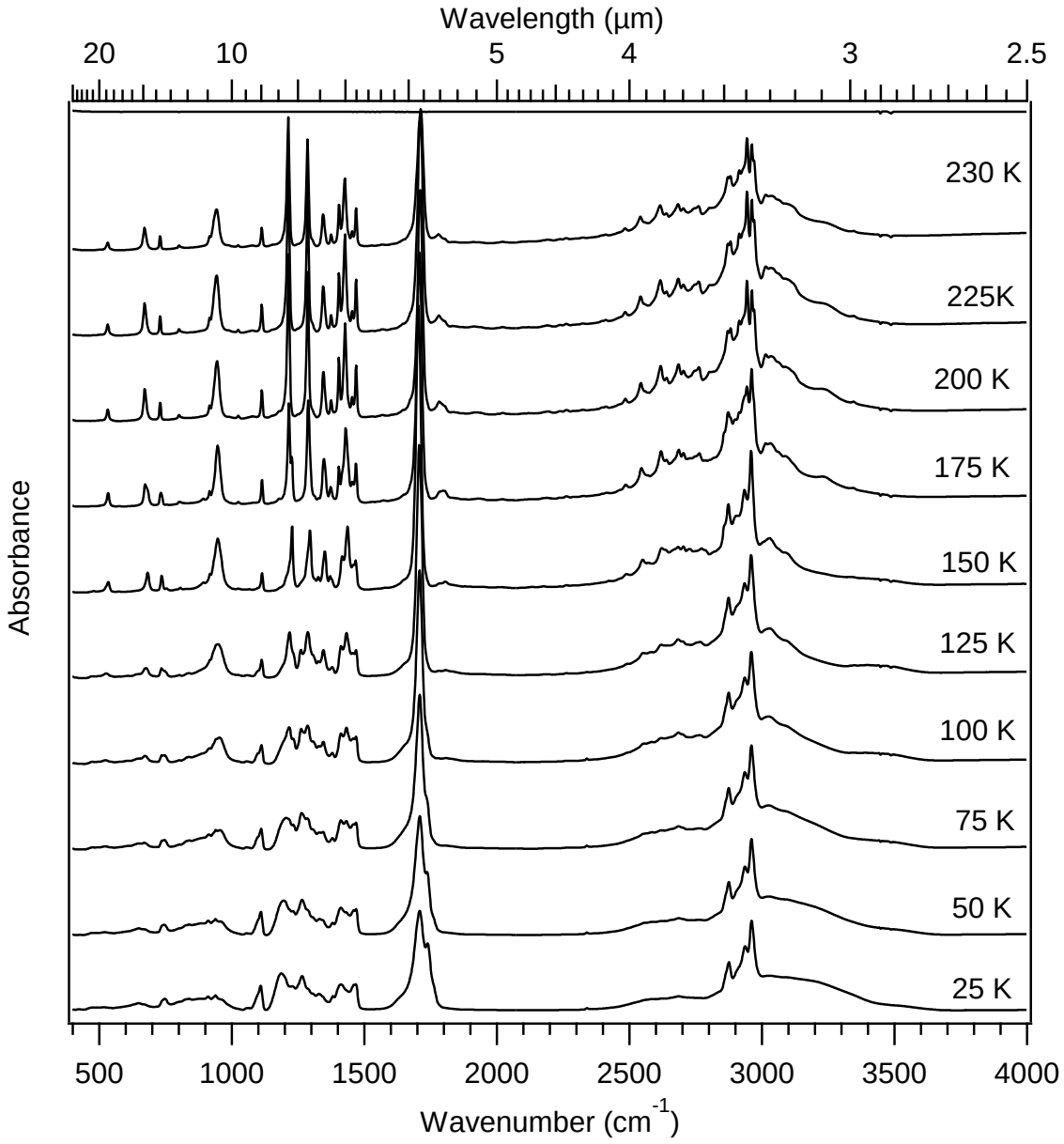

Figure 3.10. Spectral evolution of solid valeric acid (thickness 5403 ± 43 nm).

3.1.6. Fumaric acid (trans-butenedioic acid)

Fumaric acid is a dicarboxylic acid that contains carbon double bonds. This compound is solid at room temperature, accordingly spectra have been collected on a pellet at room temperature. The spectrum shares similarities with the spectra of acids presented before. We observe a broad band between 2500 cm^{-1} and 3300 cm^{-1}, due to the –OH stretching mode, C-H stretching, possibly overtones of CH bending and combination modes involving the OH end (Fig. 3.11). The intense and sharp peak at 3083 cm^{-1} is due to the CH stretching in the =C-H group. The C=C bond absorbs at 1676 cm^{-1} and C=O at 1687 cm^{-1}, on the whole this band is

sharp and intense. Table 3.6 presents the comparison of the measurement fumaric acid and reference from Spectral Database for Organic Compounds (SDBS) by AIST Japan and proposition of band assignment based on infrared handbook of organic molecules (Lin-Vien et al., 1991).

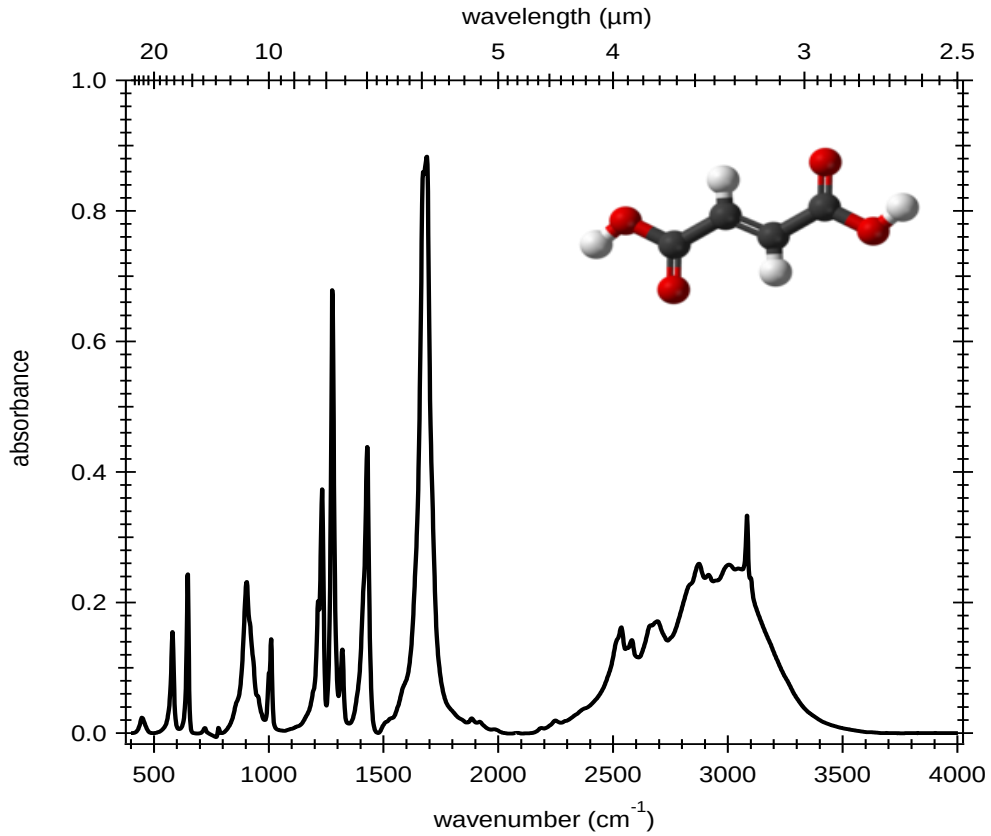

Figure 3.11. Spectrum of fumaric acid as pellet at room temperature and its structure.

Table 3.6. Band assignment of fumaric acid at room temperature

Wavenumber (cm^{-1})			**Vibration mode** (Lien-Vin et al., 1991)
measurement	**Reference** (SDBS)	**Reference** (Lien-Vin et al., 1991)	
3102			OH stretching
3082	3084	2995-3090	=C-H stretching
3009			=C-H stretching
2914			OH stretching
2877	2876		OH stretching
2695	2694	2500-2700	Overtones and combinations band
2663			
2582	2583		
2533	2538		
1687		1660-1740	C=O stretching
1676	1676	1665-1680	C=C stretching
1502	1512		

Wavenumber (cm^{-1})			Vibration mode (Lien-Vin et al., 1991)
measurement	**Reference** (SDBS)	**Reference** (Lien-Vin et al., 1991)	
1430	1431	1395-1440	C-O-H in plane band
1320	1317	1280-1315	C-O stretching
1280	1278	1280-1315	C-O stretching
1232	1232		
1215	1216		
1011	1010		
1000			
954	972	875-960	OH—O wagging
919	919		
904	907		
860			
782	792		
720	784	720-730	CH_2 rocking
647	646		
580	582		
449	456		

3.1.7. Glycolic acid (hydroxyacetic acid)

Glycolic acid is the simplest of the hydroxylated carboxylic acid. It has two C atom and one -OH group in its side (alcoholic) chain. We have collected one spectrum on a pellet, which fits very well with the spectrum provided by the NIST database.

With respect to other acids investigated before, an intense band at 3258 cm^{-1} appears, which is due to the alcoholic group –OH (Lin-Vien et al., 1991). Overall, the broad structure extending from 2500 to 3500 contains many peaks and overall a complex structure, controlled by the fundamental –OH and CH_x stretching modes, as well as combination modes for the low wavenumber features.

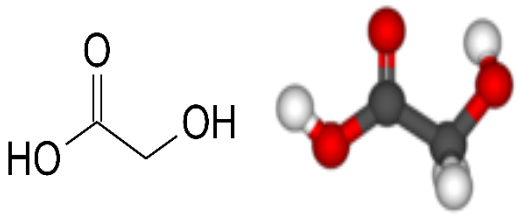

Figure 3.12. Molecule structure of glycolic acid (NIST).

The highest and sharp peak at 1731 cm^{-1} and 1255 cm^{-1} are C=O stretching and C-O stretching. Figure 3.13 shows the comparison spectra of solid glycolic acid to the NIST standard

spectrum: the fingerprint region has complicated and massive features due to bending mode and its combination.

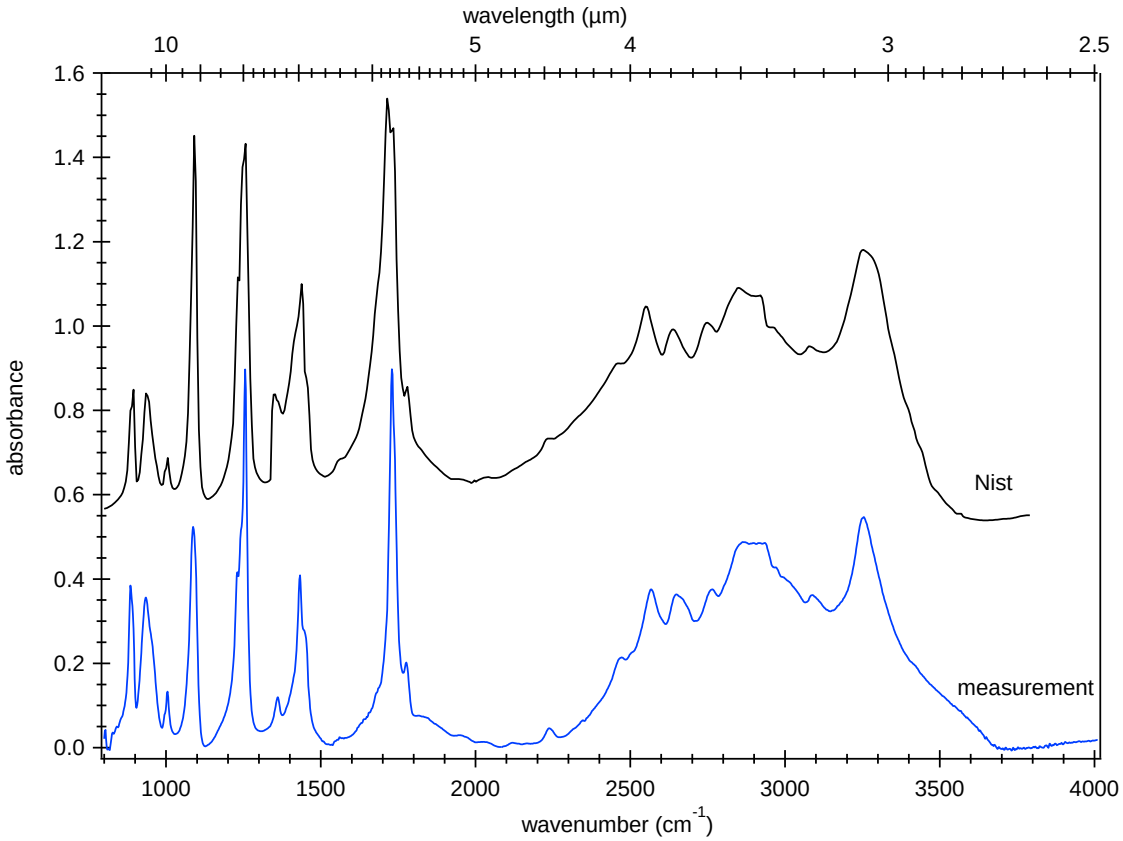

Figure 3.13. Comparison of solid glycolic acid spectrum and its NIST reference at room temperature.

3.1.8. Lactic acid

Lactic acid is also a member of the hydroxylated carboxylic acids group. It has two –OH groups in its structure, one being attached to central carbon atom. The broad feature in the range 2500-3550 cm^{-1} looks broader and less structured than in other acids. The small peak at 2946 cm^{-1} and 2996 cm^{-1} are due to CH stretching modes, while the rest of the band is controlled by –OH stretching modes and combination modes. The sharp peaks at 1729 cm^{-1} and 1126 cm^{-1} point to the C=O bond and C-O bond vibrations. Figure 3.15 shows the spectrum of lactic acid in pellet, which is similar to liquid lactic acid (SDBS, Japan database). This is question of the crystallinity in the solid phase.

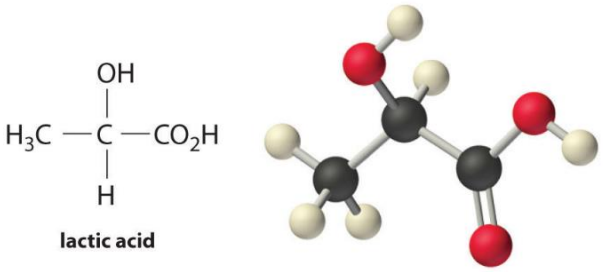

Figure 3.14. Molecule structure of lactic acid (NIST).

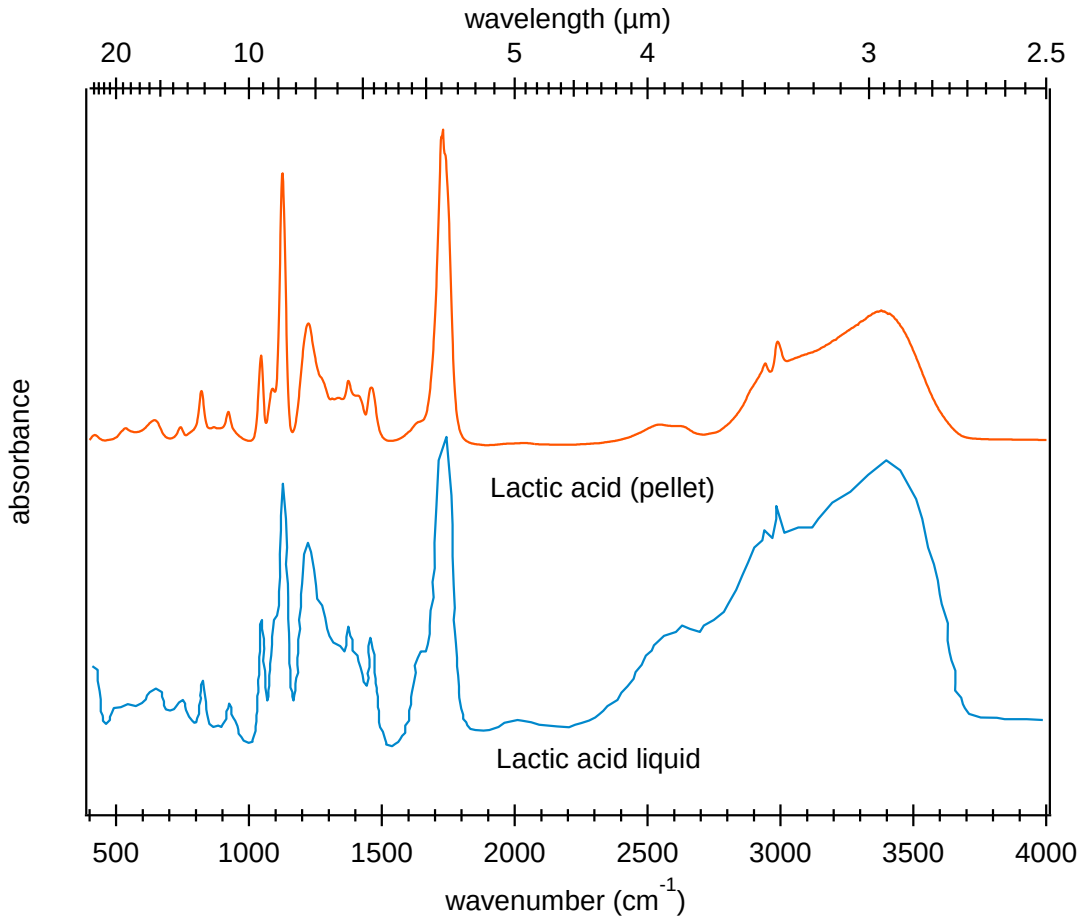

Figure 3.15. Spectrum of lactic acid at room temperature as pellet and liquid (SDBS database).

3.1.9 Methyl valeric and aromatic hydroxylated carboxylic acids

These acids are hydroxylated and contain aliphatic and aromatic side-chains, with different branching position of the hydroxyl group (Fig. 3.16). 2-Hydroxy-4-methylvaleric acid contains a –OH group on C1 in the aliphatic side chain. Three isomers of the hydroxy-2-naphtoic acid, containing a naphtoic group as the side chain have been investigated to test the effect of the

position of the –OH group: 2-Hydroxy-4-methyl-naphtoic acid , 3-hydroxy-4- naphtoic acid and 5-Hydroxy-4-methyl- naphtoic acid.

The spectra are displayed on Figure 3.17. 2-Hydroxy-4-methylvaleric shows a strong and narrow band at ~3500 cm^{-1}, which is due to the stretching mode of the hydroxyl branched on the aliphatic group. The –OH bond in the carboxylic group generates a large band between 2400 cm^{-1} and 3200 cm^{-1}, which includes several peaks and has a complex structure, and is controlled by the combination modes and overtones of the –OH group, the stretching of the carboxylic –OH and the CH stretching bands.

Interestingly, the three isomers of the naphtoic acid show different spectra. For the 2-hydroxy-2-naphtoic acid, a broad band is present from 2300 cm^{-1} up to 3300 cm^{-1}, mostly due to combination and overtones bands of the carboxylic –OH group. There is no specific signature of the hydroxyl group branched on the naphtoic group. In contrast, 3-hydroxy and 6-hydroxy displays a strong peak at 3285 cm^{-1} and 3600 cm^{-1}, respectively, due to the –OH stretching mode of the naphtoic hydroxyl group. The width of the band is also very different. Here, the distance between the hydroxyl and carboxylic groups influences the interaction of –OH with C=O, through hydrogen bonds. If the –OH hydroxyl is far from the carboxylic group, the interaction becomes weaker and –OH appears as detached single peak at higher wavenumber.

Table 3.7 shows the comparison of 1-hydroxy and 2-hydroxy naphtoic carboxylic with SDBS Japan database and band assignment from handbook of Lien-Vin et al., 1991.

a.

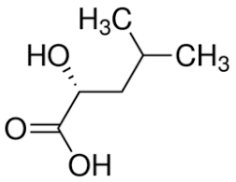

b.

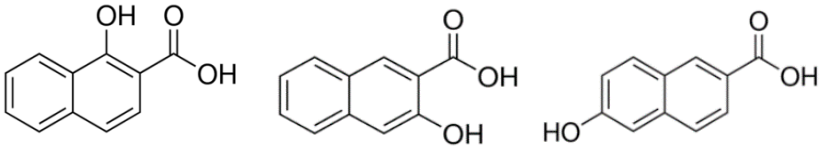

Figure 3.16. a. Structure of 2-hydroxy-4-methilvaleric acid b. Structure of 1-hydroxy-2-naphtoic acid, 3-hydroxy-2-naphtoic acid and 6-hydroxy-2-naphtoic acid (from left to the right).

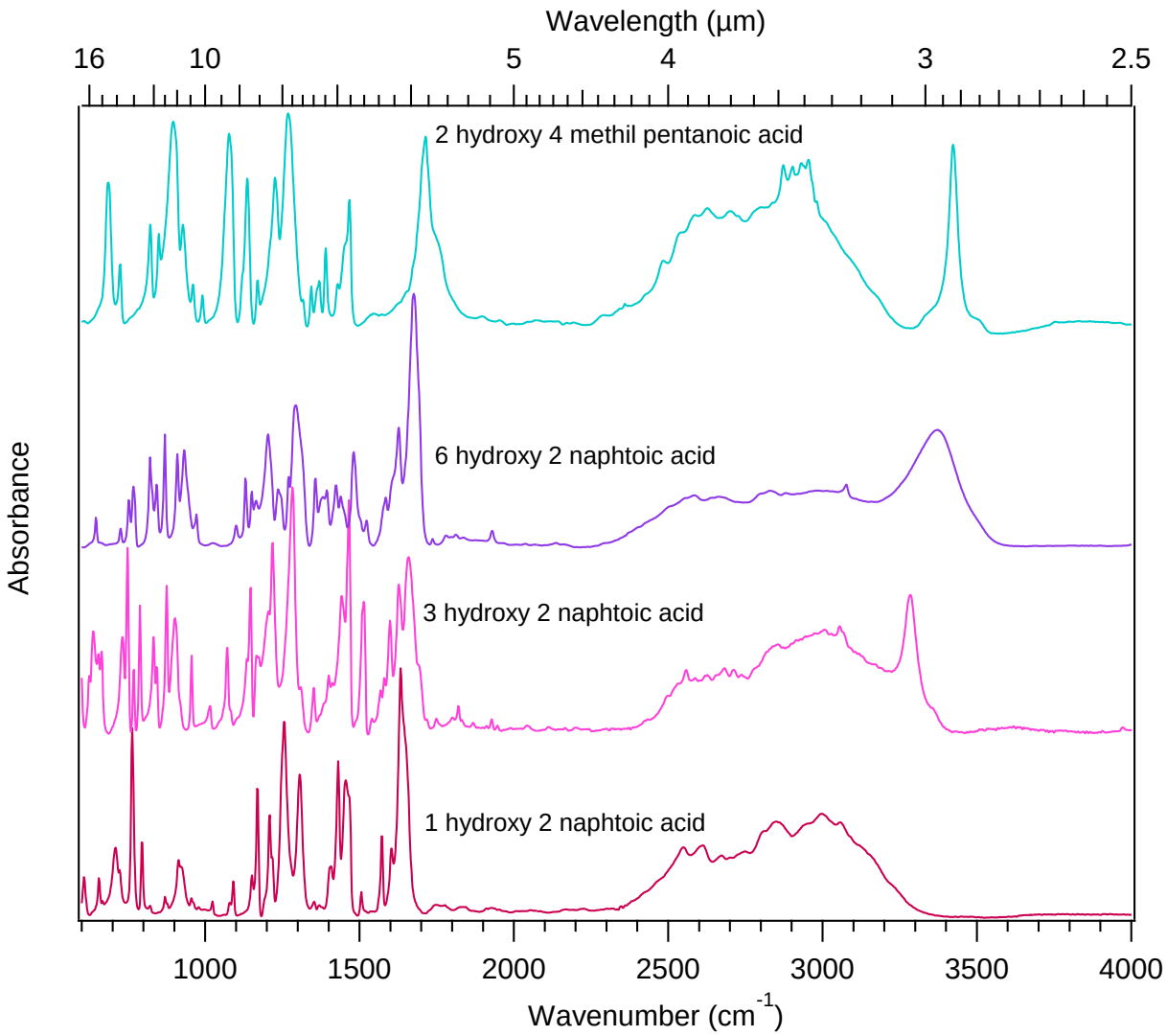

Figure 3.17. Spectra of solid methil-valeric and aromatic carboxylic acid at room temperature in pellet.

Table 3.7. Band assignment of aromatic carboxylic acid at room temperature

1-hydroxy-2naphtoic acid			**3-hydroxy-2-naphtoic acid**		
Wavenumber (cm^{-1})		**Vibration mode**	**Wavenumber (cm^{-1})**		**Vibration mode**
measurement	**Reference (SDBS)**		**Measurement**	**Reference (SDBS)**	**Lin-Vien et al., 1991**
3060	3060	CH stretching	3285	3286	OH stretching
3004	3003	CH stretching	3057	3056	CH stretching
2859	2855	CH stretching	3009		CH stretching
2750		Fermi resonance (OH stretching + Overtone CH bending)	2975		CH stretching
2671	2676		2914		CH stretching
2615	2613		2839	2856	CH stretching
2551	2550		2742		Combination and overtone band
1635	1636	C=O stretching	2713		
1604	1603		2681	2683	
1575	1573		2654		
1540			2629	2627	

1-hydroxy-2naphtoic acid			3-hydroxy-2-naphtoic acid		
Wavenumber (cm^{-1})		Vibration mode	Wavenumber (cm^{-1})		Vibration mode
measurement	Reference (SDBS)		Measurement	Reference (SDBS)	Lin-Vien et al., 1991
1506	1505		2586	2573	
1466	1469		2559	2559	
1457	1459		2534		Combination and overtone band
1432	1432	C-OH in-plane bending	2498		
1407	1409		1665	1671	C=O stretching
1306	1308	C-O stretching	1636	1632	
1256	1258		1600	1600	
1210	1209		1515	1516	
1170	1171		1467	1467	
1152	1152		1443	1443	
1091			1415		
1081	1082		1401		
1023			1352		
956		OH- - O out of plane wagging	1312	1313	C-O stretching
915	913		1285	1286	
878			1219	1219	
869		CH wagging	1206	1204	
823			1167	1167	
796	795		1147	1147	
765	765		1136		
723	723		1072	1072	
710	709		1018		
656	656		957	916	OH---O out of plane wagging
608	609		907	911	
574	572		876	878	
542	542		844	844	CH wagging
493	493		834	834	
464	466		790	791	
422			769		
			751	751,741	
			732	736	
			664	665	
			639	636	
			626	623	
			599	599	
			583		
			479	480	
			426		

3.1.10 Ammonium salts

The first comparison of ammonium salts with VIRTIS spectra were done with NH_4Cl. This compound was found suitable in terms of broadness, however no match with the positions of the peaks in the 3.2 µm were found. Here, we have investigated a range of 8 ammonium salts, with different counter-ions: chlorine, sulfate, carbonate, phosphate and acid groups. All these compounds were available as powder at room temperature, and they have been characterized as flattened grains under the HYPERION3000 FTIR microscope.

The spectra are displayed in Figures 3.18 and 3.19. We observe a broad feature in the range 2500-3500 cm^{-1} that displays different shapes, depending on the type of counter ion. The simplest ammonium salt is ammonium chloride, $NH_4^+Cl^-$. It shows a broad band in the 3 µm region with two main peaks at 3138 cm^{-1} and 3042 cm^{-1}, and a weakest one at 2813 cm^{-1}, which are assigned to the asymmetric and symmetric stretching modes and first overtone of the bending mode of the NH_4^+ ion (Schumaker and Garland, 1970). For ammonium phosphate and ammonium sulfate, we observe as well three main peaks that are due to the same vibration modes. Nevertheless, their peaks are not at the same position, and their band shape and width are different (Figure 3.19).

Ammonium formate and ammonium acetate show 3 main peaks due to the previous vibration modes, but no contribution of CH stretching modes though they are expected. We think this mode is here very weak. The spectrum of ammonium formate looks fairly similar to the spectrum of ammonium sulfate (Fig. 3.19), while the spectrum of ammonium acetate looks very different in terms of peak intensities.

Ammonium carbamate shows a very broad band, with a broad component at ~2780 cm^{-1} and a narrow one at ~ 3460 cm^{-1}, and several structures in-between (Fig; 3.18). The primary amino group NH_2 displays symmetric and anti-symmetric stretching modes in this range, around 3460 cm^{-1} and 3300 cm^{-1} (Frasco, 1964; Bossa et al., 2008). In the case of ammonium bicarbonate, combination modes of the hydrogeno-carbonate counter-ion may account for, at least, the signature around 2550 cm^{-1}. The feature is overall very broad, even broader than ammonium carbamate.

The detailed assignment of ammonium salts is presented in Table 3.8, however mostly references were down at low temperature because they were focused on transition of physical properties at certain temperature. No wondering if there are differences between the references and our measurements at room temperature.

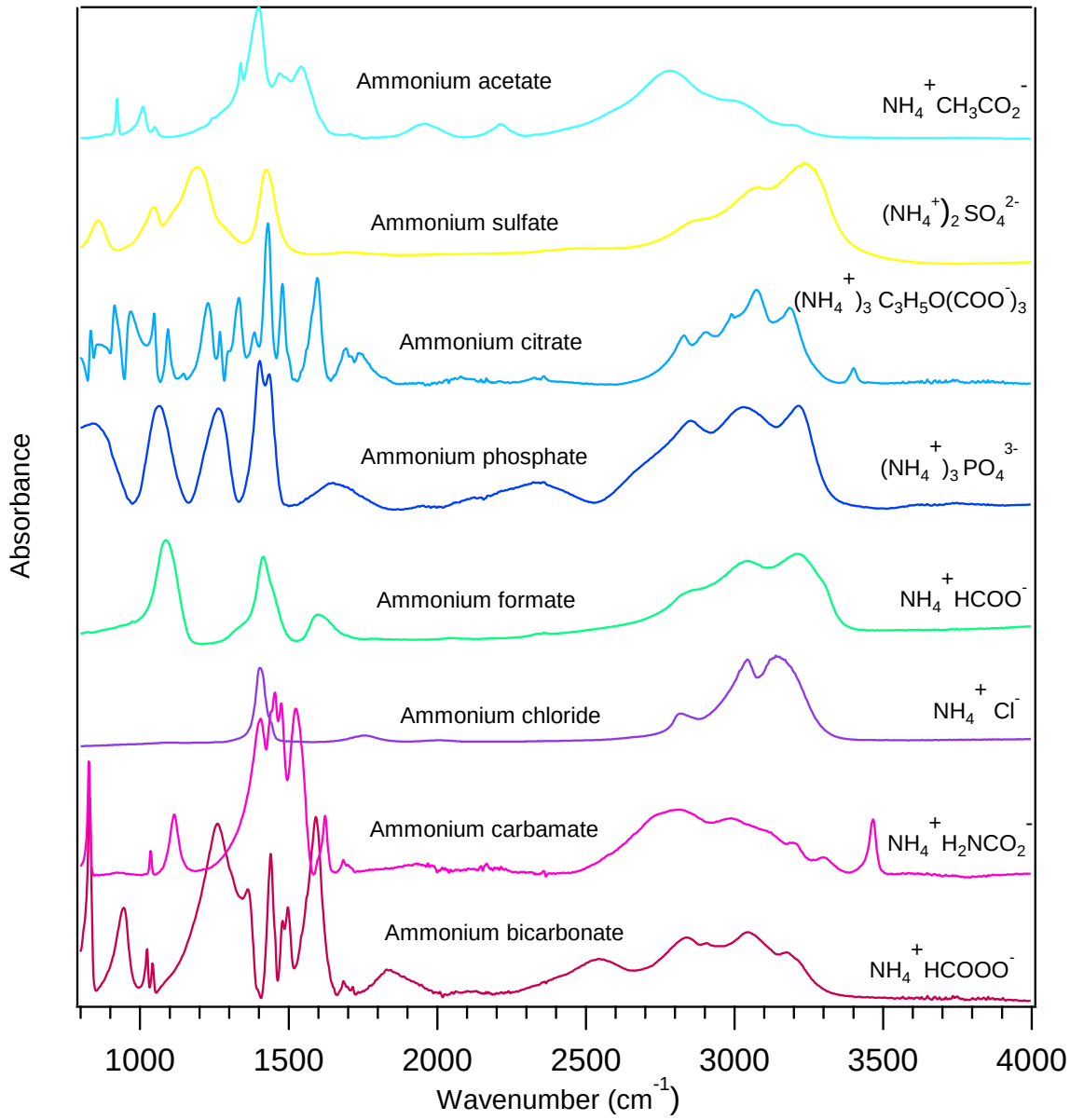

Figure 3.18. Spectra of ammonium salts at room temperature.

Table 3.8. Band assignment of ammonium salts

Ammonium Carbamate		**Ammonium formate**		**Ammonium sulfate**		**Ammonium chloride**		**Ammonium phosphate**	**Ammonium bicarbonate**	**Ammonium acetate**	**Ammonium citrate**	**Vibration mode**
This work	**Reference [a,b]**	**This work**	**Reference [c]**	**This work**	**Reference [d]**	**This work**	**Reference [e]**	**This work**	**This work**	**This work**	**This work**	
3466	3446										3400	N-H stretching (as)[a]
3293	3295	3216		3240	3212			3221		3207		N-H stretching (s)[a,c,d]
3192	3189											Overtone NH3 bending
						3138	3126		3179		3187	N-H stretching (as), fermi resonance[e]
		3045	3075	3076	3060	3042	3050	3027	3041	3033	3075	NH bending (s) + NH bending (as)[c]
2989									2908		2989	CH stretching[f]
											2905	CH stretching[f]
			2870									NH stretching[c]
		2849		2861	2850	2813	2850	2852	2841		2829	Overtones NH bending (s)[d,e]
2780										2782		Combination bands enhanced by fermi resonance[f]
				2412					2543			
								2354				
2164												
						2009	2015					NH bending +lattice mode, longitudinal optic mode[e]
1946												
						1758	1770					NH bending + transversal optic mode + longitudinal optic mode [e]
				1698								
1685	1691											C=O stretching [a,b]
1620	1624											NH2 bending

Ammonium Carbamate		Ammonium formate		Ammonium sulfate		Ammonium chloride		Ammonium phosphate	Ammonium bicarbonate	Ammonium acetate	Ammonium citrate	Vibration mode
This work	Reference [a,b]	This work	Reference [c]	This work	Reference [d]	This work	Reference [e]	This work	This work	This work	This work	
		1600	1697									NH in phase double scissoring[c]
1519	1525											CO2 stretching (as)[a]
1471	1491											NH3 bending[a]
1451												
1438												
				1424	1450	1440	1440	1435				NH bending (s)[c,d]
						1405	1403	1401				
		1414	1426									NH in phase scissoring[c]
1404	1404											C-N stretching[b]
		1328	1347									CO stretching[c]
				1190	1114							SO_4^{2-} stretching (as)[d]
1114	1115											CO2 stretching (s)
		1089	1070									CH out of plane bending[c]
				1046	1050-1150							SO_4^{2-} stretching (s)[d]
1045	1040											NH2 rocking (s)
936												
				855	952-982							SO_4^{2-} bending[d]
823	830											CO2 rocking (s)[a]
730	721											CO2 wagging (as)[a]
668	665											CO2 bending[b]

[a] Transmittance spectrum of NH_4^+ H_2NCO_2 at 83 K (Frasco, 1964)

[b] Infrared absorption bands and assignment of the products formed from the reaction of NH_3 + CO_2 at 90 K (Noble et al., 2014)

[c] Transmittance spectrum of NH_4^+ $HCOO^-$ at 298 K (Hamann and Spinner, 1977)

[d] Transmittance spectrum of $(NH_4^+)_2$ SO_4^{2-} at ambient temperature and pressure conditions (Weis and Ewing, 1996)

[e] Reflectance spectrum of NH_4^+ Cl^- at 21 K (Schumaker and Garland, 1970)

[f] Hand book of infrared (Lin-Vien et al., 1991)

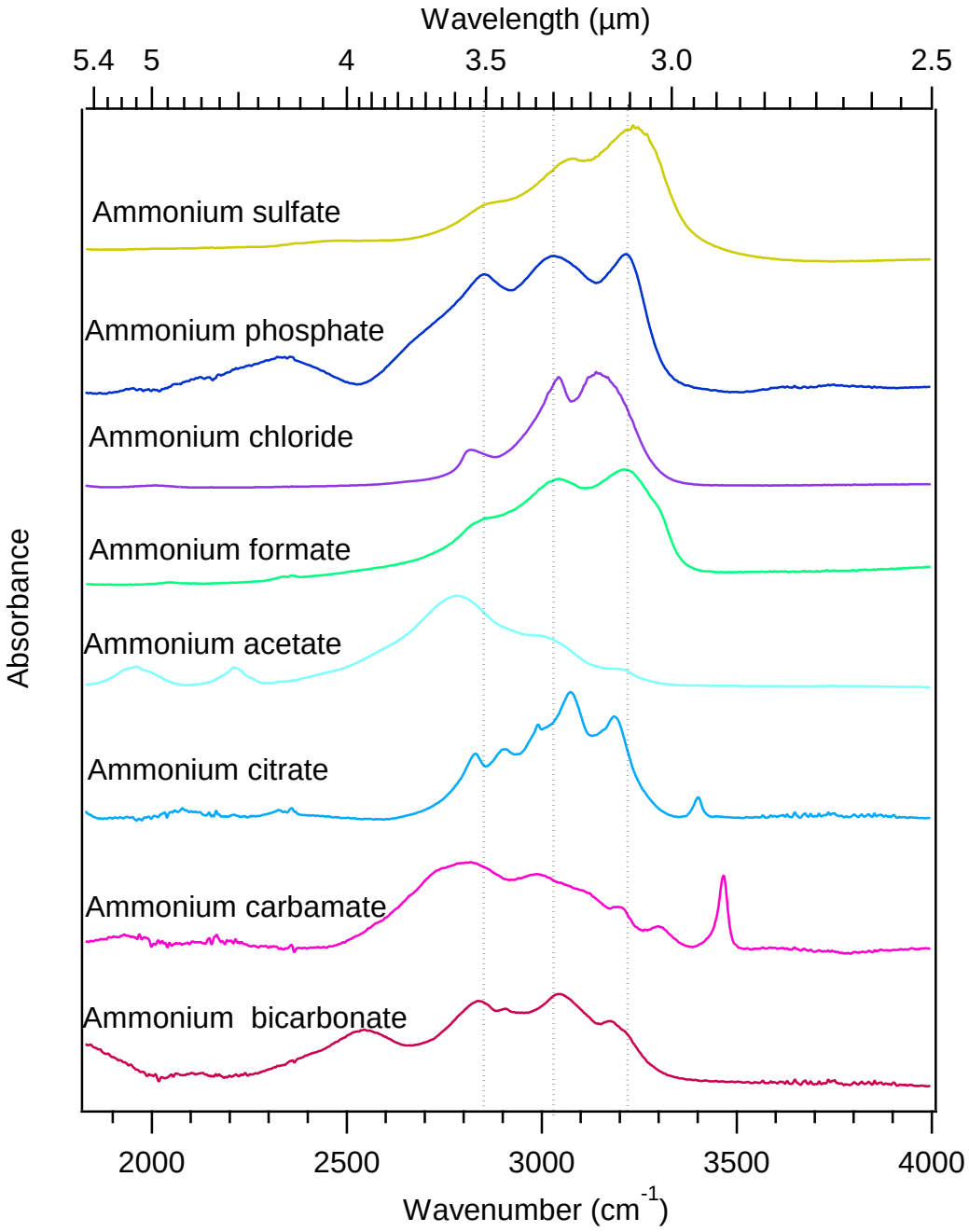

Figure 3.19. The position of N-H vibration bands for several ammonium salts.

3.2. Carboxylic acids and ammonium salts in comet 67P/CG

3.2.1. Carboxylic acids

The three mass spectrometers aboard Rosetta as ROSINA (orbiter), COSAC and Ptolemy (Lander) detected semi-volatile organic molecules at the surface (and likely in the bulk) of comet 67P/CG. The -COOH bearing molecules appeared in the mass spectra of ROSINA, as formic acid and acetic acid, which might correspond to of the fragmentation of larger -COOH bearing chains (Le Roy et al., 2017). In revisiting data of COSAC and Ptolemy, formic acid and acetic are possibly detected (Altwegg et al., 2017). COSIMA also reported that comet 67P/CG dust contains around 55 wt % of a macromolecular organic solid which presents similarities with organic matter present in carbonaceous chondrites (Fray et al., 2016; Bardyn et al., 2017; Isnard et al., 2019). In primitive carbonaceous chondrites, the dominant compounds in the soluble fraction of organic matter are carboxylic acids (Sephton, 2000). From a spectral point of view, Cappacioni et al., (2015) have suggested that carboxylic acids may account for the 3.2 μm, due the large band observed in the liquid phase of simple acids.

However, our data collected in transmission do not support this assignment. C1 to C5 simple carboxylic acids (with an aliphatic side chain) display intense combination modes in the range 3.5-4 μm, at odd with the comet 67P/CG VIRTIS spectrum (Fig. 3.20). In addition, with increasing the number of C atoms, the intensity of the CH_2/CH_3 signature around 3.4 μm increases a lot, and above C5, any carboxylic acid can be excluded. In the case of –OH groups branched on the side-chain, e.g. lactic acid, a significant effect on the shape of the band is observed, but it does not improve the match with VIRTIS data. For a dicarboxylic acid (the C4, fumaric acid), the presence of two OH bonds leads to a broad spectrum that spread from 3.1 μm until 4.2 μm, but with two intense components towards long wavelengths (Fig. 3.21).

Similar conclusions can be drawn for carboxylic acids having aromatic groups in their side chains. Hydroxylated aromatic carboxylic acids generate the broad band from 2.9 μm until 4.4 μm. The difference of position of the hydroxyl bond affects the strong band at lower wavelength. The 6-hydroxy-2-naphtoic acid spectrum starts from 2.8 μm, for 3-hydroxy from 3 μm and 1-hydroxy has narrower spectral range (Fig. 3.21). As a whole, solid carboxylic acids are not viable candidates.

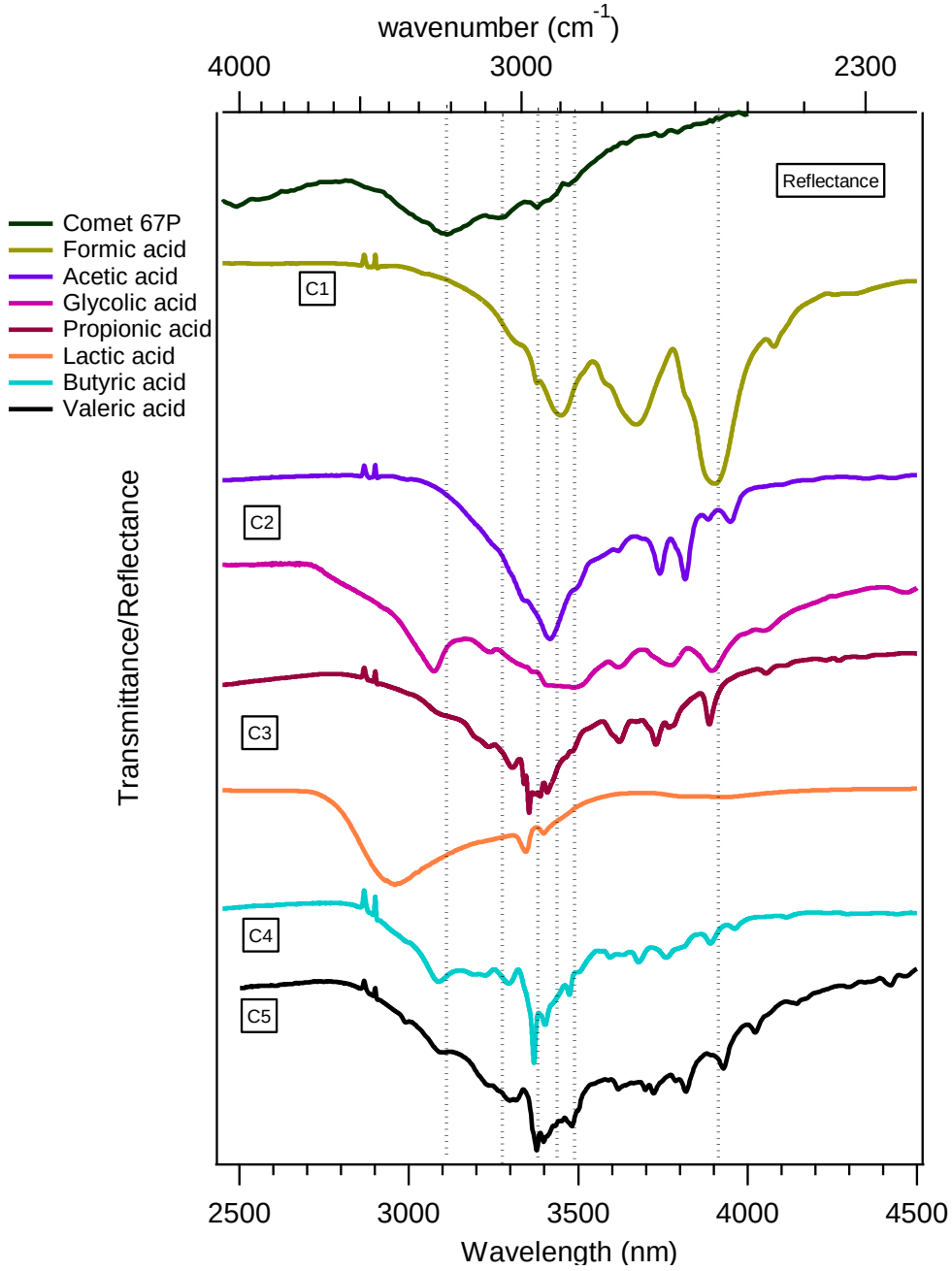

Figure 3.20. Comparison of the spectra of the comet and of simple carboxylic acids compound. The dotted lines depict the peak positions in VIRTIS spectrum.

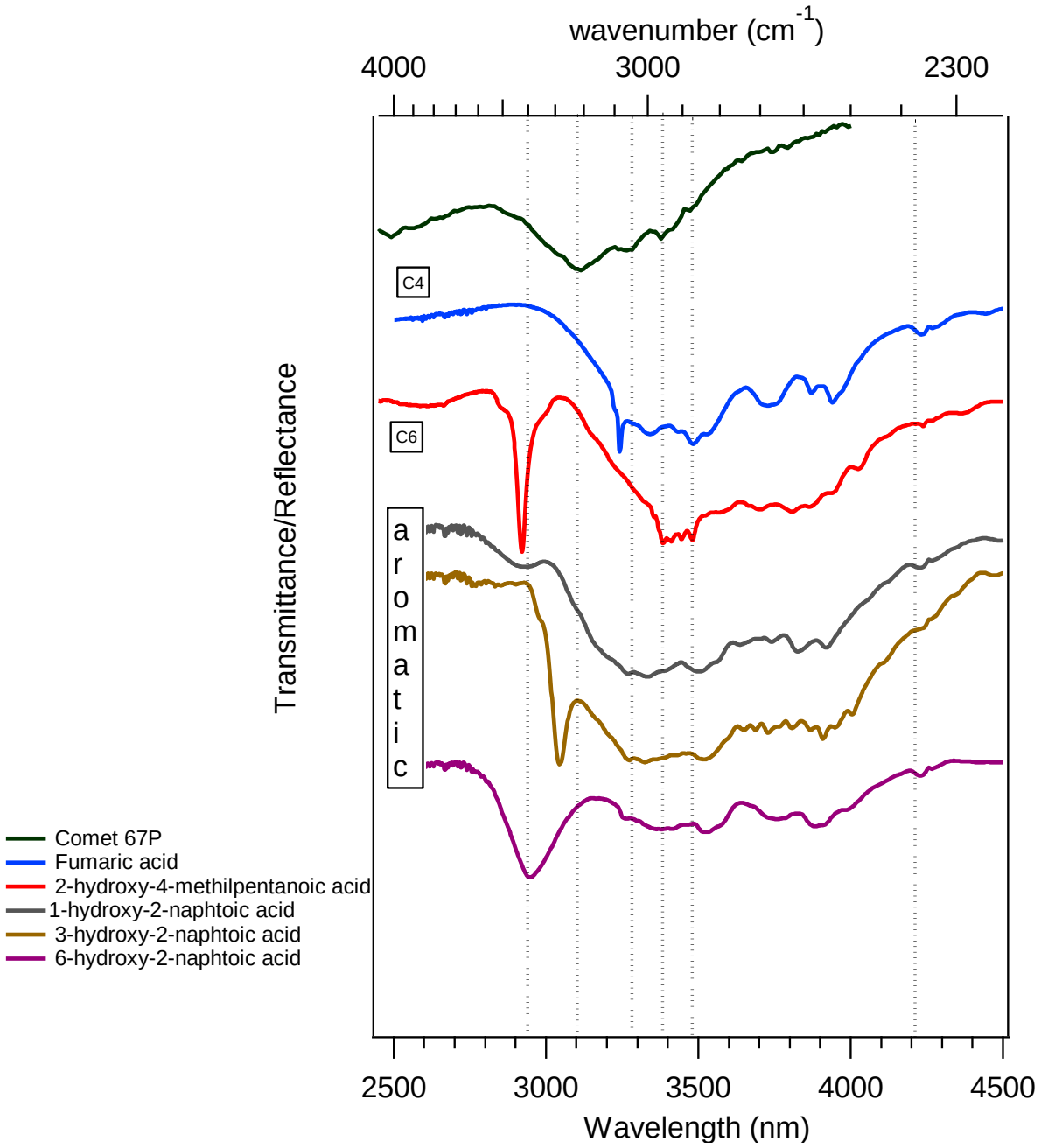

Figure 3.21. Comparison of the spectra of the comet and of aromatic carboxylic acids.

3.2.2 Ammonium salts

In contrast, several ammonium ions appear as interesting candidates. As observed earlier, NH_4Cl does not match (Quirico et al., 2016), but ammonium sulfate and formate display peaks very close to those in the VIRTIS band, except the weak features at ~3.4 μm that might be due to aliphatic modes (Fig. 3.22). Ammonium phosphate looks fine regarding band positions, but the relative intensities are less consistent. **The other compounds are not viable,**

including ammonium carbamate, which is detected in experiments simulating the reactivity of ices with a cometary composition (Bossa et al., 2008, Noble et al., 2014).

The presence of phosphate and sulfate ions is unlikely in the comet. Phosphates are quite rare, and mostly in the form of refractory compounds in the refractory dust. Sulfates are likely very rare as well, as most of sulfur is expected to be located in dust as iron sulfide (mostly pyrrhotite; Quirico et al, 2016). Sulfates are abundant in some chondrites, but they produced in the parent body or in the laboratory through reactions with liquid or gaseous water (Gounelle and Zolensky, 2005). The formate ion, in contrast, is plausible and might result from the reactions of formic acid with ammonia. Hence, chemical reactions in complex ices are generally triggered by water ice crystallisation (Bossa et al., 2008; Theulé et al., 2013, Noble at al., 2014). In such conditions, NH_3 can react with formic acid at low temperature through proton transfer:

$$NH_3 + HCOOH \rightarrow NH_4^+ + HCOO^-$$

Ammonia can also react with the more abundant CO_2 to form carbamates (Bossa et al., 2008):

$$2NH_3 + CO_2 \rightarrow NH_4^+ + NH_2COO^-$$

However, ammonium carbamate display $–NH_2$ features, and in particular a sharp feature at ~3460 cm^{-1} (Fig. 3.22). Overall, the shape of the broad band does not match that of the band of comet 67P/CG. **We can conclude that CO_2 does not react with NH_3 in the cometary nucleus, possibly due to a dilution effect (most of experimental studies are based on pure CO_2 and NH_3, e.g. Bossa et al., 2008), or a kinetic competition with other reactions.**

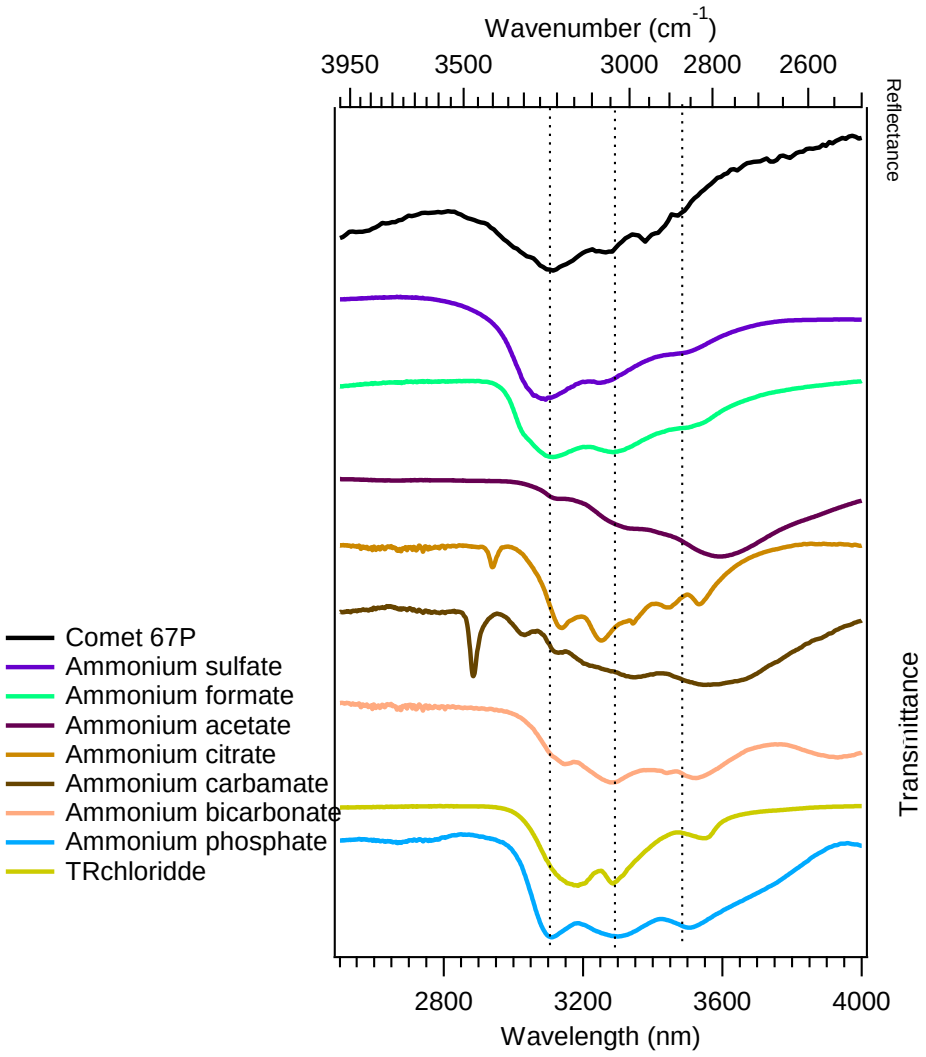

Figure 3.22. Comparison of the spectra of the comet and of ammonium salts measured at room temperature.

Chapter 4

Reflection measurements of cometary analogs

The experimental data shown in Chapter 3 provide a first appraisal of the presence of semi-volatiles at the surface of comet 67P/CG. However, VIRTIS spectra have been collected in reflectance and reflectance data have to be compared with observations, for a detailed spectroscopic study on one hand, and for quantifying the abundance of those semi-volatiles species. Here, we have favored an experimental approach consisting in producing cometary analogs in the laboratory. Two types of analogs were investigated: (1) fine-grained mixtures produced from the mechanical mixing of powders that had been previously ground with a planetary grinder; and (2) sublimation residues recovered from ice:dust analogs sublimation, produced with a nebulizer. These analogs were measured with the spectro-gonio-radiometers developed at IPAG, in the range 0.4-4.2 µm.

In this chapter, we first present our results on mechanical analogs that comprise ammonium salts and carboxylic acids mixed with various refractory materials. Our transmission experiments have shown that carboxylic acids are not plausible candidates, however these experiments are interesting in the context of a more fundamental investigation. We then present the synthesis and the optical characterization of sublimation residues of a variety of ammonium salts (and one carboxylic acid: lactic acid). We conclude by the application of these results to the interpretation of the VIRTIS/Rosetta spectral data.

4.1 Mechanical Mixture

Mixtures of carboxylic acids and ammonium salts with refractories have been prepared with two main classes of refractory materials. First, dark refractories in the VNIR range, as graphite, anthracite, pyrrhotite and an iron(ii) sulfide. These materials have been used because their optical properties fit the very low reflectance of comet 67P/CG nucleus in the visible and near-infrared ranges (Quirico et al., 2016). While iron sulfide and pyrrhotite are good analogues of opaque minerals present in cometary dust (Dobrica et al., 2009), graphite and anthracite are selected here for their optical properties. They are not relevant analogs of cometary dust in terms of chemical composition. The second type of refractory material is brighter minerals as a basalt (collected in Massif Central France), sand and olivine. Olivine is a mafic mineral that constitutes a significant fraction of cometary dust, while basalt and sand must be considered as

optical analogs of their bright component. As the results of sand and basalt are conformable, here we only report the mixture of carboxylic acids with basalt.

The typical grain size of these refractory analogs extends from hundreds of nanometers until few micrometers (see Table 2.2). Pyrrhotite-$_{fg}$ (procedure B in Table 2.2) is an homogenous sub-micrometer-sized rounded grain produced through colloidal grinding, and pyrrhotite-$_{fg\text{-}pl}$ (procedure A in Table 2.2) is composed of sub-micrometric rounded grains with around 15 % of micrometric platelets.

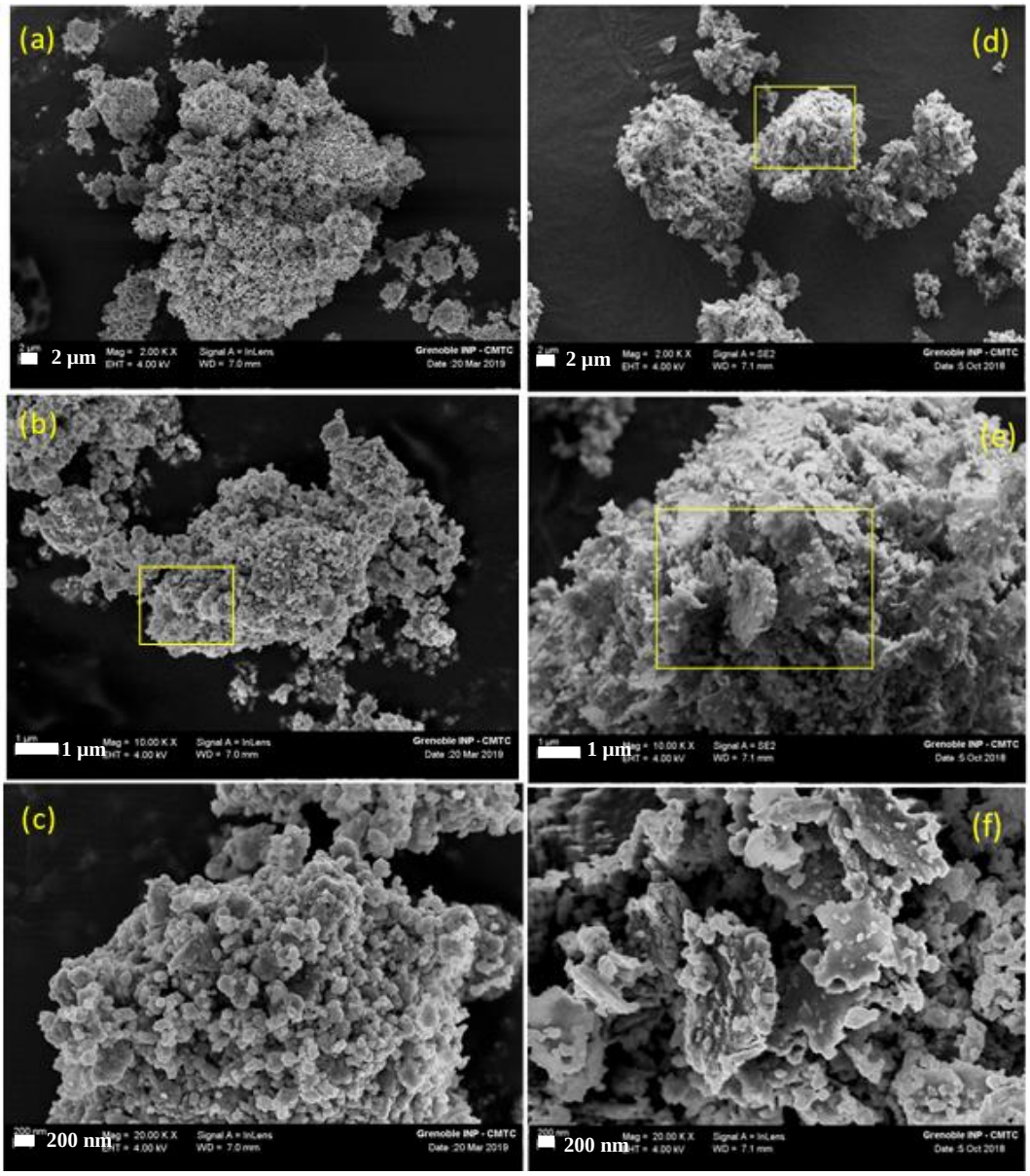

Figure 4.1. Comparison of the samples pyrrhotite-$_{fg}$ (left) and pyrrhotite-$_{fg\text{-}pl}$ (right). Secondary-electrons images show that pyrrhotite-$_{fg}$ mostly consists in sub-micrometric rounded grains (a,b,c), while pyrrhotite-$_{fg\text{-}pl}$ (d,e,f) contains micrometric platelets. They were formed due to a longer duration of grinding, which promoted the re-agglomeration of ground grains.

4.1.1 Mixture of carboxylic acids and graphite

In this section, we report the results on mechanical mixtures of graphite and carboxylic acids as described in Chapter 2. This mixture is composed of micrometric grains of graphite and carboxylic acids. The detailed compositions and preparation methods are presented in Table 4.1.

Table 4.1. Mixtures of carboxylic acids and graphite

Mixture composition in mass ratio	**Mixing**	**Environmental condition**
100 % graphite (grains 25 µ)	None	SERAC cell, few mbar, Room temperature
100 % graphite grinding (micrometric grains)	Planetary grinding	
100 % lactic acid	Mortar	
100 % glycolic acid	Mortar	
99 % graphite 1 % lactic acid	Mortar	
90 % graphite 10 % lactic acid	Mortar	
90 % graphite 10 % lactic acid	MM 200	
90 % graphite 10 % lactic acid	Diluted in ethanol	
60 % graphite 40 % lactic acid	Mortar	SERAC cell, few mbar, Room temperature until 80 °C
90 % graphite 10 % glycolic acid	Diluted in ethanol	
90 % graphite 10 % glycolic acid	Mortar	SERAC cell, few mbar, Room temperature

Figure 4.2 shows the reflectance spectra of mixtures of lactic acid and graphite. For mixtures obtained with hand mixing (mortar), we observe a strong saturation in the spectrum of pure lactic acid. This material is very soft, and the grinding was likely inefficient, leading to agglomeration and finally large grains. Increasing the concentration to 1 %, 10 % and 40 %, the reflectance slightly increases up to 10 %, and at 40 % is roughly similar to 10 % (but the shape of the continuum changes). No -OH absorption band typical of lactic acid is observed in the 3 µm region. This band was not observed as well in the sample mixed with the MM200 grinder, and for the two samples produced from the chemical deposition from ethanol+lactic acid evaporation. In the case of the MM200 sample, we observe a strong increase of the reflectance continuum (11-16 %). A similar observation was made by Rousseau et al. (2017b), which was interpreted by the the fact that MM200 generates a more efficient separation of phases. Lactic acid is a very soft and hygroscopic material, and it can play as a glue to bind the graphite grains to produce aggregates during mixing. It is likely that the MM200 grinder generates large lactic acid aggregates, which are coated by graphite flakes. This might account for a higher reflectance and the lack of lactic acid band, due to the lack of penetration of light with the core grains composed of lactic acid. Measurements were collected at room temperature, 50 °C and 80 °C do not reveal significant spectral changes, suggesting negligible melting effect.

The formation of a residue from the evaporation of graphite+liquid ethanol: lactic mixture did not improve the results. We had expected this approach would lead to a very thin lactic acid coating on the graphite grains. It seems it is more complicated, and maybe the hydrophobic nature of the graphite grains led to their segregation in the mixture.

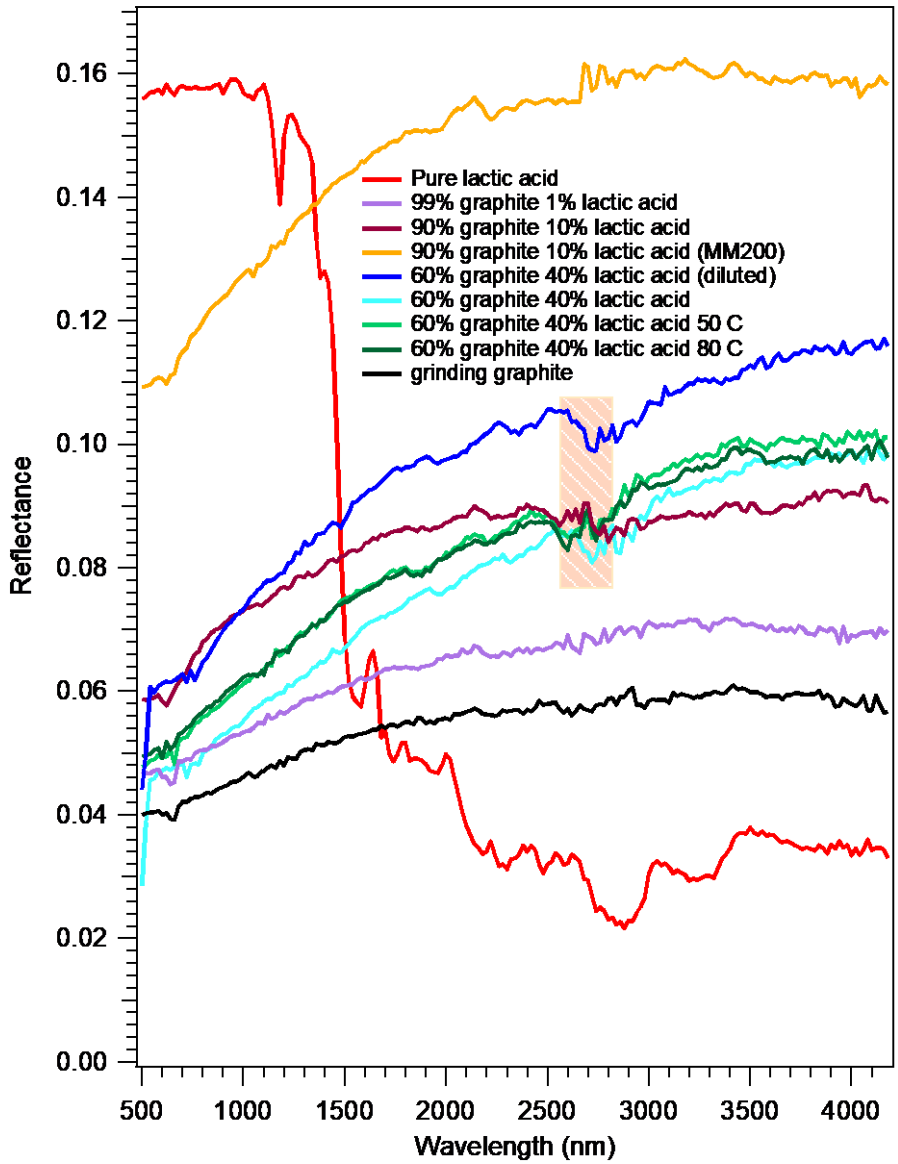

Figure 4.2. Spectra of graphite+lactic acid mixtures (abundance in mass ratio), obtained with different sample preparations: hand-mixed, MM200 mixing and ethanol evaporation (see text).

Figure 4.3 displays the spectra of four mixtures of glycolic acid and graphite. For the sample obtained by hand mixing, the result is similar to previous observations on lactic acid. For acid: ethanol + graphite samples, we observe an absorption band at 2.76 µm. The spectrum is stable when varying the temperature from 30 °C to 80 °C. However, this band does not fit the broad feature of solid glycolic acid controlled by the -OH group, after comparison with transmission

and reflection spectra of pure glycolic acid. The carrier of the feature at 2.76 µm is unclear. It does not fit either with the spectrum of liquid ethanol, whose band peaks around 3300-3400 cm^{-1} (2.85-2.95 µm), or with adsorbed water. Because graphite does not contain any -OH group, a possible explanation might be the presence of a very thin molecular layer of ethanol onto graphite grains, for which the vibration properties are modified with respect to solid.

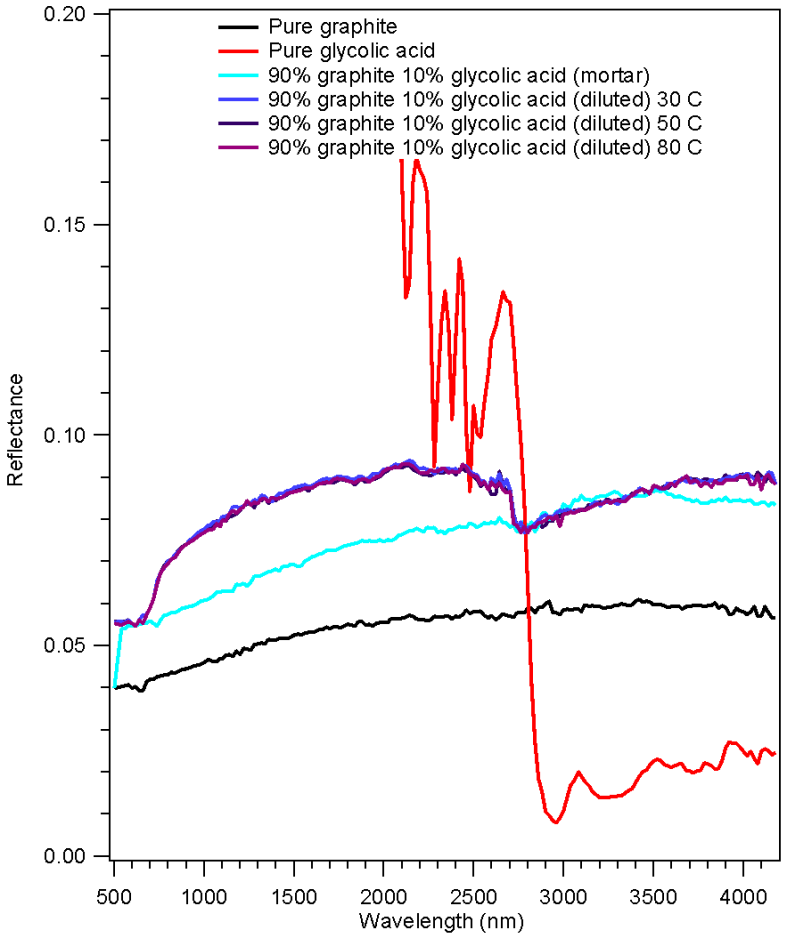

Figure 4.3. Spectra of glycolic acid+ graphite (abundance in mass ratio).

4.1.2 Mixture of carboxylic acids and basalt

Here, we report basalt+acid mixtures, obtained by hand mixing. As mentioned previously, basalt is not a good analog of cometary dust, but it offers the opportunity to simulate a moderately bright matrix (Beck et al., 2011). The experiments are compiled in Table 4.2.

Table 4.2. Mixture composition of carboxylic acids and basalt

Mixture composition in mass ratio	Mixing	Environmental condition
100 % basalt		SERAC cell, few mbar, Room temperature
99 % basalt 1 % lactic acid	Mortar	SERAC cell, few mbar, Room temperature 60 °C
98 % basalt 2 % lactic acid	Mortar	
97 % basalt 3 % lactic acid	Mortar	SERAC cell, few mbar, Room temperature 60 °C and 80 °C
90 % basalt 10 % lactic acid	Mortar	SERAC cell, few mbar, Room temperature 60 °C and 80 °C
99 % basalt 1 % glycolic acid	Mortar	SERAC cell, few mbar, Room temperature 60 °C
97 % basalt 3 % glycolic acid	Mortar	SERAC cell, few mbar, Room temperature 80 °C
90 % basalt 10 % glycolic acid	Mortar	
99 % basalt 1 % glycine	Mortar	SERAC cell, few mbar, Room temperature 60 °C
99 % basalt 1 % sarcosine	Mortar	
98 % basalt 2 % R alanine	Mortar	
98 % basalt 2 % L alanine	Mortar	

The micrometer-sized basalt powder has a reflectance factor of 0.5 in the infrared, and displays a red slope in the visible (Fig. 4.4). Though it was heated during one night under secondary vacuum, it still contains structural water that leads to a band at 2.9 μm. Adding 1 % of either lactic or glycolic acid decreases the albedo and generates a strong absorption band in the range 2.8-4.0 μm. At 80 °C the acids started sublimating and left white stains on the sapphire window of the SERAC cell. With increasing the acid concentration, the depth of the band increases and we observe changes in the band shape, which get more and more different than that in transmission spectra. In particular, we observe two narrow peaks at ~3 μm. This likely results from saturation effects. At high concentration, the hand mixing may lead to re-agglomeration and grain size growing. These results show that the bright matrix increases the optical path, in contrast with the samples produced with opaque matrices (sulfides or graphite). In the case of low concentrations (i.e. lack of saturation), the band looks fairly similar to that in transmission spectra.

Figure 4.5 displays the spectra of a series of mixed carboxylic and amino acids after baseline subtraction ($Sc = Sm - Sb$, where *Sc*, *Sm* and *Sb* are the corrected spectrum, the mixture and pure basalt spectra, respectively). Comparing with the comet, carboxylic acids have larger

absorption bands which are out of the range of the comet spectrum. Amino acids do not fit the comet spectrum as well, the broad feature due to -OH and Zwitter-ions being shifted towards long wavelengths.

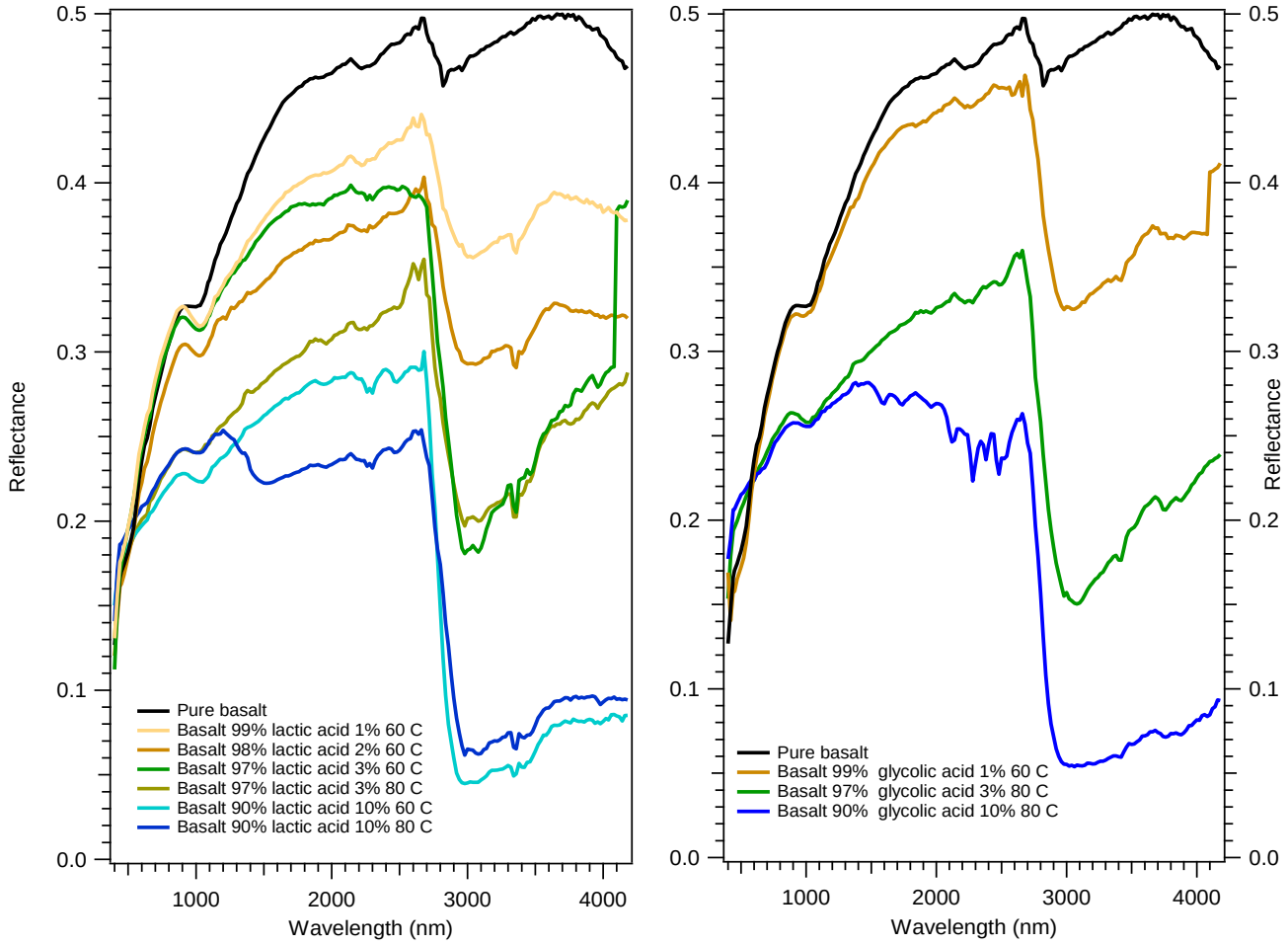

Figure 4.4. Spectra of basalt+glycolic acid mixtures (abundance in mass ratio).

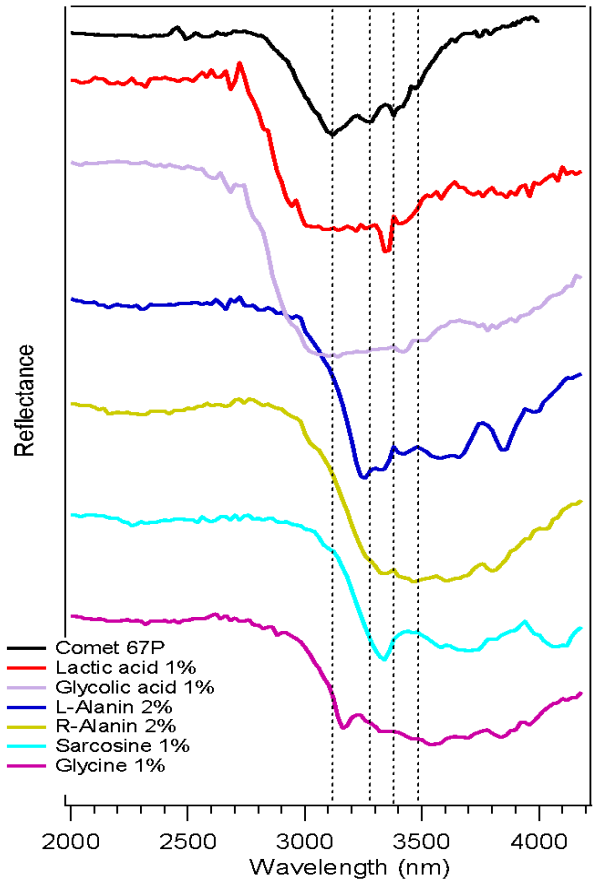

Figure 4.5. Spectra of basalt+carboxylic acids and basalt+amino acids mixture. The comet spectrum is calibrated by (Raponi et al., 2020; Poch et al., 2020) and the continuum baseline was computed by a spline interpolation (3rd order polynomials) using the reflectance of baseline anchor points typically at 2.20, 2.45, 2.68, 3.96 and 4.10 µm.

4.1.3 Mixture of ammonium salts and olivine

Ammonium salts mixed up with olivine have been measured with the SERAC cell at 0 °C, to prevent melting and interaction with atmospheric water in the case of the most hygroscopic salts. We used olivine which is dominated by micrometric grains (Table 2.2). The experiments are presented in Table 4.3.

Table 4.3. Mixture composition of ammonium salts and olivine

Mixture composition in mass ratio	Mixing	Environmental condition
99.95 % olivine 0.05 % ammonium citrate	Mortar in cold room Mortar	SERAC cell combined with Peltier, few mbar, temperature 0° C
99.9 % olivine 0.1 % ammonium citrate		
99.85 % olivine 0.15 % ammonium citrate		
99.8 % olivine 0.2 % ammonium citrate		

99.5 % olivine 0.5 % ammonium citrate	Mortar in cold room Mortar	SERAC cell combined with Peltier, few mbar, temperature 0° C
99.5 % olivine 0.5 % ammonium acetate		
99.5 % olivine 0.5 % ammonium phosphate		
98 % olivine 2 % ammonium bicarbonate		
99 % olivine 1 % anthracite		
98 % olivine 2 % anthracite		
97 % olivine 3 % anthracite		
96 % olivine 4 % anthracite		
4 % ammonium phosphate (96 % olivine 4 % anthracite)		
5 % ammonium phosphate (96 % olivine 4 % anthracite)		

Figure 4.6. shows the spectra of olivine mixed with ammonium citrate. Pure olivine has a bluer slope in the near-infrared region, this characteristic also appears in synthetic olivine (Dyar et al. 2009). The feature at 3.4 μm is due to the CH vibration of an organic contamination during storing or when preparing the mixture. By increasing the concentration of ammonium citrate, the slope in the visible does not significantly change, however it is more variable in the near-infrared region. **The depth of the ammonium absorption band increases with increasing the ammonium salt concentration, and this evolution trend is nicely linear** (at least for the first four points (out of five)) (Fig. 4.7).

Similar measurements were run for ammonium phosphate, acetate and bicarbonate. As expected, the band shape of each mixture is controlled by its counter ion (Figure 4.7). We observe an increasing depth of the ammonium band when increasing the ammonium abundance in the sample. In the case of ammonium phosphate, the trend is nicely linear (Fig. 4.7). **The band depths versus ammonium abundance curves are specific to each ammonium salt.**

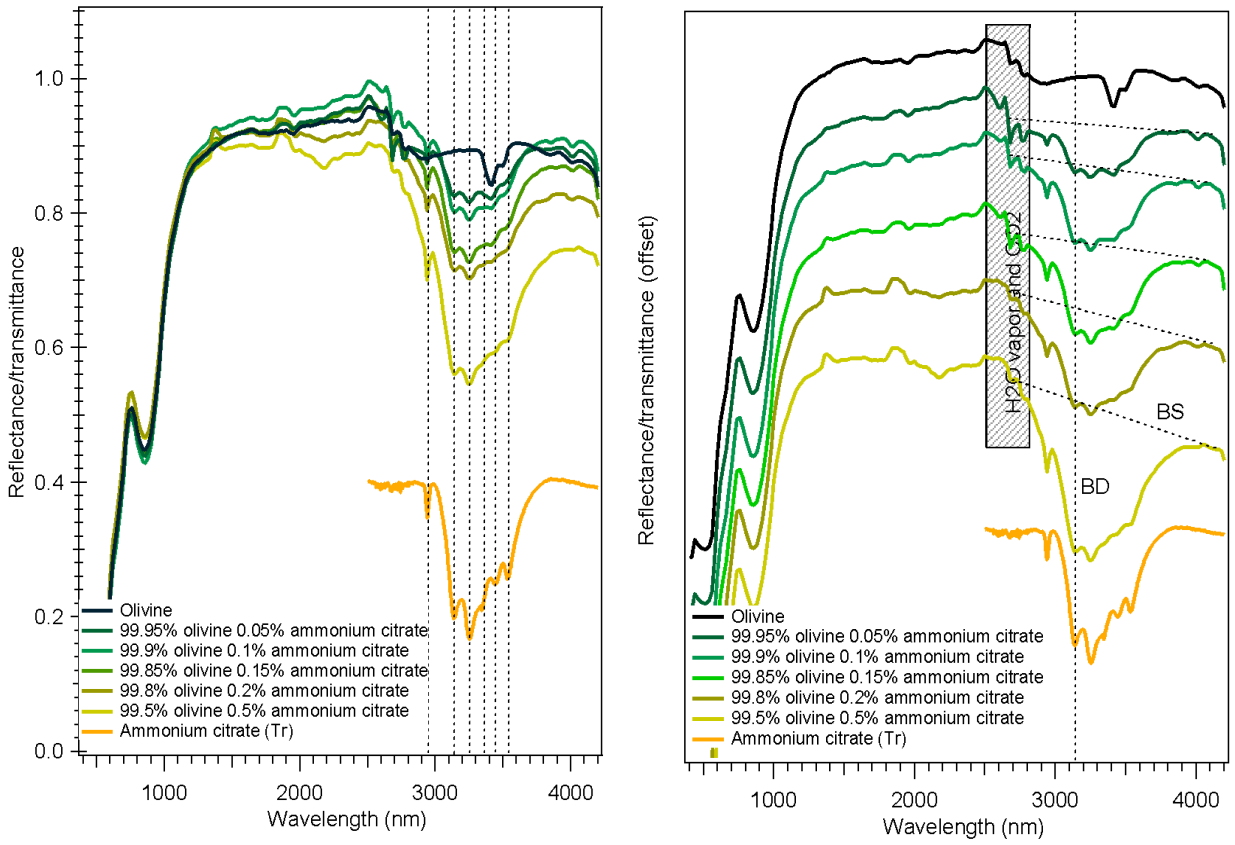

Figure 4.6. Spectra of mixtures of ammonium citrate+olivine at different concentrations. Left: the spectra with real reflectance, compared with a transmittance spectrum. Right: spectra are offsetted, the figure also depicts the baseline (BS) used to calculate the band depth (BD).

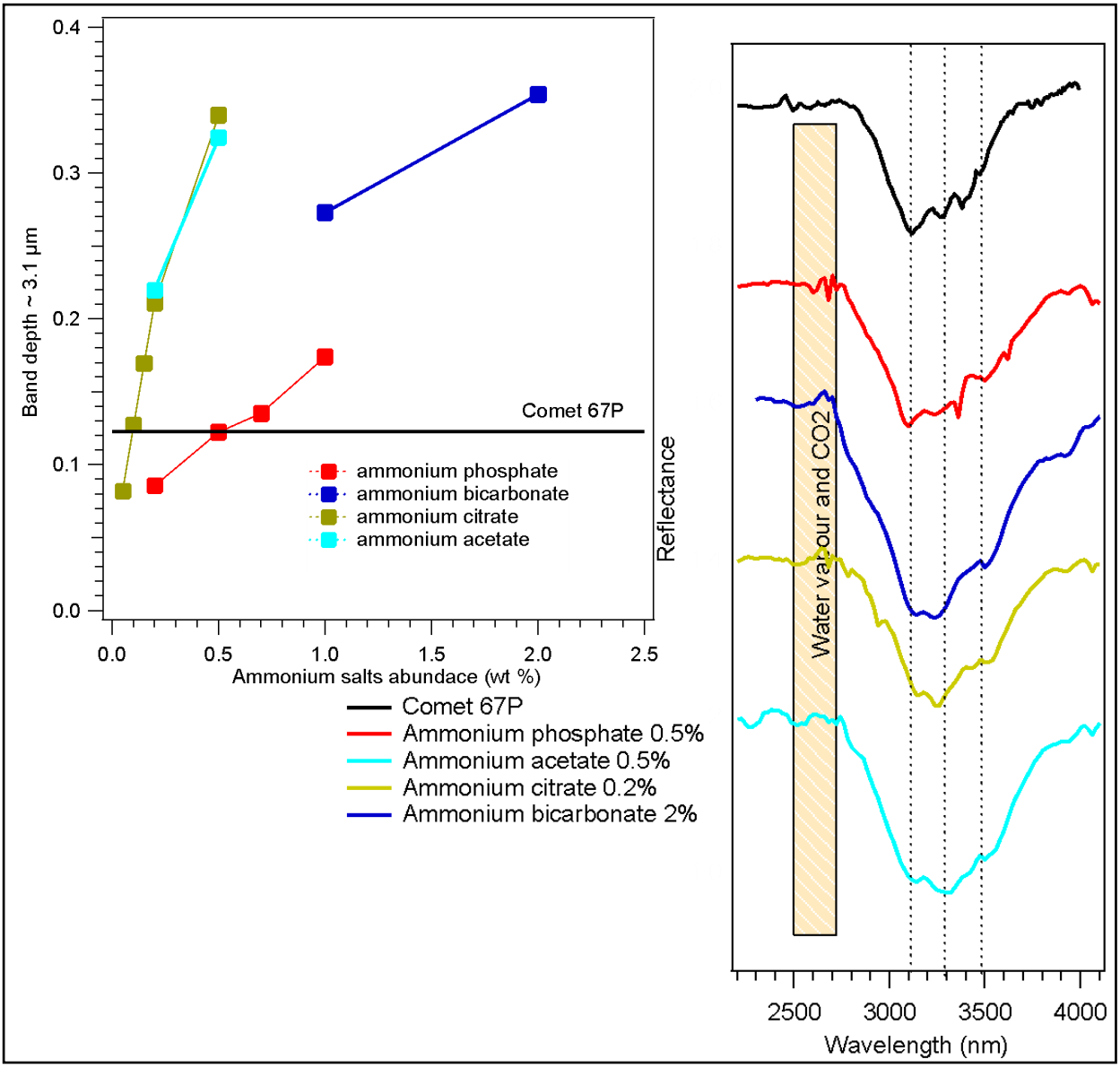

Figure 4.7. Left: Ammonium band depth versus ammonium abundance (in mass ratio). Right: the reflectance spectra (baseline-corrected+offset) for the different ammonium salts, and comparison with the spectrum of comet 67P/CG.

These samples were prepared with olivine coarse grains. SEM images (Fig. 4.8) show that the grain size of olivine reaches tens of micrometers. Micrometric grains of olivine and ammonium salt are clearly observed, nevertheless a sub-micrometric component is present as well.

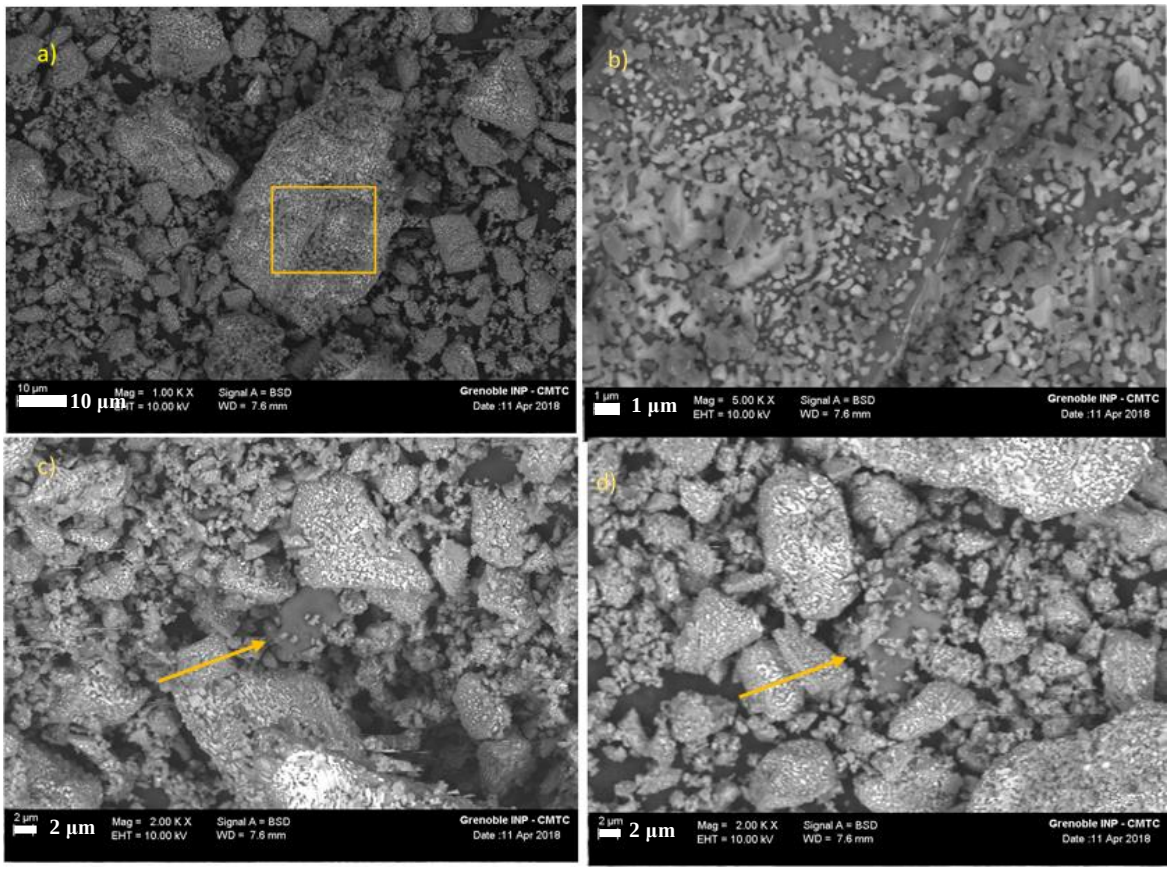

Figure 4.8. SEM images of ammonium salts mixed with olivine at different magnifications. Big chunks are olivine grains (a,b). In BSE mode, some ammonium salt grains are depicted as black grains (c,d).

4.1.4 Mixture of ammonium salts and dark refractory

We present here the spectra of mixture of dark refractory with ammonium sulfate, which is less hygroscopic and more stable at room temperature than other ammonium salts. Before mixing it with pyrrhotite or anthracite grains, the ammonium salt was ground in a mortar to obtain a fine-grained powder, composed of sub-micrometric grains with maximum size of 1-3 µm (Table 2.2). The mixing of ammonium sulfate with dark refractory material was done by hand with the mortar, or by using the planetary grinder. Measurements were run under room conditions without the SERAC environmental cell.

In this section we use the volume ratio (where ρ_{pyrr}=4.61 g cm^{-3}, ρ_{FeS}=4.84 g cm^{-3}, ρ_{anthra}=1.51 g cm^{-3}, ρ_{graph}=2.16 g cm^{-3}, $\rho_{amm\ sulfate}$=1.77 g cm^{-3}) to convert mass ratio into volumic ratio.

Table 4.4 Composition of mixture ammonium sulfate and dark refractory

No.	Sample composition in volumic ratio	Mixing method	Condition
1.	Pyrrhotite-$_{fg}$		
	Pyrrhotite-$_{fg}$ 99 % ammonium sulfate 1 %	Planetary grinder	Room condition, without environmental cell Planetary grinder: dry grinding, 450 rpm during 10 minutes with 3 balls of 1cm Mortar: 5 minutes
	Pyrrhotite-$_{fg}$ 95 % ammonium sulfate 5 %		
	Pyrrhotite-$_{fg}$ 90 % ammonium sulfate 10 %	Planetary grinder, mortar,	
	Pyrrhotite-$_{fg}$ 85 % ammonium sulfate 15 %	Planetary grinder, mortar	
	Pyrrhotite-$_{fg}$ 80 % ammonium sulfate 20 %	Planetary grinder, mortar	
	Pyrrhotite-$_{fg}$ 57 % ammonium sulfate 43 %	Planetary grinder, mortar	
2.	Iron (ii) sulfide		
	Iron (ii) sulfide 95 % ammonium sulfate 5 %	Mortar during 5 minutes	Room condition, without environmental cell
	Iron (ii) sulfide 90 % ammonium sulfate 10 %		
	Iron (ii) sulfide 80 % ammonium sulfate 20 %		
	Iron (ii) sulfide 71 % ammonium sulfate 29 %		
	Iron (ii) sulfide 53 % ammonium sulfate 47 %		
3.	Graphite		
	Graphite 84 % ammonium sulfate 16 %	Mortar during 5 minute	Room condition, without environmental cell
	Graphite 55 % ammonium sulfate 45 %		
4.	Anthracite		
	Anthracite 95 % ammonium sulfate 5 %	Mortar during 5 minute	Room condition, without environmental cell
	Anthracite 90 % ammonium sulfate 10 %		
	Anthracite 80 % ammonium sulfate 20 %		
	Anthracite 57 % ammonium sulfate 43 %	Mortar	

Pure pyrrhotite-$_{fg}$ displays a red slope in the visible and its reflectance lies around 4 % (Fig. 4.9). Adding 5 vol % of ammonium sulfate, followed by hand mixing, increases the reflectance to 0.15, and no ammonium absorption band is observed. At 10 vol % of ammonium sulfate, the band appears, with a weak intensity and a significant level of noise. For 20 vol % and 43 vol %, the depth of the band continues to increase.

Figure 4.10 reports the spectra of pyrrhotite-ammonium sulfate samples prepared with the planetary grinder. The expectation here was to get a more homogenous mixture through producing sub-micrometric grains of ammonium sulfates, intimately mixed with the dark matrix. Unfortunately, we observe that the ammonium band appears at only 20 vol %, and remains weak even at 43 vol % of ammonium sulfate.

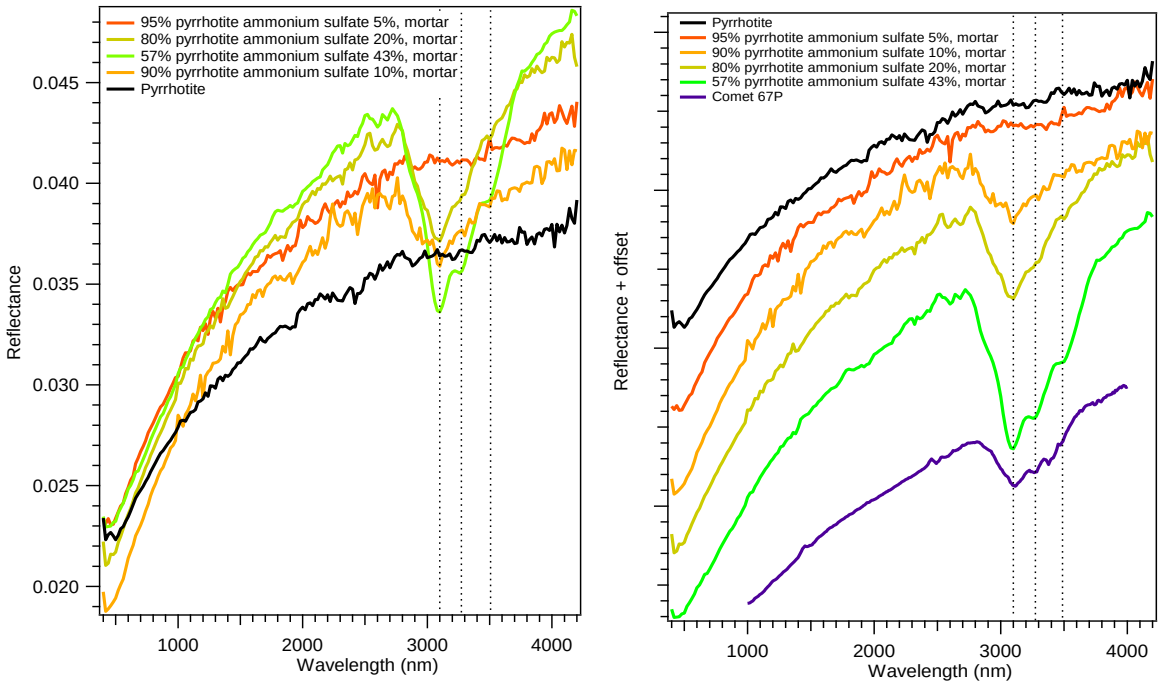

Figure 4.9. Spectra of mixtures of ammonium salt with pyrrhotite$_{-fg}$, hand-mixed in a mortar.

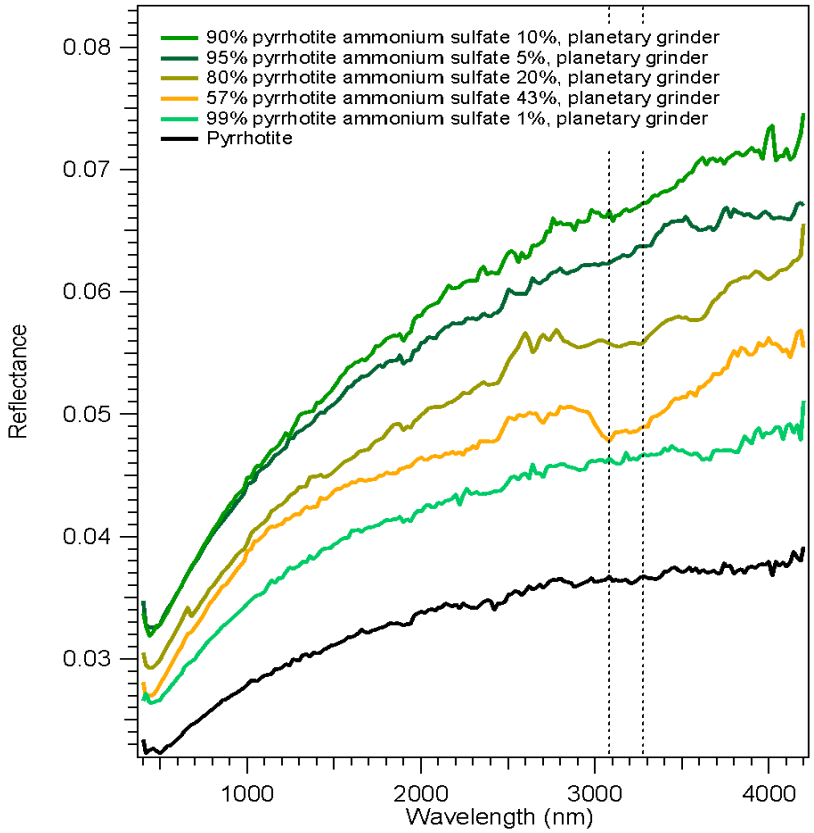

Figure 4.10. Spectra of mixtures of ammonium salt and pyrrhotite$_{-fg}$ made with the PM100 planetary grinder.

SEM analysis shed light on these observations (Fig. 4.11 and Fig. 4.12). The mechanical mixture is mostly composed of aggregates of sub-micrometric grains of pyrrhotite and ammonium sulfate, which can be distinguished in BSE or BSD modes. The texture inside the aggregates is quite compact, and the salt and pyrrhotite grains are finely intermixed. In some cases, we clearly observe that the salt is a kind of glue that sticks pyrrhotite grains together, but it is not systematic. Beside these aggregates, some kind of platelets are observed. SEM images of the sample produced by planetary grinding are quite different. They look like thin compact platelets or conchoidal grains, coated by sub-micrometric pyrrhotite grains.

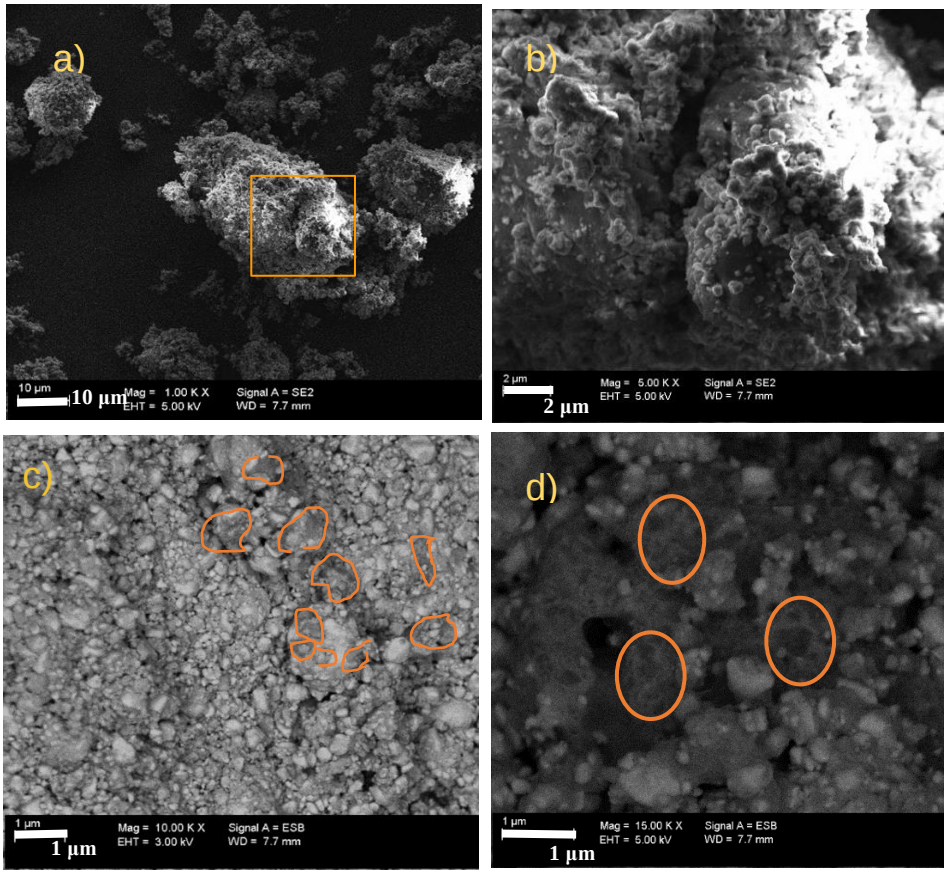

Figure 4.11. SEM images of pyrrhotite 57 vol % and ammonium sulfate 43 vol %. Image (a) shows few tens micron large aggregates in the mixture. Under higher magnification and BSE detector, image (c) and (d) do not show strong contrast between salt grains and pyrrhotite grains. The dark marks (orange circle) may point to the ammonium sulfate grains.

An extreme heterogeneity appears in BSD images: salt and pyrrhotite platelets, which point to efficient re-agglomeration processing along with a lack of mixing of the two phases, at a spatial scale of tens of micrometers. The distribution of the sub-micrometric grains are heterogeneous as well. The texture of the samples produced by the planetary grinder, composed

of large and very compact platelets, limits the penetration of the incoming light and minimizes the depth of the ammonium band. All together, these observations show that the planetary grinding provide samples of poor quality, in term of textural and chemical homogeneity. Hand mechanical mixing finally provides more relevant samples to cometary grains, except that their porosity is likely much weaker.

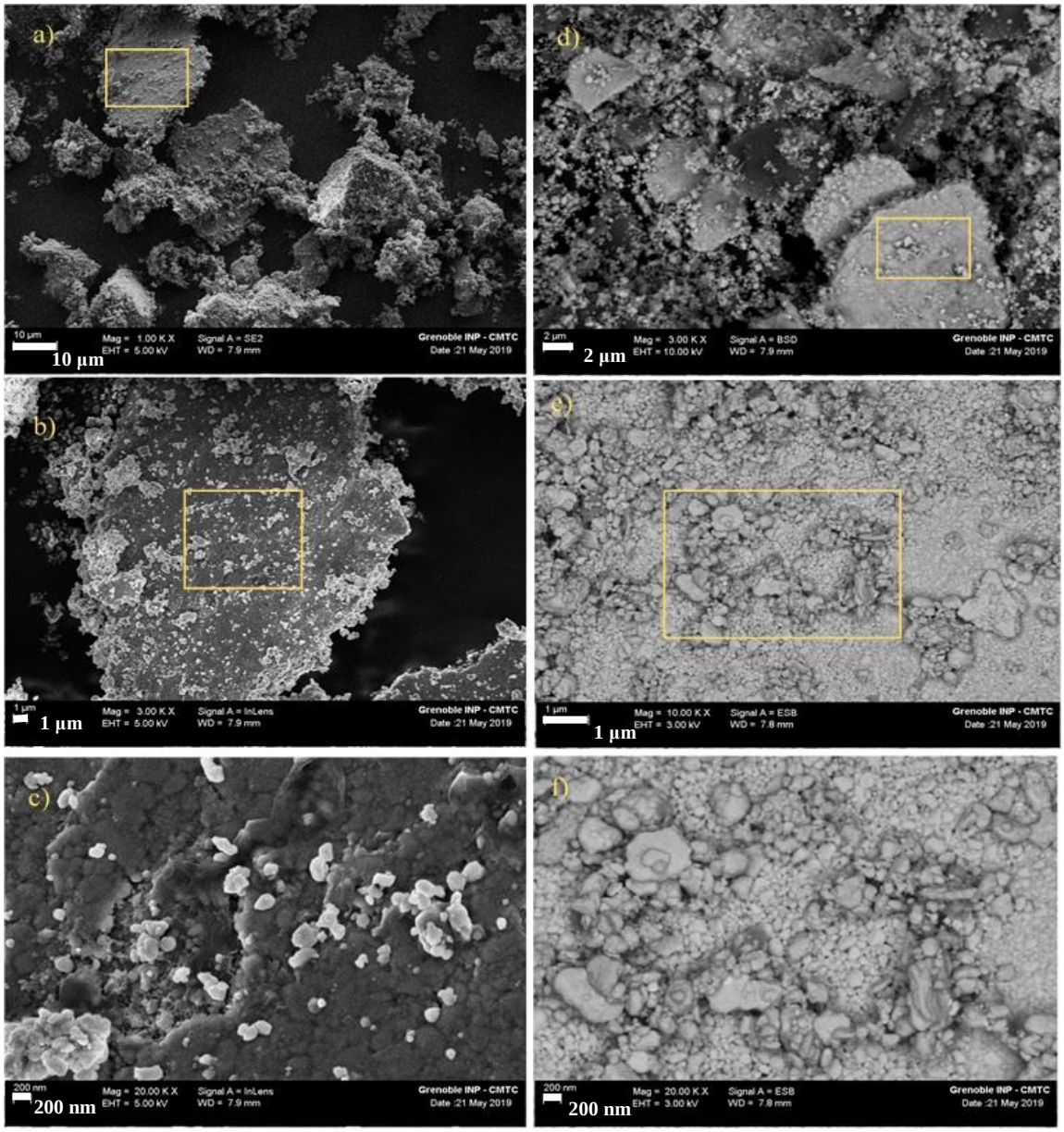

Figure 4.12. SEM images of ammonium sulfate and pyrrhotite-$_{fg}$ mixtures obtained with the planetary grinder at different magnifications under secondary electron (a,b,c) and BSE detectors (d,e,f). The agglomeration of pyrrhotite and ammonium sulfate appears in micrometric platelets (a). In BSE image, the dark marks may point ammonium sulfate grains.

Hand-mixed samples were also produced with another iron(ii) sulfide (Figure 4.13). Here the addition of ammonium sulfate produces a flat slope in the infrared, and the ammonium band appears at 29 vol %, while this feature is deep and displays two peaks at 3.1 and 3.3 µm for 47 vol %. The weak structure around 3.4 µm is likely an organic contamination. These results are basically different than those obtained with the pyrrhotite-fg sample, for which a deep band was observed from 10 vol % of ammonium sulfate. Unfortunately, we do not have SEM images of the samples with the iron(ii) sulfide.

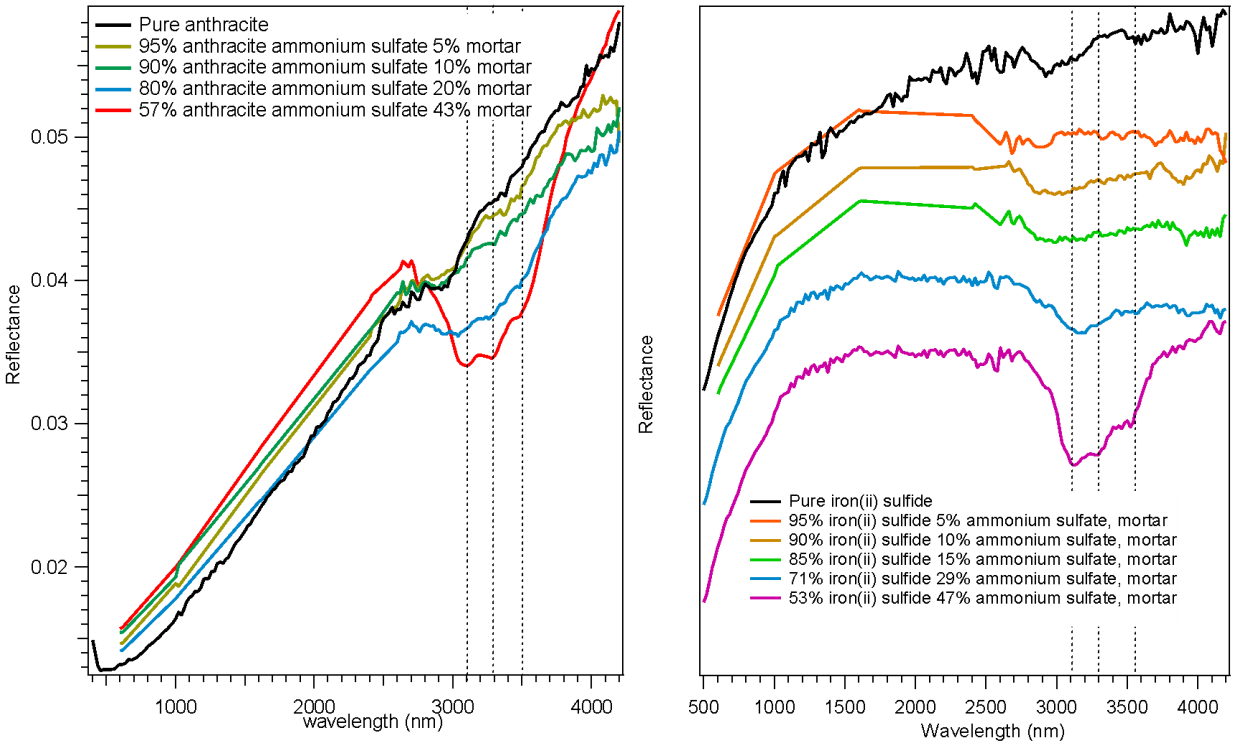

Figure 4.13. Reflectance spectra of mixture **ammonium sulfate–anthracite** (left) and **ammonium sulfate–iron sulfide** (right). The vertical smoothed lines point to the peak positions in VIRTIS spectra.

Last, some samples were produced with anthracite as the dark refractory matrix (Fig. 4.13) to test further matrix effect. Pure anthracite displays a very red slope from the visible to the infrared, with a weak absorption at 2.9 µm (likely due to -OH group in the anthracite). Adding ammonium sulfate increases slightly the reflectance in the visible, and the ammonium absorption band appears at 20 vol %, and looks deep at 43 vol %, with peaks at 3.1 and 3.3 µm. In this case, the trend of the ammonium band, in terms of optical depth, looks more similar to the results obtained with the iron(ii) sulfide.

Figure 4.14 shows the comparison of mixture ammonium sulfate with different dark refractory, and reports the band depth calculated for each one (details on band depth calculations are provided in the next section, see equation in section 4.2.5). All the mixtures display spectra basically consistent with that of comet 67P/CG, with two substructures peaking at 3.1 µm and 3.3 µm. We observe however that despite the low range of concentration 43-47 vol %, the band depth varies by a factor of ~3. The lowest band depth is observed for a mixture using graphite grains. Graphite is not a fine-grained powder, and is composed of flakes with a lateral size larger than 1 µm (99 %) (Table 2.2). These large grains are very opaque and certainly account for the very low band depth. As discussed before, the mixture produced with the planetary grinder from the fine-grained pyrrhotite-fg has a very low band depth, due to agglomeration within the ball. In contrast, the hand-ground pyrrothite-fg samples display the highest band depth. The anthracite mixture has a shallower band than this latter, but it is still large. It is consistent with the low grain size of the anthracite powder, with 75 % of particles ranging between 100 nm and 300 nm (Table 2.2). However, the iron(ii) sulfide sample has a lower band depth than the pyrrhotite$_{\text{-fg}}$ and anthracite sample. Iron(ii) sulfide has also a sub-micrometric population of grains, with 90 % of grains below 350 nm. There is thus no obvious effect of grain size. A difference is the presence of platelets, which are nevertheless not abundant. The difference between the two iron sulfides are then not straightforward to interpret. Basically, it can be due to (1) different optical indices, in particular absorption; (2) to the low reproducibility of the hand-mixing of the particles. Because the ammonium sulfate is very soft, we think this latter interpretation is plausible.

Finally, the main result is that hand-mixing provides the best results in terms of sample homogeneity, and the deepest ammonium band. However, this manual process is certainly not strictly reproducible. We lack here a SEM analysis of the mixed sample, which should be collected in the future.

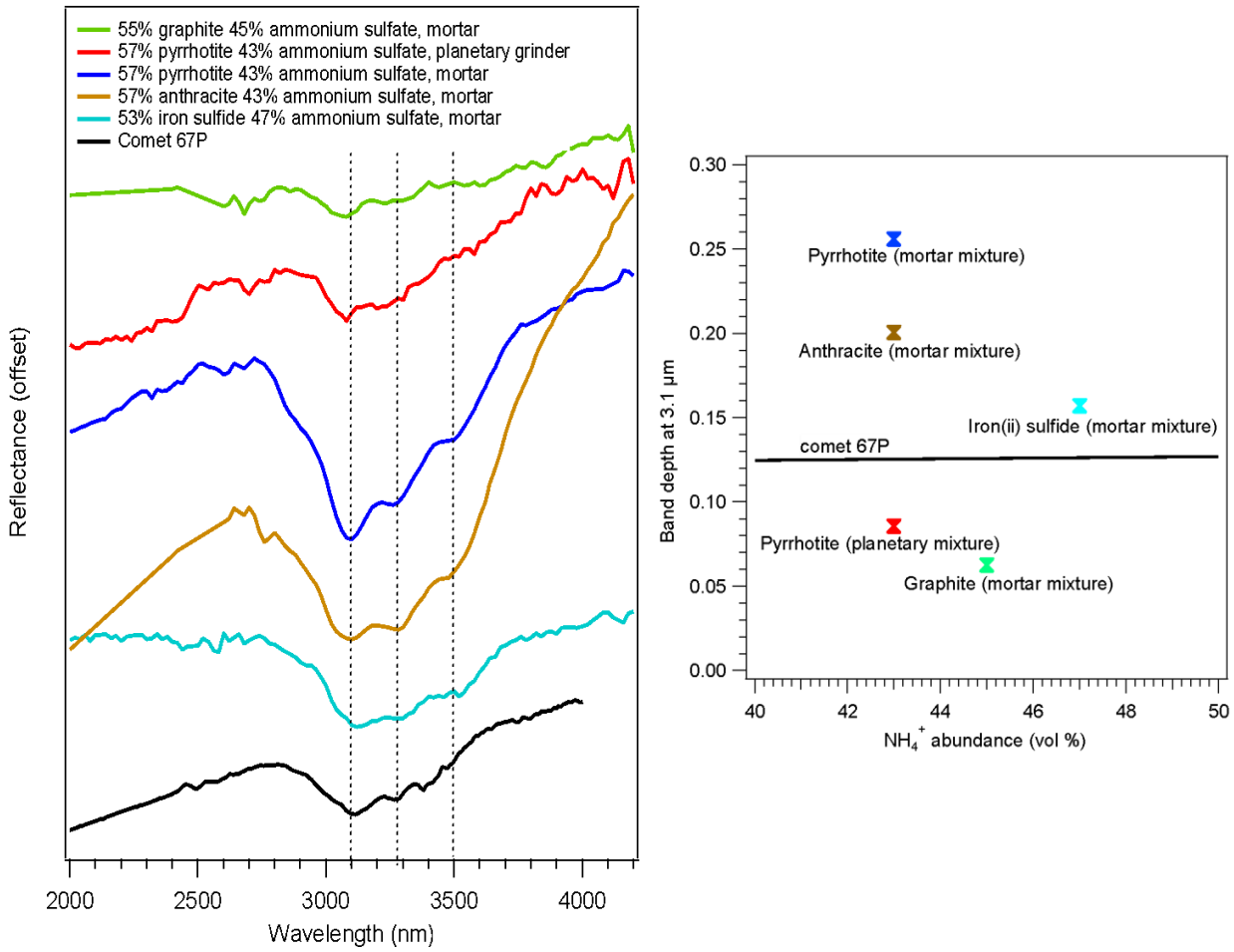

Figure 4.14. Comparison of spectra of ammonium sulfate mixed with different matrices (left) and the relevant band depth againts ammonium abundance.

4.2 Sublimation residues produced in the laboratory

Ice sublimation is a key process operating at the surface of comet 67P/CG, which triggers dust jets and forms a refractory crust. This crust is basically anhydrous, except few icy patches in the vicinity of cliffs and shadowed area (Pommerol et al., 2015; Gicquel et al., 2016; Barucci et al., 2016). During this process, we expect a mixing, at a very low spatial scale, of refractory dust and semi-volatile species. In order to provide samples more relevant to the actual cometary crust, we have run experiments inspired by the previous works of Poch et al. (2016ab). Ultra porous (porosity > 90 %) anhydrous residues were formed in a cell maintained at low pressure and low temperature (173 K). Sub-micrometric dust analogues and ammonium salts (or lactic acid) were dissolved in liquid water (intra-mixture mode), and ice-dust particles were generated through nebulization and rapid quenching in liquid nitrogen. The spherical particles were deposited into a sample holder in the CarboNIR-cell chamber (10^{-5} mbar, 173 K), and then let

to evolve freely by ice sublimation. Eventually, an anhydrous refractory residue was formed, under conditions that are more representative of cometary conditions than the mechanical mixing presented in section 4.1. The reflectance spectra were collected *in situ* with the SHINE spectro-gonio-radio-spectrometer (see Chapter 3, for extensive details on the experimental apparatus), during the whole sequence of ice sublimation. Samples were recovered under room conditions after the collection of reflectance spectra and were characterized by Scanning Electron Microscopy.

Dark refractory dust was mostly simulated by sub-micrometric grains of pyrrhotite, pyrrhotite-$_{fg}$, and pyrrhotite-$_{fg\text{-}pl}$, the second containing a significant abundance of micrometre-sized platelets (Figure 4.1). A commercially available iron sulfide was also used, as well as anthracite and olivine sub-micrometric grains. Table 4.5 summarizes the composition of the different mixtures that were studied. Note that ammonium sulfate was mostly used, due to its good stability under vacuum and under room conditions, in particular, its lower sensitivity to moisture.

Table. 4.5. Mixture composition of refractories, ammonium salts and lactic acid

Refractories	**Salts-Acids**
Pyrrhotite-$_{fg\text{-}pl}$ (77 vol %)	Lactic acid (23 vol %)
Pyrrhotite-$_{fg}$ (90 vol %)	Ammonium formate (10 vol %)
Pyrrhotite-$_{fg\text{-}pl}$ (58 vol %)	Ammonium formate (42 vol %)
Pyrrhotite-$_{fg\text{-}pl}$ (60 vol %)	Ammonium carbamate (40 vol %)
Pyrrhotite-$_{fg\text{-}pl}$ (52 vol %)	Ammonium citrate (48 vol %)
Pyrrhotite-$_{fg\text{-}pl}$ (27 vol %)	Ammonium chloride (23 vol %)
Pyrrhotite-$_{fg}$ (94 vol %)	Ammonium sulfate (6 vol %)
Pyrrhotite-$_{fg}$ (93 vol %)	Ammonium sulfate (7 vol %)
Pyrrhotite-$_{fg}$ (92 vol %)	Ammonium sulfate (8 vol %)
Pyrrhotite-$_{fg}$ (90 vol %)	Ammonium sulfate (10 vol %)
Pyrrhotite-$_{fg\text{-}pl}$ (71 vol %)	Ammonium sulfate (21 vol %)
Pyrrhotite-$_{fg}$ (57 vol %)	Ammonium sulfate (43 vol %)
Pyrrhotite-$_{fg\text{-}pl}$ (56 vol %)	Ammonium sulfate (44 vol %)
Pyrrhotite-$_{fg}$ (23.5 %) Olivine (23.5 %)	Ammonium sulfate (43 vol %)
Pyrrhotite-$_{fg}$ (47 %) Olivine (47 %)	Ammonium sulfate (6 vol %)
Pyrrhotite-$_{fg}$ (70.5 %) Olivine (23.5 %)	Ammonium sulfate (6 vol %)
Anthracite (90 %)	Ammonium sulfate (10 %)
Iron(ii) sulfide (90 %)	Ammonium sulfate (10 %)

4.2.1 Sublimation residue of pyrrhotite-$_{fg\text{-}pl}$ -ammonium salts

We first report the experiments associating pyrrhotite-$_{fg\text{-}pl}$ and different ammonium salts. Figure 4.15 shows the spectral evolution of the mixture pyrrhotite-$_{fg\text{-}pl}$ + ammonium formate. The first spectrum (at time t=0) is dominated by the vibration bands of water ice at 1.5 µm and 2.0 µm. A Fresnel effect is observed at 3.1 µm, due to the strong absorption band of water ice around 3 µm. After 35 hours, the water ice in the sample has sublimated, leaving an anhydrous and porous residue (Fig. 4.17). The residual band is that of ammonium formate.

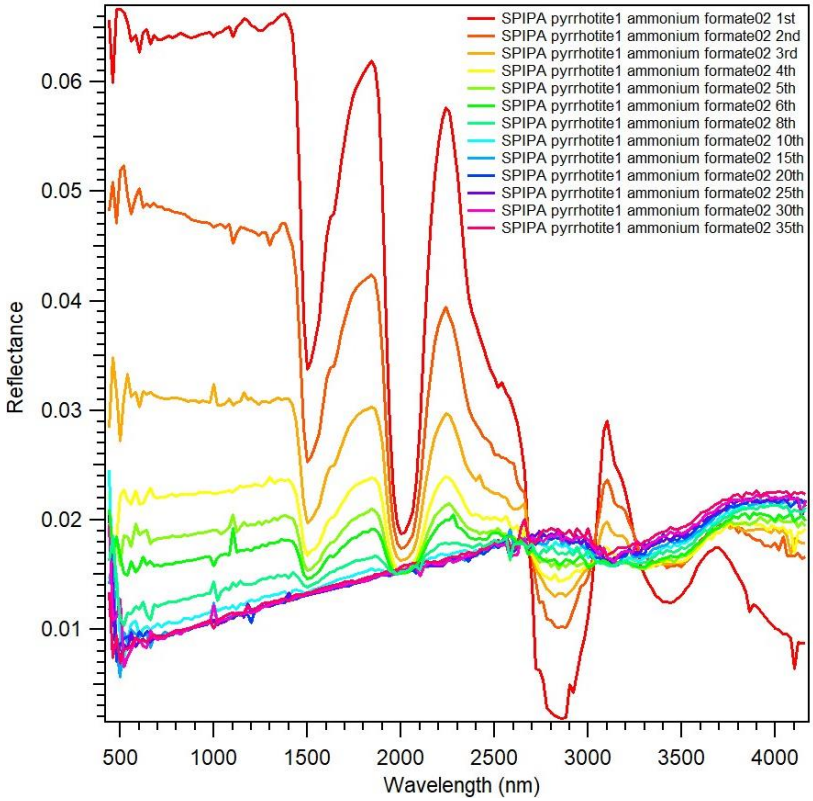

Figure 4.15. Spectral evolution upon time of a pyrrhotite-$_{fg\text{-}pl}$ and ammonium formate mixture, maintained at 173 K and 10^{-5} mbar during 35 hours.

The sublimation residues were exposed to cooling-heating cycles to test salt stability (Fig. 4.16.). It was first cooled down to 110 K, and then heated until 230 K. During the cooling stage, the absorption band of the ammonium salt did not change. In contrast, its spectral depth decreased during heating, without significant change of the shape (Fig. 4.16). These variations are controlled by the salt volatility.

In the case of ammonium sulfate, the crystal undergoes a ferroelectric transition from the ferroelectric to the paraelectric phase, between 199 K and 214 K. A change of the band shape is observed at this transition (Fortin et al, 2002), but we did not observe it. Here, the band shape

in our spectra at 173 K is similar to the paraelectric phase at 214 K measured by Fortin et al. (2002). The lack of transition in our data may be due to differences with the experimental protocol of Fortin (2002). Hence, they produced thin films of ammonium sulfate from the reaction of SO_3 with H_2O at 130 K, and increased slowly the temperature until 288 K. Here, the crystals of ammonium salt were produced at 173 K from ice sublimation.

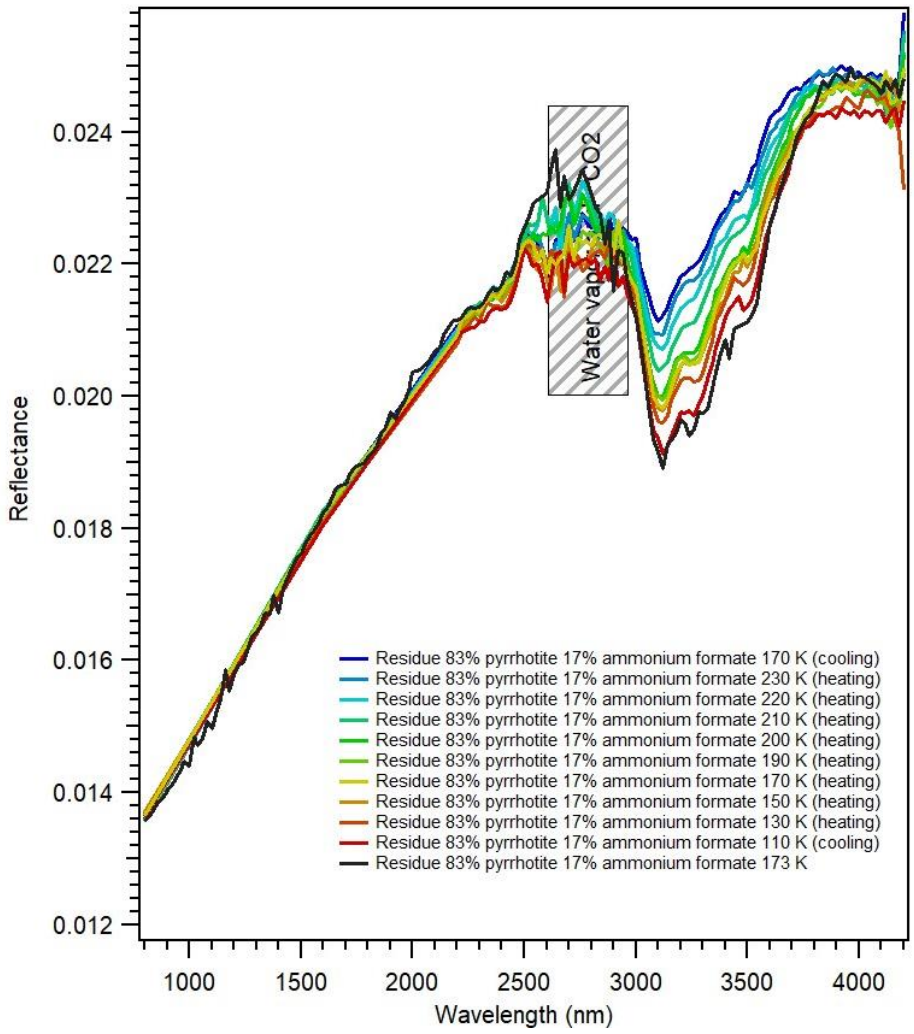

Figure 4.16. Spectral evolution an ammonium-formate residue during cooling (173 - 100 K) and heating (110-230 K).

SEM observations of the residue show a fluffy and porous material (Fig. 4.17). It is very brittle and partially collapsed after opening the chamber and manipulations. BSE images do not clearly distinguish between (bright) iron sulfides and (dark) ammonium formate materials. At best, we can suspect some ammonium coating at the surface of platelets (Fig. 4.17d). Back-scattered electrons probe a ~1 µm depth at 15 kV, which means that several sub-micrometric grains are analyzed at the same time, along with ammonium salts if they are intimately mixed

with sulfides at the sub-micrometric scale. Ammonium formate is significantly volatile in room conditions, raising the question of whether the ammonium salt have gone. SEM observations on mechanical mixtures of pyrrhotite + ammonium formate show that micrometric grains are still observable (Fig.4.18). It seems then likely that sub-micrometric pyrrhotite grains are intimately mixed with ammonium salt evaporite.

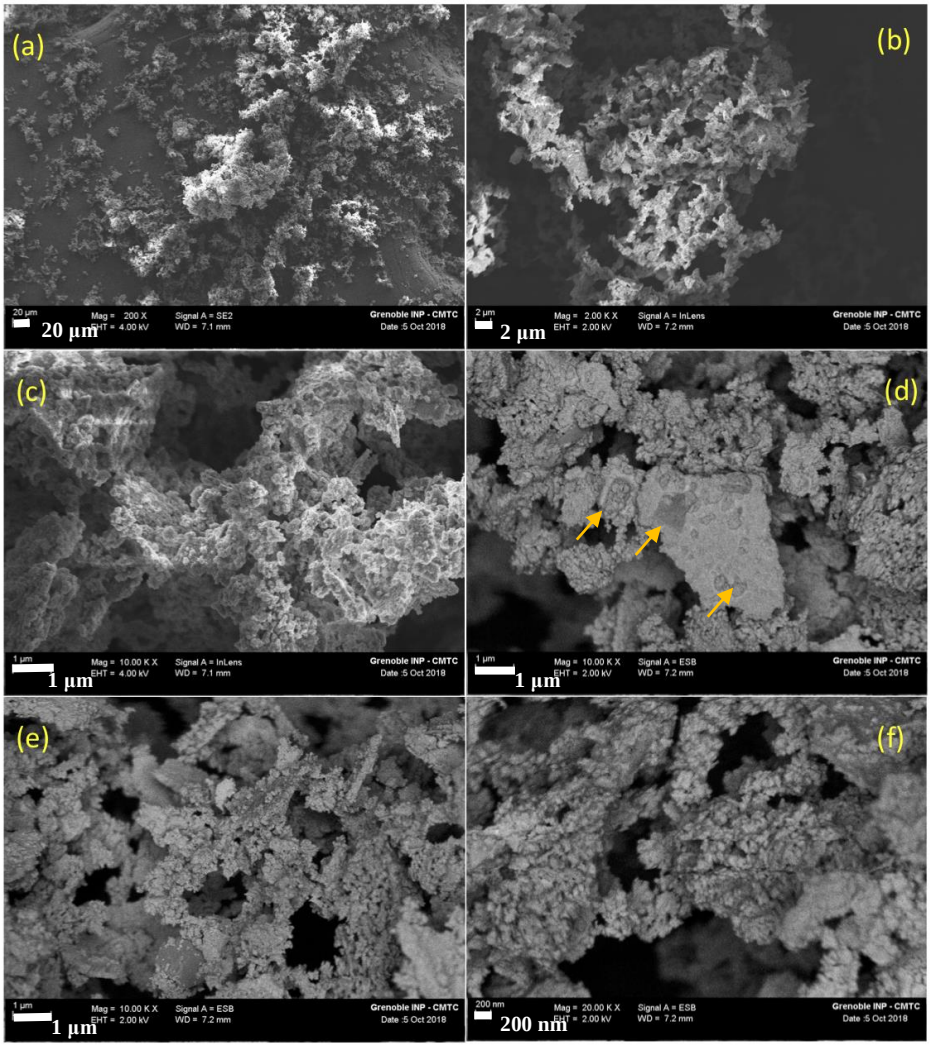

Figure 4.17. SEM image of porous sublimation residue of pyrrhotite-$_{fg\text{-}pl}$ and ammonium formate. Photos (a,b,c): secondary electrons images, revealing porous and fluffy aggregates. Photos (d,e,f): back-scattered electrons images, which do not show (a) clear dichotomy between bright sulfides and dark ammonium salts. The dark square inclusion in the platelet in photo (d) may point to an ammonium salt inclusion.

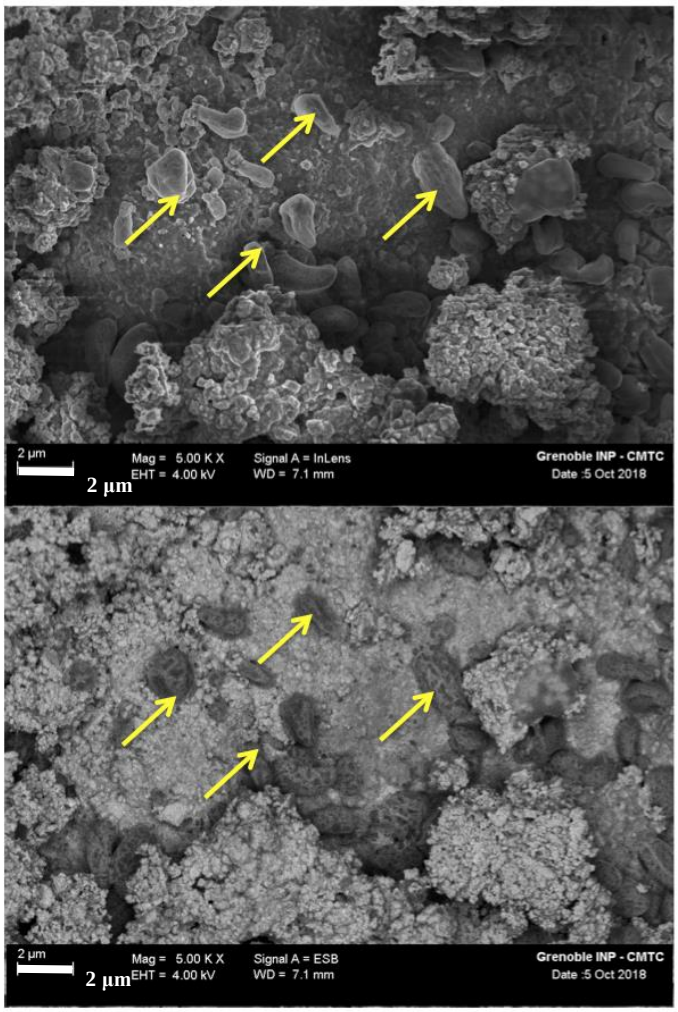

Figure 4.18. Ammonium formate salts evidenced in a pyrrhotite-ammonium salt mechanical mixture by SEM-BSE imaging (yellow arrows). Despite their volatility, the ammonium salts are present and observed.

Figure 4.19 shows the reflectance spectra of the sublimation residues formed from mixtures of ammonium salts, lactic acid and pyrrhotite. The pure pyrrhotite sample has a reflectance factor around 2 %, and a red slope that might be due to sulfide oxidation when mixed with liquid water. We observe slope variations in the spectra. With 48 vol % of ammonium citrate, we observe a blue slope in the visible and infrared ranges. For other mixtures of ammonium salts in the range 23-43 vol %, the slopes remain red. Despite the large vol % abundance of ammonium salts, the reflectance factor remains lower than 4 %, and overall consistent with the low reflectance factor of comet 67P/CG. Regarding band positions in the 3.2 µm broad band of comet 67P/CG, we observe a very good match with ammonium formate, a fair match with other salts, except NH_4Cl which do not fit the comet. These observations are in agreement with the conclusions driven from the transmission spectra (see Chapter 3).

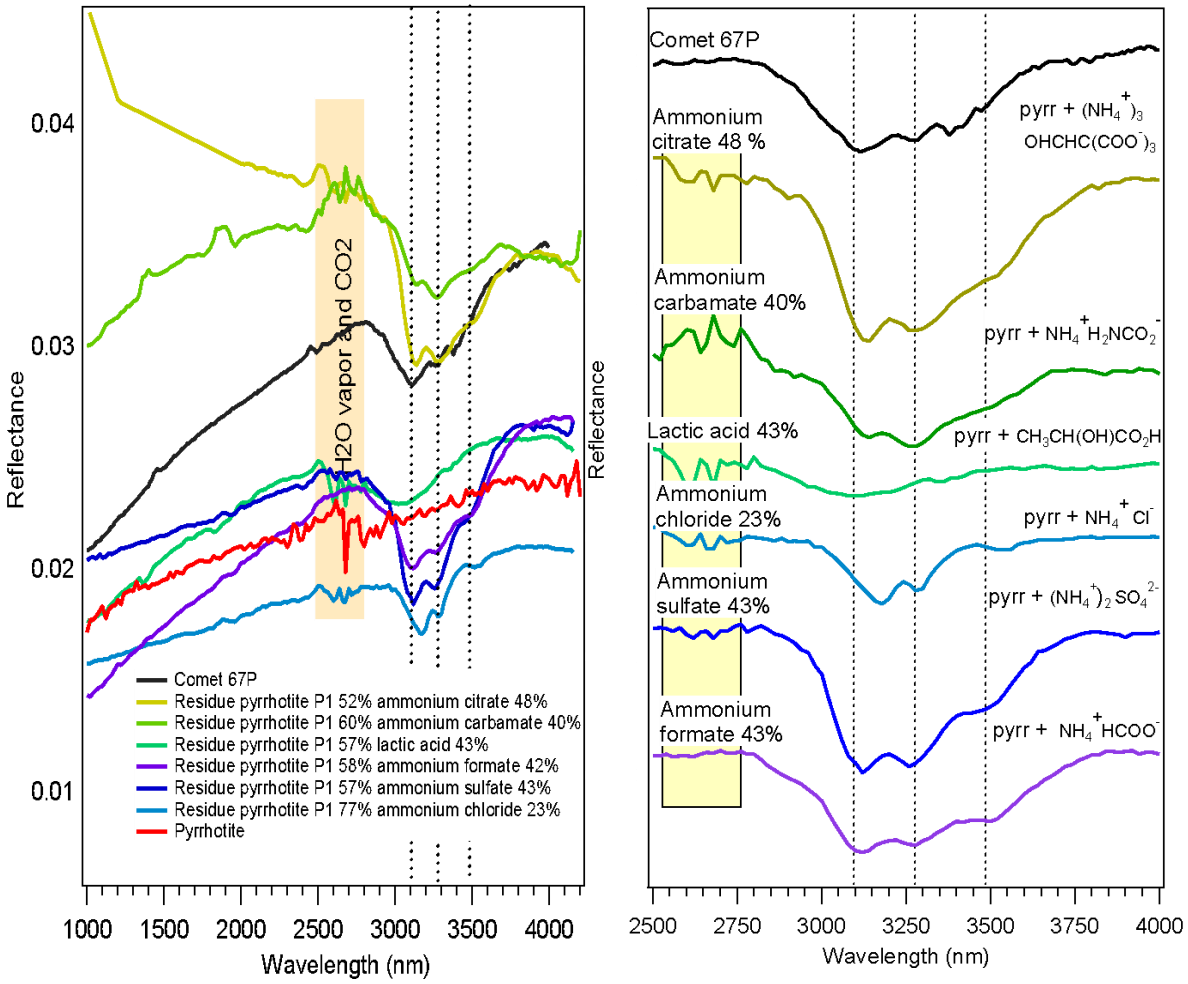

Figure 4.19. Spectra of sublimation residue of pyrrhotite + ammonium salts and lactic acid (left), and their continuum-removed spectra (right).

All ammonium salts display substructure as peaks in the mid-infrared region that fit those of transmission spectra, which indicate that the very small size of the grains (no saturation). Note however that here the definition of a grain is difficult, as we have certainly a complex texture involving sub-micrometric sulfides and coating, and/or even smaller grains intimately associated with those sulfides.

Last, note that the small absorption features observed in the spectrum of comet 67P between 3.4 and 3.5 μm are attributed to the C−H stretching modes of aliphatic functional groups from carbonaceous compounds (Raponi et al., 2020).

4.2.2 Effects of homogenous sub-micrometric pyrrhotite in sublimation residue

We prepared sublimation mixtures with the fg and fg-pl pyrrhotites to investigate the effect of grain size on sublimation residue spectra. Figure 4.20 shows the spectra of sublimation residue of ammonium sulfate with fg and fg-pl pyrrhotites. At the concentration of 43 vol % of ammonium sulfate, pyrrhotite-$_{fg}$ produces a stronger absorption band than pyrrhotite-$_{fg-pl}$, by a factor of ~3. The absorption of residue pyrrhotite-$_{fg-pl}$+ammonium sulfate 43 vol % is comparable with the band depth of the pyrrhotite-$_{fg}$+ammonium sulfate 10 vol % residue (Figure. 4.20). However, the shape of the band looks slightly different, in terms of the relative intensities of the two most prominent peaks.

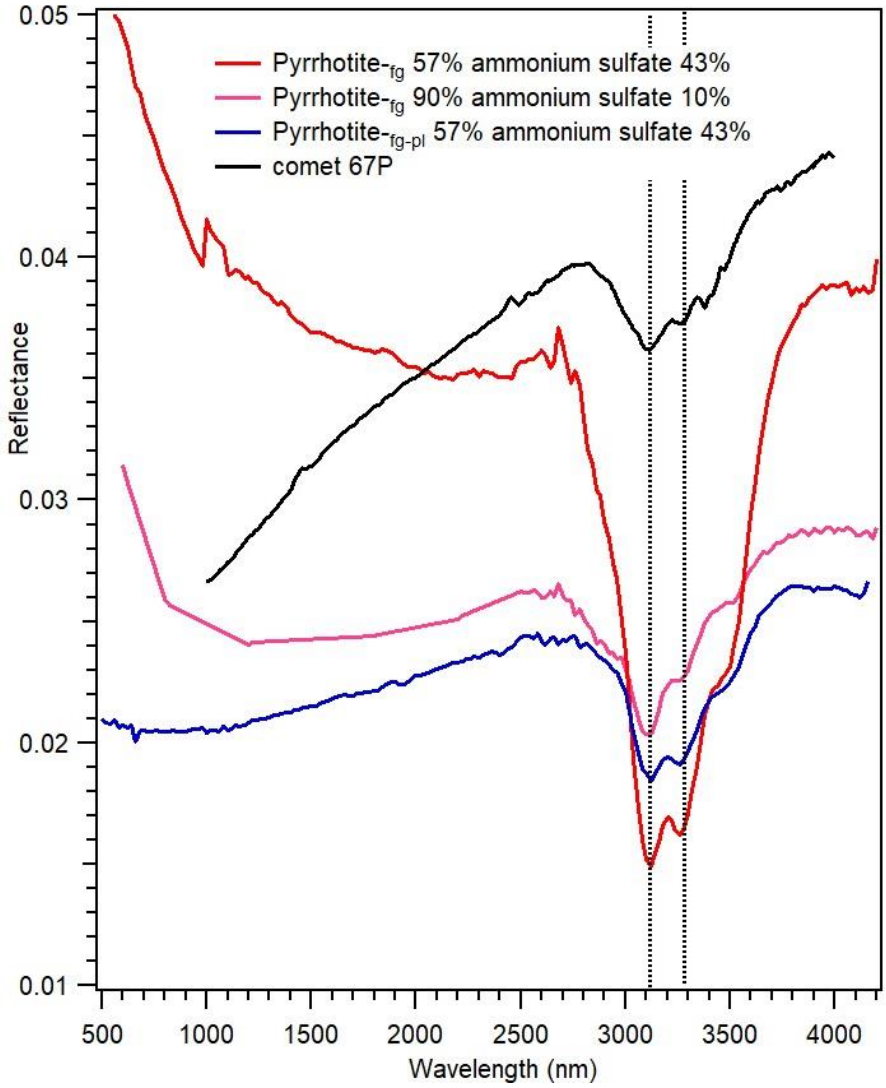

Figure 4.20. Spectra of sublimation residues of ammonium sulfate for fg and fg-pl pyrrhotites.

SEM images (Figure 4.21 and 4.22) show porous sublimation residues obtained from the two types of pyrrhotites. In Pyrrhotite-$_{fg}$ residues, ammonium salt appears as smooth boulders, filaments or needle-like structures (Fig. 4.21).

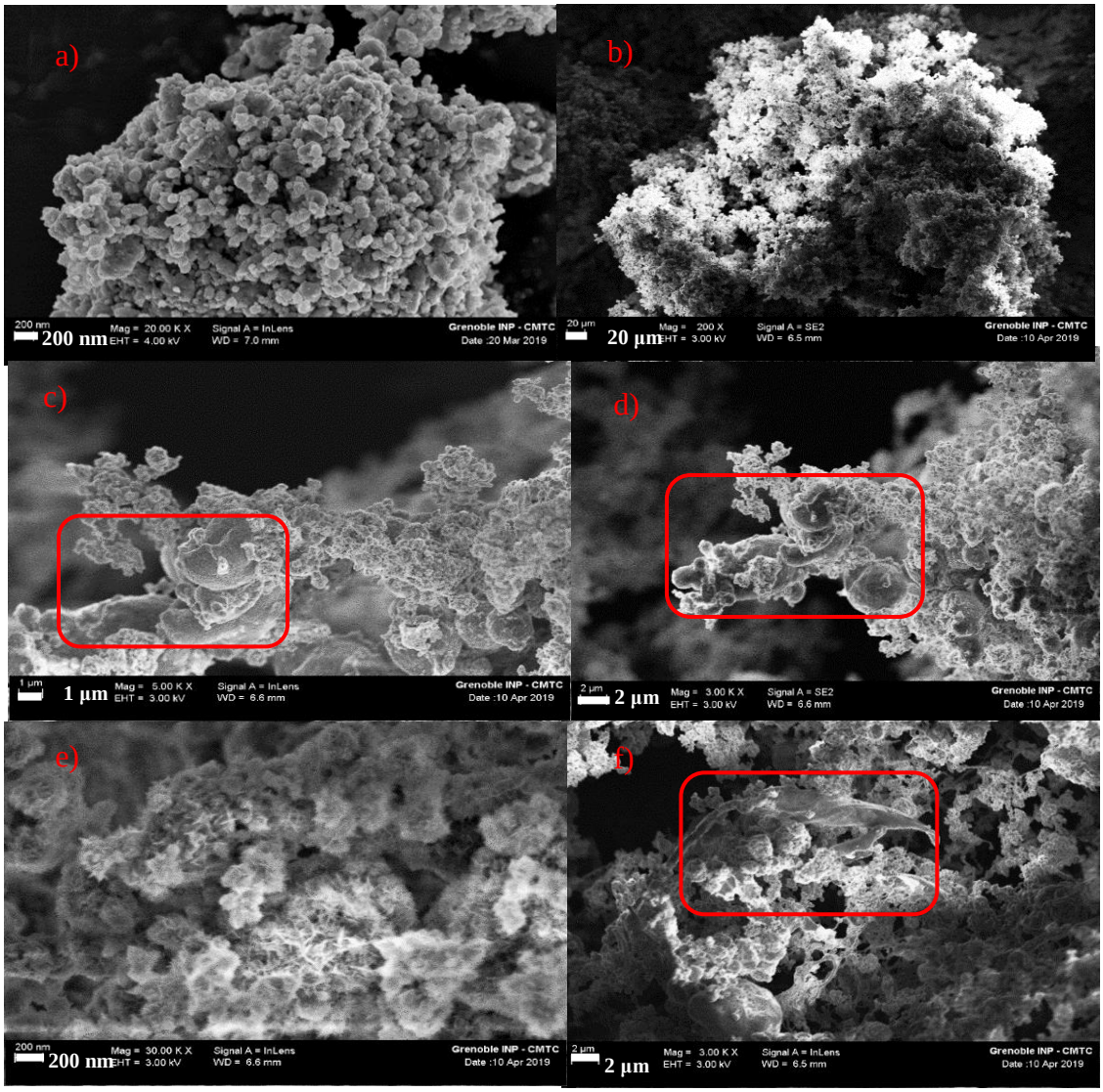

Figure 4.21. SEM images of sublimation residue of ammonium sulfate and pyrrhotite-$_{fg}$ at different magnifications. (a):pure pyrrhotite-$_{fg}$; (b): the porous structure of the sublimation residue; (c-f): ammonium grains in the structure as smooth boulders, needles and filament structures.

In pyrrhotite-$_{fg\text{-}pl}$ residues, we observe big grains with a smooth surface (that might be an ammonium salt coating), but no needle-like and filament structures. The ammonium sulfate in the mixture likely plays the role as cement that binds grains of pyrrhotite to build a porous structure. While these differences are clear from SEM images, it is premature to conclude they

are controlled by the presence of platelets. Similarly, we cannot clearly infer the textural parameters that control the depth of band.

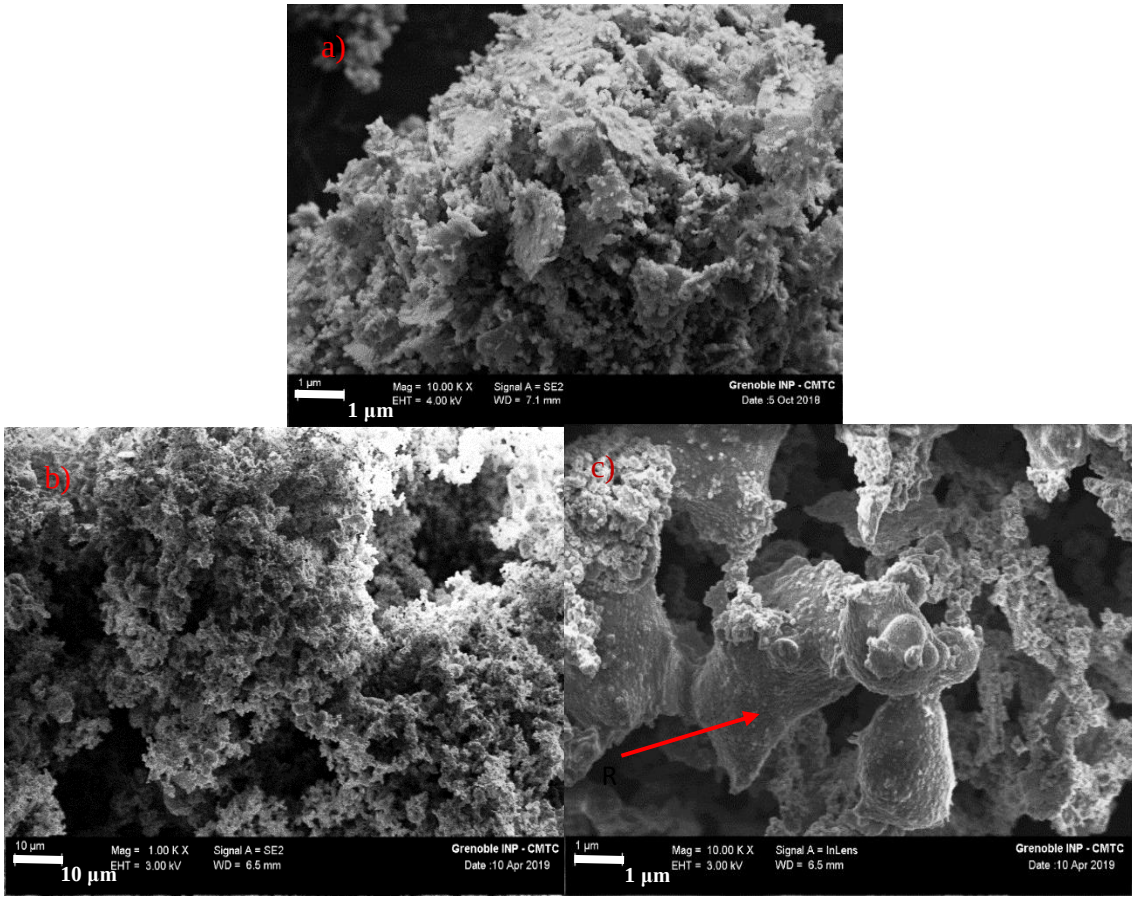

Figure 4.22. SEM images of sublimation residues of ammonium sulfate and pyrrhotite-$_{fg\text{-}pl}$ at different magnifications. (a) pure pyrrhotite-$_{fg\text{-}pl}$. (b,c) porous structure and smooth boulders of ammonium sulfate grains in pyrrhotite-$_{fg\text{-}pl}$ + ammonium salt mixture.

4.2.3 Effects of brighter refractory in sublimation residue

In the mechanical mixture section, we investigated mixtures of olivine and ammonium salts and the result was that in brighter refractory matrix we can observe strong absorption band with small concentration of ammonium salts. We have also investigated the effect of brighter refractory grains in sublimation residue, with an experiment including an olivine:pyrrhotite-$_{fg}$ = 1:1 mixture. The olivine was previously dehydrated (and oxidized), and consisted in angular shaped sub-micrometric grains (Table. 2.2.).

Figure 4.23 shows that pure olivine has a reflectance factor around 70 % in the infrared range, and lower in the visible due to the absorption of oxidized iron. Note, the deep water band

shows that dehydration was not fully completed. By mixing olivine and pyrrhotite (1:1) with ammonium sulfate (43 vol %) we obtain a flat spectrum with a factor reflectance of ~ 4 %, and a strong absorption band due to the ammonium ion. Comparing with the spectrum of pyrrhotite:ammonium (43 vol %), the reflectance is fairly similar and the absorption band deeper by a factor of ~1.5 (Fig. 4.23). Our results are basically consistent with Rousseau et al. (2017b) for the reflectance factor. A summary of the ammonium band depth for all sublimation residues and granular mixture is presented on Figure 4.25.

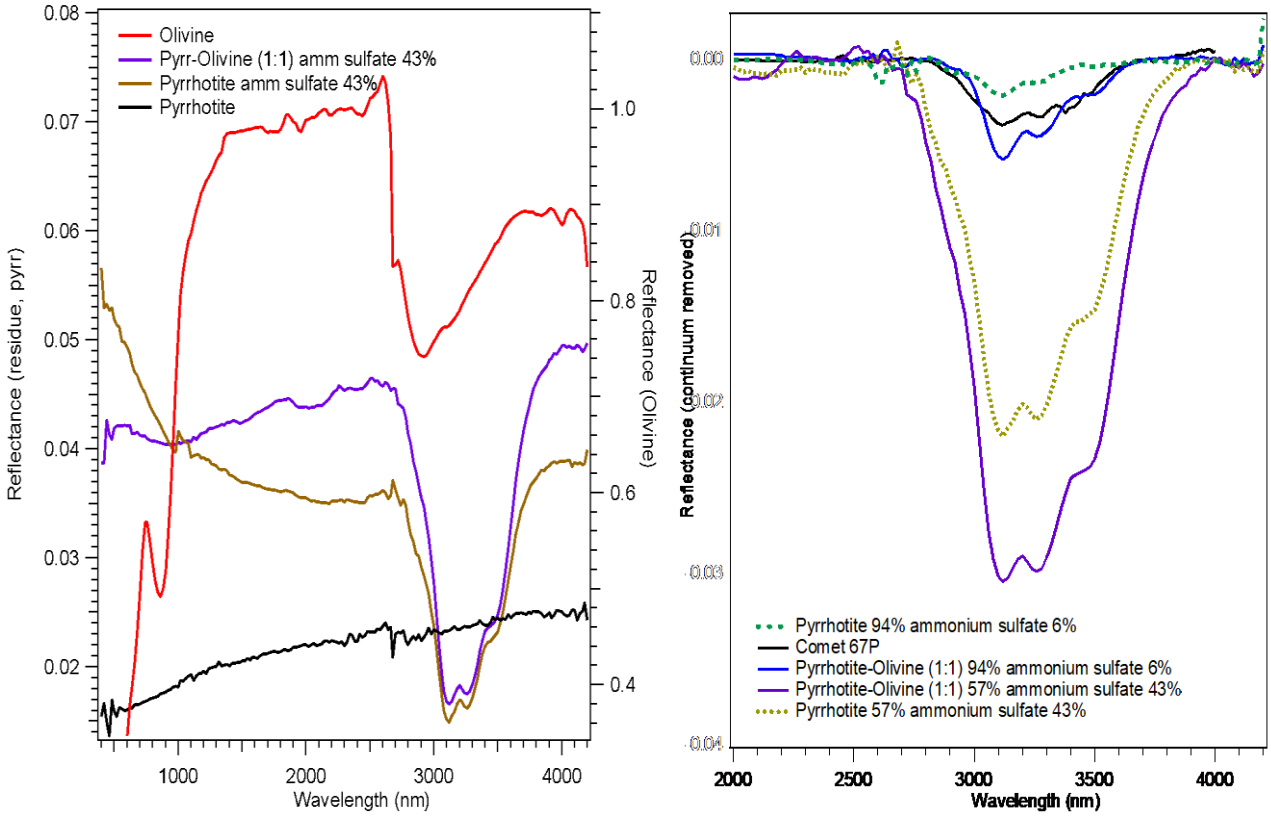

Figure 4.23. Left: Spectra of sublimation residues of ammonium sulfate with pure and mixed Pyrrhotite-$_{fg}$ with olivine. Right: continuum-corrected spectra of different mixtures.

4.2.4 Sublimation residues with different refractories

Sublimation residue with different dark refractory grains, iron sulfides and anthracite, were also investigated (Fig. 4.24). Anthracite is a mature coal that is strongly absorbent in the visible and near-infrared ranges (Quirico et al., 2016). For similar 10 vol % abundances of ammonium sulfate, we observe a slightly higher reflectance factor of the continuum of the anthracite mixture, a deeper band that displays the typical vibration modes of ammonium sulfate and a much redder slope. The iron sulfide mixture appears higher than the pyrrhotite one, and the

band depth is lower by around a factor of ~2. The shape of the band in the anthracite mixture appears different than that in other mixtures. The relative intensities of the two main peaks are very different, but the peak positions remain similar. Variations in the structure of the ammonium sulfate may induce spectral variations, for instance in the case of very thin coatings, whose vibration properties are different than the bulk crystal. However, the change of relative intensities is here very strong. Another explanation is a contamination, but we could not identify it.

Anthracite has a lower density than other refractories, even ammonium sulfate, and is also hydrophobic. During sample preparation, part of anthracite grains remain at the surface of the droplet of dust solution (water+salt+anthracite) during nebulizing, and we cannot exclude that we have a lower concentration of anthracite in the residue. This may account for the higher reflectance factor and deeper absorption band. Pyrrhotite-$_{fg}$ and iron(ii) sulfide have much higher density in comparison to ammonium sulfate and more importantly they are not hydrophobic. The differences of the depth of the ammonium band may be due to different composition of pyrrhotite and iron(ii) sulfide. We do not know this latter, but the density of pyrrhotite ranges 4.58-4.65 g cm^{-3}, and iron(ii) sulfide density is 5 g cm^{-3}. In any case, this does not explain a factor of ~2. We think that the texture of the material, which controls the radiative transfer, plays here a key role. It is however difficult to identify which parameters are involved. In the purpose of abundance quantification from observations, these fluctuations need to be accounted for by releasing the error on the estimation.

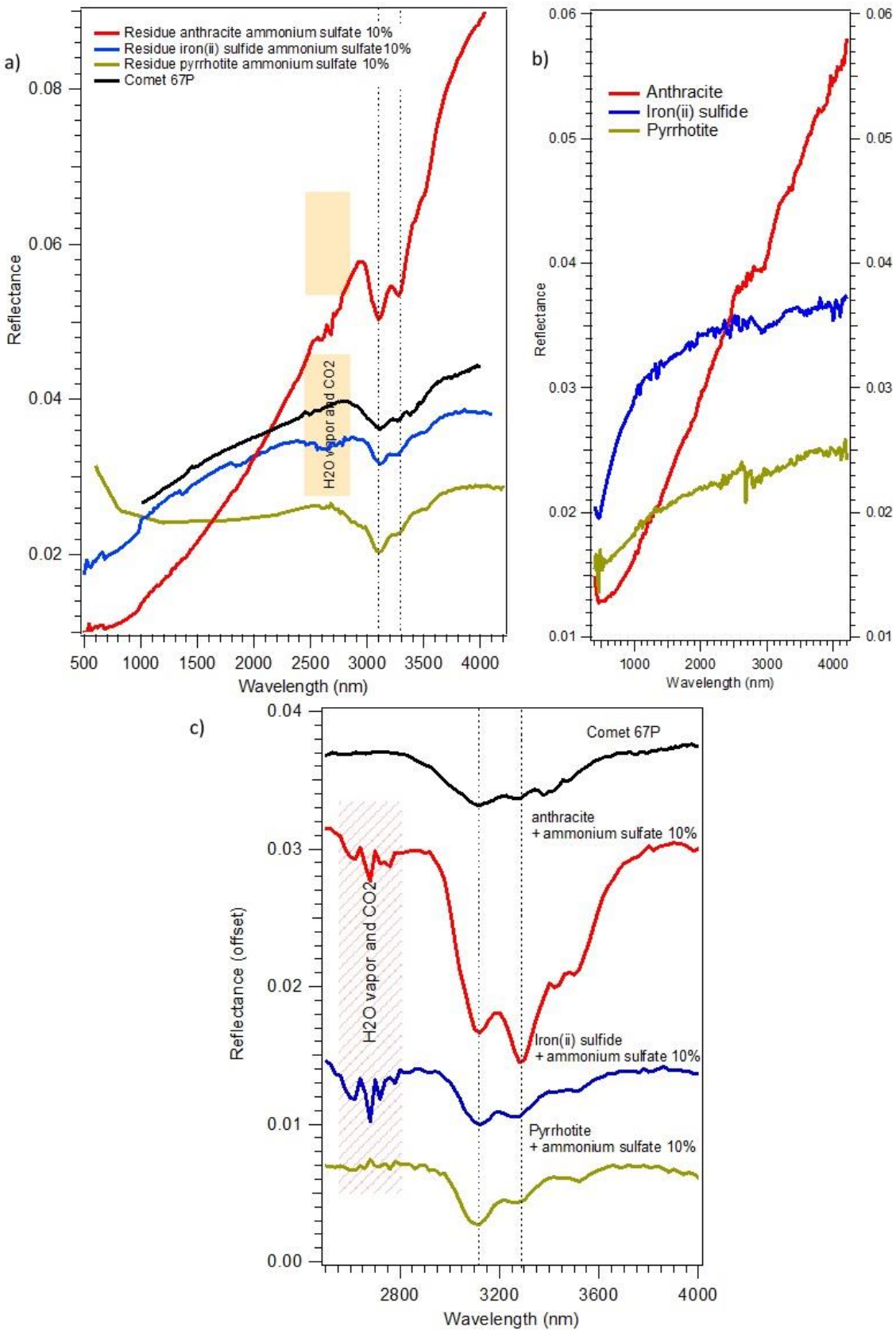

Figure 4.24. a) Spectra of sublimation residue of ammonium sulfate with different different dark refractories b) Pure dark refractories and c) Continuum-corrected spectra of different mixtures.

4.2.5 The band depth of sublimation residues

The relative band depth of ammonium salts in the sublimation residues and granular mixture can be calculated through:

$$BD = 1 - \frac{R}{R_C}$$

with:

R the reflectance factor value at the ~3.1 µm as the minimum reflectance.

R_C the reflectance value of the continuum baseline. The continuum baseline was computed with a spline interpolation (3rd order polynomials) using baseline anchor points at 2.20, 2.45, 2.68, 3.96 and 4.10 µm.

Figure 4.25 and 4.26 present the band depth of the ammonium band (at 3.1 µm) plotted against the vol % and mol % abundances of the ammonium salt, respectively, for both sublimation and mechanical mixtures. The sublimation residues produced from ammonium sulfate and pyrrhotite-fg show a quite broad range of band depth 0.02 to 0.19 for similar NH_4 molar abundances (~0.04). Only one point was obtained for a higher NH_4 abundance, which is not enough to provide a calibration curve. The addition of olivine in the refractory matrix, or the use of anthracite as the dark matrix does not lead to significant changes in band depth. The chemical composition of the dust analog does not control the spectra, which mean it cannot be extracted from this kind of observation. This observation is consistent with the experiments of Rousseau et al. (2017b).

The broad range of band depths at low NH_4 abundance shows that the quantification of ammonium ions from reflectance spectra is difficult. Ammonium sulfate is the most stable ammonium salt we have studied, and here we think that this dispersion of values largely mirror variations of the texture of the residue. This texture, however, seems to be not strictly reproducible from one experiment to another. As mentioned above, its characterization is tricky. SEM images provide insights into grain size and distribution, a rough appraisal of porosity essentially qualitative, but distinguishing salts from refractory grains is very difficult because the intrication scale is very low. At this point, we cannot provide a rigorous and quantitative comparison of the different residues that were produced.

The data points obtained from pyrrhotite$_{\text{-fg-pl}}$: ammonium sulfate mixtures do not display a continuum with the previous data. However, we observe a fair trend for all ammonium salts measured with pyrrhotite-fg-pl (triangles in Fig. 4.25). It seems that this subset of data is

significantly different than the previous one. Two explanations are possible: (1) the presence of micrometric-platelets plays a key role in the control of the texture; (2) there is a systematic bias due to variations in the physical conditions, but not identified to date. In any case, all together, even using sublimation experiments that provide fair cometary conditions, we get to the conclusion no reliable quantification can be obtained.

Regarding data for mechanical mixtures, we basically observe two points. First, even at high ammonium molar abundance, the band depth does not reach values as high as those obtained with sublimation residues. Second, there is no correlation between band depth and ammonium abundance. These observations are resulted from the experimental protocol. Hand grinding of ammonium salts at room temperature, and subsequent mixing, is poorly reproducible in terms of grain size. In addition, some salts are hygroscopic and very soft, favoring agglomeration.

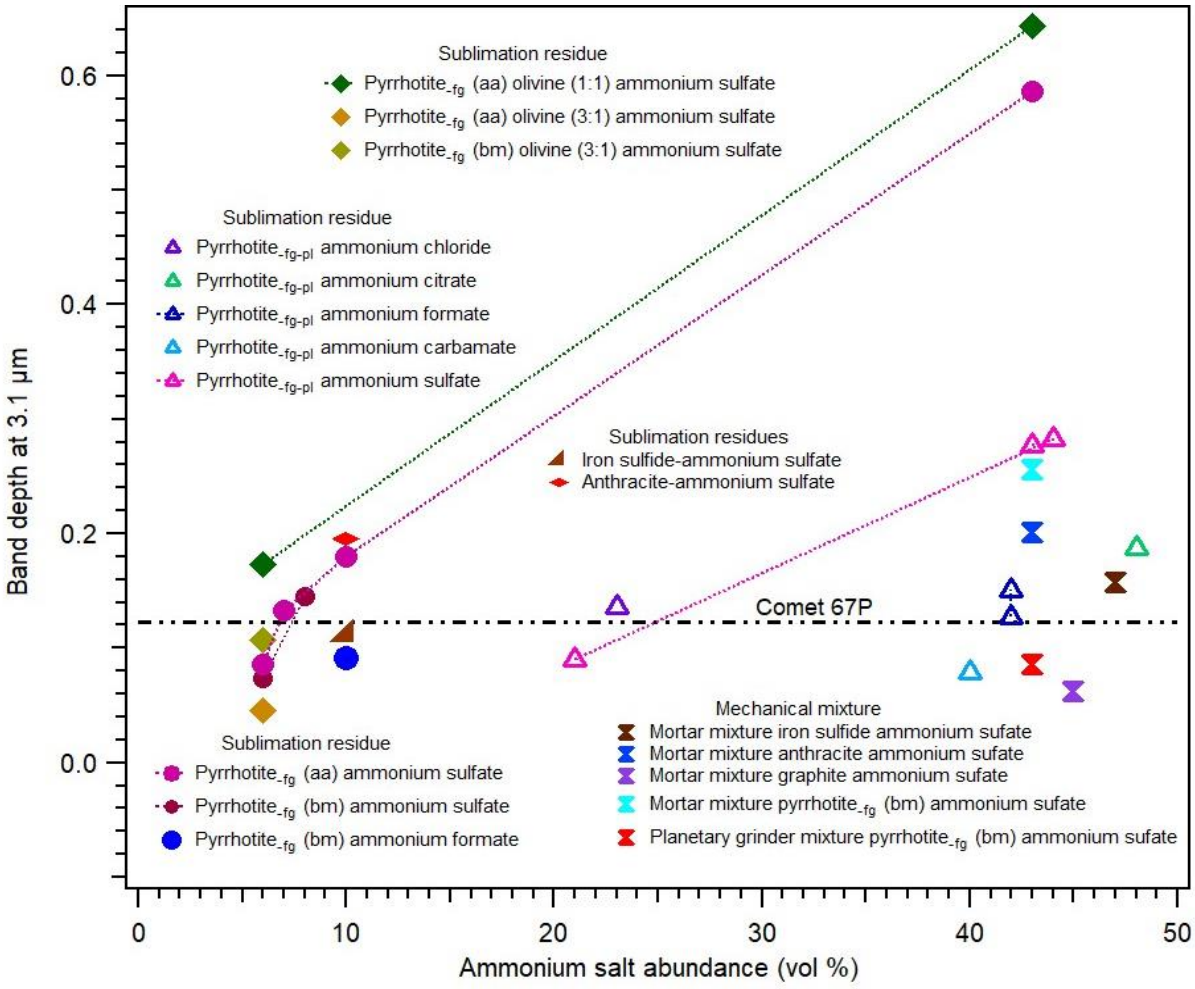

Figure 4.25. Band depth of different sublimation residues and mechanical mixtures versus ammonium abundance (vol %). Pyrrhotite-$_{fg\text{-}pl}$ (contains some platelets) is from Alfa Aesar. Pyrrhotite-$_{fg}$ (*aa*),(*bm*) is from Alfa Aesar and Bijoux Mineral respectively.

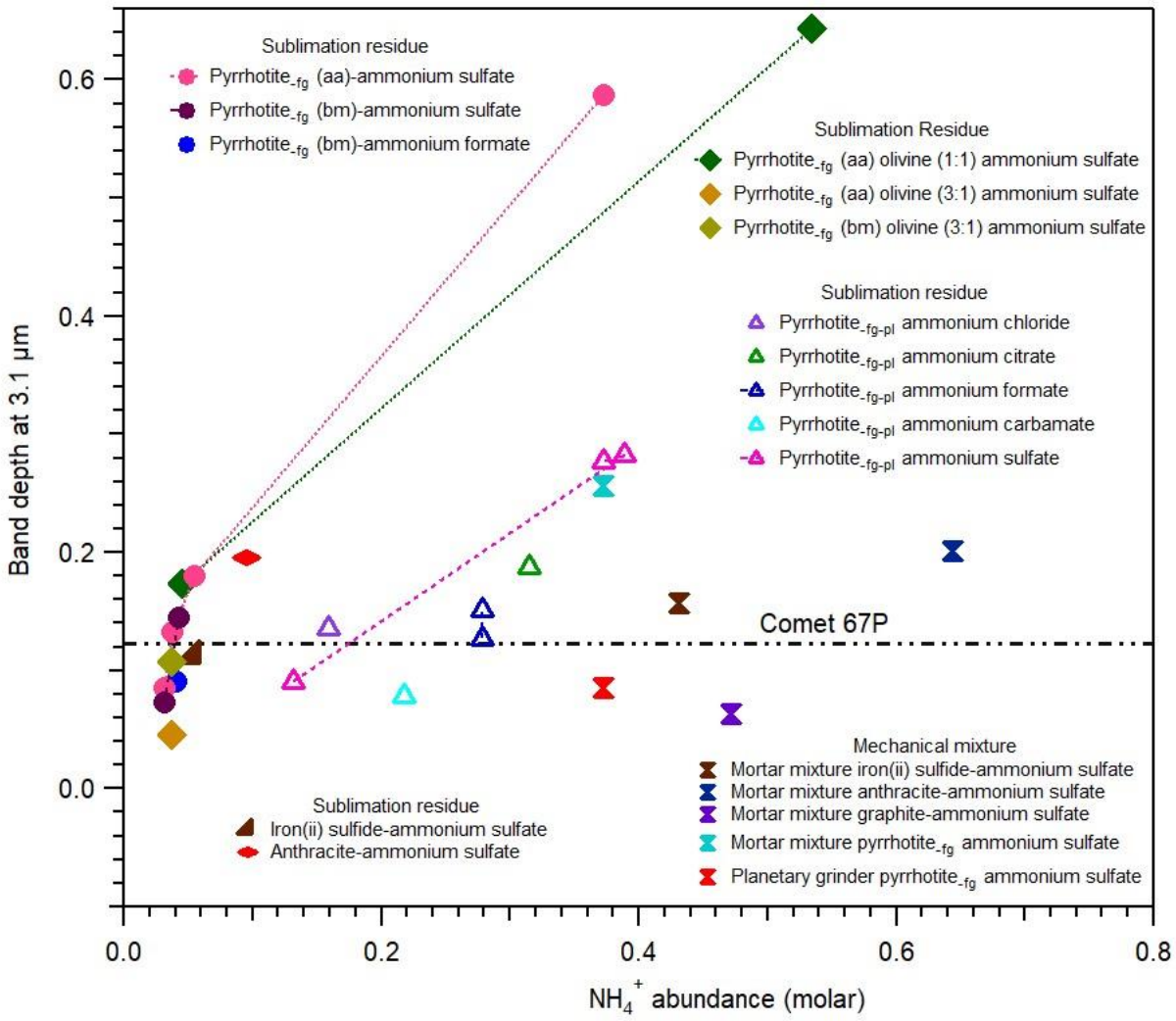

Figure 4.26. Band depth of different sublimation residues and mechanical mixtures plotted against ammonium molar abundance. Pyrrhotite-$_{fg\text{-}pl}$ (contains some platelets) is from Alfa Aesar. Pyrrhotite-$_{fg}$ (*aa*),(*bm*) is from Alfa Aesar and Bijoux Mineral respectively.

4.3. Implication for the analysis of VIRTIS reflectance spectra of comet 67P/CG

First, we summarize the main results obtained from the above experiments:

- The nature of the matrix plays a key role in the control of the reflectance spectra of semi-volatile+refractory mixtures.
- For bright matrices, a deep band in the 3 µm region is obtained even at very low concentration. For a given matrix (grain size and texture do not vary), the band depth linearly correlates with the ammonium abundance .

- For dark matrices, the texture of the sample is a major parameter. In practice, this means that the experimental protocol has a strong implication on the optical properties of the analogs.
- Mixtures produced from the mechanical mixing of previously ground dark refractories and ammonium salts require large ammonium abundances. There is no clear correlation between band depth and ammonium concentration. SEM analysis show that the samples have a broad size distribution, including micrometric grains and above. Hand-mixing provides usually granular mixtures, while grinding with a planetary grinder promotes re-agglomeration, enhancing the abundance of compact clusters.
- Mixtures produced from sublimation experiments are the most suitable for comparison with cometary surfaces. They lead to ultraporous sample and an intimate mixture of semi-volatiles and refractories at a sub-micrometric scale.
- Nevertheless, the quantification of the ammonium abundance remains a tricky issue. The control of the texture on the reflectance spectra remains unclear on the basis of the visual inspection of SEM images. We think that a future plan would be to apply image analysis algorithms for characterizing complex topologies, and techniques operating the sub-micrometric scale for discriminating the semi-volatiles compounds from the refractory matrix.

The interpretation of the VIRTIS/Rosetta spectra is detailed in the following paper, published in the Science journal. We show that ammonium salts mostly account for the presence of the 3.2 µm band, along with aliphatic organics (Raponi et al., 2020). This identification was done on the basis of some of the sublimation experiments presented before.

At the time of writing, the issue of the quantification was unclear and we have been very careful in not over interpreting our results. Finally, the experiments we run between January and June 2019 confirmed the lack of accurate quantification. Nevertheless, our results demonstrate the existence of a new nitrogen reservoir in comets, with strong implications in term of cosmochemistry. Our last experiments also confirm that we are not able to identify the counterions. The recent detection of ammonium salts by the ROSINA instrument (Altwegg et al., 2019) points to the presence of ammonium chloride, which is not detected with our approach. This paradox may be due to the fact we have used simple crystalline ammonium salts, while in the comet we expect they are present as complex mixtures with organics. This certainly has a significant effect on band position and shape. This shows that more complex mixtures should be considered in the future.

RESEARCH ARTICLE SUMMARY

COMETARY SCIENCE

Ammonium salts are a reservoir of nitrogen on a cometary nucleus and possibly on some asteroids

Olivier Poch*, Istiqomah Istiqomah, Eric Quirico, Pierre Beck, Bernard Schmitt, Patrice Theulé, Alexandre Faure, Pierre Hily-Blant, Lydie Bonal, Andrea Raponi, Mauro Ciarniello, Batiste Rousseau, Sandra Potin, Olivier Brissaud, Laurène Flandinet, Gianrico Filacchione, Antoine Pommerol, Nicolas Thomas, David Kappel, Vito Mennella, Lyuba Moroz, Vassilissa Vinogradoff, Gabriele Arnold, Stéphane Erard, Dominique Bockelée-Morvan, Cédric Leyrat, Fabrizio Capaccioni, Maria Cristina De Sanctis, Andrea Longobardo, Francesca Mancarella, Ernesto Palomba, Federico Tosi

INTRODUCTION: Comets and asteroids preserve information on the earliest stages of Solar System formation and on the composition of its building blocks. The nature of their solid material can be investigated by analyzing the sunlight scattered by their surfaces. The nucleus of comet 67P/Churyumov-Gerasimenko (hereafter 67P) was mapped by the Visible and InfraRed Thermal Imaging Spectrometer, Mapping Channel (VIRTIS-M) on the Rosetta spacecraft from 2014 to 2015. The nucleus appeared almost spectrally uniform from 0.4 to 4 μm, characterized by a low reflectance of few percent, a reddish color, and an unidentified broad absorption feature around 3.2 μm, which was ubiquitous throughout the surface. The darkness and the color of comet 67P could be due to a mixture of refractory organic molecules and opaque minerals. Although water ice may contribute to the 3.2-μm absorption, it cannot explain the entire feature.

RATIONALE: Semivolatile compounds of low molecular weight, such as carboxylic (–COOH)–bearing molecules or ammonium (NH_4^+) ions, have been proposed as potential carriers of the 3.2-μm absorption feature. To test these hypotheses, we performed laboratory experiments to measure the reflectance spectra of these compounds mixed in a porous matrix of submicrometric opaque mineral grains, under simulated comet-like conditions (170 to 200 K, $<10^{-5}$ mbar).

RESULTS: The 3.2-μm absorption feature is consistent with ammonium salts mixed with the dark cometary surface material. We attribute additional absorption features to carbonaceous compounds and traces of water ice. Several ammonium salts can match the absorption feature equally well: ammonium formate, ammonium sulfate, or ammonium citrate. A mixture of different ammonium salts could be present.

ON OUR WEBSITE

Read the full article at http://dx.doi.org/10.1126/science.aaw7462

Ammonium salts at the surface of comet 67P could have been synthesized through acid-base reactions of ammonia (NH_3) with the corresponding acid molecules in solid ices. That reaction may have occurred in the interstellar medium, in the protoplanetary disk, or during the sublimation of the ices in the cometary nucleus.

The depth of the band suggests that the cometary surface contains an upper limit of ~40 weight % (wt %) of ammonium salts, but the exact concentration remains unknown. If the amount of ammonium salts is higher than ~5 wt %, they constitute the dominant reservoir of nitrogen in the comet, containing more nitrogen than the refractory organic matter and the volatile species, such as NH_3 and N_2. Consequently, the abundance of nitrogen in this comet is closer to that of the Sun than previously thought.

CONCLUSION: Ammonium salts may dominate the reservoir of nitrogen in comets. Their presence in cometary dust may explain increases of gas-phase NH_3 and HCN observed in some comets when close to the Sun, which could be caused by the thermal dissociation of ammonium salts. Several asteroids in the Main Belt, Jupiter's Trojan asteroids, and its small moon Himalia have similar spectra to that of comet 67P, with a broad spectral absorption feature at 3.1 to 3.2 μm, which we suggest could also be due to ammonium salts. The dwarf planet Ceres has ammoniated phyllosilicates on its surface, which may have formed from ammonium ions inherited from outer Solar System objects with compositions similar to that of comet 67P. The presence of these salts on comet 67P, and possibly on other primitive Solar System bodies, suggests a compositional link between asteroids, comets, and the protosolar nebula. ■

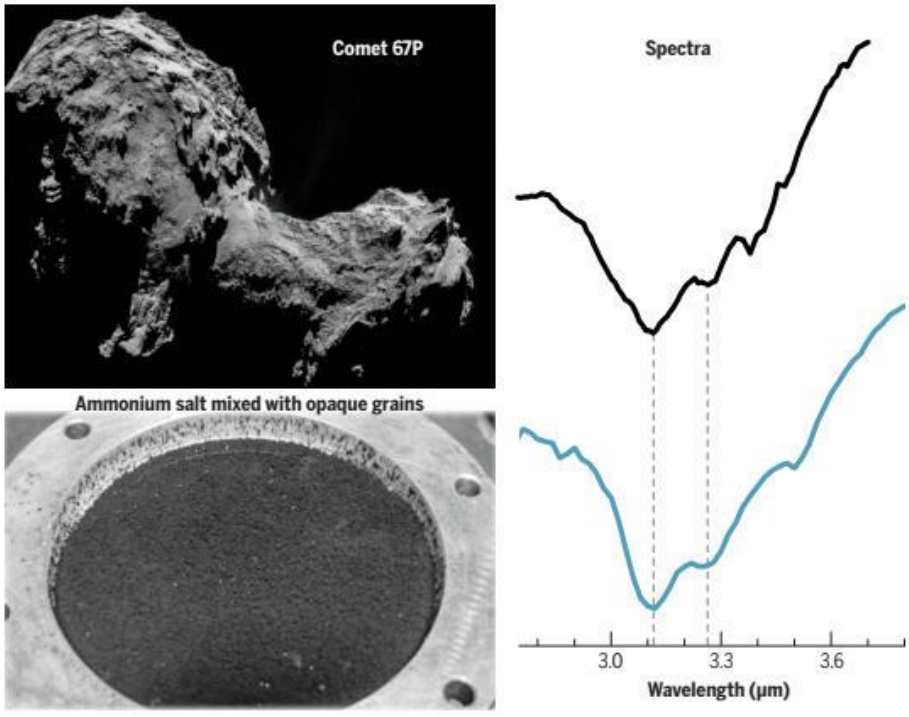

Comparison of ammonium formate spectrum with the average spectrum of comet 67P. The average reflectance spectrum of comet 67P (black line) and the spectrum of a mixture of ammonium formate (NH_4^+ $HCOO^-$) with opaque grains measured in the laboratory under comet-like conditions (blue line). Also shown are views of the 4-km-diameter comet nucleus (Credit: ESA/Rosetta/NAVCAM–CC BY-SA IGO 3.0; http://creativecommons.org/licenses/by-sa/3.0/igo) and the 48-mm-diameter laboratory sample.

The list of author affiliations is available in the full article online.
*Corresponding author. Email: olivier.poch@univ-grenoble-alpes.fr
Cite this article as O. Poch *et al.*, *Science* **367**, eaaw7462 (2020); DOI: 10.1126/science.aaw7462

RESEARCH ARTICLE

COMETARY SCIENCE

Ammonium salts are a reservoir of nitrogen on a cometary nucleus and possibly on some asteroids

Olivier Poch[1]*, Istiqomah Istiqomah[1], Eric Quirico[1], Pierre Beck[1,2], Bernard Schmitt[1], Patrice Theulé[3], Alexandre Faure[1], Pierre Hily-Blant[1], Lydie Bonal[1], Andrea Raponi[4], Mauro Ciarniello[4], Batiste Rousseau[1]†, Sandra Potin[1], Olivier Brissaud[1], Laurène Flandinet[1], Gianrico Filacchione[4], Antoine Pommerol[5], Nicolas Thomas[5], David Kappel[6,7], Vito Mennella[8], Lyuba Moroz[7], Vassilissa Vinogradoff[9], Gabriele Arnold[7], Stéphane Erard[10], Dominique Bockelée-Morvan[10], Cédric Leyrat[10], Fabrizio Capaccioni[4], Maria Cristina De Sanctis[4], Andrea Longobardo[4,11], Francesca Mancarella[12], Ernesto Palomba[4], Federico Tosi[4]

The measured nitrogen-to-carbon ratio in comets is lower than for the Sun, a discrepancy which could be alleviated if there is an unknown reservoir of nitrogen in comets. The nucleus of comet 67P/Churyumov-Gerasimenko exhibits an unidentified broad spectral reflectance feature around 3.2 micrometers, which is ubiquitous across its surface. On the basis of laboratory experiments, we attribute this absorption band to ammonium salts mixed with dust on the surface. The depth of the band indicates that semivolatile ammonium salts are a substantial reservoir of nitrogen in the comet, potentially dominating over refractory organic matter and more volatile species. Similar absorption features appear in the spectra of some asteroids, implying a compositional link between asteroids, comets, and the parent interstellar cloud.

The composition of comets and asteroids can be investigated from the light scattered by their surfaces. For objects of which the visible to near-infrared wavelength range shows no, or only weak, spectral features, analysis of the 3-μm region (between roughly 2.4 and 3.6 μm) can be used to investigate volatile and organic compounds present on their surfaces (*1*). The Visible and InfraRed Thermal Imaging Spectrometer, Mapping Channel (VIRTIS-M) instrument (*2*) on the Rosetta spacecraft observed the nucleus of comet 67P/Churyumov-Gerasimenko (hereafter 67P) in the spectral range of 0.2 to 5.1 μm (*3*). The surface imaged by VIRTIS-M appears almost spectrally uniform (*4*), characterized by a very low reflectance [geometric albedo of 6% at 0.55 μm (*5*)], positive (red) visible and infrared spectral slopes, and a broad absorption feature from 2.8 to 3.6 μm, centered at 3.2 μm (*3*, *4*).

This absorption band, which has not been detected on other comets, is observed on all types of surface terrains and was persistently observed from August 2014 when comet 67P was 3.6 astronomical units (au) from the Sun and cometary activity was weak until just before the comet reached its closest point to the Sun and experienced maximum activity in May 2015 at 1.7 au, for as long as the VIRTIS-M infrared channel could record measurements (*6*). Analyses of the VIRTIS-M reflectance spectra ascribed the darkness and slope to a refractory polyaromatic carbonaceous component mixed with opaque minerals (anhydrous Fe-sulfides and Fe–Ni alloys), but the carrier of the 3.2-μm feature remained unknown (*3*). Water ice contributes to this absorption on some parts of the surface (*6*–*9*), causing a broadening and deepening of the absorption feature from 2.7 to 3.1 μm, but cannot explain the entire feature (*3*, *10*). Except in specific ice-rich areas, the surface of the comet nucleus is uniform in composition, with a predominance of non-ice materials (*9*). Semivolatile materials of low molecular weight have been proposed as carriers of the 3.2-μm feature, with carboxylic (–COOH)–bearing molecules or NH_4^+ ions being the most plausible candidates (*11*). However, a lack of reference spectral data for these compounds has prevented a firm attribution of the feature.

Spectral identification of ammonium salts

We conducted laboratory experiments to produce analogs of cometary surface material and measured their reflectance spectra under comet-like conditions (low temperature and high vacuum) (*12*). Cometary dust is known to consist of aggregated submicrometer-sized grains (*13*), and opaque iron sulfides are probable contributors to the low albedo of comet nuclei (*11*, *14*). We therefore used submicrometer-sized grains of pyrrhotite ($Fe_{1-x}S$, with $0 < x < 0.2$) mixed with different candidate compounds (carboxylic acid, ammonium salts) to test for the 3.2-μm feature. The pyrrhotite grains and candidate compounds were mixed in liquid water then frozen to obtain ice-dust particles (*12*). By sublimating these particles in a thermal vacuum chamber, we formed very porous mixtures made of submicrometer-sized grains (hereafter "sublimate residues") (figs. S1 and S2). This is representative of the process we expect at the surface of a comet nucleus, and the resulting textures strongly influenced the band depths of the reflectance spectra (*15*), which we attempted to reproduce to allow quantification of the components of the cometary surface (*12*).

Shown in Fig. 1A is the reflectance spectrum of the sublimate residue made of pyrrhotite grains mixed with ≲17 weight % (wt %) [≲43 volume % (vol %)] ammonium formate ($NH_4^+ HCOO^-$). Also shown is an average spectrum of 67P from a combination of VIRTIS-M observations taken between August to September 2014, when Rosetta was 50 to 350 km from the nucleus and 67P was 3.6 to 3.3 AU from the Sun (*12*). The position of the cometary absorption band, its asymmetric shape, and the minima at 3.1 and 3.3 μm all match the absorption bands owing to the N–H vibration modes of NH_4^+ in ammonium formate (Fig. 1A and fig. S5). The spectral resolving power $RP \equiv \lambda/\Delta\lambda_{resolution}$ (where λ is the wavelength and $\Delta\lambda_{resolution}$ is the spectral resolution) at 3.5 μm is $RP = 90$ for the laboratory spectrum and 233 for the VIRTIS spectrum. The residual cometary spectrum, obtained by dividing the comet spectrum by the ammonium salt spectrum, is flat from 3.05 to 3.35 μm (Fig. 1A), but features in the range of 3.35 to 3.60 μm indicate the additional presence of C–H stretching modes in carbonaceous compounds (*10*). The proximity of these C–H modes, the limited spectral resolution, and the limited spectral sampling impede a search for a weaker N–H mode of ammonium salts centered around 3.50 μm (fig. S5 and table S2). Other differences between these spectra are due to the contribution of additional compounds (possibly traces of water ice around 3.0 μm)

[1]Université Grenoble Alpes, Centre National de la Recherche Scientifique (CNRS), Institut de Planétologie et d'Astrophysique de Grenoble (IPAG), 38000 Grenoble, France. [2]Institut Universitaire de France (IUF), Paris, France. [3]Aix-Marseille Université, CNRS, Centre National d'Etudes Spatiales (CNES), Laboratoire d'Astrophysique de Marseille (LAM), Marseille, France. [4]Istituto di Astrofisica e Planetologia Spaziali (IAPS), Istituto Nazionale di Astrofisica (INAF), 00133 Rome, Italy. [5]Physikalisches Institut, Sidlerstrasse 5, University of Bern, CH-3012 Bern, Switzerland. [6]Institute of Physics and Astronomy, University of Potsdam, 14476 Potsdam, Germany. [7]Institute for Planetary Research, German Aerospace Center (DLR), 12489 Berlin, Germany. [8]Istituto Nazionale di Astrofisica (INAF)–Osservatorio Astronomico di Capodimonte, Napoli, Italy. [9]CNRS, Aix-Marseille Université, Laboratoire Physique des Interactions Ioniques et Moléculaires (PIIM), Unité Mixte de Recherche (UMR) CNRS 7345, 13397 Marseille, France. [10]Laboratoire d'Etudes Spatiales et d'Instrumentation en Astrophysique (LESIA), Observatoire de Paris, Université Paris Sciences et Lettres (PSL), CNRS, Sorbonne Université, Université de Paris, 92195 Meudon, France. [11]Dipartimento di Scienze e Tecnologie (DIST), Università Parthenope, 80143 Napoli, Italy. [12]Dipartimento di Matematica e Fisica "E. De Giorgi," Università del Salento, Lecce, Italy.
*Corresponding author. Email: olivier.poch@univ-grenoble-alpes.fr
†Present address: Istituto di Astrofisica e Planetologia Spaziali (IAPS), Istituto Nazionale di Astrofisica (INAF), 00133 Rome, Italy.

and/or differing properties of the salts present on the cometary surface (such as concentration, mixing, and counter-ions). We investigated other candidate compounds—fine water ice grains, carboxylic acid, or hydrated minerals—but these do not match the 3.2-μm feature (Fig. 1B). The laboratory spectra of five ammonium salts we investigated are shown in Fig. 2. Ammonium formate, ammonium sulfate, or ammonium citrate all reproduce the 3.1- and 3.3-μm absorption bands observed on the comet. For ammonium carbamate and ammonium chloride, the corresponding bands are shifted to longer wavelengths or have different spectral shapes (Fig. 2).

The similarity of band shapes and positions leads us to conclude that NH_4^+ in ammonium salts is the main species responsible for the

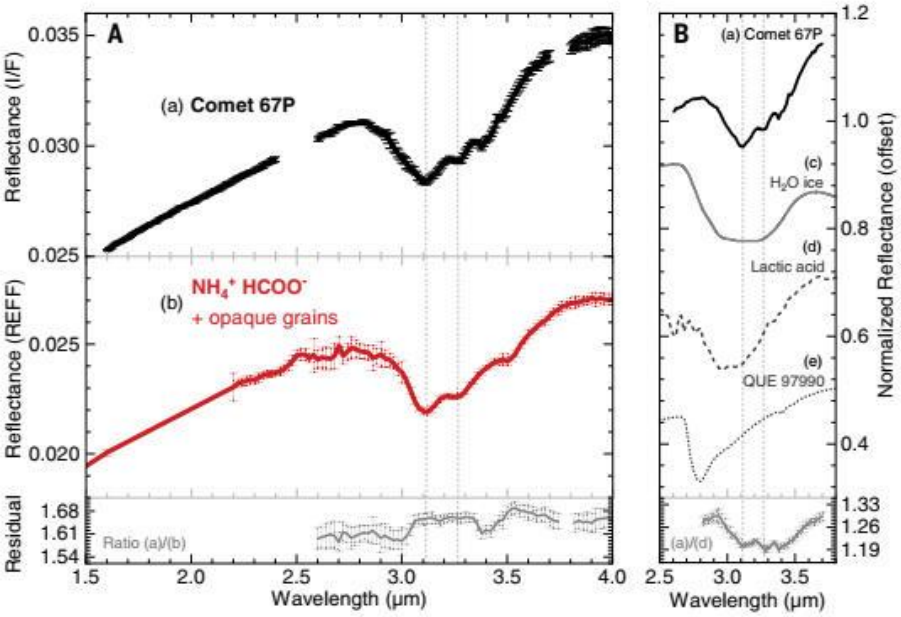

Fig. 1. Comparison of NH_4^+ $HCOO^-$ spectrum with the average spectrum of comet 67P. (**A**) The average reflectance spectrum of comet 67P in the 3.0-μm region [(a), black line; the vertical scale is given in radiance factor I/F] and the spectrum of a sublimate residue containing ≤17 wt % ammonium formate mixed with ≥83 wt % pyrrhotite grains at 170 to 200 K [(b), red line; the vertical scale is given in reflectance factor REFF]. The same spectra overlain on each other is shown in fig. S5. Gaps in the comet 67P spectrum are due to the instrument's diffraction order sorting filters. Both spectra have the same shape and minima at 3.1 and 3.3 μm (dashed gray vertical lines). (**B**) Reflectance spectra (normalized at 2.5 μm) of other compounds that do not match the comet 67P spectrum: (c) a model spectrum of 1-μm-diameter pure water ice grains (solid line) [Hapke model (*60*), using optical constants at 145 K (*61*), spectrum normalized, scaled by a factor of 0.14, and offset by −0.08]; (d) a measured spectrum of a sublimate residue containing ≤17 wt % lactic acid mixed with pyrrhotite grains at 170 to 200 K (dashed line, offset by −0.35) (*12*); and (e) spectrum of the primitive carbonaceous chondrite meteorite QUE 97990, which is rich in hydrous silicates, measured under 400 to 475 K and high vacuum (dotted line, offset by −0.55) (*62*). Between 2.5 and 2.8 μm, the spectra of sublimate residues are affected by measurement artifacts because of the presence of water vapor in the optical path. Residual spectra, calculated by dividing the comet 67P spectrum (a) by the experimental spectrum (b) or (d), are shown at the bottom of (A) and (B). Error bars indicate the ±1σ uncertainties.

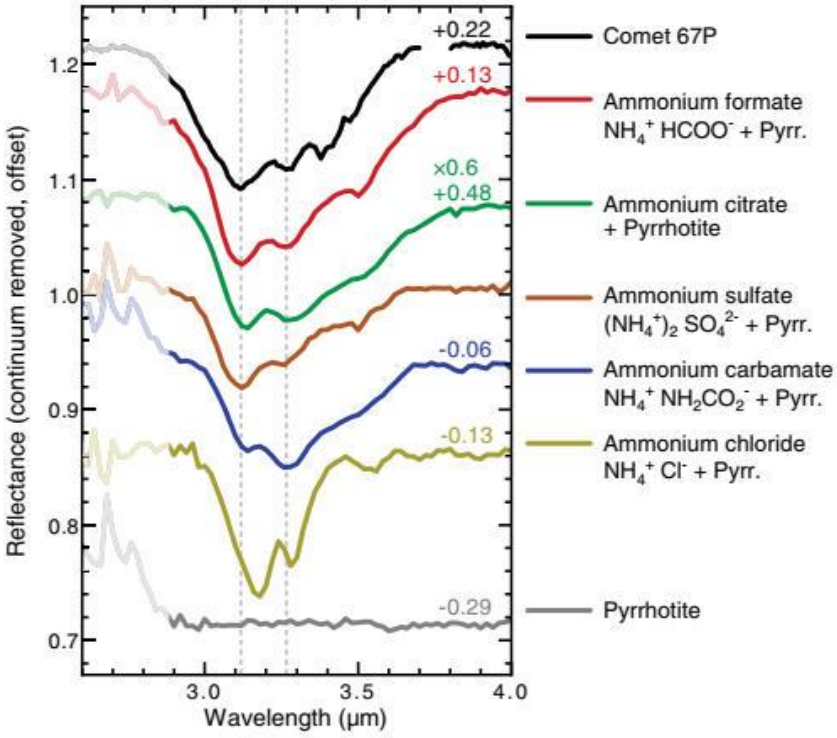

Fig. 2. Reflectance spectra of several ammonium salts. Continuum-removed reflectance spectra of sublimate residues made of ammonium salts (colored lines) mixed with pyrrhotite grains (gray line) measured in high vacuum at 170 to 200 K, compared with the observed average spectrum of comet 67P (black line). Ammonium formate, citrate, and sulfate are the closest matches to the absorption features in comet 67P. We attribute the other absorption features in the comet spectrum at 3.35 to 3.6 μm to C–H stretching modes of organic compounds (*10*). Between 2.6 and 2.8 μm, the laboratory spectra are affected by measurement artifacts because of the presence of water vapor in the optical path. The mass fractions of the salts mixed with pyrrhotite are ≤9 wt % for ammonium sulfate and chloride, ≤17 wt % for ammonium formate and carbamate, and ≤23 wt % for ammonium citrate (the latter has been scaled by a factor of 0.6 for display). These spectra are shown in fig. S6 with uncertainties and before continuum removal.

3.2-μm feature. The counter-ion (in this case, the anion) is not fully constrained. The identification of HCOOH by the Rosetta Orbiter Spectrometer for Ion and Neutral Analysis (ROSINA) mass spectrometer (*16*) and the spectrum of ammonium formate (NH_4^+ $HCOO^-$) in Fig. 2 make it our favored candidate.

Origins of ammonium salts

There are several potential pathways for the synthesis of ammonium salts present at the surface of comet 67P. Ammonia (NH_3) has a high proton affinity, allowing it to transform easily into ammonium (NH_4^+), either in the gas (*17*) or in the solid phase. Ammonium and potential counter-ions (such as $HCOO^-$, CN^-, and OCN^-) may be produced by acid-base reactions of ammonia (NH_3) with the corresponding acids (such as HCOOH, HCN, and HNCO) or by nucleophilic addition of NH_3 with CO_2 or H_2CO, even at cryogenic temperatures in the solid phase (*18*, *19*). These reactions have low activation energies and do not require an external source of photons, electrons, or cosmic rays (*18*). Some ions (such as OCN^- and $HCOO^-$) can be produced at 10 to 14 K, but most of the ions we considered (such as NH_2COO^- and CN^-) are produced at higher temperatures (*19*–*21*). Astronomical observations of interstellar ices have likely identified OCN^- (*22*–*25*) and possibly detected NH_4^+ (*25*–*28*). Ammonium salts can be formed upon sublimation of water ice containing NH_4^+ and counter ions (*19*, *29*). It is possible that the NH_4^+ detected on comet 67P could be inherited from interstellar ices. In that case, the ammonium salts would be produced during further thermal processing of the ices, either in the protoplanetary disk (*25*) or during the sublimation of the ices in the cometary nucleus, through a process similar to the one simulated in our laboratory experiments. The production of ammonium salts by means of a gas phase reaction under astrophysical conditions has not been reported in the literature. Solid-state reactions appear more likely because proton transfer or nucleophilic addition are highly facilitated by a dust surface and a solvent such as ice (*30*, *31*).

Comparison with other small bodies

The 3.2-μm absorption feature of comet 67P shares similarities with the 3-μm features observed on several asteroids, including the position and width of the band from 2.9 to 3.6 μm and the reflectance minimum at 3.1 to 3.2 μm (Fig. 3). However, the bands observed on most of these asteroids are distinct from the one of comet 67P, having a different shape and no secondary minimum at 3.3 μm (Fig. 3). Nevertheless, these spectra are compatible with the presence of ammonium salts, if the spectral differences are due to the environmental conditions at the surface of these small bodies (fig. S7). The spectra of asteroids 24 Themis and 52 Europa are representative of objects found in the asteroid Main Belt (*1*, *32*) and in orbit around Jupiter, such as the irregular moon Himalia (*33*). The dwarf planet 1 Ceres has ammonium-bearing minerals on its surface, with absorption features at 2.72 and 3.06 μm (Fig. 3), mostly in the form of phyllosilicates but with smaller amounts of salts (*34*). Our identification of ammoniated salts on a comet supports the hypothesis that materials on Ceres may have originated from the outer Solar System (*34*).

Volatility of ammonium salts

There is weak evidence for ammonium salts in meteorites, micrometeorites, and interplanetary dust particles (IDPs) (*35*, *36*). Because these salts are more volatile than most refractory material, they might not be preserved during atmospheric entry of small particles and/or during long periods of time under terrestrial environmental conditions (*35*). Ammonium salts contained in grains ejected from cometary nuclei may react and/or sublimate when heated by the Sun and act as distributed sources of gases in comae, the envelopes of gas and dust around cometary nuclei (*37*). This could explain observed increases of NH_3 and HCN when some comets reach short heliocentric distances (<1 au from the Sun), such as comet C/2012 S1 (ISON), which experienced multiple outbursts as it disrupted inside ~0.8 au (*38*, *39*). On comet 67P, the decomposition of ammonium formate (NH_4^+ $HCOO^-$) could produce formamide (NH_2CHO), which has been detected by the ROSINA instrument

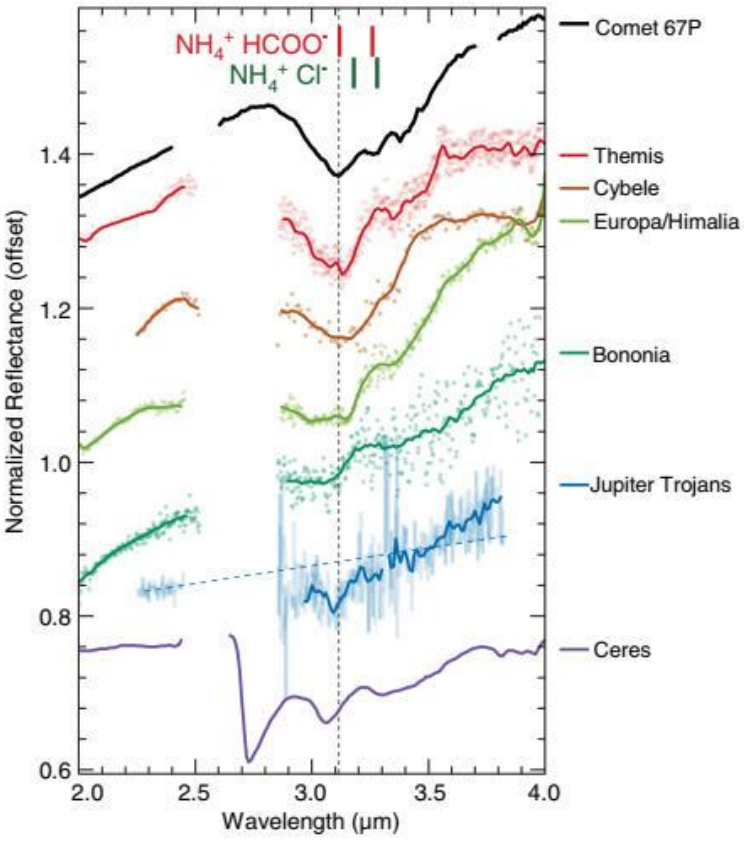

Fig. 3. The spectrum of comet 67P compared with other Solar System bodies. Reflectance spectra normalized at 2.9 μm are of comet 67P (offset by +0.45); the Main Belt asteroids 24 Themis (offset by +0.31) (*63*), 65 Cybele (offset by +0.19) (*64*), 52 Europa (*32*), and 361 Bononia (offset by +0.07) (*32*); the average spectrum of six Jupiter Trojan asteroids [(*65*), their "less red" group] (divided by 3 and offset by +0.49); and the average spectrum of 1 Ceres (scaled by a factor of 0.5, and offset by +0.19) (*34*). The spectrum of Jupiter's irregular moon Himalia is almost indistinguishable from 52 Europa (*33*). For each spectrum, the dots are the observational data (plotted directly for Europa and Bononia, digitized from the literature for the other objects), and the solid lines are running average spectra. The blue dashed line shows the averaged extrapolation of the six Jupiter Trojan's *K*-band spectra (*66*). The gray dashed line shows the position of the band at 3.11 μm on comet 67P spectrum. The red and green vertical marks indicate the positions of the maxima of absorption of ammonium formate and ammonium chloride respectively, shown in Fig. 2. Absorption features around 3.1 to 3.2 μm on some of these bodies are similar to the ammonium salt features on comet 67P. Ceres exhibits different features, which are due to ammoniated phyllosilicates (*34*).

and is compatible with the mass spectrum measured by the Cometary Sampling and Composition (COSAC) experiment on Rosetta's Philae lander (*40*–*42*). The volatility of an ammonium salt strongly depends on the anion; for example, at a pressure of 1 atm, ammonium formate decays at 389 K, ammonium sulfate at 553 K, and ammonium chloride at 611 K (*43*). Under simulated astrophysical conditions (10^{-8} mbar), the sublimation temperatures of ammonium salts are 160 to 180 K for ammonium cyanide (NH_4^+ CN^-) (*44*), 200 to 230 K for ammonium formate (NH_4^+ $HCOO^-$) (*30*, *45*), and 230 to 260 K for ammonium carbamate (NH_4^+ NH_2COO^-) (*46*). Because of these differences of volatility, the composition of ammonium salts observed on comet or asteroid surfaces, and the gases produced by their decomposition, may change with the heliocentric distance.

Nitrogen budget of comet 67P

Rosetta's Cometary Secondary Ion Mass Analyzer (COSIMA) collected coma dust grains 10 to 30 km from comet 67P's nucleus and measured their composition (*47*). Ammoniated salts were not detected, possibly because any semivolatile compounds present in the dust grains would have sublimated during the multiple-day-long pre-analysis storage of the particles at 283 K (*47*). If ammonium salts had been lost from the dust grains analyzed by COSIMA, their measured nitrogen-to-carbon ratio (N/C) would be a lower limit, missing the contribution of the semivolatile nitrogen-bearing salts. COSIMA measured an average N/C of 0.035 ± 0.011, which is similar to the ratio found in the insoluble organic matter extracted from carbonaceous chondrite meteorites and in most micrometeorites and interplanetary dust particles (*47*) but lower than the solar N/C value of 0.29 ± 0.12 (*48*). Similar depletions in nitrogen compared with the Sun have been found in the refractory dust and gas phases of other comets (*49*–*51*).

We propose that ammonium salts may constitute a substantial nitrogen reservoir in comet 67P and possibly other comets and small bodies. The 3.2-μm band observed in the spectrum of comet 67P is 5 to 20% less deep than the band of ammonium formate in our sublimate residues (fig. S6) (*12*). Assuming that the physical parameters that control the light scattering (such as mixing modes and grain sizes) of the sublimate residues are similar to that of the cometary surface, we derived an upper limit of the volumetric abundance of salts in the dark surface material of the comet of ~40 vol %. The dark surface material is a mixture of ~45 wt % organic (~1 g/cm^3) and ~55 wt % mineral (~3.4 g/cm^3) components, estimated from COSIMA measurements (*52*). Taking into account this composition, we derived an upper limit of the mass fraction of ammonium salts mixed with the dust of ~40 wt %, but we cannot determine the surface abundance of ammonium salts on the comet exactly (*12*). If the mass fraction of ammonium formate (NH_4^+ $HCOO^-$) is 5 wt % in the cometary dust, the total atomic nitrogen in the comet is distributed as ~47% N in ammonium salts, ~52% N in refractory organic matter, and ~1% N in volatiles (Fig. 4); the whole comet would then have a N/C ratio of about 0.06 (Fig. 5). If there is a mixture of

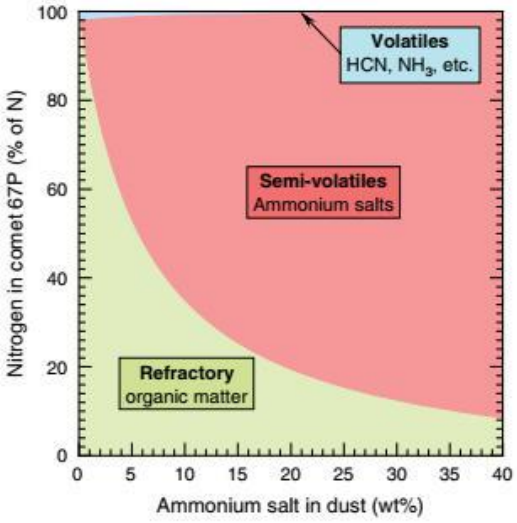

Fig. 4. Reservoirs of nitrogen in comet 67P. Nitrogen in comet 67P is present in the refractory organic matter, in semivolatile ammonium salts, and in volatile molecules. This diagram shows how all the nitrogen atoms in comet 67P are distributed among these three reservoirs, depending on the assumed mass fraction of ammonium salt in the dust (composed of minerals, refractory organic matter, and salts), calculated according to observations from several Rosetta instruments (*12*). If the cometary dust contains more than few percent of ammonium salts, then they form a substantial reservoir of nitrogen in comet 67P.

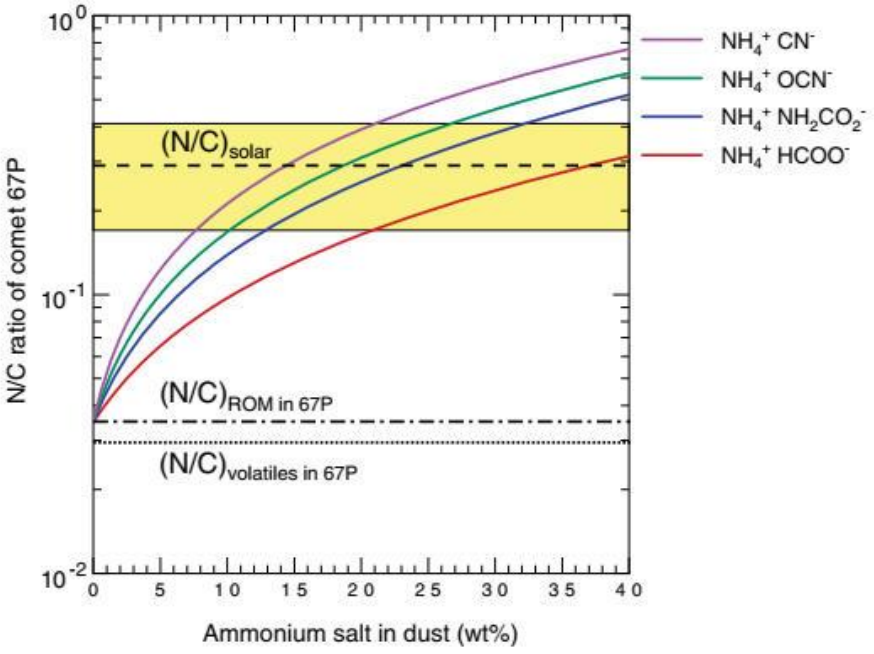

Fig. 5. Nitrogen-to-carbon ratio in comet 67P. The N/C ratio in comet 67P compared with the solar value (dashed line and yellow area indicating the ±1σ uncertainty) (*48*). The colored lines show the contributions of nitrogen in plausible ammonium salts as a function of the mixing with dust (*12*), which are added to the nitrogen in the refractory organic matter (ROM) (*47*) and in volatile species (dashed-dotted and dotted lines, respectively) (*16*). Depending on the counter-ion, the presence of 10 to 30 wt % of ammonium salts in the dust would raise the N/C ratio of comet 67P to be consistent with the solar value.

several ammonium salts, then NH_4^+ would have a range of counter-ions, some of them N-bearing, which would raise the N/C ratio. Shown in Fig. 5 is how the inferred N/C ratio of the comet increases with the assumed concentration of ammonium salts in the dust and depends on the nature of the counter-ions of NH_4^+.

Implications

The identification of ammonium salts on comet 67P shows that this comet, and possibly others, could have a N/C ratio higher than previously thought. If ammonium salts are a substantial repository of nitrogen, assessment of their $^{14}N/^{15}N$ isotopic ratio and comparing it with the proto-solar ratio could inform models of the incorporation and evolution of nitrogen in the early Solar System (*53*). If ammonium salts were also present in sufficient abundance in planetesimals during the early Solar System, they would have provided a solid form of nitrogen closer to the Sun than N_2 and NH_3 ices and therefore available for planetary accretion (*54*). Abundant ammonium salts would have lowered the melting point of water ice in the subsurface of icy bodies (*55*). When mixed in liquid water, ammonium salts are known to participate in potentially prebiotic reactions, such as the formation of pyrimidine and purine nucleobases (*56*), the production of amino acids (*57*), the phosphorylation of nucleosides (*58*), or the formation of sugar molecules (*59*).

REFERENCES AND NOTES

1. A. S. Rivkin *et al.*, Astronomical observations of volatiles on asteroids, in *Asteroids IV*, P. Michel, F. E. DeMeo, W. F. Bottke, Eds. (Univ. Arizona Press, 2015), pp. 65–87.
2. A. Coradini *et al.*, Virtis: An imaging spectrometer for the Rosetta mission. *Space Sci. Rev.* **128**, 529–559 (2007). doi: 10.1007/s11214-006-9127-5
3. F. Capaccioni *et al.*, Cometary science. The organic-rich surface of comet 67P/Churyumov-Gerasimenko as seen by VIRTIS/Rosetta. *Science* **347**, aaa0628 (2015). doi: 10.1126/science.aaa0628; pmid: 25613895
4. G. Filacchione *et al.*, The global surface composition of 67P/CG nucleus by Rosetta/VIRTIS. (I) Prelanding mission phase. *Icarus* **274**, 334–349 (2016). doi: 10.1016/j.icarus.2016.02.055
5. M. Ciarniello *et al.*, Photometric properties of comet 67P/Churyumov-Gerasimenko from VIRTIS-M onboard Rosetta. *Astron. Astrophys.* **583**, A31 (2015). doi: 10.1051/0004-6361/201526307
6. M. Ciarniello *et al.*, The global surface composition of 67P/Churyumov-Gerasimenko nucleus by Rosetta/VIRTIS. II) Diurnal and seasonal variability. *Mon. Not. R. Astron. Soc.* **462**, S443–S458 (2016). doi: 10.1093/mnras/stw3177
7. M. C. De Sanctis *et al.*, The diurnal cycle of water ice on comet 67P/Churyumov-Gerasimenko. *Nature* **525**, 500–503 (2015). doi: 10.1038/nature14869; pmid: 26399830
8. G. Filacchione *et al.*, Exposed water ice on the nucleus of comet 67P/Churyumov-Gerasimenko. *Nature* **529**, 368–372 (2016). doi: 10.1038/nature16190; pmid: 26760209
9. G. Filacchione *et al.*, Comet 67P/CG nucleus composition and comparison to other comets. *Space Sci. Rev.* **215**, 19 (2019). doi: 10.1007/s11214-019-0580-3
10. A. Raponi *et al.*, Infrared detection of aliphatic organics on a cometary nucleus. *Nature Astronomy*. (2020). doi: 10.1038/s41550-019-0992-8
11. E. Quirico *et al.*, Refractory and semi-volatile organics at the surface of comet 67P/Churyumov-Gerasimenko: Insights from the VIRTIS/Rosetta imaging spectrometer. *Icarus* **272**, 32–47 (2016). doi: 10.1016/j.icarus.2016.02.028
12. Materials and methods are available as supplementary materials.
13. A.-C. Levasseur-Regourd *et al.*, Cometary dust. *Space Sci. Rev.* **214**, 64 (2018). doi: 10.1007/s11214-018-0496-3
14. B. Rousseau *et al.*, Laboratory simulations of the Vis-NIR spectra of comet 67P using sub-µm sized cosmochemical analogues. *Icarus* **306**, 306–318 (2018). doi: 10.1016/j.icarus.2017.10.015
15. O. Poch *et al.*, Sublimation of water ice mixed with silicates and tholins: Evolution of surface texture and reflectance spectra, with implications for comets. *Icarus* **267**, 154–173 (2016). doi: 10.1016/j.icarus.2015.12.017
16. L. Le Roy *et al.*, Inventory of the volatiles on comet 67P/Churyumov-Gerasimenko from Rosetta/ROSINA. *Astron. Astrophys.* **583**, A1 (2015). doi: 10.1051/0004-6361/201526450
17. E. Carrasco, I. Tanarro, V. J. Herrero, J. Cernicharo, Proton transfer chains in cold plasmas of H_2 with small amounts of N_2. The prevalence of $NH4^+$. *Phys. Chem. Chem. Phys.* **15**, 1699–1706 (2013). doi: 10.1039/C2CP43438E; pmid: 23247609
18. P. Theulé *et al.*, Thermal reactions in interstellar ice: A step towards molecular complexity in the interstellar medium. *Adv. Space Res.* **52**, 1567–1579 (2013). doi: 10.1016/j.asr.2013.06.034
19. O. Gálvez, B. Maté, V. J. Herrero, R. Escribano, Ammonium and formate ions in interstellar ice analogs. *Astrophys. J.* **724**, 539–545 (2010). doi: 10.1088/0004-637X/724/1/539
20. W. A. Schutte *et al.*, Weak ice absorption features at 7.24 and 7.41 µm in the spectrum of the obscured young stellar object W 33A. *Astron. Astrophys.* **343**, 966–976 (1999).
21. S. Raunier, T. Chiavassa, F. Marinelli, A. Allouche, J. P. Aycard, Reactivity of HNCO with NH3 at low temperature monitored by FTIR spectroscopy: Formation of $NH4^+OCN^-$. *Chem. Phys. Lett.* **368**, 594–600 (2003). doi: 10.1016/S0009-2614(02)01919-X
22. K. Demyk *et al.*, Laboratory identification of the 4.62µm solid state absorption band in the ISO-SWS spectrum of RAFGL 7009S. *Astron. Astrophys.* **339**, 553–560 (1998).
23. F. A. van Broekhuizen, K. M. Pontoppidan, H. J. Fraser, E. F. van Dishoeck, A 3–5 µm VLT spectroscopic survey of embedded young low mass stars II: Solid OCN-. *Astron. Astrophys.* **441**, 249–260 (2005). doi: 10.1051/0004-6361:20041711
24. K. M. Pontoppidan *et al.*, A µm VLT spectroscopic survey of embedded young low mass stars I–Structure of the CO ice. *Astron. Astrophys.* **408**, 981–1007 (2003). doi: 10.1051/0004-6361:20031030
25. A. C. A. Boogert, P. A. Gerakines, D. C. B. Whittet, Observations of the icy universe. *Annu. Rev. Astron. Astrophys.* **53**, 541–581 (2015). doi: 10.1146/annurev-astro-082214-122348
26. W. Schutte, R. Khanna, Origin of the 6.85 µm band near young stellar objects: The ammonium ion ($NH4^+$) revisited. *Astron. Astrophys.* **398**, 1049–1062 (2003). doi: 10.1051/0004-6361:20021705
27. J. V. Keane, A. G. G. M. Tielens, A. C. A. Boogert, W. A. Schutte, D. C. B. Whittet, Ice absorption features in the 5-8 µm region toward embedded protostars. *Astron. Astrophys.* **376**, 254–270 (2001). doi: 10.1051/0004-6361:20010936
28. A. C. A. Boogert *et al.*, The c2d Spitzer spectroscopic survey of ices around low-mass young stellar objects. I. H_2O and the 5–8 µm bands. *Astrophys. J.* **678**, 985–1004 (2008). doi: 10.1086/533425
29. B. Maté *et al.*, Water-ammonium ices and the elusive 6.85 µm band. *Astrophys. J.* **703**, L178–L182 (2009). doi: 10.1088/0004-637X/703/2/L178
30. J. B. Bergner, K. I. Öberg, M. Rajappan, E. C. Fayolle, Kinetics and mechanisms of the acid-base reaction between NH_3 and HCOOH in interstellar ice analogs. *Astrophys. J.* **829**, 85 (2016). doi: 10.3847/0004-637X/829/2/85
31. A. Potapov, P. Theulé, C. Jäger, T. Henning, Evidence of surface catalytic effect on cosmic dust grain analogs: The ammonia and carbon dioxide surface reaction. *Astrophys. J.* **878**, L20 (2019). doi: 10.3847/2041-8213/ab2538
32. D. Takir, J. P. Emery, Outer Main Belt asteroids: Identification and distribution of four 3-µm spectral groups. *Icarus* **219**, 641–654 (2012). doi: 10.1016/j.icarus.2012.02.022
33. M. E. Brown, A. R. Rhoden, The 3 µm spectrum of Jupiter's irregular satellite himalia. *Astrophys. J.* **793**, L44 (2014). doi: 10.1088/2041-8205/793/2/L44
34. M. C. De Sanctis *et al.*, Ceres's global and localized mineralogical composition determined by Dawn's Visible and Infrared Spectrometer (VIR). *Meteorit. Planet. Sci.* **53**, 1844–1865 (2018). doi: 10.1111/maps.13104
35. M. Gounelle, M. E. Zolensky, The Orgueil meteorite: 150 years of history. *Meteorit. Planet. Sci.* **49**, 1769–1794 (2014). doi: 10.1111/maps.12351
36. S. Pizzarello, X. Feng, S. Epstein, J. R. Cronin, Isotopic analyses of nitrogenous compounds from the Murchison meteorite: Ammonia, amines, amino acids, and polar hydrocarbons. *Geochim. Cosmochim. Acta* **58**, 5579–5587 (1994). doi: 10.1016/0016-7037(94)90251-8; pmid: 11539151
37. M. J. Mumma *et al.*, paper presented at the 50th American Astronomical Society DPS meeting, Knoxville, TN, 12-26 October 2018; http://adsabs.harvard.edu/abs/2018DPS....5020902M
38. M. A. DiSanti *et al.*, En route to destruction: The evolution in composition of ices in comet D/2012 S1 (ISON) between 1.2 and 0.34 AU from the sun as revealed at infrared wavelengths. *Astrophys. J.* **820**, 34 (2016). doi: 10.3847/0004-637X/820/1/34
39. N. Dello Russo *et al.*, The compositional evolution of C/2012 S1 (ISON) from ground-based high-resolution infrared spectroscopy as part of a worldwide observing campaign. *Icarus* **266**, 152–172 (2016). doi: 10.1016/j.icarus.2015.11.030
40. K. Altwegg *et al.*, Organics in comet 67P–A first comparative analysis of mass spectra from ROSINA–DFMS, COSAC and Ptolemy. *Mon. Not. R. Astron. Soc.* **469** (Suppl_2), S130–S141 (2017). doi: 10.1093/mnras/stx1415
41. F. Goesmann *et al.*, Organic compounds on comet 67P/Churyumov-Gerasimenko revealed by COSAC mass spectrometry. *Science* **349**, aab0689 (2015). doi: 10.1126/science.aab0689; pmid: 26228156
42. N. Hänni *et al.*, Ammonium salts as a source of small molecules observed with high-resolution electron-impact ionization mass spectrometry. *J. Phys. Chem. A* **123**, 5805–5814 (2019). doi: 10.1021/acs.jpca.9b03534; pmid: 31257892
43. D. R. Lide, Physical constants of inorganic compounds, in *CRC Handbook of Chemistry and Physics* (CRC Press, ed. 90, 2009), pp. 4-46–4-48.
44. G. Danger *et al.*, Experimental investigation of aminoacetonitrile formation through the Strecker synthesis in astrophysical-like conditions: Reactivity of methanimine (CH_2NH), ammonia (NH_3), and hydrogen cyanide (HCN). *Astron. Astrophys.* **535**, A47 (2011). doi: 10.1051/0004-6361/201117602
45. V. Vinogradoff, F. Duvernay, G. Danger, P. Theulé, T. Chiavassa, New insight into the formation of hexamethylenetetramine (HMT) in interstellar and cometary ice analogs. *Astron. Astrophys.* **530**, A128 (2011). doi: 10.1051/0004-6361/201116688
46. J. B. Bossa, P. Theulé, F. Duvernay, F. Borget, T. Chiavassa, Carbamic acid and carbamate formation in NH_3:CO_2 ices–UV irradiation versus thermal processes. *Astron. Astrophys.* **492**, 719–724 (2008). doi: 10.1051/0004-6361:200810536
47. N. Fray *et al.*, Nitrogen-to-carbon atomic ratio measured by COSIMA in the particles of comet 67P/Churyumov–Gerasimenko. *Mon. Not. R. Astron. Soc.* **469** (Suppl_2), S506–S516 (2017). doi: 10.1093/mnras/stx2002
48. K. Lodders, in *Principles and Perspectives in Cosmochemistry* (Springer, 2010). *Astrophysics and Space Science Proceedings*, pp. 379–417.
49. N. Dello Russo, H. Kawakita, R. J. Vervack Jr., H. A. Weaver, Emerging trends and a comet taxonomy based on the volatile chemistry measured in thirty comets with high-resolution infrared spectroscopy between 1997 and 2013. *Icarus* **278**, 301–332 (2016). doi: 10.1016/j.icarus.2016.05.039
50. M. Rubin *et al.*, Molecular nitrogen in comet 67P/Churyumov-Gerasimenko indicates a low formation temperature. *Science* **348**, 232–235 (2015). doi: 10.1126/science.aaa6100; pmid: 25791084
51. S. Wyckoff, S. C. Tegler, L. Engel, Nitrogen abundance in Comet Halley. *Astrophys. J.* **367**, 641 (1991). doi: 10.1086/169659
52. A. Bardyn *et al.*, Carbon-rich dust in comet 67P/Churyumov-Gerasimenko measured by COSIMA/Rosetta. *Mon. Not. R. Astron. Soc.* **469** (Suppl_2), S712–S722 (2017). doi: 10.1093/mnras/stx2640
53. E. Füri, B. Marty, Nitrogen isotope variations in the Solar System. *Nat. Geosci.* **8**, 515–522 (2015). doi: 10.1038/ngeo2451
54. K. Lodders, Jupiter formed with more tar than ice. *Astrophys. J.* **611**, 587–597 (2004). doi: 10.1086/421970
55. J. S. Kargel, Ammonia-water volcanism on icy satellites: Phase relations at 1 atmosphere. *Icarus* **100**, 556–574 (1992). doi: 10.1016/0019-1035(92)90118-Q

56. M. P. Callahan *et al.*, Carbonaceous meteorites contain a wide range of extraterrestrial nucleobases. *Proc. Natl. Acad. Sci. U.S.A.* **108**, 13995–13998 (2011). doi: 10.1073/pnas.1106493108; pmid: 21836052
57. N. R. Lerner, G. W. Cooper, Iminodicarboxylic acids in the Murchison meteorite: Evidence of Strecker reactions. *Geochim. Cosmochim. Acta* **69**, 2901–2906 (2005). doi: 10.1016/j.gca.2004.12.024
58. B. Burcar *et al.*, Darwin's warm little pond: A one-pot reaction for prebiotic phosphorylation and the mobilization of phosphate from minerals in a urea-based solvent. *Angew. Chem. Int. Ed.* **55**, 13249–13253 (2016). doi: 10.1002/anie.201606239; pmid: 27532228
59. P. Dziedzic, A. Bartoszewicz, A. Córdova, Inorganic ammonium salts as catalysts for direct aldol reactions in the presence of water. *Tetrahedron Lett.* **50**, 7242–7245 (2009). doi: 10.1016/j.tetlet.2009.10.014
60. B. Hapke, *Theory of Reflectance and Emittance Spectroscopy* (Cambridge Univ. Press, ed. 2, 2012).
61. B. Schmitt, Near and Mid-IR optical constants of crystalline H2O ice Ih at 140–145K. SSHADE/GhoSST (OSUG Data Center). Dataset/Spectral Data. (2004); doi: 10.26302/SSHADE/EXPERIMENT_BS_20200103_001
62. D. Takir *et al.*, Nature and degree of aqueous alteration in CM and CI carbonaceous chondrites. *Meteorit. Planet. Sci.* **48**, 1618–1637 (2013). doi: 10.1111/maps.12171
63. A. S. Rivkin, J. P. Emery, Detection of ice and organics on an asteroidal surface. *Nature* **464**, 1322–1323 (2010). doi: 10.1038/nature09028; pmid: 20428165
64. J. Licandro *et al.*, (65) Cybele: Detection of small silicate grains, water-ice, and organics. *Astron. Astrophys.* **525**, A34 (2011). doi: 10.1051/0004-6361/201015339
65. M. E. Brown, The 3-4 μm spectra of Jupiter Trojan asteroids. *Astron. J.* **152**, 159 (2016). doi: 10.3847/0004-6256/152/6/159
66. J. P. Emery, D. M. Burr, D. P. Cruikshank, Near-infrared spectroscopy of Trojan Asteroids: Evidence for two compositional groups. *Astron. J.* **141**, 25 (2011). doi: 10.1088/0004-6256/141/1/25
67. O. Poch, I. Istiqomah, Vis-NIR bidirectional reflection spectra of several ammonium salts mixed with pyrrhotite grains in sublimate residues at 173 K. SSHADE/GhoSST (OSUG Data Center) Dataset/Spectral Data (2018); doi: 10.26302/SSHADE/EXPERIMENT_OP_20191119_001
68. O. Poch, Vis-NIR bidirectional reflection spectra of several ammonium salts mixed with graphite powder at 296 K. SSHADE/GhoSST (OSUG Data Center) Dataset/Spectral Data (2018); doi: 10.26302/SSHADE/EXPERIMENT_OP_20200212_001

ACKNOWLEDGMENTS

O.P., I.I., and E.Q. thank F. Charlot of the Consortium des Moyens Technologiques Communs (CMTC) at the Institut National Polytechnique de Grenoble (INP) for the Scanning Electron Microscopy images of the samples. We acknowledge M. Faure for work on the VIRTIS data and the collaboration of the International Space Science Institute (ISSI) international team number 397 "Comet 67P/Churyumov-Gerasimenko Surface Composition as a Playground for Radiative Transfer Modeling and Laboratory Measurements." O.P. thanks C. Pilorget for insightful comments. **Funding:** O.P. acknowledges a postdoctoral fellowship from the Centre National d'Etudes Spatiales (CNES). I.I. acknowledges a thesis grant from the Lembaga Pengelola Dana Pendidikan (LPDP) Indonesian scholarship. L.M. acknowledges the Deutsche Forschungsgemeinschaft (DFG) grant MO 3007/1-1. D.K. acknowledges DFG-grant KA 3757/2-1. The work of O.P., I.I., E.Q., P.B., B.S., and L.B. was supported by the CNES and the French Agence Nationale de la Recherche (program Classy, ANR-17-CE31-0004). P.B. acknowledges funding from the European Research Council under the SOLARYS grant (ERC-CoG2017-771691). P.H.-B. acknowledges the LabEx Observatoire des Sciences de l'Univers de Grenoble OSUG @ 2020 for funding. S.P. is supported by Université Grenoble Alpes (UGA), Initiatives de Recherche Stratégiques (IRS), and Initiatives d'Excellence UGA (IDEX UGA). The development of the CarboN-IR environmental chamber was supported by the French National Program of Planetology (PNP), the development of the reflectance goniometers was supported by the University of Grenoble Alpes (Initiative de Recherche Stratégique). Université Grenoble Alpes (UGA) and CNES supported the instrumental facilities and activities at IPAG. The following institutions and agencies supported the Rosetta mission: the Italian Space Agency (ASI, Italy), Centre National d'Etudes Spatiales (CNES, France), Deutsches Zentrum für Luft- und Raumfahrt (DLR, Germany), the National Aeronautic and Space Administration (NASA, United States) Rosetta Program and the Science and Technology Facilities Council (United Kingdom). VIRTIS was built by a consortium including Italy, France, and Germany, under the scientific responsibility of the Istituto di Astrofisica e Planetologia Spaziali of INAF, Italy, which also guided scientific operations. The development of the VIRTIS instrument was funded and managed by ASI, with contributions from Observatoire de Meudon, financed by CNES, and from DLR. A.R., M.C., G.F., F.C., M.C.D.S., A.L., E.P., and F.T. acknowledge financial support from the National Institute for Astrophysics (INAF, Italy) and the Italian Space Agency (ASI, Italy) through contract I/024/12/2. Computational resources were provided by INAF-IAPS through the DataWell project. The work of A.P. and N.T. was carried out within the framework of the National Centre of Competence in Research (NCCR) PlanetS supported by the Swiss National Science Foundation. **Author contributions:** O.P. and I.I. carried out the laboratory experiments. O.P. wrote the manuscript with assistance from P.B., E.Q., and B.S., who also contributed to interpreting the results. E.Q., P.H.-B., A.F., and P.B. calculated the nitrogen distribution and N/C ratio. O.P., E.Q., and A.F. produced the figures. A.R., M.C., and G.F. provided the calibrated average reflectance spectrum of comet 67P and wrote parts of the supplementary materials. O.B., S.P., B.R., and L.F. contributed to the experimental work. N.T. and A.P. contributed to the early development of spectroscopic studies of sublimate residues. All co-authors contributed to the preparation of the manuscript. **Competing interests:** We declare no competing interests. **Data and materials availability:** The laboratory reflectance spectra are available in the Grenoble Astrophysics and Planetology Solid Spectroscopy and Thermodynamics (GhoSST) database (*67*, *68*). The average reflectance spectrum of comet 67P measured by VIRTIS is available from (*10*), their 'source data Fig. 1.' The reference spectra of Mars and Lutetia are available from the Planetary Science Archive https://archives.esac.esa.int/psa/#!Table%20View by selecting Mars or 21 Lutetia as the target, VIRTIS (Rosetta) as the instrument, clicking search, then filtering by observation IDs I1_00130974021 for Mars or I1_00237396952 for Lutetia.

SUPPLEMENTARY MATERIALS

science.sciencemag.org/content/367/6483/eaaw7462/suppl/DC1
Materials and Methods
Figs. S1 to S9
Tables S1 and S2
References (*69*–*89*)

21 January 2019; resubmitted 11 October 2019
Accepted 14 February 2020
10.1126/science.aaw7462

science.sciencemag.org/content/367/6483/eaaw7462/suppl/DC1

Supplementary Material for

Ammonium salts are a reservoir of nitrogen on a cometary nucleus and possibly on some asteroids

Olivier Poch*, Istiqomah Istiqomah, Eric Quirico, Pierre Beck, Bernard Schmitt, Patrice Theulé, Alexandre Faure, Pierre Hily-Blant, Lydie Bonal, Andrea Raponi, Mauro Ciarniello, Batiste Rousseau, Sandra Potin, Olivier Brissaud, Laurène Flandinet, Gianrico Filacchione, Antoine Pommerol, Nicolas Thomas, David Kappel, Vito Mennella, Lyuba Moroz, Vassilissa Vinogradoff, Gabriele Arnold, Stéphane Erard, Dominique Bockelée-Morvan, Cédric Leyrat, Fabrizio Capaccioni, Maria Cristina De Sanctis, Andrea Longobardo, Francesca Mancarella, Ernesto Palomba, Federico Tosi

*Corresponding author. Email: olivier.poch@univ-grenoble-alpes.fr

Published 13 March 2020, *Science* **367**, eaaw7462 (2020)
DOI: 10.1126/science.aaw7462

This PDF file includes:

Materials and Methods

Preparation of the cometary analogs

We performed experiments to measure the reflectance spectra of ammonium salts and a carboxylic acid when they are mixed in a porous matrix of opaque sub-micrometer-sized grains, designed to simulate the mixing mode found on a cometary nucleus. Previous work has shown that the sublimation of water ice particles containing inclusions of non-volatile components produces porous sublimate residues (*15*, *69*). We prepared sublimate residues of an opaque mineral and salts following the same protocol (*15*, *69*).

For the dust component, we used pure pyrrhotite ($Fe_{1-x}S$, with $0 < x < 0.2$) because it is an opaque mineral proposed as a possible darkening agent of the cometary nucleus at infrared wavelengths (*11*, *14*). Millimeter-sized pyrrhotite grains were purchased from Alfa-Aesar (ref. 42652) and ground to sub-micrometer sized grains (*14*, their section 2.2). Most of the ammonium salts and the carboxylic acid were purchased from Sigma-Aldrich: ammonium formate ≥ 99.995 % (ref. 516961), ammonium sulfate ≥ 99 % (ref. A4418), ammonium carbamate 99 % (ref. 292834). The ammonium chloride ≥ 99.5 % was from Carlo Erba (ref. 419417), L-lactic acid anhydrous 98 % from Alfa-Aesar (ref. L13242), and ammonium citrate dibasic ≥ 99 % from Fluka (ref. 09831) whose detailed formula is $(NH_4^+)_2\ CH_2COOH\text{-}C(OH)COO^-\text{-}CH_2COO^-$.

The salts or the carboxylic acid were dissolved in ultra-pure liquid water. For example, in the case of the ammonium formate, 0.04 g of salt powder was dissolved in 20 mL of ultra-pure water, resulting in a mass ratio of 0.002. Then, 0.2 g of sub-micrometer sized pyrrhotite grains were dispersed in this solution (1 wt%) via ultrasonication, to destroy the aggregates and obtain a homogeneous mixture (*69*, their section 2.2.2). The ice particles were prepared from this liquid mixture using the Setup for the Production of Icy Planetary Analogs – B (SPIPA-B) (*15*, their section 2.3.4.2). The SPIPA-B ice particles are spherical, with a mean diameter of 67 ± 31 μm as measured by Cryo-Scanning Electron Microscopy (*15*). The pyrrhotite grains and the salt are contained inside each of these particles, this mixing mode being referred to as "intra-mixture" (*15*). The produced ice/dust particles were placed in a cylindrical aluminum sample holder of 48 mm diameter and 5 mm deep, by direct sieving through a 400 μm sieve to exclude large agglomerates and to obtain homogeneous surface and internal density (~0.5 g/cm^3) (Fig. S1B).

The sample holder containing the ice/dust mixture was maintained at a temperature lower than 170 K and under a dry atmosphere in an insulating box containing liquid nitrogen before being placed inside the CarboN-IR simulation chamber (*70*). Inside the chamber, the sample was kept at 170-200 K using a helium cryostat and under high vacuum (< 10^{-5} mbar). The surface of the sample absorbs thermal infrared radiation emitted from the top and the walls of the chamber, so the water ice sublimates progressively. As the surface dehydrates, it becomes darker because of the formation of a sublimate residue composed of pyrrhotite grains and salts or acid (Fig. S1). After about 48 hours, all the water ice has sublimated (Fig. S1C). Scanning Electron Microscopy images of these sublimate residues show a porous network of sub-μm pyrrhotite grains where the salts or acid may be present as coating or cement between the grains (Fig. S2). For initial ice particles containing 1 wt% pyrrhotite and 0.2 wt% salt, we estimate that the sublimate residue is made of 83 wt% pyrrhotite and 17 wt% salt, but a fraction of the salt might have sublimated with the water so the quantity of salt in the final residue may be lower.

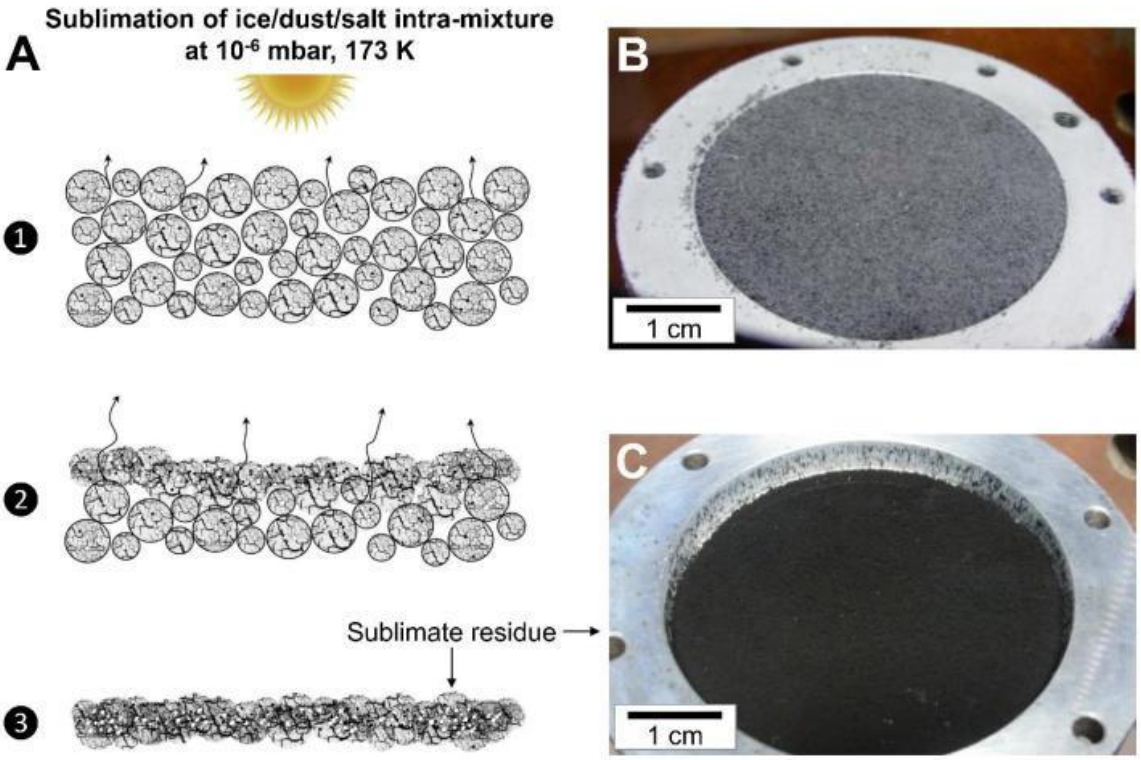

Fig. S1. Production of a sublimate residue. (**A**) Preparation of the cometary surface analog – a sublimate residue made of dust and salt – in the laboratory. Spherical water ice particles containing 1 wt% pyrrhotite and 0.2 wt% ammonium formate ($NH_4^+HCOO^-$) are placed in a thermal vacuum chamber under high vacuum (< 10^{-5} mbar) and 170-200 K. The sublimation of the water, triggered by thermal infrared or visible light, results in the formation of a porous residue made of pyrrhotite grains containing 17 wt% or less of $NH_4^+HCOO^-$. (**B**) Photograph of the initial sample made of water ice particles containing 1 wt% pyrrhotite and 0.2 wt% ammonium formate, before sublimation. (**C**) Photograph of the same sample after sublimation of the water ice.

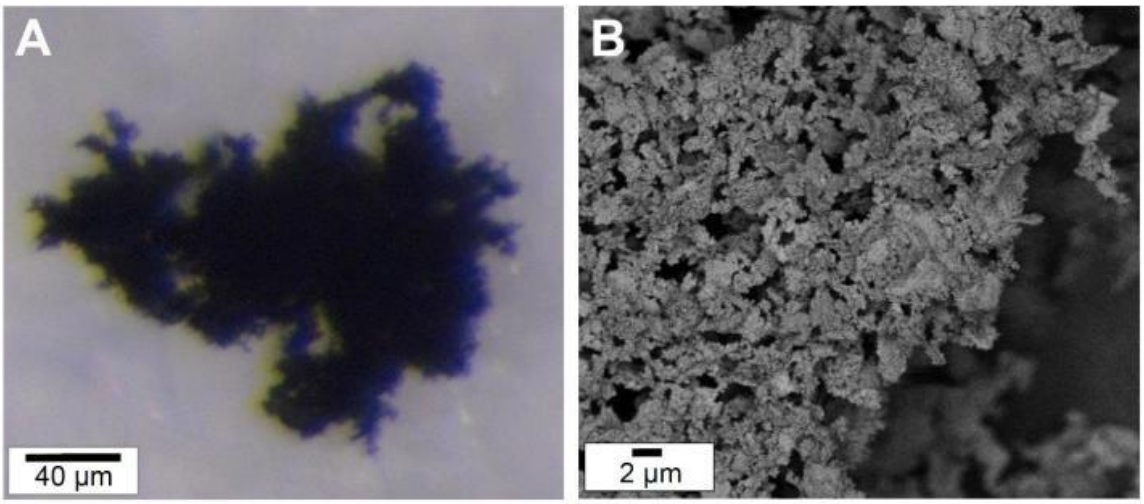

Fig. S2. Micro-structure of a sublimate residue. (**A**) Optical microscopy image of a fragment of the sublimate residue shown in Fig. S1C, showing its fluffy structure. (**B**) Backscattered electron image obtained by Scanning Electron Microscopy of the sublimate residue, showing sub-micrometric-sized grains of pyrrhotite arranged in a porous structure as a result of the freezing and sublimation processes. The ammonium salt probably coats and/or cements the pyrrhotite grains.

Reflectance measurements in the laboratory

The reflectance measurements were performed using the SpectropHotometer with variable INcidence and Emergence (SHINE) of the Institut d'Astrophysique et de Planétologie de Grenoble (IPAG). The instrument (*71*) consists of two goniometer arms: the first illuminates the sample with a monochromatic beam, provided by a monochromator, and the second holds two detectors covering the 0.5-5.0 µm spectral range. A transparent sapphire window allows the sample to be illuminated and viewed inside the CarboN-IR simulation chamber, positioned at the basis of the arms. SHINE was designed to measure bright samples of ice, but the sublimate residues rich in pyrrhotite are much darker samples. Therefore, we focused the illumination of the sample onto a smaller area of 6 mm in diameter, in order to increase the signal-to-noise ratio of our measurements (*72*, their section D.2). For the computation of the reflectance factor (REFF) (*60*) we also measured two surfaces made of Spectralon® and Infragold® (Labsphere Inc.) as references, corrected for their non-ideal spectral and photometric behavior (*73*). All the reflectance spectra were measured with a nadir incidence (illumination) and an emission (observation) angle of 30°. Spectral sampling $\Delta\lambda_{sampling}$ = 0.020 µm was constant throughout the overall wavelength range, but the spectral resolution varies, with higher resolutions at shorter wavelengths and lower resolutions at longer wavelengths. The spectral resolution was $\Delta\lambda_{resolution}$ = 0.019 µm in the wavelength range of 1.4-3.0 µm, and $\Delta\lambda_{resolution}$ = 0.039 µm in the range of 3.0-4.2 µm. The abrupt change of spectral resolution at 3.0 µm is due to a change of grating in the monochromator. The average resolving power over these wavelength intervals is thus $RP \equiv \lambda/\Delta\lambda_{resolution} \approx 100$ where λ is the wavelength, which is lower than that of VIRTIS-M ($\lambda/\Delta\lambda_{resolution} \approx 230$). The absolute radiometric precision of the laboratory measurement was better than 3% over the whole spectral range. The spectrum shown in Figs. 1 and S5 is the average of 30 individual spectra measured over a period of 16 hours.

Reflectance spectrum of the average surface of comet 67P

The reflectance spectrum of comet 67P shown in Figs. 1, 2, S5, S6 and S7 was obtained from a recalibration of data acquired by the VIRTIS-M (Visual Infrared and Thermal Imaging Spectrometer – Mapper) Infrared (IR) channel (*2*), reducing instrumental artifacts and improving the radiometric accuracy. We summarize the data reduction below; full details have been published elsewhere *(10)*.

Average spectrum of comet 67P surface

The VIRTIS-M IR channel acquired hyperspectral images in the range 1 - 5 μm, across 432 spectral bands, and through 256 spatial samples of 250 μrad Instantaneous Field Of View (IFOV).

To calculate an average spectrum of the surface of comet 67P we consider the whole dataset acquired during the first mapping phase of the Rosetta mission in August-September 2014 (~2.7 million spectra) at a distance ranging from 350 to 10 km from the center of the nucleus. These observations revealed a spectrally uniform surface (*3, 4, 9*). Spatial pixels corresponding to shadowed areas are filtered out and not used in the processing because they contain a very low signal-to-noise ratio.

By deriving an average spectrum from the full dataset, we reduce the Poisson noise to a level negligible. However, systematic instrumental effects in the conversion from digital number to radiance, varying from sample to sample (linearly dependent on the signal) contaminate the spectra. They generate artifacts on the signal visible at small spectral scale when comparing spectra of comet 67P and the spectra of a different target observed by VIRTIS with the same spatial sampling (Fig. S3).

To remove such artifacts, we produced average spectra of the comet nucleus independently for each spatial sample. The same average has been computed for asteroid Lutetia, which Rosetta flew past during the cruise phase of the mission (*74*). The ratio between the average spectra of comet 67P and Lutetia has been calculated independently for each sample, to eliminate spectral artifacts while keeping information of the real features. We assume absorption bands in the comet 67P spectrum to lie in spectral ranges where the asteroid Lutetia spectrum is featureless (as shown by VIRTIS-H observations of Lutetia (*74*) and confirmed by applying the same process to a reference Mars spectrum. To obtain the absolute spectrum of comet 67P, the ratio of the 67P and the Lutetia spectra is then multiplied by a 9-degree polynomial model fitted to the Lutetia spectrum (which we label 'interp'), to produce an artifact-removed (AR) average spectrum of comet 67P for each sample (*s*) (Fig. S3):

$$\frac{I}{F}(\lambda,s)_{67P}^{AR} = \frac{\frac{I}{F}(\lambda,s)_{67P}}{\frac{I}{F}(\lambda,s)_{\text{Lutetia}}} \cdot \frac{I}{F}(\lambda,s)_{\substack{\text{interp}\\ \text{Lutetia}}} \quad \text{(S1)}$$

where *I/F* is the radiance factor (π times bidirectional reflectance), $\frac{I}{F}(\lambda,s)_{67P}^{AR}$ the radiance factor of the artifact-removed average spectrum of comet 67P, $\frac{I}{F}(\lambda,s)_{67P}$ and $\frac{I}{F}(\lambda,s)_{\text{Lutetia}}$ are the radiance factor of the absolute spectrum of comet 67P and Lutetia

respectively, and $\frac{I}{F}(\lambda, s)_{\substack{\text{interp} \\ \text{Lutetia}}}$ is the radiance factor of the polynomial fit of the Lutetia spectrum.

The resulting average spectra are affected by a further source of non-Poissonian and non-systematic noise: due to the detector's architecture, the even and odd spectral bands are controlled by two independent sets of electronics. Small differences in their responses introduce an oscillation along the wavelengths (*65*). The response of the even bands is spuriously affected by the instrument temperature. Thus, we replaced the signals of the even bands by an average of the contiguous odd spectral bands. Nominally, the VIRTIS-M IR channel has a bandpass of 0.015 μm with a sampling of 0.010 μm. After removal of the even bands, the sampling is degraded to 0.020 μm.

Finally, the average spectrum of the comet 67P surface $\frac{I}{F}(\lambda)_{67\mathrm{P}}^{\mathrm{AR}}$ has been calculated by applying a median filter to $\frac{I}{F}(\lambda, s)_{67\mathrm{P}}^{\mathrm{AR}}$ over all samples.

The *I/F* uncertainty associated with each spectral band is obtained from the standard deviation over all $\frac{I}{F}(\lambda, s)_{67\mathrm{P}}^{\mathrm{AR}}$, as each sample can be considered as an independent detector. To exclude from this calculation signal variations due to different viewing geometry and illumination conditions of the comet nucleus as seen along the spectral slit, we calculated the standard deviation after scaling $\frac{I}{F}(\lambda, s)_{67\mathrm{P}}^{\mathrm{AR}}$ to the median spectrum $\frac{I}{F}(\lambda)_{67\mathrm{P}}^{\mathrm{AR}}$ using the ratio of the medians over the spectral bands as scaling factor. These uncertainties are assumed to represent the relative errors on the spectral shape.

Absolute calibration with star observations

Both VIRTIS-Rosetta and the Visual and Infrared Mapping Spectrometer (VIMS) on the Cassini-Huygens spacecraft measured the flux of the star Arcturus. Comparing two observations of Arcturus by VIRTIS-M-IR with six observations by VIMS (*76*) we performed an inter-calibration. The ratio of the average fluxes observed by the two instruments provides a correction factor as a function of wavelength, which can be applied to the final average spectrum of comet 67P (Fig. S3). We rely on VIMS consolidated calibration (*77*) because it was tested and improved over the duration of the Cassini mission.

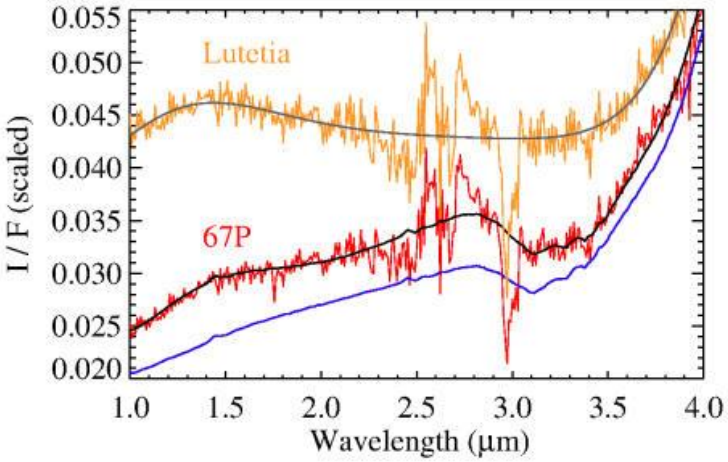

Fig. S3. Absolute calibration of VIRTIS-M observations of comet 67P. Average spectrum over all spatial pixels (~10000) that show illuminated areas of 67P nucleus acquired by a selected single spatial sample (red line). For comparison, the average spectrum of Lutetia for the same spatial sample, scaled for display (orange line) (original spectrum scaled by a factor of 0.56), and a polynomial model fitted to the data (gray line) are shown. The detector temperature and integration time for the observation of 67P and Lutetia are indicated in Table S1. The black line is the calibrated spectrum after artifact and odd-even effect removal, computed from the orange, red and gray curves using Equation S1. The final spectrum after application of the stellar calibration factor is represented as a blue line. After *(10*, their supplementary figure S3*)*, used with permission.

Object	Detector DN range (3.0-3.5 μm)	Detector temperature (K)	Detector exposure time (s)	File names
Asteroid Lutetia	7700 ± 300	87.74	0.7	I1_00237396952
Comet 67P	8200 ± 300	87.69 ± 0.22	1, 1.5, 2, 3, 10	(*10*)

Table S1. Parameters of VIRTIS-M detector. Ranges of Data Numbers (DN) (in the spectral range 3.0-3.5 μm), detector temperature and exposure time during the observations of asteroid Lutetia and comet 67P by VIRTIS-M. For Lutetia, the file name from the Planetary Science Archive. For comet 67P, the data used to obtain the average spectrum is from more than 257 cubes measured from August to September 2014 (*10*).

Thermal emission removal

Thermal emission of the comet nucleus produces a steep spectral slope increasing longward of 3 μm. To compare the observed average spectrum with laboratory measurements, the contribution of the thermal emission must be estimated and removed. We modeled the total signal longward of 2.2 μm as the sum of the thermal emission and the solar flux reflected from the surface.

The thermal emission is modeled as gray body radiation, assuming no spectral variation of the directional emissivity (*60*). This assumption is consistent with the low albedo of the comet and its small variability in the spectral range considered (*78*). Temperature and effective emissivity are free parameters for the thermal emission modeling. The reflectance is modeled as a linear function with the corresponding intercept and spectral slope as free parameters.

The free parameters of the model are retrieved by a fitting procedure in the 2.2 – 2.8 μm and 3.6 – 4.15 μm spectral ranges, thereby excluding the wavelengths covering the broad 3.2 μm absorption. The modeled thermal emission has been removed over the entire spectral range longward of 2.2 μm (Fig. S4).

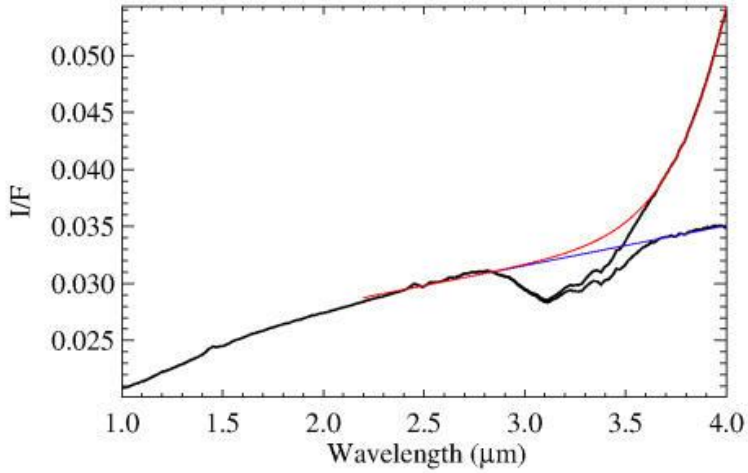

Fig. S4. Thermal emission removal on VIRTIS-M observations of comet 67P. The total modeled continuum signal (red line) is given by the sum of the modeled reflectance continuum (blue line) and the thermal emission. The latter is subtracted from the measured calibrated signal (upper black line), yielding the thermal emission removed spectrum (lower black line). Reproduced from *(10*, their supplementary figure S4*)*, used with permission.

Comparisons of experimental reflectance spectra with the average comet 67P spectrum

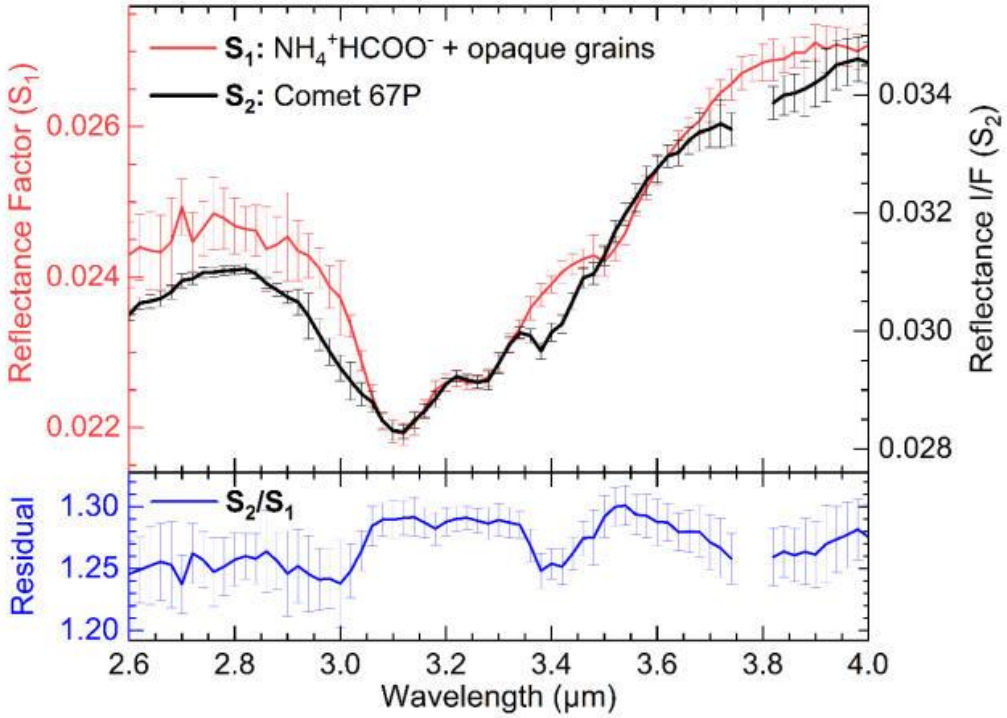

Fig. S5. Comparison of NH_4^+ $HCOO^-$ spectrum with the average spectrum of comet 67P. Reflectance spectra of the average of the nucleus of comet 67P (S_1, black line) and of a sublimate residue containing $\lesssim$ 17 wt% ammonium formate mixed with $\gtrsim$ 83 wt% pyrrhotite grains at 170-200 K (S_2, red line). The ratio calculated by dividing the two spectra (blue curve) is also shown. Error bars indicate the $\pm 1\sigma$ uncertainty. I/F is the radiance factor.

The similarity of the overall shape of the band and the similarity of the spectra in the range from 3.05 and 3.35 μm on Fig. S5 indicates the presence of ammonium salts on the comet. Differences between these spectra are due to the contribution of other compounds (possibly water ice, carbonaceous compounds) and possibly to different properties of the salts (counter-ions, concentration, mixing etc.) present on the cometary surface. The estimated signal-to-noise ratio is ~70 for the absorption feature at 3.1 μm, ~20 for the feature at 3.3 μm, and ~7 for the feature at 3.4 μm. The spectral ratio between 3.35-3.60 μm indicates the presence of the C−H stretching modes in carbonaceous compounds (*10*). Ammonium salts also exhibit a weaker reflectance minimum centered around 3.50 μm whose identification on the spectrum of comet 67P is impeded by its proximity with the C−H stretching modes and the limited spectral resolution and sampling (respectively of $\Delta\lambda_{resolution} = 0.039$ μm and $\Delta\lambda_{sampling} = 0.020$ μm for the laboratory spectrum and of $\Delta\lambda_{resolution} = 0.015$ μm and $\Delta\lambda_{sampling} = 0.020$ μm for the VIRTIS spectrum after removal of the even bands, as explained above). The position and strength of this ammonium bending mode at around 3.50 μm varies depending on the counter-ions (e.g. it is weak for ammonium citrate and carbamate in Fig. 2) and temperature and/or matrix interaction (Fig. S7A).

A detailed assignment of the bands observed on the cometary spectrum (Figs. 1 and S5) is provided in Table S2.

Several ammonium salts also have absorption bands at shorter wavelengths (at about 1.6-1.7 μm and 2.1-2.3 μm) (*79*). In the comet 67P spectrum and our experimental spectra of sublimate residues, these bands are absent because the salts are mixed with opaque mineral grains, which cause a decrease of the salts' band depths, resulting in a disappearance of the bands at 1.6-1.7 μm and 2.1-2.3 μm because they have lower coefficients of absorption than the ones at 3.1-3.3 μm.

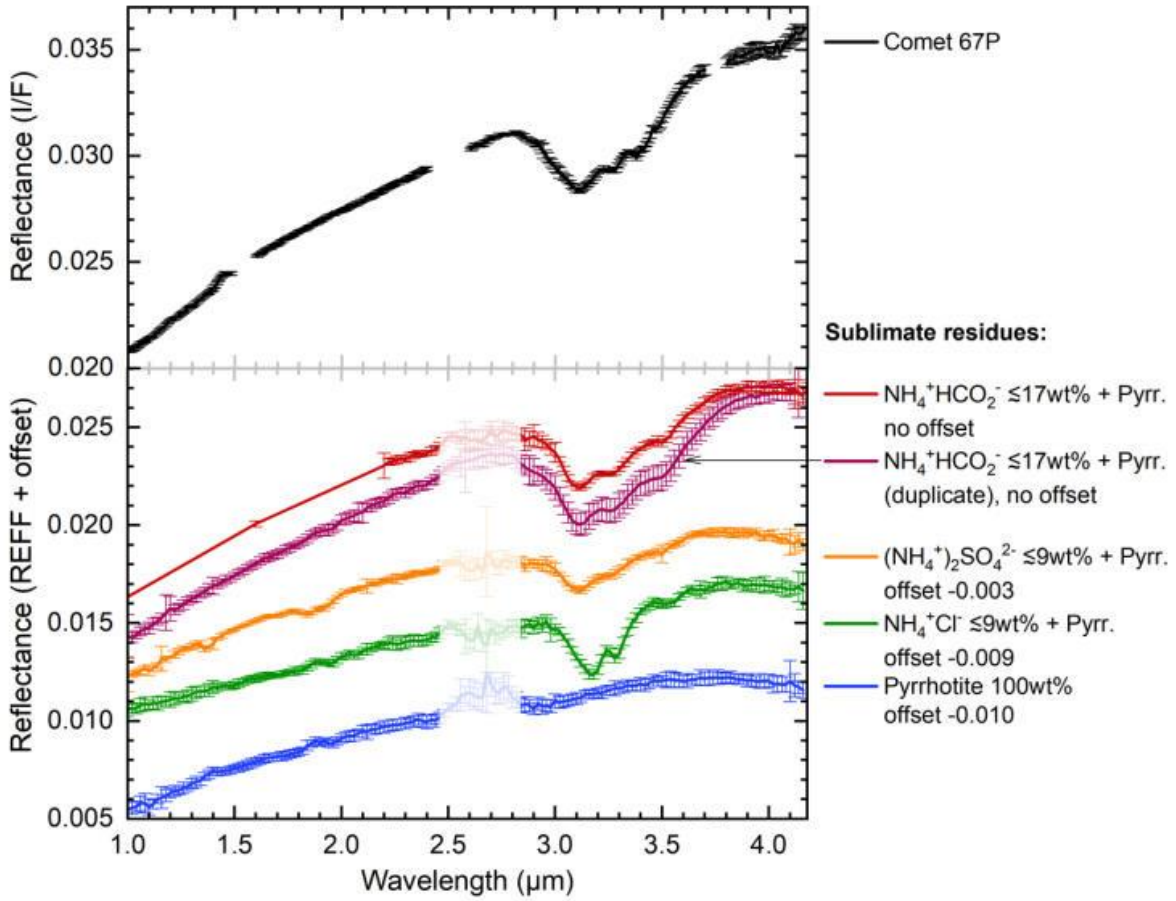

Fig. S6. Reflectance spectra of sublimate residues containing sub-micrometric-sized pyrrhotite grains pure or mixed with ammonium salts at different concentrations. These spectra are averages computed from 12 to 30 individual spectra. The red and violet curves show two spectra of sublimate residues containing pyrrhotite grains mixed with ≲ 17 wt% (≲ 43 vol%) ammonium formate (NH_4^+ $HCOO^-$), obtained after two duplicated experiments. The error bars reflect the photometric uncertainty and any variation of the samples between individual spectra. Between 2.5 and 2.8 μm, the laboratory spectra are affected by measurement artifacts due to the presence of water vapor in the optical path. Error bars indicate the ±1σ uncertainty. Figure 2 shows these spectra after continuum normalization. I/F is the radiance factor. REFF is the reflectance factor.

The pyrrhotite grains used for the sublimation experiments form a matrix of opaque grains, which are spectrally featureless in the 3-μm region (Fig. 2 and Fig. S6). Mixing ammonium salts with other darkening agents gives similar reflectance spectra. As an example, Fig. S7 shows reflectance spectra of mixtures of ammonium salts and graphite grains mixed in a mortar and measured under ambient conditions.

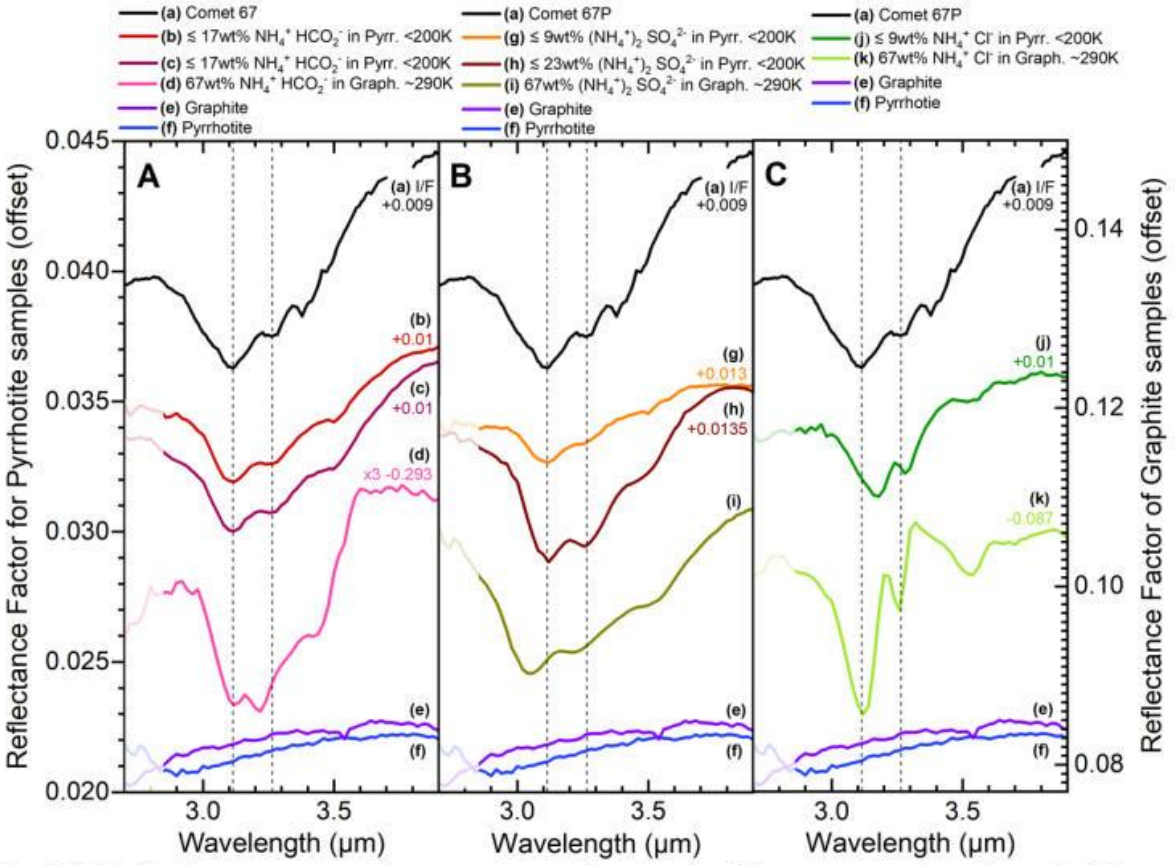

Fig. S7. Reflectance spectra of ammonium salts mixed with opaque grains of pyrrhotite or graphite. (**A**) Ammonium formate (NH_4^+ $HCOO^-$). (**B**) Ammonium sulfate ($(NH_4^+)_2$ SO_4^{2-}). (**C**) Ammonium chloride (NH_4^+ Cl^-). The mixtures with pyrrhotite (Pyrr.) were obtained by sublimation and were measured under high vacuum (< 10^{-5} mbar) and 170-200 K. The mixtures with graphite (Graph.) were obtained by mixing the salt and the graphite grains in a mortar and were measured under ambient temperature and pressure conditions (~290 K). The average reflectance spectrum of the nucleus of comet 67P and the spectra of pure pyrrhotite and graphite grains are also shown for comparison. Between 2.7 and 2.9 μm, the laboratory spectra are affected by measurement artifacts due to the presence of water vapor in the optical path.

The relative amplitudes and the positions of most of the minima of reflectance of the 3.2-μm band of the salts are different in the spectra of the mixtures in graphite compared to the sublimate residues in pyrrhotite. These differences are probably due to the environmental conditions (temperature, difference of interaction with pyrrhotite vs. graphite matrixes etc.) which these ionic species appear to be sensitive to.

Quantity of ammonium salts mixed with the dust of comet 67P

The laboratory reflectance spectrum which is the closest match to comet 67P is obtained with a sublimate residue containing pyrrhotite grains mixed with $\lesssim 17$ wt% ammonium formate (NH_4^+ $HCOO^-$) as shown in Fig. 1, Fig. 2 and Fig. S5. However, this upper limit mass fraction of ammonium formate cannot be directly applied to the cometary surface, because this surface is composed of dust grains (made of refractory organic matter and various minerals) much less dense than the pyrrhotite grains present in the sublimate residues. Therefore, for the same mass fraction of salt, the cometary surface layer contains a larger volume of refractory grains than our samples. In order to compare the band depths in our experimental spectra and in the comet spectrum in terms of abundance of salt, we use the volume fraction of the salt in the surface material rather than its mass fraction. Ideally, we would use the cross section of the salt that interacts with the photons, but this value is unknown. Fig. S2 shows that the grains of salt in the sublimate residues are probably sub-micrometric, so we are likely far from the saturation regime of the strong vibration modes of the salts in the 3-μm region.

The upper limit of the volume fraction of salt in the sublimate residue is calculated as follows.

For a two-endmember mixture of A and B, we define the following parameters:

M: total mass ($M = M_A + M_B$)

V: total volume ($V = V_A + V_B$)

M_A^*: mass fraction of A ($M_A^* = \frac{M_A}{M}$)

M_B^*: mass fraction of B

V_A^*: volume fraction of A ($V_A^* = \frac{V_A}{V}$)

V_B^*: volume fraction of B

ρ_A: density of A

ρ_B: density of B

By definition, we have:

$$\frac{M_A^*}{M_B^*} = \frac{M_A}{M_B} = \frac{V_A \cdot \rho_A}{V_B \cdot \rho_B} = \frac{V_A^* \cdot \rho_A}{V_B^* \cdot \rho_B} \qquad \text{(S2)}$$

and

$$V_A^* + V_B^* = 1 \quad \text{(S3)}$$
$$M_A^* + M_B^* = 1 \quad \text{(S4)}$$

By combining these equations, we obtain:

$$V_A^* = \frac{1}{1 + \frac{M_B^* \cdot \rho_A}{M_A^* \cdot \rho_B}} \qquad \text{(S5)}$$

with:

A = ammonium formate (NH_4^+ $HCOO^-$), $M_A^* = 0.17$, $\rho_A = 1.26$ g/cm^3,

B = pyrrhotite ($Fe_{1-x}S$, with $0 < x < 0.2$), $M_B^* = 0.83$, $\rho_B = 4.61$ g/cm^3.

From Equation S5 we derive an upper limit of the volume fraction of salt of 43 vol% in the sublimate residue.

Fig. S6 shows two spectra of sublimate residues containing pyrrhotite grains mixed with ≲ 17 wt% (≲ 43 vol%) ammonium formate (NH_4^+ $HCOO^-$), obtained in duplicated experiments. We calculated the relative band depth at 3.1 μm (BD) via

$$BD = 1 - \frac{R}{R_C} \qquad \text{(S6)}$$

with:

R the reflectance value at the wavelength with the minimum reflectance,

R_C the reflectance value of the continuum baseline at this wavelength. The continuum baseline was computed via a spline interpolation (3rd order polynomials) using the reflectance of baseline anchor points typically at 2.20, 2.32, 2.78, 3.96 and 4.12 μm.

The band depths obtained are 0.123 for the comet 67P spectrum and 0.127 and 0.149 for the experimental spectra. Because the band depth of the 3.1 μm absorption band in the spectrum of comet 67P is lower than the band depth of the sublimate residues, the volume fraction of salt on comet 67P should be less than 43 vol%. However, the band depth is controlled by a multitude of parameters in addition to the salt content, such as possible contributions of other surface constituents, grain sizes, porosity and mixing mode of the dust layer, which may differ in our laboratory samples compared to the comet. Even if our samples share some properties with cometary dust (sub-μm grains, porosity, production via crystallization/sublimation of ice), we cannot exclude that the upper limit of ammonium salts on comet 67P is lower or higher than our estimation.

The dark surface material (i.e. dust) of the comet is not composed only of pyrrhotite but of refractory organic matter (ROM) mixed with minerals (MIN). An approximate composition of this material was derived from the analysis of COSIMA data (*52*), resulting in respective abundances of ROM and minerals of $M_{ROM}{}^* = 0.45$ and $M_{MIN}{}^* = 0.55$. Assuming a density of $\rho_{ROM} = 1$ g/cm^3 for the ROM and a mean chondritic density of $\rho_{MIN} = 3.4$ g/cm^3 for the minerals, we determine:

$$\rho_B = \frac{M_B}{V_B} = \frac{V_{ROM} \cdot \rho_{ROM} + V_{MIN} \cdot \rho_{MIN}}{V_B} = V_{ROM}{}^* \cdot \rho_{ROM} + V_{MIN}{}^* \cdot \rho_{MIN} \qquad \text{(S7)}$$

with:

B = cometary dust,

$V_{ROM}{}^*$ and $V_{MIN}{}^*$ derived from Equation S5, giving $V_{ROM}{}^* = 0.74$ and $V_{MIN}{}^* = 0.26$.

From Equation S7, we find $\rho_B = 1.63$ g/cm^3.

Finally, to calculate the mass fraction of salt corresponding to 43 vol% in the cometary dust, we use

$$M_A{}^* = \frac{1}{1 + \frac{V_B{}^* \cdot \rho_B}{V_A{}^* \cdot \rho_A}} \qquad \text{(S8)}$$

with:

A = ammonium formate (NH_4^+ $HCOO^-$), $M_A{}^* = 0.17$, $\rho_A = 1.26$ g/cm^3,

B = cometary dust.

Finally, from Equation S8 we obtain $M_A^* = 0.37$

To conclude, on the cometary surface we estimate an upper limit of $\lesssim 40$ vol% salts, equivalent to $\lesssim 40$ wt% salts, mixed with the dark surface material.

Calculation of the nitrogen distribution and nitrogen-to-carbon ratio

To calculate the nitrogen budget of comet 67P, we distinguished three main components: i) volatiles; ii) refractory dust grains, made of minerals and ROM; and iii) semi-volatile ammonium salts in the form of ammonium formate (NH_4^+ $HCOO^-$, although NH_4^+ could have multiple counter-ions on the comet).

The balance of their respective mass fractions can be written:

$$M_V^* + M_R^* + M_S^* = 1 \qquad \text{(S9)}$$

with M_V^*, M_R^* and M_S^* the mass fractions of the volatiles, the refractory dust grains and the semi-volatile ammonium salts respectively.

The dust-to-ice mass ratio R is taken as 4 ± 2 (*80*).

X is the mass fraction of ammonium salts with respect to refractory dust:

$$X = \frac{M_S^*}{M_S^* + M_R^*} \qquad \text{(S10)}$$

The terms above can then be rewritten as:

$$M_V^* = \frac{1}{R+1} \quad \text{(S11)}\,; \qquad M_S^* = X\frac{R}{R+1} \quad \text{(S12)}\,; \qquad M_R^* = \frac{R}{R+1}(1-X) \quad \text{(S13)}$$

The refractory dust is composed of minerals (MIN) and refractory organic matter (ROM), whose approximate mass ratio was derived from the analysis of COSIMA data (*52*). We assume that COSIMA did not sample the most volatile compounds of the cometary dust, including the ammonium salts that could have sublimated during the pre-analysis storage of the particles at 283 K inside the COSIMA instrument (*47*). Therefore, we have:

$$X = \frac{M_S^*}{M_S^* + M_R^*} \qquad \text{(S14)}$$

$$M_R^* = M_{MIN}^* + M_{ROM}^* \quad \text{(S15)} \qquad \frac{M_{MIN}^*}{M_{ROM}^*} = \frac{55}{45} \quad \text{(S16)}$$

with M_{MIN}^* and M_{ROM}^* the mass fractions of the minerals and the ROM respectively.

By combining these equations, we obtain:

$$M_{ROM}^* = \frac{M_R^*}{1 + \frac{M_{MIN}^*}{M_{ROM}^*}} = \frac{R(1-X)}{(R+1)(1 + \frac{M_{MIN}^*}{M_{ROM}^*})} \qquad \text{(S17)}$$

Moles are derived from the mass fractions through:

$$n_V = \frac{M_V^*}{M_V} \quad \text{(S18)} ; \qquad n_S = \frac{M_S^*}{M_S} \quad \text{(S19)} ; \qquad n_{ROM} = \frac{M_{ROM}^*}{M_{ROM}} \quad \text{(S20)}$$

with:

M_{ROM} = 18.29 g/mol, obtained from the elemental composition $HCO_{0.3}N_{0.035}$ estimated from COSIMA data (*47, 52*),

M_S = 63.06 g/mol, assuming ammonium salts are in the form of ammonium formate.

M_V = 18.96 g/mol, assuming the volatiles are composed of the sixteen most abundant molecules detected in the summer hemisphere by the ROSINA instrument onboard Rosetta (*16, 50*): H_2O, CO, CO_2, CH_4, C_2H_2, C_2H_6, H_2CO, HCOOH, CH_2OHCH_2OH, $HCOOCH_3$, NH_3, HCN, N_2, CH_3CHO, HNCO, CH_3CN. We assume that the bulk comet has the same composition than the coma, which might not be valid for super-volatiles (*81*). Nevertheless, the contribution of ices to the nitrogen budget is small, so this assumption should have a negligible impact.

Finally, the total number of carbon (n^C) and nitrogen (n^N) atoms is calculated for each reservoir:

$$n_V^C = f_V^C . n_V \quad \text{(S21)} ; \qquad n_S^C = f_S^C . n_S \quad \text{(S22)} ; \qquad n_{ROM}^C = f_{ROM}^C . n_{ROM} \quad \text{(S23)}$$
$$n_V^N = f_V^N . n_V \quad \text{(S24)} ; \qquad n_S^N = f_S^N . n_S \quad \text{(S25)} ; \qquad n_{ROM}^N = f_{ROM}^N . n_{ROM} \quad \text{(S26)}$$

with f^C and f^N respectively the fractions of carbon and nitrogen atoms per mole of each reservoir.

The N/C ratio is calculated via:

$$N/C = \frac{n_V^N + n_S^N + n_{ROM}^N}{n_V^C + n_S^C + n_{ROM}^C} \quad \text{(S27)}$$

The results when varying X from 0 to 40 wt% are shown in Figure 4 for pure ammonium formate, and in Figure 5 for different ammonium salts.

The volatiles contribute little to the nitrogen budget (less than 1% N), whatever the dust-to-ice mass ratio within the range from 2 to 6. Fig. 4 shows that the main nitrogen reservoirs are then located in the ROM (presumably in aromatic rings and cyanide chemical groups) and in semi-volatile ammonium ions with their (potentially nitrogen-bearing) counter-ions. Fig. 5 shows ammonium salts may considerably increase the N/C ratio of the whole comet, from 0.035 possibly up to values close to the solar value of 0.29 ± 0.12 (*48*).

These calculations rely on the single value of 0.035 for the N/C ratio in the ROM, which is based on the analysis of a few tens of grains (*47*). We can further test the sensitivity of the nitrogen budget to this parameter by considering a N/C of 0.120, consistent with reported values for N-rich IDPs and micrometeorites of plausible cometary origin (*82*). The distribution of the nitrogen resulting from this calculation is shown in Fig. S8 and the N/C ratio in Fig. S9. Such high N/C values in the ROM were only measured in very rare ultra-carbonaceous Antarctic micro-meteorites (*82*), and such particles are unlikely to represent the bulk N/C of the refractory carbon of a whole comet.

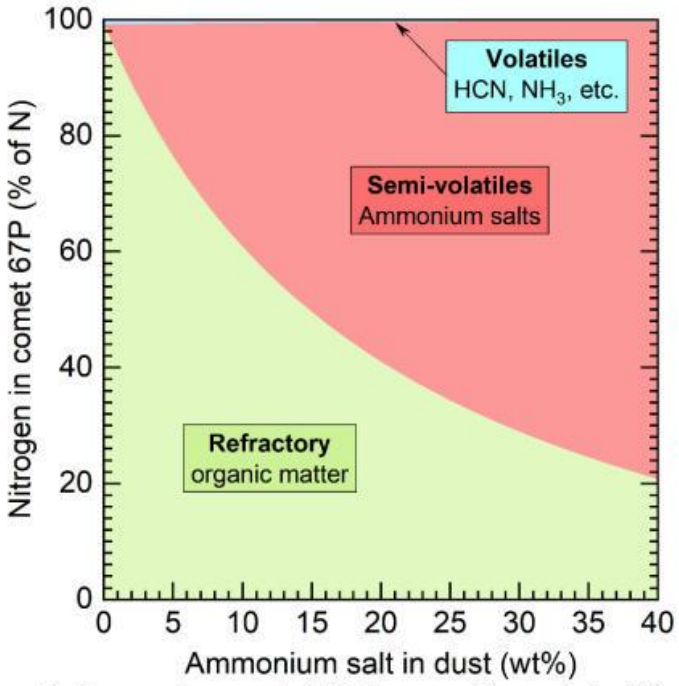

Fig. S8. Distribution of nitrogen in comet 67P. Same as Figure 4, but for a refractory organic matter having a $(N/C)_{ROM}$ ratio of 0.120.

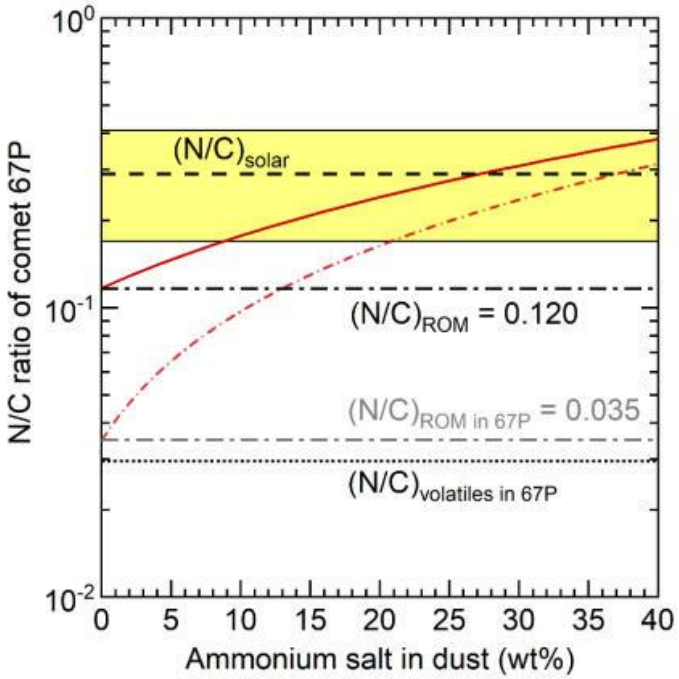

Fig. S9. Nitrogen-to-carbon ratio in comet 67P. Same as Figure 5, but for $(N/C)_{ROM}$ = 0.120 (red line). The case with $(N/C)_{ROM}$ = 0.035 (red short dashed-dotted line) is also shown. The ammonium salt is assumed to be made only of ammonium formate (NH_4^+ $HCOO^-$) in this example.

Observed positions of absorption maxima (±0.01 μm)									Assignment
Comet 67P	**NH_4^+ $HCOO^-$**		**$(NH_4^+)_2$ SO_4^{2-}**		**NH_4^+ Cl^-**		**NH_4^+ CN^-**	**NH_4^+ OCN^-**	
Ref. [a, b]	This work*	Ref. [c]	This work*	Ref. [d, e]	This work*	Ref. [f, g]	Ref. [h]	Ref. [i, k]	
				3.03					NH_4^+ asym. stretching ν_3 [d, e]
3.11	3.12	3.13	3.12	3.10-3.11				3.12 [k]	NH_4^+ comb. ν_1 (sym.) + ν_5 (lattice) [j]
							3.15	3.15-3.16	NH_4^+ asym. stretching ν_3 and/or ν_2 (sym. bending) + ν_4 (asym. bending) [j, h]
					3.18	3.17-3.20			NH_4^+ asym. stretching ν_3 [j]
3.26	3.26	3.25	3.26	3.26-3.28	3.28	3.28			NH_4^+ asym. stretching ν_3 and/or ν_2 (sym. bending) + ν_4 (asym. bending) [j]
							3.29	3.29	NH_4^+ asym. stretching ν_3 and/or ν_2 (sym. bending) + ν_4 (asym. bending) [h]
		3.32							N−H stretching in NH_4^+ [c]
3.38									C−H stretching [a]
3.42									C−H stretching [a]
3.47		3.48							C−H stretching [a] N−H stretching in NH_4^+ [c]
	3.5		3.5	3.50-3.52	3.52-3.56	3.52	3.49	3.50-3.51	NH_4^+ asym. bending overtone $2\nu_4$ [j, h]
		3.56							C−H stretching in $HCOO^-$ [c]
		3.69							2 × C−H in plane bending in $HCOO^-$ [c]

Table S2. Observed absorption bands in the spectra of the nucleus of comet 67P and of some ammonium salts, with their assignments. The absorption bands at 3.11 and 3.26 μm in the spectrum of the comet 67P are assigned to fundamental and/or combination modes of N−H vibrations in NH_4^+ in ammonium salts, such as ammonium formate and sulfate. Ammonium cyanide and cyanate (although not measured under the same conditions) could also partly contribute to the broad absorption band in the 67P spectrum, but their band centers appear shifted toward longer wavelengths. Ammonium chloride appears as a less likely contributor. The absorptions at 3.38, 3.42 and 3.47 μm in the comet spectrum are attributed to C−H stretching vibrations of organic compounds (*10*). The identification on the spectrum of comet 67P of a weaker N−H mode of ammonium salts centered around 3.50 μm is impeded by the proximity of the C−H stretching modes and the limited spectral resolution and sampling (respectively of 0.039 μm and 0.020 μm for the laboratory spectrum and of 0.015 μm and 0.020 μm for the VIRTIS spectrum). Complementary spectroscopic data on ammonium nitrates, phosphates, carbonates and oxalates have been published (*79*).

[*] Reflectance spectra of the ammonium salts in sublimate residues with pyrrhotite sub-micrometric-sized grains at 170-200 K and under high vacuum (< 10^{-5} mbar). The fundamental vibrations of NH_4^+ listed here are ν_1, the symmetric stretching mode, ν_2, the symmetric bending mode, ν_3, the asymmetric stretching mode, ν_4, the asymmetric bending mode, and ν_5 is a lattice mode.

[a] Average reflectance spectrum of the surface of comet 67P obtained from our VIRTIS-M data. The absorption features observed at 3.38, 3.42 and 3.47 μm in this spectrum are attributed to C−H stretching from organic matter (*10*).

[b] Average reflectance spectrum of the surface of comet 67P obtained from VIRTIS-M data (previous calibration) (*5*)

[c] Transmittance spectrum of NH_4^+ $HCOO^-$ at 298 K (*83*)

[d] Transmittance spectrum of $(NH_4^+)_2$ SO_4^{2-} at ambient temperature and pressure conditions (*84*)

[e] Transmittance spectra of $(NH_4^+)_2$ SO_4^{2-} from 288 to 183 K in (*85*). The relative amplitude of the absorptions at 3.1 and 3.3 μm change dramatically with the temperature (*85*).

[f] Reflectance spectrum of NH_4^+ Cl^- at 123 K (*86*)

[g] Transmittance spectrum of NH_4^+ Cl^- at 250 K (*87*)

[h] Transmittance spectrum of NH_4^+ CN^- at 125 K (*88*)

[i] Transmittance spectrum of NH_4^+ OCN^- at 250 K (*87*)

[j] Assignment according to (*89*). The intense absorptions of ammonium salts in the 3.2-μm region are proposed to be due to Fermi resonance between the fundamental ν_3 and the combination $\nu_2 + \nu_4$ (*86*, *89*).

[k] Transmittance spectrum of NH_4^+ OCN^- at 160 K (*21*)

References and Notes

1. A. S. Rivkin *et al.*, Astronomical observations of volatiles on asteroids, in *Asteroids IV*, P. Michel, F. E. DeMeo, W. F. Bottke, Eds. (Univ. Arizona Press, 2015), pp. 65–87.

2. A. Coradini, F. Capaccioni, P. Drossart, G. Arnold, E. Ammannito, F. Angrilli, A. Barucci, G. Bellucci, J. Benkhoff, G. Bianchini, J. P. Bibring, M. Blecka, D. Bockelee-Morvan, M. T. Capria, R. Carlson, U. Carsenty, P. Cerroni, L. Colangeli, M. Combes, M. Combi, J. Crovisier, M. C. Desanctis, E. T. Encrenaz, S. Erard, C. Federico, G. Filacchione, U. Fink, S. Fonti, V. Formisano, W. H. Ip, R. Jaumann, E. Kuehrt, Y. Langevin, G. Magni, T. Mccord, V. Mennella, S. Mottola, G. Neukum, P. Palumbo, G. Piccioni, H. Rauer, B. Saggin, B. Schmitt, D. Tiphene, G. Tozzi, Virtis: An imaging spectrometer for the Rosetta mission. *Space Sci. Rev.* **128**, 529–559 (2007). doi:10.1007/s11214-006-9127-5

3. F. Capaccioni, A. Coradini, G. Filacchione, S. Erard, G. Arnold, P. Drossart, M. C. De Sanctis, D. Bockelee-Morvan, M. T. Capria, F. Tosi, C. Leyrat, B. Schmitt, E. Quirico, P. Cerroni, V. Mennella, A. Raponi, M. Ciarniello, T. McCord, L. Moroz, E. Palomba, E. Ammannito, M. A. Barucci, G. Bellucci, J. Benkhoff, J. P. Bibring, A. Blanco, M. Blecka, R. Carlson, U. Carsenty, L. Colangeli, M. Combes, M. Combi, J. Crovisier, T. Encrenaz, C. Federico, U. Fink, S. Fonti, W. H. Ip, P. Irwin, R. Jaumann, E. Kuehrt, Y. Langevin, G. Magni, S. Mottola, V. Orofino, P. Palumbo, G. Piccioni, U. Schade, F. Taylor, D. Tiphene, G. P. Tozzi, P. Beck, N. Biver, L. Bonal, J.-P. Combe, D. Despan, E. Flamini, S. Fornasier, A. Frigeri, D. Grassi, M. Gudipati, A. Longobardo, K. Markus, F. Merlin, R. Orosei, G. Rinaldi, K. Stephan, M. Cartacci, A. Cicchetti, S. Giuppi, Y. Hello, F. Henry, S. Jacquinod, R. Noschese, G. Peter, R. Politi, J. M. Reess, A. Semery, Cometary science. The organic-rich surface of comet 67P/Churyumov-Gerasimenko as seen by VIRTIS/Rosetta. *Science* **347**, aaa0628 (2015). doi:10.1126/science.aaa0628 Medline

4. G. Filacchione, F. Capaccioni, M. Ciarniello, A. Raponi, F. Tosi, M. C. De Sanctis, S. Erard, D. B. Morvan, C. Leyrat, G. Arnold, B. Schmitt, E. Quirico, G. Piccioni, A. Migliorini, M. T. Capria, E. Palomba, P. Cerroni, A. Longobardo, A. Barucci, S. Fornasier, R. W. Carlson, R. Jaumann, K. Stephan, L. V. Moroz, D. Kappel, B. Rousseau, S. Fonti, F. Mancarella, D. Despan, M. Faure, The global surface composition of 67P/CG nucleus by Rosetta/VIRTIS. (I) Prelanding mission phase. *Icarus* **274**, 334–349 (2016). doi:10.1016/j.icarus.2016.02.055

5. M. Ciarniello, F. Capaccioni, G. Filacchione, A. Raponi, F. Tosi, M. C. De Sanctis, M. T. Capria, S. Erard, D. Bockelee-Morvan, C. Leyrat, G. Arnold, A. Barucci, P. Beck, G. Bellucci, S. Fornasier, A. Longobardo, S. Mottola, E. Palomba, E. Quirico, B. Schmitt, Photometric properties of comet 67P/Churyumov-Gerasimenko from VIRTIS-M onboard Rosetta. *Astron. Astrophys.* **583**, A31 (2015). doi:10.1051/0004-6361/201526307

6. M. Ciarniello, A. Raponi, F. Capaccioni, G. Filacchione, F. Tosi, M. C. DeSanctis, D. Kappel, B. Rousseau, G. Arnold, M. T. Capria, M. A. Barucci, E. Quirico, A. Longobardo, E. Kuehrt, S. Mottola, S. Erard, D. Bockelee-Morvan, C. Leyrat, A. Migliorini, A. Zinzi, E. Palomba, B. Schmitt, G. Piccioni, P. Cerroni, W.-H. Ip, G. Rinaldi, M. Salatti, The global surface composition of 67P/Churyumov-Gerasimenko nucleus by Rosetta/VIRTIS. II)

Diurnal and seasonal variability. *Mon. Not. R. Astron. Soc.* **462**, S443–S458 (2016). doi:10.1093/mnras/stw3177

7. M. C. De Sanctis, F. Capaccioni, M. Ciarniello, G. Filacchione, M. Formisano, S. Mottola, A. Raponi, F. Tosi, D. Bockelée-Morvan, S. Erard, C. Leyrat, B. Schmitt, E. Ammannito, G. Arnold, M. A. Barucci, M. Combi, M. T. Capria, P. Cerroni, W.-H. Ip, E. Kuehrt, T. B. McCord, E. Palomba, P. Beck, E. Quirico; VIRTIS Team, The diurnal cycle of water ice on comet 67P/Churyumov-Gerasimenko. *Nature* **525**, 500–503 (2015). doi:10.1038/nature14869 Medline

8. G. Filacchione, M. C. De Sanctis, F. Capaccioni, A. Raponi, F. Tosi, M. Ciarniello, P. Cerroni, G. Piccioni, M. T. Capria, E. Palomba, G. Bellucci, S. Erard, D. Bockelee-Morvan, C. Leyrat, G. Arnold, M. A. Barucci, M. Fulchignoni, B. Schmitt, E. Quirico, R. Jaumann, K. Stephan, A. Longobardo, V. Mennella, A. Migliorini, E. Ammannito, J. Benkhoff, J. P. Bibring, A. Blanco, M. I. Blecka, R. Carlson, U. Carsenty, L. Colangeli, M. Combes, M. Combi, J. Crovisier, P. Drossart, T. Encrenaz, C. Federico, U. Fink, S. Fonti, W. H. Ip, P. Irwin, E. Kuehrt, Y. Langevin, G. Magni, T. McCord, L. Moroz, S. Mottola, V. Orofino, U. Schade, F. Taylor, D. Tiphene, G. P. Tozzi, P. Beck, N. Biver, L. Bonal, J.-P. Combe, D. Despan, E. Flamini, M. Formisano, S. Fornasier, A. Frigeri, D. Grassi, M. S. Gudipati, D. Kappel, F. Mancarella, K. Markus, F. Merlin, R. Orosei, G. Rinaldi, M. Cartacci, A. Cicchetti, S. Giuppi, Y. Hello, F. Henry, S. Jacquinod, J. M. Reess, R. Noschese, R. Politi, G. Peter, Exposed water ice on the nucleus of comet 67P/Churyumov-Gerasimenko. *Nature* **529**, 368–372 (2016). doi:10.1038/nature16190 Medline

9. G. Filacchione, O. Groussin, C. Herny, D. Kappel, S. Mottola, N. Oklay, A. Pommerol, I. Wright, Z. Yoldi, M. Ciarniello, L. Moroz, A. Raponi, Comet 67P/CG nucleus composition and comparison to other comets. *Space Sci. Rev.* **215**, 19 (2019). doi:10.1007/s11214-019-0580-3

10. A. Raponi *et al*., Infrared detection of aliphatic organics on a cometary nucleus. *Nature Astronomy*. doi: 10.1038/s41550-019-0992-8 (2020).

11. E. Quirico, L. V. Moroz, B. Schmitt, G. Arnold, M. Faure, P. Beck, L. Bonal, M. Ciarniello, F. Capaccioni, G. Filacchione, S. Erard, C. Leyrat, D. Bockelée-Morvan, A. Zinzi, E. Palomba, P. Drossart, F. Tosi, M. T. Capria, M. C. De Sanctis, A. Raponi, S. Fonti, F. Mancarella, V. Orofino, A. Barucci, M. I. Blecka, R. Carlson, D. Despan, A. Faure, S. Fornasier, M. S. Gudipati, A. Longobardo, K. Markus, V. Mennella, F. Merlin, G. Piccioni, B. Rousseau, F. Taylor, Refractory and semi-volatile organics at the surface of comet 67P/Churyumov-Gerasimenko: Insights from the VIRTIS/Rosetta imaging spectrometer. *Icarus* **272**, 32–47 (2016). doi:10.1016/j.icarus.2016.02.028

12. Materials and methods are available as supplementary materials.

13. A.-C. Levasseur-Regourd, J. Agarwal, H. Cottin, C. Engrand, G. Flynn, M. Fulle, T. Gombosi, Y. Langevin, J. Lasue, T. Mannel, S. Merouane, O. Poch, N. Thomas, A. Westphal, Cometary dust. *Space Sci. Rev.* **214**, 64 (2018). doi:10.1007/s11214-018-0496-3

14. B. Rousseau, S. Érard, P. Beck, É. Quirico, B. Schmitt, O. Brissaud, G. Montes-Hernandez, F. Capaccioni, G. Filacchione, D. Bockelée-Morvan, C. Leyrat, M. Ciarniello, A. Raponi,

D. Kappel, G. Arnold, L. V. Moroz, E. Palomba, F. Tosi, Laboratory simulations of the Vis-NIR spectra of comet 67P using sub-μm sized cosmochemical analogues. *Icarus* **306**, 306–318 (2018). doi:10.1016/j.icarus.2017.10.015

15. O. Poch, A. Pommerol, B. Jost, N. Carrasco, C. Szopa, N. Thomas, Sublimation of water ice mixed with silicates and tholins: Evolution of surface texture and reflectance spectra, with implications for comets. *Icarus* **267**, 154–173 (2016). doi:10.1016/j.icarus.2015.12.017

16. L. Le Roy, K. Altwegg, H. Balsiger, J.-J. Berthelier, A. Bieler, C. Briois, U. Calmonte, M. R. Combi, J. De Keyser, F. Dhooghe, B. Fiethe, S. A. Fuselier, S. Gasc, T. I. Gombosi, M. Hässig, A. Jäckel, M. Rubin, C.-Y. Tzou, Inventory of the volatiles on comet 67P/Churyumov-Gerasimenko from Rosetta/ROSINA. *Astron. Astrophys.* **583**, A1 (2015). doi:10.1051/0004-6361/201526450

17. E. Carrasco, I. Tanarro, V. J. Herrero, J. Cernicharo, Proton transfer chains in cold plasmas of H_2 with small amounts of N_2. The prevalence of $NH4^+$. *Phys. Chem. Chem. Phys.* **15**, 1699–1706 (2013). doi:10.1039/C2CP43438E Medline

18. P. Theulé, F. Duvernay, G. Danger, F. Borget, J. B. Bossa, V. Vinogradoff, F. Mispelaer, T. Chiavassa, Thermal reactions in interstellar ice: A step towards molecular complexity in the interstellar medium. *Adv. Space Res.* **52**, 1567–1579 (2013). doi:10.1016/j.asr.2013.06.034

19. O. Gálvez, B. Maté, V. J. Herrero, R. Escribano, Ammonium and formate ions in interstellar ice analogs. *Astrophys. J.* **724**, 539–545 (2010). doi:10.1088/0004-637X/724/1/539

20. W. A. Schutte *et al*., Weak ice absorption features at 7.24 and 7.41 μm in the spectrum of the obscured young stellar object W 33A. *Astron. Astrophys.* **343**, 966–976 (1999).

21. S. Raunier, T. Chiavassa, F. Marinelli, A. Allouche, J. P. Aycard, Reactivity of HNCO with NH3 at low temperature monitored by FTIR spectroscopy: Formation of $NH4^+OCN^-$. *Chem. Phys. Lett.* **368**, 594–600 (2003). doi:10.1016/S0009-2614(02)01919-X

22. K. Demyk *et al*., Laboratory identification of the 4.62μm solid state absorption band in the ISO-SWS spectrum of RAFGL 7009S. *Astron. Astrophys.* **339**, 553–560 (1998).

23. F. A. van Broekhuizen, K. M. Pontoppidan, H. J. Fraser, E. F. van Dishoeck, A 3–5 μm VLT spectroscopic survey of embedded young low mass stars II: Solid OCN-. *Astron. Astrophys.* **441**, 249–260 (2005). doi:10.1051/0004-6361:20041711

24. K. M. Pontoppidan, H. J. Fraser, E. Dartois, W.-F. Thi, E. F. van Dishoeck, A. C. A. Boogert, L. d'Hendecourt, A. G. G. M. Tielens, S. E. Bisschop, A μm VLT spectroscopic survey of embedded young low mass stars I–Structure of the CO ice. *Astron. Astrophys.* **408**, 981–1007 (2003). doi:10.1051/0004-6361:20031030

25. A. C. A. Boogert, P. A. Gerakines, D. C. B. Whittet, Observations of the icy universe. *Annu. Rev. Astron. Astrophys.* **53**, 541–581 (2015). doi:10.1146/annurev-astro-082214-122348

26. W. Schutte, R. Khanna, Origin of the 6.85 μm band near young stellar objects: The ammonium ion ($NH4^+$) revisited. *Astron. Astrophys.* **398**, 1049–1062 (2003). doi:10.1051/0004-6361:20021705

27. J. V. Keane, A. G. G. M. Tielens, A. C. A. Boogert, W. A. Schutte, D. C. B. Whittet, Ice absorption features in the 5-8 μm region toward embedded protostars. *Astron. Astrophys.* **376**, 254–270 (2001). doi:10.1051/0004-6361:20010936

28. A. C. A. Boogert, K. M. Pontoppidan, C. Knez, F. Lahuis, J. Kessler-Silacci, E. F. van Dishoeck, G. A. Blake, J.-C. Augereau, S. E. Bisschop, S. Bottinelli, T. Y. Brooke, J. Brown, A. Crapsi, N. J. Evans II, H. J. Fraser, V. Geers, T. L. Huard, J. K. Jørgensen, K. I. Öberg, L. E. Allen, P. M. Harvey, D. W. Koerner, L. G. Mundy, D. L. Padgett, A. I. Sargent, K. R. Stapelfeldt, The c2d Spitzer spectroscopic survey of ices around low-mass young stellar objects. I. H_2O and the 5–8 μm bands. *Astrophys. J.* **678**, 985–1004 (2008). doi:10.1086/533425

29. B. Maté, O. Gálvez, V. J. Herrero, D. Fernández-Torre, M. A. Moreno, R. Escribano, Water-ammonium ices and the elusive 6.85 μm band. *Astrophys. J.* **703**, L178–L182 (2009). doi:10.1088/0004-637X/703/2/L178

30. J. B. Bergner, K. I. Öberg, M. Rajappan, E. C. Fayolle, Kinetics and mechanisms of the acid-base reaction between NH_3 and HCOOH in interstellar ice analogs. *Astrophys. J.* **829**, 85 (2016). doi:10.3847/0004-637X/829/2/85

31. A. Potapov, P. Theulé, C. Jäger, T. Henning, Evidence of surface catalytic effect on cosmic dust grain analogs: The ammonia and carbon dioxide surface reaction. *Astrophys. J.* **878**, L20 (2019). doi:10.3847/2041-8213/ab2538

32. D. Takir, J. P. Emery, Outer Main Belt asteroids: Identification and distribution of four 3-μm spectral groups. *Icarus* **219**, 641–654 (2012). doi:10.1016/j.icarus.2012.02.022

33. M. E. Brown, A. R. Rhoden, The 3 μm spectrum of Jupiter's irregular satellite himalia. *Astrophys. J.* **793**, L44 (2014). doi:10.1088/2041-8205/793/2/L44

34. M. C. De Sanctis, E. Ammannito, F. G. Carrozzo, M. Ciarniello, M. Giardino, A. Frigeri, S. Fonte, H. Y. McSween, A. Raponi, F. Tosi, F. Zambon, C. A. Raymond, C. T. Russell, Ceres's global and localized mineralogical composition determined by Dawn's Visible and Infrared Spectrometer (VIR). *Meteorit. Planet. Sci.* **53**, 1844–1865 (2018). doi:10.1111/maps.13104

35. M. Gounelle, M. E. Zolensky, The Orgueil meteorite: 150 years of history. *Meteorit. Planet. Sci.* **49**, 1769–1794 (2014). doi:10.1111/maps.12351

36. S. Pizzarello, X. Feng, S. Epstein, J. R. Cronin, Isotopic analyses of nitrogenous compounds from the Murchison meteorite: Ammonia, amines, amino acids, and polar hydrocarbons. *Geochim. Cosmochim. Acta* **58**, 5579–5587 (1994). doi:10.1016/0016-7037(94)90251-8 Medline

37. M. J. Mumma *et al*., paper presented at the 50th American Astronomical Society DPS meeting, Knoxville, TN, 12-26 October 2018; http://adsabs.harvard.edu/abs/2018DPS....5020902M

38. M. A. DiSanti, B. P. Bonev, E. L. Gibb, L. Paganini, G. L. Villanueva, M. J. Mumma, J. V. Keane, G. A. Blake, N. D. Russo, K. J. Meech, R. J. Vervack Jr., A. J. McKay, En route to destruction: The evolution in composition of ices in comet D/2012 S1 (ISON) between 1.2 and 0.34 AU from the sun as revealed at infrared wavelengths. *Astrophys. J.* **820**, 34 (2016). doi:10.3847/0004-637X/820/1/34

39. N. Dello Russo, R. J. Vervack Jr., H. Kawakita, A. Cochran, A. J. McKay, W. M. Harris, H. A. Weaver, C. M. Lisse, M. A. DiSanti, H. Kobayashi, N. Biver, D. Bockelée-Morvan, J. Crovisier, C. Opitom, E. Jehin, The compositional evolution of C/2012 S1 (ISON) from ground-based high-resolution infrared spectroscopy as part of a worldwide observing campaign. *Icarus* **266**, 152–172 (2016). doi:10.1016/j.icarus.2015.11.030

40. K. Altwegg, H. Balsiger, J. J. Berthelier, A. Bieler, U. Calmonte, S. A. Fuselier, F. Goesmann, S. Gasc, T. I. Gombosi, L. Le Roy, J. de Keyser, A. Morse, M. Rubin, M. Schuhmann, M. G. G. T. Taylor, C.-Y. Tzou, I. Wright, Organics in comet 67P–A first comparative analysis of mass spectra from ROSINA–DFMS, COSAC and Ptolemy. *Mon. Not. R. Astron. Soc.* **469** (Suppl_2), S130–S141 (2017). doi:10.1093/mnras/stx1415

41. F. Goesmann, H. Rosenbauer, J. H. Bredehöft, M. Cabane, P. Ehrenfreund, T. Gautier, C. Giri, H. Krüger, L. Le Roy, A. J. MacDermott, S. McKenna-Lawlor, U. J. Meierhenrich, G. M. Muñoz Caro, F. Raulin, R. Roll, A. Steele, H. Steininger, R. Sternberg, C. Szopa, W. Thiemann, S. Ulamec, Organic compounds on comet 67P/Churyumov-Gerasimenko revealed by COSAC mass spectrometry. *Science* **349**, aab0689 (2015). doi:10.1126/science.aab0689 Medline

42. N. Hänni, S. Gasc, A. Etter, M. Schuhmann, I. Schroeder, S. F. Wampfler, S. Schürch, M. Rubin, K. Altwegg, Ammonium salts as a source of small molecules observed with high-resolution electron-impact ionization mass spectrometry. *J. Phys. Chem. A* **123**, 5805–5814 (2019). doi:10.1021/acs.jpca.9b03534 Medline

43. D. R. Lide, Physical constants of inorganic compounds, in *CRC Handbook of Chemistry and Physics* (CRC Press, ed. 90, 2009), pp. 4-46–4-48.

44. G. Danger, F. Borget, M. Chomat, F. Duvernay, P. Theulé, J.-C. Guillemin, L. Le Sergeant d'Hendecourt, T. Chiavassa, Experimental investigation of aminoacetonitrile formation through the Strecker synthesis in astrophysical-like conditions: Reactivity of methanimine (CH_2NH), ammonia (NH_3), and hydrogen cyanide (HCN). *Astron. Astrophys.* **535**, A47 (2011). doi:10.1051/0004-6361/201117602

45. V. Vinogradoff, F. Duvernay, G. Danger, P. Theulé, T. Chiavassa, New insight into the formation of hexamethylenetetramine (HMT) in interstellar and cometary ice analogs. *Astron. Astrophys.* **530**, A128 (2011). doi:10.1051/0004-6361/201116688

46. J. B. Bossa, P. Theulé, F. Duvernay, F. Borget, T. Chiavassa, Carbamic acid and carbamate formation in NH_3:CO_2 ices–UV irradiation versus thermal processes. *Astron. Astrophys.* **492**, 719–724 (2008). doi:10.1051/0004-6361:200810536

47. N. Fray, A. Bardyn, H. Cottin, D. Baklouti, C. Briois, C. Engrand, H. Fischer, K. Hornung, R. Isnard, Y. Langevin, H. Lehto, L. Le Roy, E. M. Mellado, S. Merouane, P. Modica, F.-R. Orthous-Daunay, J. Paquette, J. Rynö, R. Schulz, J. Silén, S. Siljeström, O. Stenzel, L. Thirkell, K. Varmuza, B. Zaprudin, J. Kissel, M. Hilchenbach, Nitrogen-to-carbon atomic ratio measured by COSIMA in the particles of comet 67P/Churyumov–Gerasimenko. *Mon. Not. R. Astron. Soc.* **469** (Suppl_2), S506–S516 (2017). doi:10.1093/mnras/stx2002

48. K. Lodders, in *Principles and Perspectives in Cosmochemistry* (Springer, 2010), *Astrophysics and Space Science Proceedings*, pp. 379–417.

49. N. Dello Russo, H. Kawakita, R. J. Vervack Jr., H. A. Weaver, Emerging trends and a comet taxonomy based on the volatile chemistry measured in thirty comets with high-resolution infrared spectroscopy between 1997 and 2013. *Icarus* **278**, 301–332 (2016). doi:10.1016/j.icarus.2016.05.039

50. M. Rubin, K. Altwegg, H. Balsiger, A. Bar-Nun, J.-J. Berthelier, A. Bieler, P. Bochsler, C. Briois, U. Calmonte, M. Combi, J. De Keyser, F. Dhooghe, P. Eberhardt, B. Fiethe, S. A. Fuselier, S. Gasc, T. I. Gombosi, K. C. Hansen, M. Hässig, A. Jäckel, E. Kopp, A. Korth, L. Le Roy, U. Mall, B. Marty, O. Mousis, T. Owen, H. Rème, T. Sémon, C.-Y. Tzou, J. H. Waite, P. Wurz, Molecular nitrogen in comet 67P/Churyumov-Gerasimenko indicates a low formation temperature. *Science* **348**, 232–235 (2015). doi:10.1126/science.aaa6100 Medline

51. S. Wyckoff, S. C. Tegler, L. Engel, Nitrogen abundance in Comet Halley. *Astrophys. J.* **367**, 641 (1991). doi:10.1086/169659

52. A. Bardyn, D. Baklouti, H. Cottin, N. Fray, C. Briois, J. Paquette, O. Stenzel, C. Engrand, H. Fischer, K. Hornung, R. Isnard, Y. Langevin, H. Lehto, L. Le Roy, N. Ligier, S. Merouane, P. Modica, F.-R. Orthous-Daunay, J. Rynö, R. Schulz, J. Silén, L. Thirkell, K. Varmuza, B. Zaprudin, J. Kissel, M. Hilchenbach, Carbon-rich dust in comet 67P/Churyumov-Gerasimenko measured by COSIMA/Rosetta. *Mon. Not. R. Astron. Soc.* **469** (Suppl_2), S712–S722 (2017). doi:10.1093/mnras/stx2640

53. E. Füri, B. Marty, Nitrogen isotope variations in the Solar System. *Nat. Geosci.* **8**, 515–522 (2015). doi:10.1038/ngeo2451

54. K. Lodders, Jupiter formed with more tar than ice. *Astrophys. J.* **611**, 587–597 (2004). doi:10.1086/421970

55. J. S. Kargel, Ammonia-water volcanism on icy satellites: Phase relations at 1 atmosphere. *Icarus* **100**, 556–574 (1992). doi:10.1016/0019-1035(92)90118-Q

56. M. P. Callahan, K. E. Smith, H. J. Cleaves 2nd, J. Ruzicka, J. C. Stern, D. P. Glavin, C. H. House, J. P. Dworkin, Carbonaceous meteorites contain a wide range of extraterrestrial nucleobases. *Proc. Natl. Acad. Sci. U.S.A.* **108**, 13995–13998 (2011). doi:10.1073/pnas.1106493108 Medline

57. N. R. Lerner, G. W. Cooper, Iminodicarboxylic acids in the Murchison meteorite: Evidence of Strecker reactions. *Geochim. Cosmochim. Acta* **69**, 2901–2906 (2005). doi:10.1016/j.gca.2004.12.024

58. B. Burcar, M. Pasek, M. Gull, B. J. Cafferty, F. Velasco, N. V. Hud, C. Menor-Salván, Darwin's warm little pond: A one-pot reaction for prebiotic phosphorylation and the mobilization of phosphate from minerals in a urea-based solvent. *Angew. Chem. Int. Ed.* **55**, 13249–13253 (2016). doi:10.1002/anie.201606239 Medline

59. P. Dziedzic, A. Bartoszewicz, A. Córdova, Inorganic ammonium salts as catalysts for direct aldol reactions in the presence of water. *Tetrahedron Lett.* **50**, 7242–7245 (2009). doi:10.1016/j.tetlet.2009.10.014

60. B. Hapke, *Theory of Reflectance and Emittance Spectroscopy* (Cambridge Univ. Press, ed. 2, 2012).

61. B. Schmitt, Near and Mid-IR optical constants of crystalline H2O ice Ih at 140–145K. SSHADE/GhoSST (OSUG Data Center). Dataset/Spectral Data. (2004); doi:10.26302/SSHADE/EXPERIMENT_BS_20200103_001

62. D. Takir, J. P. Emery, H. Y. Mcsween Jr., C. A. Hibbitts, R. N. Clark, N. Pearson, A. Wang, Nature and degree of aqueous alteration in CM and CI carbonaceous chondrites. *Meteorit. Planet. Sci.* **48**, 1618–1637 (2013). doi:10.1111/maps.12171

63. A. S. Rivkin, J. P. Emery, Detection of ice and organics on an asteroidal surface. *Nature* **464**, 1322–1323 (2010). doi:10.1038/nature09028 Medline

64. J. Licandro, H. Campins, M. Kelley, K. Hargrove, N. Pinilla-Alonso, D. Cruikshank, A. S. Rivkin, J. Emery, (65) Cybele: Detection of small silicate grains, water-ice, and organics. *Astron. Astrophys.* **525**, A34 (2011). doi:10.1051/0004-6361/201015339

65. M. E. Brown, The 3-4 μm spectra of Jupiter Trojan asteroids. *Astron. J.* **152**, 159 (2016). doi:10.3847/0004-6256/152/6/159

66. J. P. Emery, D. M. Burr, D. P. Cruikshank, Near-infrared spectroscopy of Trojan Asteroids: Evidence for two compositional groups. *Astron. J.* **141**, 25 (2011). doi:10.1088/0004-6256/141/1/25

67. O. Poch, I. Istiqomah, Vis-NIR bidirectional reflection spectra of several ammonium salts mixed with pyrrhotite grains in sublimate residues at 173 K. SSHADE/GhoSST (OSUG Data Center) Dataset/Spectral Data (2018); doi:10.26302/SSHADE/EXPERIMENT_OP_20191119_001

68. O. Poch, Vis-NIR bidirectional reflection spectra of several ammonium salts mixed with graphite powder at 296 K. SSHADE/GhoSST (OSUG Data Center) Dataset/Spectral Data (2018); doi:10.26302/SSHADE/EXPERIMENT_OP_20200212_001

69. O. Poch, A. Pommerol, B. Jost, N. Carrasco, C. Szopa, N. Thomas, Sublimation of ice–tholins mixtures: A morphological and spectro-photometric study. *Icarus* **266**, 288–305 (2016). doi:10.1016/j.icarus.2015.11.006

70. F. Grisolle *et al*., paper presented at the European Planetary Science Congress, Cascais, Portugal, 7–12 September 2014; http://meetingorganizer.copernicus.org/EPSC2014/EPSC2014-635-1.pdf

71. O. Brissaud, B. Schmitt, N. Bonnefoy, S. Douté, P. Rabou, W. Grundy, M. Fily, Spectrogonio radiometer for the study of the bidirectional reflectance and polarization functions of planetary surfaces. 1. Design and tests. *Appl. Opt.* **43**, 1926–1937 (2004). doi:10.1364/AO.43.001926 Medline

72. S. Potin, O. Brissaud, P. Beck, B. Schmitt, Y. Magnard, J.-J. Correia, P. Rabou, L. Jocou, SHADOWS: a spectro-gonio radiometer for bidirectional reflectance studies of dark meteorites and terrestrial analogs: design, calibrations, and performances on challenging surfaces. *Appl. Opt.* **57**, 8279–8296 (2018). doi:10.1364/AO.57.008279 Medline

73. N. Bonnefoy, thesis, Université Joseph Fourier, Grenoble, France (2001).

74. A. Coradini, F. Capaccioni, S. Erard, G. Arnold, M. C. De Sanctis, G. Filacchione, F. Tosi, M. A. Barucci, M. T. Capria, E. Ammannito, D. Grassi, G. Piccioni, S. Giuppi, G. Bellucci, J. Benkhoff, J. P. Bibring, A. Blanco, M. Blecka, D. Bockelee-Morvan, F.

Carraro, R. Carlson, U. Carsenty, P. Cerroni, L. Colangeli, M. Combes, M. Combi, J. Crovisier, P. Drossart, E. T. Encrenaz, C. Federico, U. Fink, S. Fonti, L. Giacomini, W. H. Ip, R. Jaumann, E. Kuehrt, Y. Langevin, G. Magni, T. McCord, V. Mennella, S. Mottola, G. Neukum, V. Orofino, P. Palumbo, U. Schade, B. Schmitt, F. Taylor, D. Tiphene, G. Tozzi, The surface composition and temperature of asteroid 21 Lutetia as observed by Rosetta/VIRTIS. *Science* **334**, 492–494 (2011). doi:10.1126/science.1204062 Medline

75. G. Filacchione, thesis, Università di Napoli Federico II, Napoli, Italy (2006).

76. P. N. Stewart *et al*., An atlas of bright star spectra in the near-infrared from Cassini-VIMS. *The Astrophysical Journal Supplement Series*. **221**, article id. 30, 10 (2015).

77. R. H. Brown, K. H. Baines, G. Bellucci, J.-P. Bibring, B. J. Buratti, F. Capaccioni, P. Cerroni, R. N. Clark, A. Coradini, D. P. Cruikshank, P. Drossart, V. Formisano, R. Jaumann, Y. Langevin, D. L. Matson, T. B. Mccord, V. Mennella, E. Miller, R. M. Nelson, P. D. Nicholson, B. Sicardy, C. Sotin, The Cassini Visual And Infrared Mapping Spectrometer (VIMS) Investigation. *Space Sci. Rev.* **115**, 111–168 (2004). doi:10.1007/s11214-004-1453-x

78. A. Raponi, M. Ciarniello, F. Capaccioni, G. Filacchione, F. Tosi, M. C. De Sanctis, M. T. Capria, M. A. Barucci, A. Longobardo, E. Palomba, D. Kappel, G. Arnold, S. Mottola, B. Rousseau, E. Quirico, G. Rinaldi, S. Erard, D. Bockelee-Morvan, C. Leyrat, The temporal evolution of exposed water ice-rich areas on the surface of 67P/Churyumov-Gerasimenko: Spectral analysis. *Mon. Not. R. Astron. Soc.* **462**, S476–S490 (2016). doi:10.1093/mnras/stw3281

79. B. L. Berg, E. A. Cloutis, P. Beck, P. Vernazza, J. L. Bishop, D. Takir, V. Reddy, D. Applin, P. Mann, Reflectance spectroscopy (0.35–8μm) of ammonium-bearing minerals and qualitative comparison to Ceres-like asteroids. *Icarus* **265**, 218–237 (2016). doi:10.1016/j.icarus.2015.10.028

80. A. Rotundi, H. Sierks, V. Della Corte, M. Fulle, P. J. Gutierrez, L. Lara, C. Barbieri, P. L. Lamy, R. Rodrigo, D. Koschny, H. Rickman, H. U. Keller, J. J. López-Moreno, M. Accolla, J. Agarwal, M. F. A'Hearn, N. Altobelli, F. Angrilli, M. A. Barucci, J.-L. Bertaux, I. Bertini, D. Bodewits, E. Bussoletti, L. Colangeli, M. Cosi, G. Cremonese, J.-F. Crifo, V. Da Deppo, B. Davidsson, S. Debei, M. De Cecco, F. Esposito, M. Ferrari, S. Fornasier, F. Giovane, B. Gustafson, S. F. Green, O. Groussin, E. Grün, C. Güttler, M. L. Herranz, S. F. Hviid, W. Ip, S. Ivanovski, J. M. Jerónimo, L. Jorda, J. Knollenberg, R. Kramm, E. Kührt, M. Küppers, M. Lazzarin, M. R. Leese, A. C. López-Jiménez, F. Lucarelli, S. C. Lowry, F. Marzari, E. M. Epifani, J. A. M. McDonnell, V. Mennella, H. Michalik, A. Molina, R. Morales, F. Moreno, S. Mottola, G. Naletto, N. Oklay, J. L. Ortiz, E. Palomba, P. Palumbo, J.-M. Perrin, J. Rodríguez, L. Sabau, C. Snodgrass, R. Sordini, N. Thomas, C. Tubiana, J.-B. Vincent, P. Weissman, K.-P. Wenzel, V. Zakharov, J. C. Zarnecki, Cometary science. Dust measurements in the coma of comet 67P/Churyumov-Gerasimenko inbound to the Sun. *Science* **347**, aaa3905 (2015). doi:10.1126/science.aaa3905 Medline

81. U. Marboeuf, B. Schmitt, How to link the relative abundances of gas species in coma of comets to their initial chemical composition? *Icarus* **242**, 225–248 (2014). doi:10.1016/j.icarus.2014.07.001

82. E. Dartois, C. Engrand, J. Duprat, M. Godard, E. Charon, L. Delauche, C. Sandt, F. Borondics, Dome C ultracarbonaceous Antarctic micrometeorites: Infrared and Raman fingerprints. *Astron. Astrophys.* **609**, A65 (2018). doi:10.1051/0004-6361/201731322

83. S. Hamann, E. Spinner, The effect of pressure on the infrared spectrum of ammonium formate: HCO_2NH_4, DCO_2NH_4, HCO_2ND_4, DCO_2ND_4. An unusual intermolecular coupling of non-identical vibrations in phase II. *Aust. J. Chem.* **30**, 2591 (1977). doi:10.1071/CH9772591

84. D. D. Weis, G. E. Ewing, Infrared spectroscopic signatures of $(NH_4)_2SO_4$ aerosols. *J. Geophys. Res. D Atmospheres* **101**, 18709–18720 (1996). doi:10.1029/96JD01543

85. T. J. Fortin, J. E. Shilling, M. A. Tolbert, Infrared spectroscopic study of the low-temperature phase behavior of ammonium sulfate. *J. Geophys. Res. D Atmospheres* **107**, AAC 4-1–AAC 4-9 (2002). doi:10.1029/2001JD000677

86. L. F. H. Bovey, The infrared absorption and reflection spectra of the ammonium halides. *J. Opt. Soc. Am.* **41**, 836 (1951). doi:10.1364/JOSA.41.000836

87. M. H. Moore, R. L. Hudson, R. F. Ferrante, Radiation products in processed ices relevant to Edgeworth-Kuiper-Belt objects. *Earth Moon Planets* **92**, 291–306 (2003). doi:10.1023/B:MOON.0000031946.53696.f6

88. D. R. Clutter, W. E. Thompson, Infrared spectroscopic study of polycrystalline NH_4CN. *J. Chem. Phys.* **51**, 153–159 (1969). doi:10.1063/1.1671702

89. E. L. Wagner, D. F. Hornig, The vibrational spectra of molecules and complex ions in crystals III. Ammonium chloride and deutero-ammonium chloride. *J. Chem. Phys.* **18**, 296–304 (1950). doi:10.1063/1.1747622

Conclusions and perspectives

In this thesis, we have focused on the interpretation of the 3.2 µm band that appears in the VIRTIS-M spectrum of the surface of 67P/Churyumov-Gerasimenko. We have tested two candidates for accounting for the presence of this band: (i) carboxylic acids and (ii) ammonium salts. **We have shown, on the basis of laboratory experiments that the band is due to ammonium salts. There is in addition a weak contribution of organic C-H bonds contributing around 3.4 µm.**

From a methodological point of view, we have tested different protocols of sample preparation, in particular hand-mixed samples and sublimation residues. **Hand-mixed samples are not relevant analogs of the cometary crust, while sublimation residues fit well with the high porosity of the cometary material and its sub-micrometric texture.**

However, several issues are still pending:

- **The determination of the ammonium abundance form reflectance spectra is still a major question.** Even for sublimation residue, there is no clear relationship between the ammonium band depth and its abundance in the sample. The parameter that controls the band depth then remains unclear. Overall, for these dark samples, note that Hapke's models are definitely not suitable and that quantification reported in literature should be considered as non-reliable.
- The description of the texture of the samples has been restricted to a (rough) appraisal of the grain size distribution. However, **porosity, and overall the geometry of the texture certainly play a major role but they are unknown.**
- **Pure ammonium salts have been considered, but we expect more complex mixtures at the surface of the comet.** More relevant materials should be considered.

In the future, new experiments addressing these issues should be conducted. The characterization of the sample texture could be investigated *in situ* in environmental Scanning Electron Microscope. Under such conditions, the sample would never be in contact with the atmosphere (no collapse with porosity decreases, interaction of hygroscopic salt with moisture).

The characterization of the texture geometry from SEM images should be investigated. Different approaches might be possible. First, image processing by dedicated software, thanks

to collaboration with specialists of the field. Second, complementary characterization: for instance gas adsorption for quantifying *in situ* the porosity, or *ex situ* analysis for quantifying the local and global abundance of ammonium ions across the samples. This could be achieved by, for instance, Thermo Gravimetric Analysis coupled to FTIR (available at the ISTerre institute on the campus), AFM-IR that allows collecting infrared spectra at a nanometric spatial scale (~40 nm).

Finally, the thermal stability of the ammonium ions should be investigated through systematic experiments. This is a key issue, as the local temperature at the surface of the comet is close to the sublimation temperature.

Appendix

Absorption coefficient of carboxylic acids at 25 K and 175 K

Table A.1 Absorption coefficient of formic acid.

HCOOH 25 K (amorphous)		**HCOOH 175 K (crystalline)**	
Wavenumber (cm^{-1})	**Absorption Coefficient in (cm^{-1})**	**Wavenumber (cm^{-1})**	**Absorption Coefficient in (cm^{-1})**
3111	4191 + 35	2997	2357 + 20
3048	5658 + 47		
2953	6287 + 52	2962	3667 + 31
		2898	5763 + 48
2753	3929 + 33	2784	4191 + 35
2583	3405 + 29	2561	6025 + 50
		2451	9954 + 83
		2120	4453 + 37
1890	487 + 4	1890	786 + 7
1713	16502 + 138	1709	1179 + 10
1640	4977 + 42	1610	2096 + 17
1391	1572 + 13	1390	13097 + 110
1371	1310 + 11	1372	7858 + 66
1211	8225 + 69	1254	3929 + 33
		1218	11787 + 98
1072	1100 + 9	1081	10478 + 87
927	2567 + 21	966	3405 + 28
713	2279 + 19	720	6811 + 57

Table A.2. Absorption coefficient of acetic acid.

CH3COOH 25 K (amorphous)		**CH3COOH 175 K (crystalline)**	
Wavenumber (cm^{-1})	**Absorption Coefficient in (cm^{-1})**	**Wavenumber (cm^{-1})**	**Absorption Coefficient in (cm^{-1})**
3026	5084 + 51	2992	5620 + 56
2994	4817 + 48	2930	8028 + 80
2942	4522 + 45	2762	3211 + 32
2812	2355 + 24		
2804	2367 + 24	2762	4549 + 45
2740	1935 + 19	2676	1873 + 19
2690	2168 + 22	2621	5620 + 56
2641	2221 + 22	2532	8028 + 80
2578	1873 +19	1741	12845 + 128
1759	3880 + 38	1700	2542 + 25
1713	12845 + 129	1659	10169 + 102
		1646	8296 + 83
		1528	535 + 5
1517	85 + 1	1445	1739 + 17
1438	2408 + 24	1409	6155 + 62
1412	3586 + 36	1368	2408 + 24
1365	2141 + 21	1353	2408 + 24
1308	4282 + 43	1283	21943 + 219
1284	5218 + 52	1230	1338 + 13
1247	2596 + 26	1051	1338 + 13
1053	12845 + 129	1024	3746 + 37
1021	2061 + 21	915	5620 + 56
957	1525 + 15	902	5084 + 51
900	1606 + 16	886	2408 + 24
		709	241 + 2
628	1258 + 13	633	4683 + 47
		598	214 + 2
		492	107 + 1
		474	1606 + 16

Bibliography

Abdellaoui, M and Gaffet, E. 1995. The physics of mechanical alloying in a planetary ball mill: Mathematical treatment. Acta Metallurgica et Materialia 43:1087-1098.

A'Hearn, M.F., Belton, M.J.S., Delamere, W.A., Kissel, J., Klaasen, K.P., McFadden, L.A., Meech, K.J., Melosh, H.J., Schultz, P.H., Sunshine, J.M., Thomas, P.C., Veverka, J., Yeomans, D.K., Baca, M.W., Busko, I., Crockett, C.J., Collins, S.M., Desnoyer, M., Eberhardy, C.A., Ernst, C.M., Farnham, T.L., Feaga, L., Groussin, O., Hampton, D., Ipatov, S.I., Li, J.-Y., Lindler, D., Lisse, C.M., Mastrodemos, N., Owen, W.M. Jr., Richardson, J.E., Wellnitz, D.D., and White, R.L.. 2005. Deep Impact: excavating comet Tempel 1. Science. 310. 258–264.

A'Hearn, M.F. 2006. Whence comets?. Science. 314. 1708–1709.

Altwegg, K. H. Balsiger, J.J. Berthelier, A. Bieler, U. Calmonte, S.A. Fuselier, F. Goesmann, S. Gasc, T. I. Gombosi,L. Le Roy, J. deKeyser,A. Morse, M. Rubin, M. Schuhmann, M. G. G. T Taylor,C.-Y. Tzou, I. Wright et al. 2017. Organics in comet 67P - a first comparative analysis of mass spectra from ROSINA-DFMS, COSAC and Ptolemy. Monthly Notices of the Royal Astronomical Society, 469(Suppl 2) S130-S141.

Altwegg, K., H. Balsiger, J.-J. Berthelier, C. Briois, M. Combi, H. Cottin, J. De Keyser, F. Dhooghe, B. Fiethe, S. A. Fuselier, T. I. Gombosi, N. Hänni, M. Rubin, M. Schuhmann, I. Schroeder, T. Sémon, S. Wampfler. 2019. Evidence of ammonium salts in comet 67P as explanation for the nitrogen depletion in cometary comae. Nature astronomy (accepted)

Bardyn, A., D. Baklouti,H. Cottin,N.Fray, C. Briois, J. Paquette, O. Stenzel, C. Engrand, H. Fischer, K. Hornung, R. Isnard, Y. Langevin, H. Lehto,L. Le Roy,N.Ligier, S. Merouane, P. Modica, F.R Orthous-Daunay,J. Ryno, R. Schulz, J. Silén, L. Thirkell, K. Varmuza, B. Zaprudin, J. Kissel and M. Hilchenbach. 2017. Carbon-rich dust in comet 67P/Churyumov-Gerasimenko measured by COSIMA/Rosetta. Monthly Notices of the Astronomical Society, 469, S712–S722.

Barucci, M. A., G. Filacchione, S. Fornasier, A. Raponi, J. D. P. Deshapriya, F. Tosi, C. Feller, M. Ciarniello, H. Sierks, F. Capaccioni, A. Pommerol, M. Massironi, N. Oklay, F. Merlin, J.-B. Vincent, M. Fulchignoni, A. Guilbert-Lepoutre, D. Perna, M. T. Capria, P. H. Hasselmann, B. Rousseau, C. Barbieri, D. Bockelée-Morvan, P. L. Lamy, C. De Sanctis, R. Rodrigo, S. Erard, D. Koschny, C. Leyrat, H. Rickman, P. Drossart, H. U. Keller, M. F. A'Hearn, G. Arnold, J.-L. Bertaux, I. Bertini, P. Cerroni, G. Cremonese, V. Da Deppo, B. J. R. Davidsson, M. R. El-Maarry, S. Fonti, M. Fulle, O. Groussin, C. Güttler, S. F. Hviid, W. Ip, L. Jorda, D. Kappel, J. Knollenberg, J.-R. Kramm, E. Kührt, M. Küppers, L. Lara, M. Lazzarin, J. J. Lopez Moreno, F. Mancarella, F. Marzari, S. Mottola, G. Naletto, M. Pajola, E. Palomba, E. Quirico, B. Schmitt, N. Thomas and C. Tubiana. 2016. Detection of exposed H2O ice on the nucleus of comet 67P/Churyumov-Gerasimenko as observed by Rosetta OSIRIS and VIRTIS instruments. A&A 595, A10.

Battandier, Manon. 2019. Etude d'une série de micrométéorites antarctiques : caractérisation multi-analytique et comparaison à des chondrites carbonées. PhD thesis.

Beck, P., E. Quirico, G. Montes-Hernandez, L. Bonal, J. Bollard, F.-R. Orthous-Daunay, K. Howard, B. Schmitt, O. Brissaud, F. Deschamps, et al. 2010. Hydrousmieralogy of CM and CI chondites from infrared spectroscopy and their relationshipwith low albedo asteroids. Geochimica et Cosmochimica Acta, 74(16) :4881–4892.

Beck, P. , Quirico, E. , Sevestre, D. , et al. , 2011. Goethite as an alternative origin of the 3.1 μm band on dark asteroids. Astronomy Astrophysics. 526, A85.

Bennett, C. J., and Ralf I. Kaiser. 2007. The formation of acetic acid (CH3COOH) in interstellar analogs, The astrophysical journal. 660:1289-1295.

Bentley, M. S., Schmied, R., Mannel, T., Torkar, K., Jeszenszky, H., Romstedt, J., Levasseur-Regourd, A.-C., Weber, I., Jessberger, E. K., Ehrenfreund, P., Koeberl, C., and Havnes, O. 2016. Aggregate dust particles at comet 67P/Churyumov-Gerasimenko. Nature, 537(7618) :73–75.

Bisschop,S.E., G. W. Fuchs, A. C. A. Boogert, E. F. van Dishoeck, and H. Linnartz. 2007. Infrared spectroscopy of HCOOH in interstellar ice analogues. Astronomy & Astrophysics. 470. 749-759.

Bossa, J. B., P. Theulé, F. Dauvernay, F. Borget, T. Chiavassa. 2008. Carbamic acid and carbamate formation in NH_3:CO_2 ices – UV irradiation versus thermal processes. A&A.492, 719-724.

Bouilloud, M., N. Fary, Y. Bénilan, H. Cottin, M.-c. Gazeau and A. Jolly. 2015. Bibliographic review and new measurements of the infrared band strengths of pure molecules at 25 K: H2O, CO2, CO, CH4, NH3, CH3OH, HCOOH and H2CO. MNRAS 451, 2145–2160.

Brandt, J.C. and Chapman, R.D. 2004.Introduction to Comets, 2nd edn, Cambridge University Press, Cambridge.

Bratoz, S., D. Hadzi and N. Sheppard, 1956, The-Infrared absorption bands associated with the COOH and COOF groups in dimeric carboxylic acids-II. The region from 3700 to 1500 cm^{-1}. Spectrochimica Acta. Vol.8. 249-261.

Brissaud, O. , Schmitt, B. , Bonnefoy, N. , et al. , 2014. Spectrogonio radiometer for thestudy of the bidirectional reflectance and polarization functions of planetarysurfaces. 1. Design and Tests.. Appl. Optics 43, 1926–1937.

Brownlee, D., Horz, F., Newburn, R.L., Zolensky, M., Duxbury, T.C., Sandford, S., Sekanina, Z., Tsou, P., Hanner, M.S., Clark, B.C., Green, S.F., and Kissel, J.. 2004. Surface of young Jupiter family comet 81 P/Wild 2: view from the Stardust Spacecraft. Science. 304. 1764–1769.

Capaccioni, F. A. Coradini, G. Filacchione, S. Erard, G. Arnold, P. Drossart, M. C. De Sanctis, D. Bockelee-Morvan, M. T. Capria, F. Tosi, C. Leyrat, B. Schmitt, E. Quirico, P. Cerroni,

V. Mennella, A. Raponi, M. Ciarniello, T. McCord, L. Moroz,E. Palomba, E. Ammannito, M. A. Barucci, G. Bellucci, J. Benkhoff, J. P. Bibring, A. Blanco, M. Blecka, R. Carlson, U. Carsenty, L. Colangeli, M. Combes, M. Combi, J. Crovisier, T. Encrenaz, C. Federico, U. Fink, S. Fonti, W. H. Ip, P. Irwin, R. Jaumann, E. Kuehrt, Y. Langevin, G. Magni, S. Mottola, V. Orofino, P. Palumbo, G. Piccioni, U. Schade, F. Taylor, D. Tiphene, G. P. Tozzi, P. Beck, N. Biver, L. Bonal, J.-Ph. Combe, D. Despan,2 E. Flamini, S. Fornasier, A. Frigeri, D. Grassi, M. Gudipati, A. Longobardo, K. Markus, F. Merlin, R. Orosei, G. Rinaldi, K. Stephan, M. Cartacci, A. Cicchetti, S. Giuppi, Y. Hello, F. Henry, S. Jacquinod, R. Noschese, G. Peter, R. Politi, J. M. Reess, A. Semery. 2015. The organic-rich surface of comet 67P/Churyumov-Gerasimenko as seen by VIRTIS/Rosetta.*Science,* 347. Issue 6220, aaa0628.

Ciarletti, V., S. Clifford, D. Plettemeier, A. Le Gall, Y. Herve, S.Dorizon, C. Quantin-Nataf, W-S Benedix, S.usanne Schwenzer,E. Pettinelli, E. Heggy, A. Herique, J-J Berthelier, W. Kofman, J. L. Vago, S-E Hamran, and the WISDOM team. 2017. The WISDOM Radar: Unveiling the Subsurface Beneath the ExoMars Rover and Identifying the Best Locations for Drilling. Astrobiology. Volume 17. Numbers 6 and 7.

Ciarniello, M., F. Capaccioni, G. Filacchione, A. Raponi, F. Tosi, M. C. De Sanctis, M. T. Capria, S. Erard, D. Bockelee-Morvan, C. Leyrat, G. Arnold, A. Barucci, P. Beck, G. Bellucci, S. Fornasier, A. Longobardo, S. Mottola, E. Palomba, E. Quirico and B. Schmitt. 2015. Photometric properties of comet 67P/Churyumov-Gerasimenko from VIRTIS-M onboard Rosetta. Astronomy & Astrophysics. 583. A31

Chelli, R., R. Righini, S. Califano. 2005. Struture of liquid formic acid investigated by first principle and classical molecular dynamics simulation. J.Phys. Chem.B. 109. 17006-1713.

Coradini, A., F. Capaccioni, P. Drossart, G. Arnold, E. Ammannito, F. Angrilli, A. Barucci, G. Bellucci, J. Benkhoff, G. Bianchini, J. P. Bibring, M. Blecka, D. Bockelee-Morvan, M. T. Capria, R. Carlson, U. Carsenty, P. Cerroni, L. Colangeli, M. Combes, M. Combi, J. Crovisier, M. C. Desanctis, E. T. Encrenaz, S. Erard, C. Federico, G. Filacchione, U. Fink, S. Fonti, V. Formisano, W. H. Ip, R. Jaumann, E. Kuehrt, Y. Langevin, G. Magni, T. Mccord, V. Mennella, S. Mottola, G. Neukum, P. Palumbo, G. Piccioni, H. Rauer, B. Saggin, B. Schmitt, D. Tiphene, G. Tozzi 2007. Virtis : An Imaging Spectrometer for the Rosetta Mission. Space Science Reviews. 128 :529–559.

Cyriac, R. and T. Pradeep. 2004. Structural transformation in formic acid on ultra cold ice surfaces. Chemical Physics Letters. 402.116–120.

Dyar, M.D., E.C. Skulte, O.N. Menzies, P.A. Bland, D. Lindsley, T. Glotch, M.D. Lane, M.W. Schaefer, R. Klima, J.L. Bishop, T. Hiroi, C. Pieters, and J. Sunshine. 2009. Spectroscopic characteristics of synthetic olivine: An integrated multi-wavelength and multi-technique approach. American Mineralogist, Volume 94, pages 883–898.

Dobrica, E. , Engrand, C. , Duprat, J. , et al. , 2009. Connection between micrometeorites and Wild 2 particles from Antarctic snow to cometary ices. Met. Plan. Sci. 44.1643–1661.

Eberhardt, P. 1999. Comet Halley's gas composition and extended sources: results from the neutral mass spectrometer on Giotto. Space Sci. Rev., 90. 45–52.

Faure, Mathilde. 2016. Évolution des glaces et des composés organiques interstellaires et cométaires : Étude expérimentale et analyse des données VIRTIS/ROSETTA. PhD Thesis.

Filacchione, G., F. Capaccioni, M. Ciarniello, A. Raponi, F. Tosi, M. Cristina De Sanctis, S. Erard, D. Bockelee Morvan, C. Leyrat, G. Arnold, B. Schmitt, E. Quirico, G. Piccioni, A. Migliorini, M. T. Capria, Ernesto Palomba, Priscilla Cerroni, Andrea Longobardo, Antonella Barucci, S. Fornasier, Robert W. Carlson, R. Jaumann, K. Stephan, Lyuba V. Moroz, David Kappel, Batiste Rousseau, Sergio Fonti, F. Mancarella, D. Despan, M. Faure. 2016. The global surface composition of 67P/CG nucleus by Rosetta/VIRTIS. (I) Prelanding mission phase. *Icarus*. **274**, 334–349.

Fomenkova, M. N. and Chang, S. 1994. Carbon in comet Halley dust particle. In Analysis of Interplanetary Dust, eds. M. E. Zolensky, T.L. Wilson, F. J. M. Rietmeijer, and G. J. Flynn (New York: Am. Inst. Phys.), pp 193-202.

Fornasier,S., P. H. Hasselmann, M. A. Barucci, C. Feller1, S. Besse, C. Leyrat, L. Lara, P. J. Gutierrez, N. Oklay, C. Tubiana, F. Scholten, H. Sierks, C. Barbieri, P. L. Lamy, R. Rodrigo, D. Koschny, H. Rickman, H. U. Keller, J. Agarwal, M. F. A'Hearn, J.-L. Bertaux, I. Bertini, G. Cremonese, V. Da Deppo, B. Davidsson, S. Debei, M. De Cecco, M. Fulle, O. Groussin, C. Güttler, S. F. Hviid, W. Ip, L. Jorda, J. Knollenberg, G. Kovacs, R. Kramm, E. Kührt, M. Küppers, F. La Forgia, M. Lazzarin, J. J. Lopez Moreno, F. Marzari, K.-D. Matz, H. Michalik, F. Moreno, S. Mottola, G. Naletto, M. Pajola, A. Pommerol, F. Preusker, X. Shi, C. Snodgrass6, N. Thomas, and J.-B. Vincent. 2015. Spectrophotometric properties of the nucleus of comet 67P/Churyumov-Gerasimenko from the OSIRIS instrument onboard the ROSETTA spacecraft. A&A 583, A30.

Fortin, T. J.et al 2002. Infrared spectroscopic study of the low-temperature phase behavior of ammonium sulfate. Journal of Geophysical Research: Atmospheres 107.

Fray, N., A. Bardyn1, H. Cottin, K. Altwegg, D. Baklouti, C. Briois, L. Colangeli, C. Engrand, H. Fischer, A. Glasmachers, E. Grün, G. Haerendel, H. Henkel,H. Höfner, K, Hornung, E. K. Jessberger, A. Koch, H. Krüger, Y. Langevin, H. Lehto, K. Lehto L. Le Roy, S. Merouane, P. Modica, F-R Orthous-Daunay, J. Paquette, F. Raulin, J. Rynö, R. Schulz, J. Silén, S. Siljeström, W. Steiger, O. Stenzel,T. Stephan, L. Thirkell, R. Thomas, K. Torkar, K. Varmuza, K-Peter Wanczek24, B. Zaprudin, J. Kissel & M. Hilchenbach. 2016. High-molecular-weight organic matter in the particles of comet 67P/Churyumov Gerasimenko. Nature,538(7623), pp.72-74.

Frasco, D.L. 1964. Infrared Spectra of Ammonium Carbamate and Deuteroammonium Carbamate The Journal of Chemical Physics **41**, 2134.

Gicquel.A, J.-B. Vincent, J. Agarwal, M. F. A'Hearn, I. Bertini, D. Bodewits,H. Sierks, Z.-Y. Lin, C. Barbieri, P. L. Lamy, R. Rodrigo, D. Koschny, H. Rickman, H. U. Keller, M. A. Barucci, J.-L. Bertaux, S. Besse,G. Cremonese, V. Da Deppo, B. Davidsson, S. Debei, J. Deller, M. De Cecco, E. Frattin, M. R. El-Maarry, S. Fornasier, M. Fulle, O. Groussin, P. J.

Guti´errez, P. Guti´errez-Marquez, C. G¨uttler, S. H¨ofner,M. Hofmann, X. Hu, S. F. Hviid, W.-H. Ip, L. Jorda, J. Knollenberg, G. Kovacs,1, J.-R. Kramm, E. K¨uhrt, M. K¨uppers, L. M. Lara, M. Lazzarin, J. J. Lopez Moreno, S. Lowry, F. Marzari, N. Masoumzadeh, M. Massironi, F. Moreno, S. Mottola, G. Naletto, N. Oklay, M. Pajola, A. Pommerol,F. Preusker, F. Scholten, X. Shi, N. Thomas, I. Toth, and C. Tubiana. 2016. Sublimation of icy aggregates in the coma of comet 67P/Churyumov–Gerasimenko detected with the OSIRIS cameras on board Rosetta. MNRAS. 462. S57–S66.

Gounelle, M. and Zolensky, M.E. , 2001. A terrestrial origin for sulfate veins in CI1 chondrites.Met. Plan. Sci. 36, 1321–1329.

Hamann, S and E. Spinner, 1977. The effect of pressure on the infrared spectrum of ammonium formate: HCO_2NH_4 . DCO_2NH_4 . HCO_2ND_4 . DCO_2ND_4 . An unusual intermolecular coupling of non-identical vibrations in phase II. Australian Journal of Chemistry**. 30**. 2591 (1977).

Hapke, B. 2012. Theory of reflectance and emittance spectroscopy 2nd ed. University Press Cambridge.

Isnard, A. Bardyn, N. Fray, C. Briois, H. Cottin1, J. Paquette, O. Stenzel, C. Alexander, D. Baklouti,C. Engrand, F.-R. Orthous-Daunay7, S. Siljeström, K. Varmuza, and M. Hilchenbach. 2019. H/C elemental ratio of the refractory organic matter in cometary particles of 67P/Churyumov-Gerasimenko.Aastronomy & Astrophysics. 630. A27.

Keller, H.U., Arpigny, C., Barbieri, C., Bonnet, R.M., Cazes, S., Coradini, M., Cosmovici, C.B., Delamere, W.A., Huebner, W.F., Hughes, D.W., Jamar, C., Malaise, D., Reitsema, H.J., Schmidt, H.U., Schmidt, W.K.H., Seige, P., Whipple, F.L., andWilhelm, K. 1986. First Halley multicolour camera imaging results from Giotto. Nature. 321. 320–326.

Keller, H.U., Delamere, W.A., Huebner, W.F., Reitsema, H.J., Schmidt, H.U., Whipple, F.L., Wilhelm, K., Curdt, W., Kramm, R., Thomas, N., Arpigny, C., Barbieri, C., Bonnet, R.M., Cazes, S., Coradini, M., Cosmovici, C.B., Hughes, D.W., Jamar, C., Malaise, D., Schmidt, K., Schmidt, W.K.H., and Seige, P. 1987. Comet P/Halley's nucleus and its activity. Astronomy & Astrophysics. 187. 807–823.

Kremnev, R.S., Linkin, V.M., Lipatov,A. N., Pichkadze, K.M., Shurupov, A.A., Terterashvili, A.V., Bakitko, R.V., Blamont, J.E., Malique, C., Ragent, B., Preston, R.A., Elson, L.S., and Crisp, D. 1986. Vega balloon system and instrumentation. Science, 231, 1408–1411.

Le Roy, L. K. Altwegg, H. Balsiger, J.-J. Berthelier, A. Bieler, C. Briois, U. Calmonte, M. R. Combi, J. De Keyser, F. Dhooghe, B. Fiethe, S. A. Fuselier, Sébastien Gasc, Tamas I. Gombosi, Myrtha Hässig, A. Jäckel, M. Rubin2 and Chia-Yu Tzou. 2015. Inventory of the volatiles on comet 67P/Churyumov-Gerasimenko from Rosetta/ROSINA. Astronomy & Astrophysics. 583, A1.

Lewandowski, H., E. Koglin, Robert J. Meier. 2005. Computational study of the infrared spectrum of acetic acid,its cyclic dimer, and its methyl ester. Vibrational Spectroscopy. 39. 15–22.

Lin-Vien, D. , Colthup, N.B. , Fateley, W.G., Grasseli, J.G., 1991. The Handbook of Infrared and Raman Characteristic Frequencies of Organic Molecules. Academic Press, San Diego, p. 503.

Millikan,R.C. and K.S. Pitzer.1958. The infrared spectra of dimeric and crystalline formic acid J. Am. Chem. Soc. 81.3515.

Mumma, M.J., DiSanti, M.A., Magee-Sauer, K., Bonev, B.P., Villanueva, G.L., Kawakita, H., Dello Russo, N., Gibb, E.L., Blake, G.A., Lyke, J.E., Campbell, R.D., Aycock, J., Conrad, A., and Hill, G.M. . 2005. Parent volatiles in comet 9P/Tempel 1: before and after impact. Science. 310. 270–274.

Mumma, M. J. and Charnley, S. B. 2011. The Chemical Composition of Comets—Emerging Taxonomies and Natal Heritage. Annual Review of Astronomy and Astrophysics, 49(1) :471–524.

Noble, J.A., P. Theule, F. Duvernay, G. Danger,T. Chiavassa, P. Ghesquiere, T. Mineva and D. Talbi. 2014. Kinetics of the NH_3 and CO_2 solid-state reaction at low temperature. Phys.Chem.Chem.Phys. 16. 23604.

Oort, J.H. .1990.in Physics and Chemistry of Comets (ed. W.F. Huebner). Springer. Heidelberg. pp. 235–244.

Poch, O., et al. 2016a. Sublimation of ice-tholins mixtre : A morphological and spectrophotometric study. Icarus.266.288-305.

Poch, O., et al. 2016b. Sublimation of water ice mixed with silicate and tholins: Evolution of surface texture and reflectance spectra, with implication for comet. Icarus. 267. 154-173.

Poch, O., I.Istiqomah, E. Quirico, P. Beck, B. Schmitt, P. Theulé, A. Faure, P. Hily-Blant, B. Rousseau, S. Potin, O. Brissaud, L. Flandinet, L. Bonal, A. Raponi, M. Ciarniello, G. Filacchione, A. Pommerol, N. Thomas, D. Kappel, V. Mennella, L. Moroz, V. Vinogradoff, G. Arnold, D. Bockelée-Morvan, F. Capaccioni, M. C. De Sanctis, S. Erard, C. Leyrat, A. Longobardo, F. Mancarella, E. Palomba, F. Tosi. 2020. First detection of ammonium salts on a cometary nucleus, revealing a new reservoir of nitrogen. Science. 1212.

Pommerol, A., B.Jost, O.Poch, M.R.El-Maarry, B.Vuitel,c, N.Thomas. 2015. The SCITEAS experiment: Optical characterizations of sublimating icy planetary analogues. Planetary and Space Science. 109-110. 106–122

Quirico, E., L.V. Moroz , B. Schmitt, G. Arnold, M. Faure, P. Beck, L. Bonal, M. Ciarniello, F. Capaccioni, G. Filacchione, S. Erard, C. Leyrat, D. Bockelée-Morvan, A. Zinzi, E. Palomba, P. Drossart, F. Tosi, M.T. Capria, M.C. De Sanctis, A. Raponi, S. Fonti, F. Mancarella, V. Orofino, A. Barucci, M.I. Blecka, R. Carlson, D. Despan, A. Faure, S. Fornasier, M.S. Gudipati, A. Longobardo, K. Markus, V. Mennella, F. Merlin, G. Piccioni, B. Rousseau, F. Taylor. 2016. Refractory and semi-volatile organics at the surface of comet 67P/Churyumov-Gerasimenko: Insights from the VIRTIS/Rosetta imaging spectrometer. Icarus 272, 32-47.

Raponi et al. 2020. Aliphatic organics on comet 67P/Churyumov-Gerasimenko: from interstellar dust to pristine solar system. Nature Astronomy.

Reinhard, R. 1986. The Giotto encounter with comet Halley. Nature. 321. 313–318.

Rickman, H. and Huebner, W.F. 1990. in Physics and Chemistry of Comets (ed.W.F. Huebner). Springer. Heidelberg.pp. 245–304.

Rotundi, A., Sierks, H., Della Corte, V., Fulle, M., Gutierrez, P. J., Lara, L., Barbieri, C., Lamy, P. L., Rodrigo, R., Koschny, D., Rickman, H., Keller, H. U., López-Moreno, J. J., Accolla, M., Agarwal, J., A'Hearn, M. F., Altobelli, N., Angrilli, F., Barucci, M. A., Bertaux, J.-L., Bertini, I., Bodewits, D., Bussoletti, E., Colangeli, L., Cosi, M., Cremonese, G., Crifo, J.-F., Da Deppo, V., Davidsson, B., Debei, S., De Cecco, M., Esposito, F., Ferrari, M., Fornasier, S., Giovane, F., Gustafson, B., Green, S. F., Groussin, O., Grün, E., Güttler, C., Herranz, M. L., Hviid, S. F., Ip, W., Ivanovski, S., Jerónimo, J. M., Jorda, L., Knollenberg, J., Kramm, R., Kührt, E., Küppers, M., Lazzarin, M., Leese, M. R., López- Jiménez, A. C., Lucarelli, F., Lowry, S. C., Marzari, F., Epifani, E. M., McDonnell, J. A. M., Mennella, V., Michalik, H., Molina, A., Morales, R., Moreno, F., Mottola, S., Naletto, G., Oklay, N., Ortiz, J. L., Palomba, E., Palumbo, P., Perrin, J.-M., Rodríguez, J., Sabau, L., Snodgrass, C., Sord ni, R., Thomas, N., Tubiana, C., Vincent, J.-B., Weissman, P., Wenzel, K.-P., Zakharov, V., and Zarnecki, J. C. 2015. Dust measurements in the coma of comet 67P/Churyumov-Gerasimenko inbound to the Sun. Science, 347(1) :aaa3905.

Rousseau, B. 2017a. Étude de la composition et des propriétés physiques de surface de la comète 67P/Churyumov-Gerasimenko. Interprétation des données VIRTIS/Rosetta et mesure en réflectance d'analogues cométaires. PhD Thesis.

Rousseau, B., S.Érard, P.Beck, É.Quirico, B.Schmitt, O.Brissaud, G.Montes-Hernandez, F.Capaccioni, G.Filacchione, D.Bockelée-Morvan, C.Leyrat, M.Ciarniello, A.Raponi, D.Kappel, G.Arnold, L.V.Moroze, E.Palomba, F.Tosidth, VIRTIS Team. 2017b. Laboratory simulations of the Vis-NIR spectra of comet 67P using sub-µm sized cosmochemical analogues. Icarus. 306, 306–318.

Rubin, M. Altwegg K., Balsiger H., Bar-Nun A., Berthelier JJ, Bieler A, Bochsler P., Briois C., Calmonte U., Combi M., De Keyser J., Dhooghe F., Eberhardt P., Fiethe B., Fuselier SA., Gasc S., Gombosi T., Hansen KC., Hässig M., Jäckel A., Kopp E., Korth A., Le Roy L., Mall U., Marty B., Mousis O., Owen T., Rème H., Sémon T, Tzou CY., Waite JH, Wurz P.. 2015. Molecular nitrogen in comet 67P/Churyumov-Gerasimenko indicates a low formation temperature. Science. 348. 232–235

Sandford, S.A., Aléon, J., Alexander, C.M.O.'.D., Araki, T., Bajt, S., Baratta, G.A., Borg, J., Bradley, J.P., Brownlee, D.E., Brucato, J.R., Burchell, M.J., Busemann, H., Butterworth, A., Clemett, S.J., Cody, G., Colangeli, L., Cooper, G., d'Hendecourt, L., Djouadi, Z., Dworkin, J.P., Ferrini, G., Fleckenstein, H., Flynn, G.J., Franchi,I.A., Fries, M., Gilles, M.K., Glavin, D.P., Gounelle, M., Grossemy, F., Jacobsen, C., Keller, L.P., Kilcoyne, A.L.D., Leitner, J., Matrajt, G., Meibom, A., Mennella, V., Mostefaoui, S., Nittler, L.R., Palumbo, M.E., Papanastassiou, D.A., Robert, F., Rotundi, A., Snead, C.J., Spencer, M.K.,

Stadermann, F.J., Steele, A., Stephan, T., Tsou, P., Tyliszczak, T., Westphal, A.J., Wirick, S., Wopenka, B., Yabuta, H., Zare, R.N., and Zolensky, M.E. 2006. Organics captured from comet 81P/Wild 2 by the Stardust spacecraft. Science. 314. 1720–1724.

Schulz, R. and Schwehm, G. 1996. 46P/Wirtanen : necessary observations in support of ROSETTA. Planetary Space Science, 44 :619–624.

Schumaker, Norman E. and Carl W. Garland. 1970. Infrared Investigation of Structural and Ordering Changes in Ammonium Chloride and Bromide. J. Chem. Phys. 53, 392.

Sephton M.A. 2000. Organic matter in meteorite. A&G.April.Vol 45.

Sephton M.A. 2002. Organic compounds in carbonaceous meteorites. Nat. prod. Rep. 19, 292-311.

Soderblom, L.A., Becker, T.L., Bennett, G., Boice, D.C., Britt, D.T., Brown, R.H., Buratti, B.J., Isbell, C., Giese, B., Hare, T., Hicks, M.D., Howington-Kraus, E., Kirk, R.L., Lee, M., Nelson, R.M., Oberst, J., Owen, T.C., Rayman, M.D., Sandel, B.R., Stern, S.A., Thomas, N., and Yelle, R.V.. 2002. Observations of comet 19P/Borrelly by the miniature integrated camera and spectrometer aboard Deep Space 1. Science. 296.1087–1091.

Sung, C-M., R.B. Singer, K. M. Parkin, R.G. Burns, M. Osborne. 1977. Temperature dependence of Fe^{2+}crystal field spectra: Implications to mineralogical mapping of planetary surfaces. Proceeding Lunar Science Conference 8^{th}. 1063-1079.

Theulé, P., F.Duvernay, G.Danger, F.Borget, J.B.Bossa, V.Vinogradoff, F.Mispelaer, T.Chiavassa. 2013. Thermal reactions in interstellar ice: A step towards molecular complexity in the interstellar medium. Advances in Space Research. **52**, 1567–1579

Veverka, J., K.Klaasen, M.A'Hearn, M.Belton, D.Brownlee, S.Chesley, B.Clark, T.Economou, R.Farquhar, S.F.Green, O.Groussin, A.Harris, J.Kissel, J.-Y.LicK, Meech, J.Melosh, J.Richardson, P.Schultz, J.Silen, J.Sunshine, P.Thomas, S.Bhaskaran, D.Bodewits, B.Carcich, A.Cheuvront, T.Farnham, S.Sackett, D.Wellnitz, A.Wolfb. 2013. Return to comet Tempel 1: overview of Stardust- NExT results. Icarus. 222. 424–435.

Weis, D.D and G. E. Ewing. Infrared spectroscopic signatures of $(NH_4)_2 SO_4$ aerosols. Journal of Geophysical Research: Atmospheres. 101. 18709–18720 (1996).

Weissman, P.R., Bottke, W.F. Jr., and Levison, H.F.. 2002. in Asteroids III. (eds W.F. Bottke Jr., A. Cellino, P. Paolicchi, and R.P. Binzel). University of Arizona Press. Tucson. AZ. pp.669–686.

Whipple, F.L. 1950. A comet model. I. The acceleration of comet Encke. Astrophysics Journal. 111. 375–394.

Yoldi, Z. A. Pommerol, B. Jost, O. Poch, J. Gouman, N. Thomas., 2015. VIS–NIR reflectance of water ice/regolith analogue mixtures and implications for the detectability of ice mixed within planetary regoliths. Geophys. Res. Lett. 42, 6205–6212